Influence of the Alpine Orogeny on Siderite-hosted Five-Element Veins: Reconstruction of a 240 to 6 Ma Multi-Stage Bi-Co-Ni-Fe-As-S-(U) System in the Penninic Alps, Switzerland

-Genetic Controls on Mineralogical Features in Five-Element Veins-

Dissertation
der Mathematisch-Naturwissenschaftlichen Fakultät
der Eberhard Karls Universität Tübingen
zur Erlangung des Grades eines
Doktors der Naturwissenschaften
(Dr. rer. nat.)

vorgelegt von
M.Sc. Stefan Kreißl
aus Kirchheim u. Teck

Tübingen
2018

Gedruckt mit Genehmigung der Mathematisch-Naturwissenschaftlichen Fakultät der Eberhard Karls Universität Tübingen.

Tag der mündlichen Qualifikation:	04.06.2018
Dekan:	Prof. Dr. Wolfgang Rosenstiel
1. Berichterstatter:	Prof. Dr. Gregor Markl
2. Berichterstatter:	PD Dr. Thomas Wenzel

Für Jasmin

Copyright information

This work includes contents of the article “Reconstruction of a >200 Ma multi-stage “five element” Bi-Co-Ni-Fe-As-S system in the Penninic Alps, Switzerland” published in Ore Geology Reviews under the corresponding DOI:
https://doi.org/10.1016/j.oregeorev.2018.02.008

Danksagung

Zuerst möchte ich meinen besonderen Dank an Prof. Dr. Gregor Markl für die Vergabe meines Promotionsthemas und sein mir damit entgegengebrachtes Vertrauen aussprechen. Nur durch sein Verständnis für meine Arbeitsweiße und seine unentwegte Hilfe bei der Publikation meiner gewonnenen Ergebnisse stehe ich heute dort, wo ich bin. Ebenso danke ich Gregor für die finanzielle Unterstützung während des Beginns meiner Doktorarbeit und darüber hinaus.

Für die Zweitbetreuung meiner Arbeit und seine ständige Unterstützung bei den Mikrosondenmessungen möchte ich PD. Dr. Thomas Wenzel meinen großen Dank aussprechen. Ebenso danke ich Ihm für zahlreiche und hilfreiche Gespräche, das Korrekturlesen von Manuskripten und vor allem für seinen großen Einfluss währen meiner Ausbildung in Tübingen.

Dr. Udo Neumann möchte ich für seine Hilfe bei der Mikroskopie, das Bereitstellen von Literatur sowie dem Korrekturlesen von Manuskripten danken. Ebenso möchte ich Ihm einen besonderen Dank aussprechen, da er meine Fähigkeiten in der Erz-Mikroskopie stark beeinflusst hat.

Für das Bereitstellen der Probensammlungen von Prof. Dr. Huttenlocher und Markus Schafer danke ich Prof. Dr. Beda Hofmann vom Naturhistorischem Museum in Bern und Dr. Nicolas Meisser vom Musée Cantonal de Géologie in Lausanne. Entsprechende Verwendung des Probenmaterials und Umbenennung geht aus Table A1 im Anhang (Appendix) hervor. Die Hilfe von Stefan Ansermet und Johann Grill bedanke ich für die Begleitung während der Geländearbeit im Wallis und den Niederen Tauern.

Einen besonderen Dank möchte ich and Prof. Dr. Marcus Nowak und PD Dr. Michael Marks richten, die wie Gregor, Thomas und Udo maßgeblich an meiner Ausbildung in Tübingen beteiligt waren. Beide konnten -nicht nur in dieser Arbeit- mit ihrer unermüdlichen und konstruktiven Kritik immer neue Sichtweisen eröffnen.

Meinen Kollegen Maximilian Keim, Manuel Scharrer, Dr. Sebastian Staude, Dr. Benjamin Walter, Tatjana Epp, Dr. Mathias Burisch, Rainer Babiel, Johannes Giebel, Simon Braunger, Marguerita Duchoslav, Petya Atanasova und Anja Allabar -sowie allen die ich möglicherweise vergaß- möchte ich herzlichst für die gemeinsame Bearbeitung verschiedenster Projekte das Korrekturlesen meiner Arbeit sowie die tolle Zeit in Tübingen danken.

Für die Hilfe und Unterstützung bei der Analytik bedanke ich mich vielmals bei Dr. Axel Gerdes, Linda Marko, Dr. Thomas Theye, Dr. Melanie Keuper, Dr. Tobias Kiemle, Dr. Mathias Burisch, Dr. Benjamin Walter, Maximilian Keim, Dr. Christoph Berthold und Ann-Kathrin Fetzer.

Für die herausragende Probenpräparation und Ihre unentwegte Hilfe bedanke ich mich herzlichst bei Simone Schafflick. Clemens Gabriel Gacmenga danke ich für seine tadellose und interessierte Mithilfe bei Vorbereitungen der Präparate zur Isotopenmessung.

Den Koautoren meiner Publikationen Dr. Axel Gerdes, Prof. Dr. Gregor Markl, Manuel Scharrer, Dr. Udo Neumann, PD Dr. Thomas Wenzel und Dr. Benjamin Walter danke ich für die gute Zusammenarbeit.

Mein ganz besonderer Dank meinen Eltern, ihren Partnern, meinen Großeltern und Freunden. Zuletzt möchte ich insbesondere meiner Freundin für Ihre Liebe und Unterstützung in den letzten 8 Jahren danken. Unsere Zukunft ist das, was mich jeden Tag antreibt!

Table of content

Zusammenfassung

Zu den sogenannten Fünf Element Gängen („five-element veins”) werden hydrothermale Ganglagerstätten gezählt, welche meist dendritisch bzw. skelettartig ausgebildeten Metalle aufweisen und im weiteren Kristallisationsverlauf von Fe-Co-Ni Arseniden, -Sulfarseniden und letztlich von Karbonaten eingeschlossen werden. Obwohl deren Klassifizierung auf die Charakterisierung spezieller Ganglagerstätten mit gediegenem Silber, Nickel- und Cobalterz zurückgeht (Bastin 1939), ist die Bezeichnung „five-element veins“ seit der Arbeit von Halls and Stumpfl (1972) und dessen Bezug auf die fünf Elemente Ag, Co, Ni, Bi und As ein anerkannter Begriff geworden. Der außerordentlichen Diversität solcher Ganglagerstätten wird dieser Ausdruck nicht gerecht, so ist Fe fast immer als Arsenid oder Sulfarsenid gebunden und zusätzlich können z.B. S, Sb und U vorhanden sein. Generell werden hydrothermale Systeme, in welchen sich Fünf Element Gänge entwickeln, in folgende Stadien unterteilt (Kissin 1992):

Stadium 1: Quarz-Sulfid Vorphase
Stadium 2: Uraninit-Quarz Vorphase (nur vereinzelt beobachtet)
Stadium 3: fünf Element Hauptphase
(gediegen Ag/Bi → Fe-Co-Ni Arsenide/-Sulfarsenide → Karbonat)
Stadium 4: Sulfid-Karbonat-Quarz Nachphase
Stadium 5: Tieftemperatur Karbonat Phase (meist Calcit)

Vorhergehende Arbeiten erklären die Entwicklung von konventionellen, sulfidischen Systemen mit Quarz hin zur Präzipitation gediegener Metalle und Arseniden mit Karbonat durch die Zufuhr von Methan und/oder anderen Kohlenwasserstoffen in ein existierendes Hydrothermalsystem, welches zuvor keinen Kohlenstoff beinhaltete. Im Zuge einer gekoppelten Reaktion, werden die zuvor wässrig gelösten As- und Bi-Spezies $As^{3+}(OH)_3$, $Bi^{3+}Cl_4^-$ und $Ag^{1+}Cl_2^-$ zu Ag^0, Bi^0, As^0 und As^{-1} reduziert und als gediegen Wismut oder Silber und Fe-Co-Ni-Arsenide/-Sulfarsenide ausgefällt. Die kontinuierliche Oxydation der Kohlenwasserstoffe (z.B. $C^{4-}H_4$; $C_2^{3-}H_6$) zu $C^{4+}O_2$ oder $HC^{4+}O_3^-$ resultiert in der Präzipitation von Karbonaten anstatt von Quarz.

Vorhergehender Arbeiten zeigen, dass eine Reduktion bei verschiedenen pH-Werten entweder gediegen Arsen-dominierte, Arsenid-dominierte oder gediegen Wismut- bzw. gediegen Silber-dominierte Mineralisationen bevorzugt. Jedoch ist die mineralogische Diversität zwischen den verschiedenen Mono-, Di- und Triarseniden sowie deren Fe-Co-Ni-Variationen noch nicht gänzlich geklärt worden. Obwohl einige Arbeiten neben der Beeinflussung durch Kohlenwasserstoffe auch die Oxydation von Eisen(II)-haltigen Sulfiden oder Silikaten für eine Fluidreduktion vorschlagen, wurde die Auflösung von Siderit und die damit gekoppelten Erniedrigung der Sauerstofffugazität bisher nicht in Betracht gezogen. Hierdurch bedingte pH Veränderungen können jedoch den Ursprung der mineralogischen Variabilität erklären.

Die vorliegende Arbeit belegt verschiedene Prozesse, die zur mineralogischen, kompositionellen und strukturellen Diversität von Bi-Fe-Co-Ni-As-S-U mineralisierten Siderit-Dolomit-Ankerit Gängen aus der penninischen Siviez-Mischabel-Decke der Walliser Alpen geführt haben. Um variable Fluidbedingungen (pH, Temperatur, Metall-, Arsen- und Schwefelaktivitäten) zu untersuchen, wurden strukturelle Beziehungen, Mineralchemie, Fluideinschlusszusammensetzungen (Mikrothermometrie und Raman-Spektroskopie) und stabile C-O-S-Isotopensysteme mit thermodynamischen Fluidentwicklungsmodellen kombiniert. Erztexturen, C-O-Isotope und

Fluideinschlüsse deuten darauf hin, dass die Auflösung von primärem Siderit, die Oxidation von Eisen(II) und dessen Ausscheidung als Magnetit die Reduktion der Fluide zur Folge hatte. Dies führte zur Ausfällung von gediegenem Wismut, Fe-Co-Ni-Arseniden und -Sulfarseniden (Bi^0, As^{3-} und As^{-1}) aus ihren oxidierten, wässrigen Spezies wie beispielsweise $Bi^{3+}Cl_4^-$ und $As^{3+}(OH)_3$ bei Temperaturen zwischen 200-300°C. Dieser Prozess und der Vergleich zu Na-Ca-Variationen der Fluideinschlüsse belegen, dass absinkende Fluide mit bereits existierendem Siderit reagierten und beim Abstieg durch das sedimentäre Deck- und kristalline Grundgebirge zusätzlich chemischen Veränderungen unterworfen waren (Deckgebirge: Karbonat-, Sulfat- und Halit- Auflösung; Grundgebirge: Albitisierung von Plagioklas, Auflösung von Biotit und Hornblende).

Veränderungen von Fe-reichen zu Ni-Co reichen und letztendlich Fe-Co-Ni-reichen Arsenid- und Sulfarsenid-Zusammensetzungen weisen auf eine primär verstärkte Siderit-Auflösung hin, welche sukzessiv durch die zunehmende Fluid-Gesteins-Wechselwirkung des Hydrothermalsystems mit den Nebengesteinen beeinflusst wird. Während des Wechsels von primären hin zu umgelagerten Erzmineralisationen zeigen sinkende S-Isotopen- und As/S-Signaturen zudem auf eine zunehmende Schwefel-Mobilisierung aus den Sulfid-haltigen Nebengesteinen (im Fachjargon Fahlbänder genannt) hin.

Da Fünf Element Gänge im zeitlichen und geotektonischen Kontext meist an großtektonische Grabenbruchsysteme gebunden sind, gibt es weder Informationen darüber wie sich solche Lagerstättentypen während einer Metamorphose verhalten noch darüber, ob die Kompressionsphase eines orogenen Zyklus primäre Bildungen begünstigen kann. Die Kombination von komplex zonierter Mikrostrukturen mit deren Mineralchemie und zugehörigen ortsaufgelösten U-Pb Altersdatierungen zeigen eine fast lückenlose zeitliche Einordnung der Prozesse von der primären Erzausfällung bis hin zur sekundären Elementumverteilung und Modifikation durch die alpine Deformation. Hierfür konnten U-Pb Thera-Wasserburg-Alter an einzelnen Karbonaten und Magnetiten aber auch an paragenetisch assoziierten Multi-Mineral-Fraktionen berechnet werden, welche Fe-Co-Ni-Arsenide, -Sulfarsenide, Fe-Ti-Oxide, Chlorit, Albit und Annabergit beinhalten. Die ermittelten Alter lassen eine Einteilung in sechs verschiedene Stadien zu. Diese enthalten unter anderem primäre Bildungen von gediegenem Wismut, Arseniden und Sulfarsenides im Trias und Jura (Stadien II und IV) sowie deren sekundäre Umverteilung während der Alpenbildung (Stadien Va und Vb). Die vier Stadien der Bi-Fe-Co-Ni-As-S-U mineralisierten Bildungsphasen können wie folgt definiert werden:

Stadium II:	Bildung von gediegenem Wismut, Löllingit, Skutterudit, Magnetit und Dolomit aus ursprünglich sedimentären Fluiden, welche Siderit auflösen (233±10 Ma);
Stadium IV:	Ausfällung von gediegenem Wismut, Nickelin, Gersdorffit, Skutterudit, Magnetit und Ankerit durch den sukzessiven Eintrag von Nickel, Kobalt und Schwefel (188±32 Ma);
Stadium Va:	Rekristallisierung und Umverteilung der primären Erztexturen durch prograde Metamorphose und weitere Mobilisierung von Schwefel aus dem Nebengestein (71.1±1.4Ma - 44.6±1.5 Ma); und
Stadium Vb:	erneute Ausfällung von gediegenem Wismut, Safflorit, Cobaltit und Skutterudit, welche den primären Fünf Element Gängen mineralogisch und strukturell ähnlich sind (28.2±1.1 Ma).

Basierend auf der Kombination von U-Pb Altern, paläotektonischer Rekonstruktionen, Deformationsstrukturen sowie mineralogischer und chemischer Variabilität können folgende Gründe für die primäre Erzbildung im Trias und deren sukzessive Beanspruchung bis hin zu postalpinen Prozessen eingeteilt werden:

Stadien II-IV: Präalpine Erzbildung durch Extension, hervorgerufen durch die Öffnung des Meliata Ozeans und der Alpinen Tethys;
Stadium Va: synalpine Auflösung und Wiederausfällung der Erze durch die europäisch-adriatische Kontinent-Kontinent Kollision; und
Stadium Vb: spätalpine Prozesse, welche durch laterale Extrusion und transtensionaler Extension zur erneuten Bildung von Fünf Element Gängen und die Umverteilung von gediegenem Wismut führten

Vergleichbare mineralogische Trends zwischen den Fünf Element Gängen im Wallis und anderen Arsenid-dominierten Gängen in Mitteleuropa und thermodynamische Modelle zeigen, dass die häufig in Erscheinung tretenden Wechsel zwischen Mono-, Di- und Triarsenides sowie deren konsistente Ni→Co→Fe Entwicklung durch eine einfache Reduktion von erzhaltigen Fluiden entstehen können. Durch geringfügig unterschiedliche Fluidzusammensetzungen und unterschiedliche pH-Werte ist zudem eine weitere und generelle Unterteilung für die Arsenid-dominierten Fünf Element Gänge in folgende Gruppen möglich:

1. Fe-Co-Arsenid dominierte Erze
2. Ni-Co-Arsenid dominierte Erze
3. Ni-Co-Fe-Arsenid dominierte Erze

Abstract

Hydrothermal five-element veins (Ag-Co-Ni-Bi-As) are mineral successions of native metals, encapsulated by Fe-Co-Ni arsenides and carbonates. Recent studies focused on the evolution from ordinary base-metal systems (sulfide-rich) to five-element veins (sulfide-poor) and revealed the importance of hydrocarbon-dominated fluids as an essential redox agent in these fluid systems. The fluid pH is stated to subdivide this type of mineralization into arsenide-, native arsenic- and native silver or bismuth-dominated vein types, but the mineralogical diversity upon the arsenides (MeAs, $MeAs_2$ and $MeAs_3$) and their transition metal variations (Me: Fe, Co and Ni) are not well understood yet. Although different studies suggested fluid reduction by oxidation of ferrous iron from sulfides and silicates, the impact of siderite dissolution as redox mechanism and its potential to diversify mineralogical features and fluid properties (such as pH) has not been considered.

This is the first case study explaining mineralogical, compositional, and textural features of unique Bi-Fe-Co-Ni-As-S-U mineralized siderite-dolomite-ankerite veins from the Middle Penninic basement of the Siviez-Mischabel Nappe (Valais Alps, Switzerland). Textural relationships, mineral chemistries, fluid inclusion compositions (microthermometry and Raman spectroscopy) and stable C-O-S-isotopes were combined to thermodynamic fluid evolution models to investigate changing fluid conditions (pH, temperature, metal-, arsenic- and sulfur-activities). Ore textures, C-O-isotopes and fluid inclusion studies indicate that the dissolution of primary siderite, oxidation of ferrous iron and its precipitation as magnetite was the most important redox couple to precipitate native Bi, arsenides and sulfarsenides (Bi^0, As^{3-} and As^{-1}) from their oxidized aqueous species $Bi^{3+}Cl_4^-$, and $As^{3+}(OH)_3$ at temperatures between 200-300°C. These processes and comparative Ca-Na variations suggest that a single fluid equilibrated with cover rocks during fluid descent and later interacted in-situ with preexisting siderite veins and adjacent host rocks within the basement (i.e. cover rocks: carbonate, sulfate and halite dissolution; basement rocks: albitisation of plagioclase, alteration of biotite and hornblende).

Shifts of transition metal signatures from Fe- to Co-Ni- and lastly to ternary Fe-Co-Ni-dominated compositions, show a first dominance of siderite dissolution and further increased host rock mobilization during the successive evolution of the hydrothermal system. From primary to the secondary ores, stable S-isotopes and As/S-signatures of sulfides and sulfarsenides indicate an increasing sulfur mobilization from host rock sulfides (i.e. fahlbands).

Since most five-element veins spatially and temporally link to large scale rifting, information is limited about their behavior during metamorphism or the possibility of a primary formation during compressive orogenic cycles. In the present case, the comparison of complex zoned microstructures, mineral chemistries and in-situ U-Pb ages reveal the processes and timing of primary ore formation, interaction with the sulphide-bearing host rocks and secondary modifications by deformation and elemental redistribution during the Alpine Orogeny. It was possible to determine U-Pb Tera-Wasserburg ages of paragenetic mineral fractions of carbonates, magnetite and multi-mineral isochrons including Fe-Co-Ni-arsenides, -sulfarsenides, Fe-Ti-oxides, chlorite, albite and annabergite. Observed ages constrain the classification of stages I-VI, at which primary precipitation of native Bi, arsenides and sulfarsenides happened during Triassic and Jurassic times (stages II and IV) and secondary redistribution processes of these ores affected by Alpine processes (stages Va and Vb). These stages of five-element vein precipitation and corresponding mechanisms of their primary formation and remobilization are:

Stage II: Native Bi-löllingite-skutterudite-magnetite-dolomite precipitation from pristine sedimentary brines dissolving earlier siderite at 233±10 Ma;

Stage IV: native Bi-niccolite-gersdorffite-skutterudite-magnetite-ankerite ores, which indicate progressive fluid-host rock interaction and consequential influx of Ni, Co and S at 188±32 Ma;

Stage Va: in-situ recrystallization and overprint of the primary assemblages as ternary Fe-Co-Ni sulfarsenides accompanied by prograde metamorphism and further mobilization of the host rock sulfides between 71.1±1.4 and 44.6±1.5 Ma; and

Stage Vb: native Bi-safflorite-cobaltite-skutterudite stage with similar textures and mineralogies to the primary stages and common for five-element veins at 28.2±1.1 Ma.

Based on compared U-Pb ages, paleotectonic reconstructions, deformation textures, mineralogical variabilities and chemical variations, following tectonic processes caused the primary Triassic formation and its succession to post-Alpine tectonics:

Stage II-IV: Primary and pre-Alpine ore formation due to rift-induced extensive tectonics during the Meliata and Alpine Tethys Rifts;

Stage Va: syn-Alpine in-situ remobilization and deformation during European-Adriatic continent-continent collision; and

Stage Vb: late-Alpine neoformation of five-element mineralogies and native Bi remobilization due to lateral extrusion and transtensional extension of the Western Alpine arc.

The comparison of hydrochemical and mineralogical trends of the very special occurrences in the Penninic Alps to similar arsenide-dominated five-element veins in Central Europe reveals that frequently occurring mineralogical shifts between mono-, di- and triarsenides as well as the Ni→Co→Fe transition established due to simple fluid reduction of hydrothermal system. Due to differences in the fluid chemistries and pH conditions, this work suggests a further and general subdivision of arsenide-dominated five element veins into the following classes:

1. Fe-Co arsenide-dominated ores
2. Ni-Co arsenide-dominated ores
3. Ni-Co-Fe arsenide-dominate ores

1. Introduction

Five-element veins are hydrothermal vein type deposits with a characteristic association of native metals (Bi, Ag and As), Fe-Co-Ni-arsenides and -sulfarsenides hosted by carbonate gangue. Although the nomenclature was based on the five elements Ni-Co-As-Ag-Bi (Halls and Stumpfl 1972; Kissin 1992), Fe is present in the most cases and the mineralization types show substantial textural and mineralogical variability. Different subtypes can occur with only a subset of these five elements and/or additional elements such as S, Sb and U (Bastin 1939). Disregarding this variability, most studies on five-element veins explain the idealized paragenetic sequence as an evolution from common hydrothermal systems precipitating (i) quartz with Pb-Cu-Zn-Fe-sulfides, followed by a succession of (ii) native metals, Fe-Co-Ni-arsenides and -sulfarsenides hosted by carbonates, and finally again precipitating (iii) base metal sulfides, but hosted by carbonates (Bastin 1939; Kissin 1992). Such five-element veins occur worldwide and have been the subject of extensive research for almost a century (Bugge 1931; Keil 1933; Petruk 1968; Berry 1971; Robinson and Ohmoto 1973; Andrews 1986; Andrews et al. 1986a; Andrews et al. 1986b; Changkakoti and Morton 1986; Changkakoti et al. 1986; Franklin et al. 1986; Goodz et al. 1986; Kerrich et al. 1986; Leblanc 1986; Wilkerson et al. 1988; Cheilletz et al. 2002; Wagner and Lorenz 2002; Lipp and Flach 2003b; Ondrus et al. 2003a; Ondrus et al. 2003b; Ondrus et al. 2003c; Fanlo et al. 2004; Fanlo et al. 2006; Ahmed et al. 2009; Gervilla et al. 2012; Bouabdellah et al. 2016; Essarraj et al. 2016; Levresse et al. 2016; Markl et al. 2016; Burisch et al. 2017; Essarraj et al. 2017; Kiefer et al. 2017; Kotková et al. 2017; Manuel et al. 2018).

Several authors discussed diverse formation mechanisms, since five-element veins are neither host rock related (sediment-, unconformity- or basement-hosted) nor their physicochemical parameters are similar in all deposits (formation temperatures, fluid chemistry and isotope characteristics). Although fluid mixing has been proposed as an important precipitation mechanism (Kissin 1992; Marshall et al. 1993; Staude et al. 2012b), the metal bearing fluids are controversially discussed and either originate from magmatic reservoirs (Bastin 1939; Sampson and Hriskevich 1957; Jambor 1971; Conte et al. 2016; Levresse et al. 2016) or from host rock leaching during hydrothermal/metamorphic processes (Boyle and Dass 1971; Kerrich et al. 1986; Smyk and Watkinson 1990).

A recent model for five-element vein formation by Markl et al. (2016) provides an explanation for the unique textures and the shift of a conventional base metal hydrothermal system with quartz to the sequence of native metals, Fe-Co-Ni-arsenides and carbonate gangue. The model suggests an influx of methane and/or other hydrocarbon species into a hydrothermal system, which previously was free of carbon and the aqueous arsenic and metal species were predominantly dissolved as

$As^{3+}(OH)_3$, $Bi^{3+}Cl_4^-$, and $Ag^{1+}Cl_2^-$. This process causes a coupled reduction of the arsenic and metal species to As^0, As^{-1}, Bi^0 and Ag^0, and a continuous oxidation of the hydrocarbons to CO_2 resulting in the precipitation of carbonates instead of quartz after re-equilibration of the system to the host rocks. This model has then been applied to the five-element veins in the Odenwald (Germany) by Burisch et al. (2017), including a ternary mixing of a metal-rich basement brine and a sulfide-bearing basinal/sedimentary brine with a methane-dominated fluid. Ore fluids containing CO_2, methane, propane and ethane had also been observed from similar deposits at Cobalt-Gowganda (Kerrich et al. 1986) and Bou Azzer (Essarraj et al. 2005). In addition to five-element veins, deposition of native Ag in the Anti-Atlas region has been attributed to the mixing of meteoric, low-salinity, low-density N_2-CH_4-CO_2 fluids to metal-bearing, high salinity basinal brines and successive cooling (Ag-Hg stage; Essarraj et al. 2016; Essarraj et al. 2017). These studies implicate that the metal bearing fluids which are related to metamorphic basement brines evolved from residual sedimentary brines.

Generally, the majority of five-element veins are linked to large-scale extensional settings, showing anomalous heat flow, fault-fracture meshes, enhanced rock permeability, fluid mobilization and migration (Kutina 1972; Norman 1978; Garson and Mitchell 1981; Andrews 1986; Kissin 1988; Kissin 1992; Sibson 1996; Essarraj et al. 2005; Essarraj et al. 2016; Burisch et al. 2017; Essarraj et al. 2017). In contrast, the deposits investigated in the present study are located in mid-crustal rocks affected by the compressive regime of the Alpine Orogeny.

Occurrences of such Alpine hosted five-element veins are numerous and have been described from the Pennine Alps, Switzerland; Niedere Tauern region, Austria; Belledonne Massive, France; and Piemont Alps, Italy (Henwood 1871; Huttenlocher 1925; Hießleitner 1929; Friedrich 1933; Bastin 1939; Gilliéron 1946; Clavel 1963; Ypma 1963; Ypma 1972; Paar and Chen 1979; Sartori and Della Valle 1986; Schmutz 1986; Woodtli et al. 1987; Fuchs 1988; Della Valle 1992; Schafer 1996; Feitzinger et al. 1998; Meisser 2003; Castelli et al. 2011; Ansermet 2012; Rossi and Gattiglia 2013; Rossi et al. 2013; Rossi and Gattiglia 2015). Although the mineralogical appearance has been detailed investigated and the affiliation to five-element veins is unambiguous, the paragenetic sequences and textures are scarcely documented (Niedere Tauern, Zinkwand/Vetternspitze: Friedrich 1933; Belledonne Massive, Les Chalances/Allemont: Ypma 1963; Piemont Alps, Usseglio: Castelli et al. 2011; Penninic Alps, Val d'Anniviers/Turtmanntal: Ansermet 2012). Additional deposits from settings related to the Alpine Belt formation are described in more detail from the Pyrenees, Sardinia and Western Carpathians (Fanlo et al. 2004; Fanlo et al. 2006; Naitza et al. 2013; Naitza et al. 2015; Conte et al. 2016; Kiefer et al. 2017; Naitza et al. 2017; Manuel et al. 2018).

Since siderite is abundant in most of these localities, a formation process triggered by the oxidation of ferrous iron as a potent redox agent is speculative, but never been investigated in detail. Furthermore, studies of the deposits hosted in the Alpine Belt do not distinguish between different fluid reservoirs, do not present detailed formation models and especially do not correlate age data and the temporal relation of the deposit to the various stages of the Alpine orogeny. Additionally, a detailed analogy of mineralogical and genetic properties between these deposits is missing in literature.

2. Scientific Aims

The affiliation of the Bi-Fe-Co-Ni-As-S-U mineralized siderite-dolomite ankerite veins in the Penninic sections of the Western Alps to the so-called "five-element veins" is undisputed. Nevertheless, no detailed and modern studies exist that define the processes of ore formation and especially the impact of siderite, what differentiates the observed occurrences from other known five-element veins. Additionally, the question arises if these occurrences are the result of pre-, syn- or post-Alpine processes. If pre-Alpine processes triggered these hydrothermal veins, cumulative information from occurrences with different grades of tectonic conditions lead to a better understanding of how five-element veins behave during orogenic cycles.

Due to mineralogical, compositional, and textural features compared to fluid inclusion compositions, stable C-O-S-isotopes, U-Pb ages and thermodynamic fluid evolution models it is possible for the first time to:

- Investigate if siderite dissolution and ferrous iron oxidation is a relevant redox process in five-element vein precipitation.
- Clarify the temporal conditions of five-element ore formation upon the Alpine Orogeny.
- Reconstruct five-element ore genesis from primary mineralization settings to the polyphase tectonometamorphic overprint and remobilization (i.e. chemical and mineralogical changes with time).
- Investigate the possibility of a primary formation during compressive regimes in orogenic cycles.
- Understand the processes of element input and chemical changes during ore precipitation in a long-lived hydrothermal system (i.e. hydrothermal fluid sources, mobilization from host rock lithologies, and redistribution during prograde and retrograde metamorphism).
- Contribute to an improved understanding of mineralogical variabilities that result from similar first order processes, only modified by slight changes of the hydrothermal fluid conditions.

3. Alpine geotectonic context and regional geology

The Bi-Co-Ni-Fe-As-S-(U) mineralized siderite-dolomite-ankerite veins at Kaltenberg, Grand Praz, Pipji and Collioux Inférieur are located in the Penninic Alps of the Western Alpine arc (Figure 1a). Their host rocks belong to the Middle Penninic basement nappe (Briançonnais terrane) between the underlying Lower Penninic (formerly northern Valais Trough) and the overlying Upper Penninic (formerly Alpine Tethys/Piemont Ocean) (Biju-Duval et al. 1977; Frisch 1979; Thélin et al. 1993; Figure 1b). According to Figure 2a, the Middle Penninic realm was previously placed between the Helvetic in the north and Austroalpine in the south and formerly represented the southern continuation of the Variscan basement (Pfiffner 2015). This region was successively stressed by extensional tectonics and subsidence due to the breakup of the Neotethys/Meliata Ocean in the Middle Triassic and Alpine Tethys/Upper Penninic and Lower Penninic in the Early and Middle Jurassic (Figure 2a-c and h). Escher et al. (1997) showed that during the Eoalpine stage, the Upper Penninic Ocean subducted southwards under the Austroalpine terrane (110-85 Ma); and the Lower Penninic Valais Trough placed in same direction below the Middle Penninic terrane (85-60 Ma) (Figure 2c, d). The Lower- to Middle Penninic nappe-pile consequently collided with, and underthrusted the Upper Penninic- to Austroalpine nappe-pile in S-SE direction resulting in major thrust faults, folds and the further “differentiation” of the Middle Penninic nappe (Mesoalpine phase, 45-30 Ma) (Figure 2e). Penecontemporaneously, the European continental margin (Helvetic Nappes and External Massifs) and Alpine foreland (post-Variscan sedimentary cover) north of the Valais Trough were overthrusted. From bottom to top, External Massifs, post-Variscan sedimentary cover, Lower-, Middle- and Upper Penninic, and Lower Austroalpine nappes form the present nappe pile of the Western Alpine Arc (Figure 1b).

Today, the Middle Penninic tectonic units subdivide into the Zone Houillère (ZH), Pontis (P), Siviez Mischabel (SM) and Mont Fort Nappes (MF) (Figure 1; Escher et al. 1997), whereas Sartori et al. (2006) connect the ZH and P Nappes to one single unit in the studied area. The veins considered in this work restrict to the SM Nappe, a NW-vergent recumbent fold of more than 35 km length in the north and an S-SE-vergent backfold in its internal southern part (Figure 1b). The NW-vergence and formation of the Middle Penninic nappe pile (i.e. SM, MF and P) is the result of the Mesoalpine collision (Alpine deformation D1 and D2; cf. Figure 2e, g and h). The intensive S-SE-vergent backfold was formed along with the Alpine deformation D3 as response to uplift and strong backthrusting due to dextral strike-slip tectonics at Neoalpine times 30-25 Ma ago (Sartori 1990; Escher et al. 1997) (Figure 2f-h).

The Middle Penninic Nappes comprise a basement core of Proterozoic to Ordovician age, tectonically enclosed by a Carboniferous to Eocene metasedimentary cover from its normal to

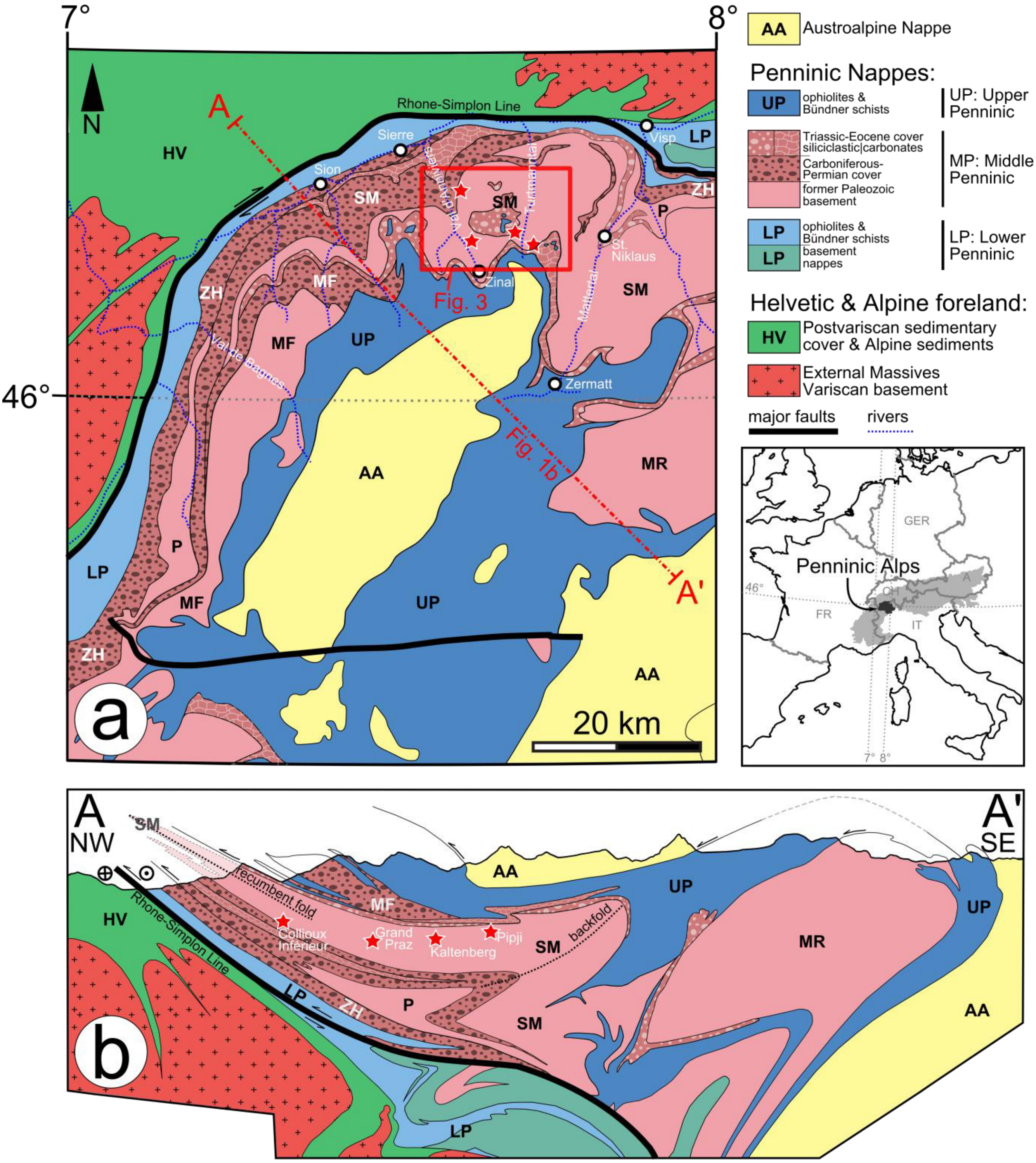

Figure 1: (a) Geological map of the Penninic Alps after Schmid et al. (2004) and Marthaler et al. (2008). (b) NW-SE profile A-A' of the Penninic Alps domain (after Escher et al. 1993). Extrapolated projection of the five-element veins indicate the position of the occurrences Collioux Inférieur, Grand Praz, Kaltenberg and Pipji. Middle Penninic rocks are ZH: Zone Houillère, P: Pontis, SM: Siviez Mischabel, MF: Mont Fort and MR: Monte Rosa. HV: Helvetic nappe, LP: Lower Penninic, SP: Sub-Penninic, UP: Upper Penninic, AA: Austroalpine.

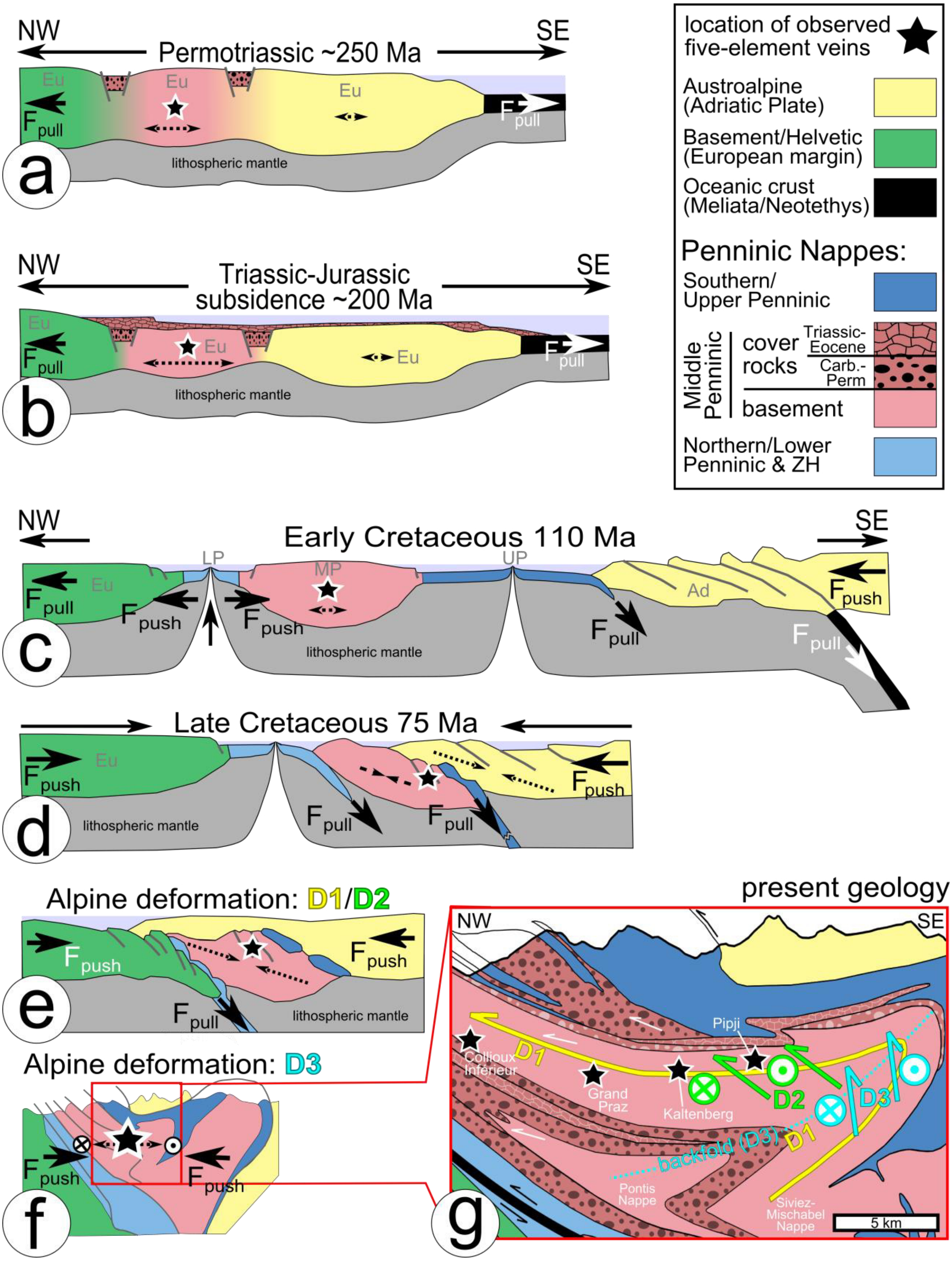
location of observed five-element veins ★
Austroalpine (Adriatic Plate)
Basement/Helvetic (European margin)
Oceanic crust (Meliata/Neotethys)
Penninic Nappes:
Southern/ Upper Penninic
Middle Penninic
cover rocks
Triassic-Eocene
Carb.-Perm
basement
Northern/Lower Penninic & ZH
NW
SE
Permotriassic ~250 Ma
Eu
F pull
lithospheric mantle
a
Triassic-Jurassic subsidence ~200 Ma
b
Early Cretaceous 110 Ma
LP
MP
UP
Ad
F push
c
Late Cretaceous 75 Ma
d
Alpine deformation: D1/D2
e
Alpine deformation: D3
f
present geology
Collioux Inférieur
Grand Praz
Kaltenberg
Pipji
D1
D2
D3
backfold (D3)
Pontis Nappe
Siviez-Mischabel Nappe
5 km
g

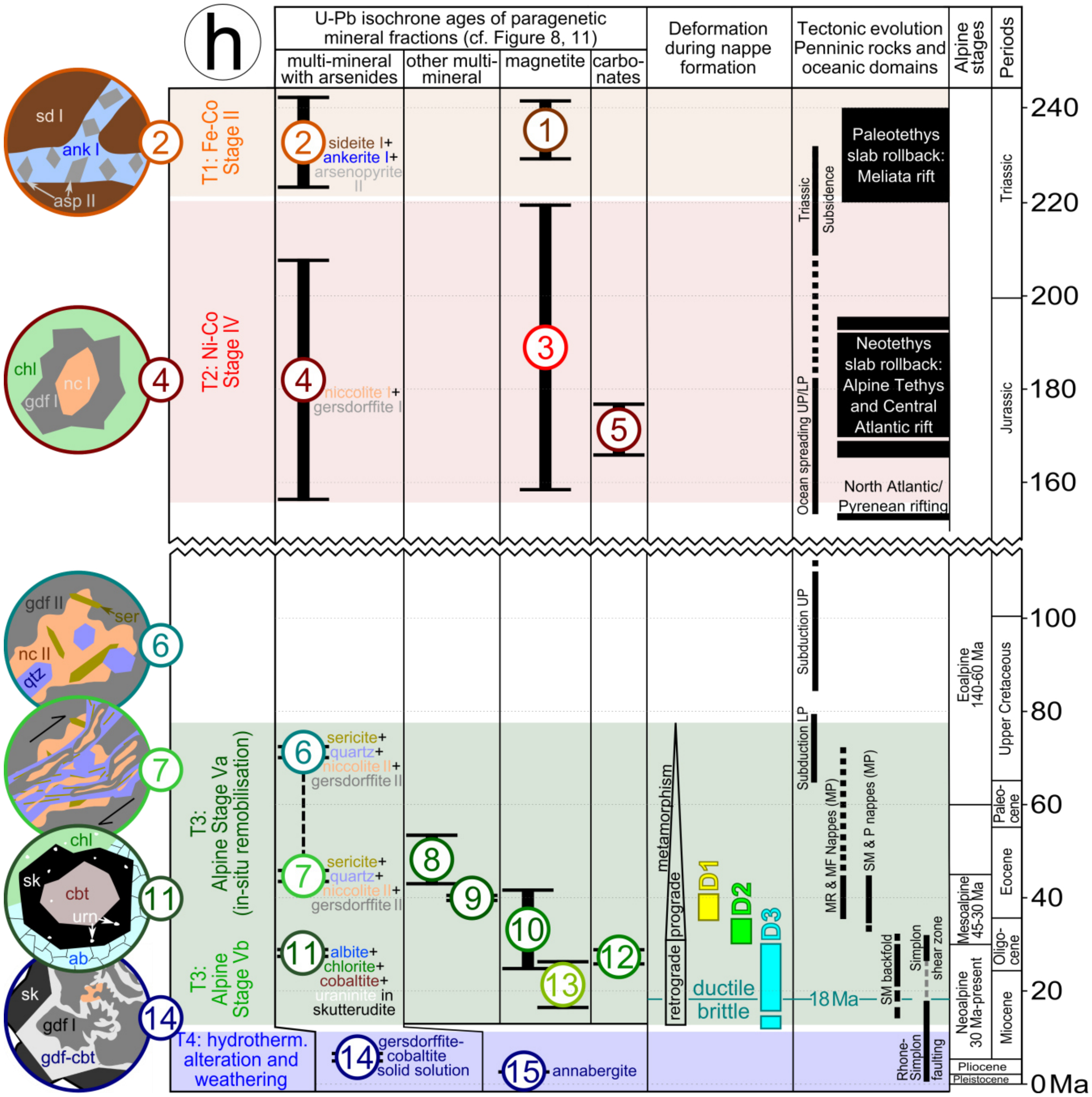

Figure 2: (a)-(g) Illustration of the plate tectonic evolution of the Alpine realm. F$_{pull}$ and F$_{push}$ indicates if effective motion was caused by extensive or compressive regimes, respectively. (h) Purposed mineralization events by the observed U-Pb isochrone ages of the studied samples including isochrons 1-15 (left; cf. Figure 8 and 11) compared to the paleotectonic evolution of the Alps and the Penninic Nappes (right) and the deformation model (middle). Ages of geologic and tectonic events according to Escher et al. (1997); Sartori (1990); Seward and Mancktelow (1994); Stampfli et al. (2002). Nappe abbreviations are UP: Upper Penninic, MP: Middle Penninic, LP: Lower Penninic, MR: Monte Rosa, MF: Mont Fort, SM: Siviez Mischabel, P: Pontis. Eu: European plate, Ad: Adriatic plate.

Ist inverted limb (cf. Figure 1b). Prior to Alpine tectonics, the former sedimentary cover consisted of Carboniferous to Permian detrital series and acid volcanic rocks overlain by Triassic to Eocene siliciclastic series, evaporites and lime- to dolostones (Sartori 1990; Escher et al. 1997; Sartori et al. 2006). Magmatic parts of the basement comprise metagabbros (504±2 Ma), the Mont-Rogneux meta-granite (500±4 Ma), the Randa meta-granite and correlated meta-rhyolites (267-282 Ma) (Thélin et al. 1993; Sartori et al. 2006). Stratigraphically, Sartori et al. (2006) subdivided the internal part of the basement core into Proterozoic, mostly polycyclic paragneisses and mica schists, including relictic pre-Alpine retro-eclogites within amphibolite lenses and layers (Ergischhorn and Adlerflüe formation); and Cambrian to Ordovician metavolcanic basites to metasedimentary rocks (Lirec, Distulberg and Métailler formation) (Figure 3a). Thélin et al. (1993) observed multiple (Variscan and Alpine) and single metamorphosed (Alpine greenschist facies) regions within the basement core, whereas this transition is located within the Cambrian to Ordovician section. Large amounts of disseminated sulfides (fahlbands; cf. Figure 3a), which show a volcano-sedimentary or hydrothermal origin (Della Valle 1992), are exclusively confined to the multiple metamorphosed mica schist and amphibolite strata. Most five-element veins occur in their vicinity but also at regions where only amphibolites are adjacent.

Structural observations show three major Alpine deformation events (cf. D1, D2 and D3 in Figure 2; Sartori 1990). Phase D1 is present in the whole SM nappe, whereas D2 is rather restricted to the rocks in the vicinity to Pipji and Kaltenberg and D3 only at the SE part of the upper Val d'Anniviers and Turtmanntal next to Pipji (cf. Figure 2g and Figure 3b). The major foliation (S1, ± parallel to preexisting lithostratigraphy) and large-scale isoclinal folds formed during D1 in the Upper Eocene due to overthrusting and the SM nappe formation (41-36 Ma, Markley et al. 1998). According to Sartori (1990), the subsequent D2 crenulation foliation (S2) developed in the Lower Oligocene by localized dextral shear between nappe formation and backfolding. Due to Upper Oligocene to Lower Miocene dextral transtensional strike-slip tectonics, backfolding and backthrusting, phase D3 developed an additional SE-vergent crenulation foliation (S3). Most likely, D2 and D3 are linked to the ductile, SW-directed dextral Simplon shear zone (since ~32 Ma) and the SE-vergent Vanzone backfold (since ~30 Ma), respectively (cf. Figure 2h; Steck 2008). Since the Upper Miocene, brittle deformation occurs as the presently active dextral Rhone-Simplon fault (Steck 2008; Bergemann et al. 2017).

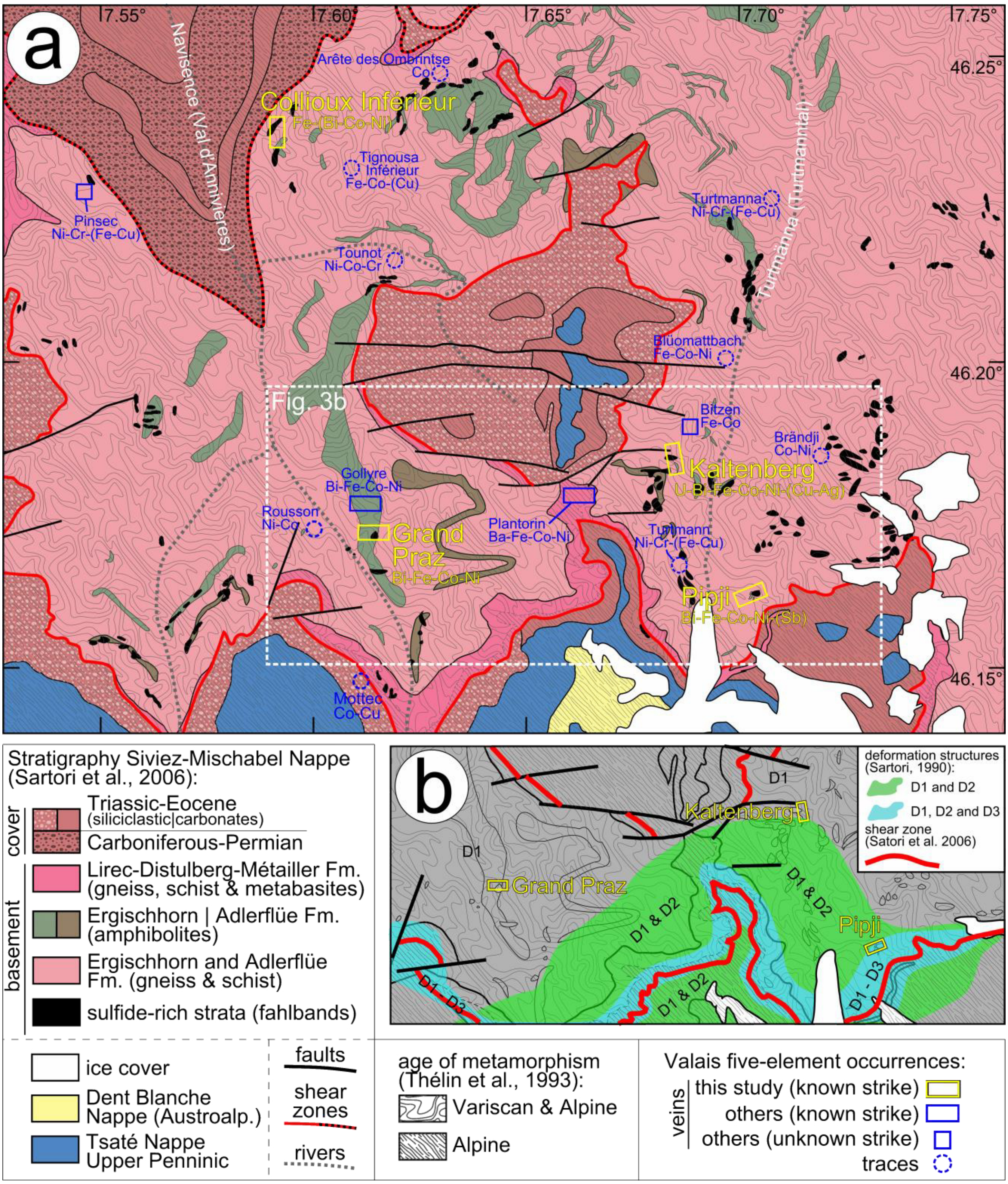

Figure 3: (a) Combined geological map of the Siviez Mischabel Nappe, the sulfide-bearing fahlbands and the five-element veins localized in the work area at the upper Turtmanntal and Val d'Anniviers (Bearth 1978; Della Valle 1992; Escher 1988; Marthaler et al. 2008; Sartori et al. 2006). Age of metamorphism according to Thélin et al. (1993); localities of the five-element occurrences and vein strike orientations as yellow and blue bars according to Cavalli et al. (1998). (b) Deformation structures D1, D2 and D3 as green and cyan colored regions and shear zones as red lines according to Sartori (1990) and Sartori et al. (2006), respectively.

4. The localities Kaltenberg, Pipji, Grand Praz and Collioux Inférieur

4.1 Geotectonic position

Detailed ore prospection showed three mineralized districts in the Penninic basement between the Val de Bagnes and the eastern flank of the Turtmanntal (Woodtli 1985; Woodtli et al. 1987; Figure 1). They contain Pb-Zn-Cu-, Cu-Bi- or Ni-Co-ores. The Ni-Co-veins (i.e. the Penninic five-element veins) exclusively developed in the SM nappe at the upper parts of the Val d'Anniviers and Turtmanntal following an E-W or NE-SW direction (Figure 3) The most important of these (admittably very small) occurrences with the highest ore grades and the largest mineralogical variability are the former mines Grand Praz (280 t: 14% Ni, 8% Co) and Kaltenberg (50 t: 2% Ni, 8% Co) (Schmidt 1920; Meisser 2003). Both World Wars promoted intensive mining activities at both localities during the first half of the 20th century. The five-element vein at Pipji, however, was discovered in 1982 and has not yet been mined, which provides ideal prerequisites for observing completely preserved spatial structures (Woodtli 1985; Sartori and Della Valle 1986). Veins at Collioux Inférieur show the least mineralogical diversity but the most intense stress during Alpine deformation and tectonic.

Based on field observations and outcrop elevation, these occurrences show a stockwork-like arrangement across the Ergischhorn Formation of the SM nappe from Collioux Inférieur (1680 m), to Grand Praz (1605-1710 m) to Kaltenberg (2480-2520 m) to Pipji (2610-2650 m) (cf. Heusler 1876). Grand Praz is located within the very central part of the basement core, whereas Kaltenberg and Pipji are located in the upper regions near the overthrust plane and the metasedimentary cover of the SM nappe's normal limb (Figure 1). Collioux Inférieur, however, is located at the inverted limb directly above the former basement core to sediment cover boundary. Highest strain affected the veins at Collioux Inférieur, whereas Pipji, Kaltenberg and finally Grand Praz show successively decreasing quantities. The complete lithostratigraphic section from the Adlerflüe Formation up to the metasedimentary cover overlays the Ergischhorn formation SW of Kaltenberg (cf. Figure 1b and Figure 3a). Pipji, however, is located further in the SE, where the overburden lithologies tectonically pinch out. It is, therefore, in direct contact to the Triassic-Eocene cover and the overthrusting shear zone. The observed mineralizations occur close to sulfide-rich fahlbands (Figure 3a). These fahlbands are metamorphosed layers or lenses parallel to the main foliation, mostly folded and always containing disseminated pyrite, pyrrhotite, and minor chalcopyrite, galena, sphalerite and arsenopyrite (Della Valle 1992). They have been considered as prime candidates for the metal source of the five-element veins (Della Valle 1992; Schafer 1996). A genetic relationship between Pipji (PI), Kaltenberg (KB), Grand Praz (GP) and other five-element occurrences in the SM nappe is indicated, as they occur along a common E-W striking structure.

4.2 Geology and structural relationships

4.2.1 Kaltenberg (KB)

Detailed geologic and tectonic investigations were performed by Heusler (1876), Huttenlocher (1925), Gilliéron (1946), Della Valle (1992) and Schafer (1996). Spatial relations in the KB area are shown in Figure 4a according to their descriptions and own field work. At least seven subparallel veins are known, whereas the current study deals with observations from vein 3 and 5. Vein 3 includes the major ore shoots and crosscuts host rock schists and a fahlband layer, while vein 5 shows only minor ores and occurs in schists only. Underground mining intersected three levels of vein 3, distinctive for its textural occurrence, while vein 5 was only mined at the entrance of the mine site and shows similar relations like vein 3 in the uppermost level (cf. Figure 4a and Appendix: Figure A1).

In the **upper level**, vein 3 is 1-5 cm wide, dips 15-20° to SW-W and only in parts follows the main foliation (S1) within sericite-chlorite-schists. The vein consists of siderite-ankerite-quartz-chlorite gangue and appears nearly linear (albeit showing variable thickness, i.e. as connected lenses); sometimes, the vein split into two or more parallel sub-veins (Figure 5a and b, respectively). The lenses and veins show minor amounts of Ni-Co ores and magnetite as 2-5 cm large nests. The Ni-Co ores consist of relic niccolite and rammelsbergite, overgrown by different generations of gersdorffite and skutterudite together with native Bi.

Similar to some parts of vein 3, vein 5 lies slightly discordantly within the sericite-chlorite-schists, but it is intensively folded and contains only minor amounts of Co ores in a 1-5 cm wide siderite and albite gangue (Figure 5c). Here, safflorite (relic), cobaltite, skutterudite, native Bi and albite developed as 1-5 mm thick, prolonged aggregates crosscutting the prior siderite vein. Additionally, strongly boudinaged lenses of pure siderite occurs in both veins (Figure 5d).

At the **mid-level**, vein 3 appears as incoherent and nearly pure (Ni-free) Fe-Co ore lenses (10-15 cm thick; Figure 4a and Figure 5e). This Fe-Co mineralized part shows only minor amounts of siderite-dolomite-ankerite-chlorite gangue, whereas siderite forms separated domains and dolomite or ankerite occur together with the Fe-Co ores. The ores consist of mostly monomineralic löllingite with occurrences of native Bi and skutterudite or minor traces of arsenopyrite. The vein gently crosscuts the foliation of the hornblende-epidote-albite-schists with disseminated pyrite (hence, this is the fahlband, Figure 5f).

Within the mid-level, another pure calcite vein with minor hematite, pyrite and chalcopyrite crosscuts the main veins; dipping 65° SE (cf. Figure 4a and Figure 5g).

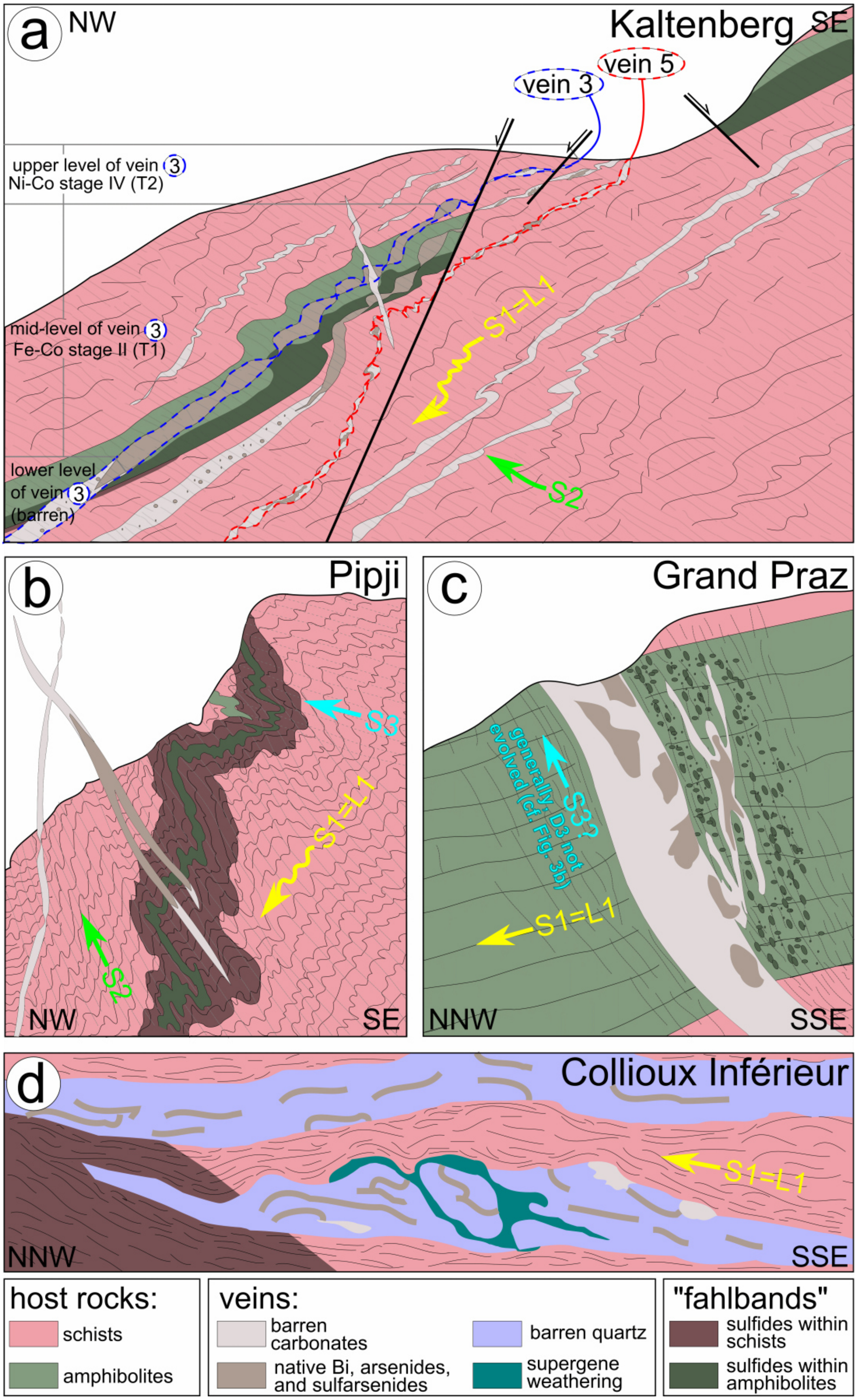

Figure 4: Geotectonic profile sketches of the five-element veins at (a) Kaltenberg, (b) Pipji, (c) Grand Praz and Collioux Inférieur. Inferred from own field observations and descriptions of Heusler (1876), Huttenlocher (1925), Gilliéron (1946), Della Valle (1992) and Schafer (1996). Sections are parallel to the L1 lineation whereas S1 is parallel to L1.

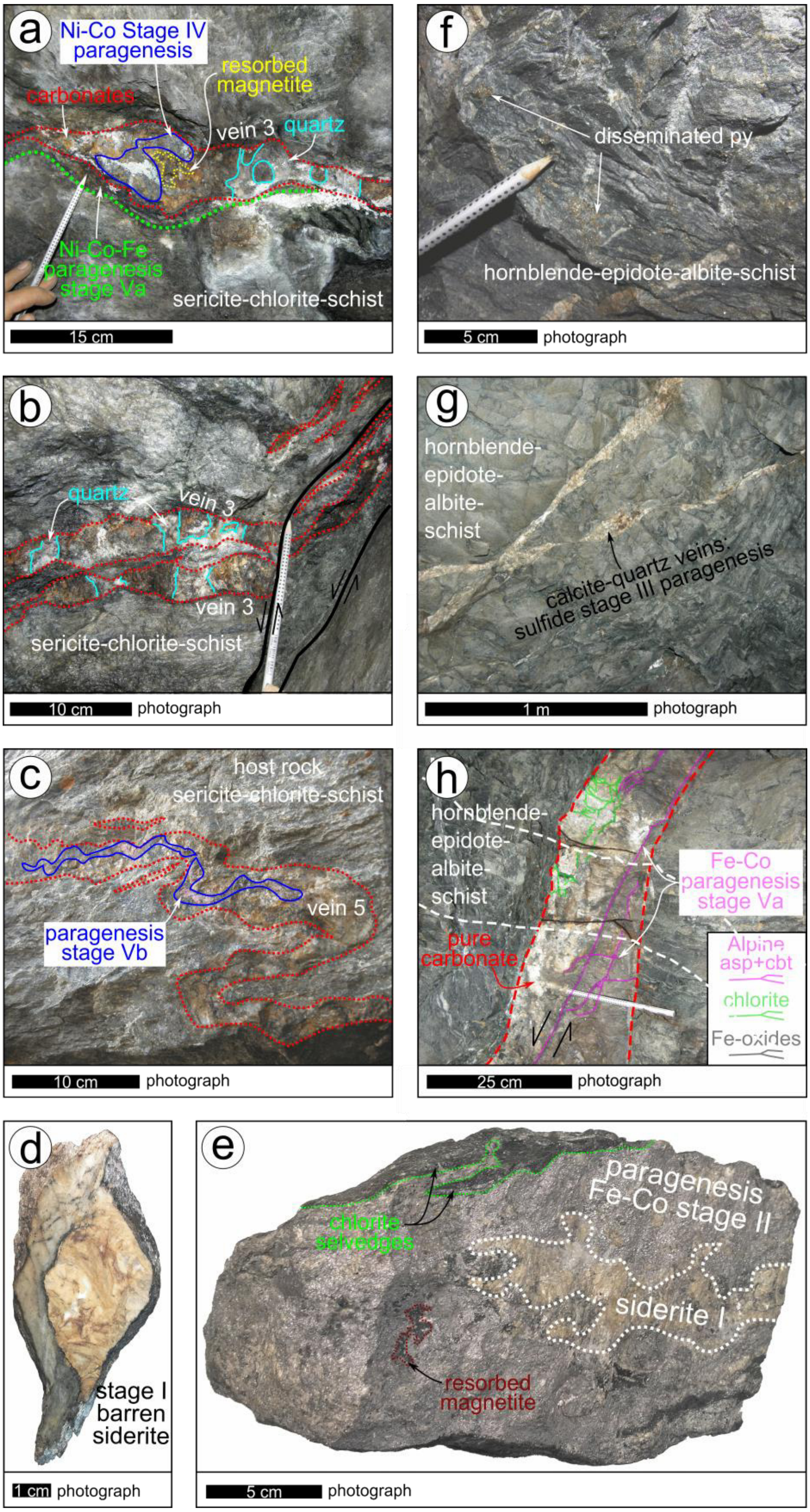

Figure 5: Photographs of the different vein sections at the Kaltenberg mine. (a-d) veins developed within the sericite-chlorite-schist host rock, (e-h) veins/rock within the hornblende-epidote-albite-schist host rock. For their position within the different levels, see Figure A1a. (a) Single boudinaged Ni-Co-mineralized vein including quartz, dolomite, ankerite as well as siderite II (cf. yellow weathering cover) and Ni-Co-ores (grey). Latter also covered by bloom of erythrite and annabergite. (b) Subparallel double veins mineralized same as in (a), stripped by a fault system. (c) Intensively folded vein of the lower set including quartz, carbonates, albite and minor Co-ores (cf. pink erythrite bloom). (d) Massively boudinaged lens separated from the continuous vein, mineralized by siderite-I (brownish-grey) and minor quartz only. (e) Massive ore from the middle level galleries mostly including Ni-Co-ores (grey), siderite-II (yellowish-brown) and dolomite/ankerite/quartz (backside) (sample from the Naturhistorisches Museum Bern, Switzerland). (f) Fahlband of the Kaltenberg mine, a hornblende-epidote-albite-schist including disseminated pyrite (py). (g) Remaining and mostly barren part of the middle level galleries. Vein of calcite (cal), py and chalcopyrite (cpy) crosscutting the boudinaged main vein. (h) Mostly pure carbonate and magnetite vein of the lower level galleries showing only minor dispersed Co-mineralization as ert bloom at the selvedges and thrust planes. ert: erythrite, anb: annabergite, py: pyrite.

At the **lower level**, vein 3 occurs as a continuous, mostly undeformed, 10-80° S-SSW dipping and up to 40 cm thick pure carbonate vein. The carbonates consist of brecciated, mm-cm sized dolomite clasts cemented by fine grained ankerite including disseminated pyrite, magnetite and chlorite. Pink crusts of supergene cobalt minerals and brownish crusts of supergene Fe-oxides indicate minor amounts of disseminated cobaltite and arsenopyrite. Both predominate along shear bands, crosscutting the carbonate vein (Figure 5h).

Observations of Gilliéron (1946) and Schafer (1996), that the veins propagate along the main foliation S1 show minor amounts of ores and parts affected by the crenulation foliation S2 the strongest ore enrichment, cannot be confirmed from our findings (Figure 4a). The crosscutting relationship discordant to S1, the intensive boudinage structure and partial folding along S2 record a pre-, syn- or post-D1 emplacement (Schafer 1996). Microscopic observations of Gilliéron (1946) during active mining periods indicate an increasing magnetite content towards the selvedges and within the host rocks adjacent to the veins.

4.2.2 Pipji (PI)

Investigations by Sartori and Della Valle (1986) and Della Valle (1992) show a structural development different from Kaltenberg (Figure 4b), as the whole occurrence at Pipji develops rather along the crenulation foliation (S2) than along the main foliation (S1). It consists of a 50° SSE-dipping, 16 m long and up to 60 cm thick, nearly pure arsenide and sulfarsenide ore vein (Figure 6a), which splits into two smaller ones developing into barren siderite-quartz-pyrite ends (Figure 6b). The overall length is 40 m. Where the mineralized part turns into the barren vein, dolomite and ankerite replaced siderite (Figure 6c). Additionally, siderite is replaced by the ores, and all carbonates are finally overgrown and brecciated by quartz.

The vein parts hosting the ores are not folded or boudinaged. A second, N-S striking siderite-quartz-pyrite vein, however, crosscuts the main vein steeply and shows an intensive boudinage along S2 (Figure 4b). The host rocks are chlorite-mica-schists and an amphibolite layer, both concordant to S1 and including disseminated pyrite (i.e. a fahlband). In contrast to the interpretation of the veins' structural relationship as a post-D2 to syn-D3 feature (Sartori and Della Valle 1986), the ores are brecciated along small cracks parallel to S1 and with an angle to the S2 direction; the latter direction is cemented by alpine quartz, implying a pre-D1 and pre-D2 emplacement (Figure 6a).

On a macroscopic scale, the ores show either regions with bright, metallic luster or regions with darker, dull tarnishing colors. The latter regions occur either at the brecciated parts of the vein or at intersects of the bright parts as an ameboid-textured front (Figure 6a, d-g). As documented in Figure 6 and chapter 6.5.1, the bright areas of zone A predominantly consist of Fe-Co ores (arsenopyrite-löllingite-skutterudite). The darker areas consist of Ni-Co-rich ores and further

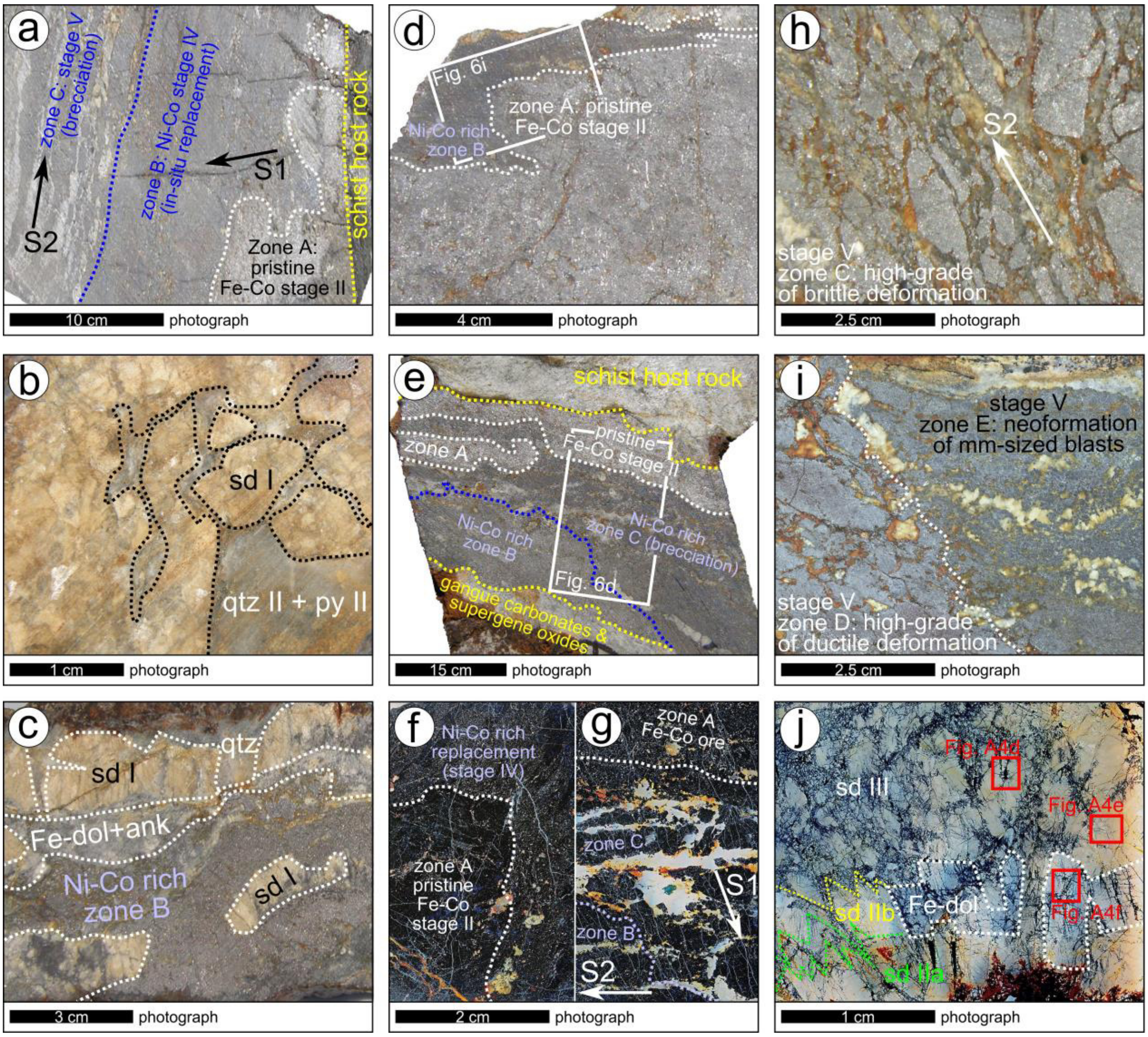

Figure 6: Photographs of different vein sections at Pipji. (a) Massive ores of the main mineralized vein. (b) Region of the barren siderite vein, infiltrated by later quartz and pyrite. (c) Region, where the Ni-Co mineralized part turns into the barren siderite vein. (d-g) spatial relationship between zone A, B and C. (h) Zone C concerned by brecciation. (i) Transition between zone D (ductile deformation) and zone E (including neoformation of arsenide blasts). (j) Carbonates, showing intensive infiltration of blackish, secondary, trail like native Bi. For further information see text.

subdivide into replacement textures in zone B (krutovite-skutterudite); intensive ore brecciation in zone C; ductile ore deformation in zone D; and neoformation of mm-sized blasts in zone E (gersdorffite-löllingite-skutterudite). Zones C and D genetically unify the reworking of previous ore stages but they show variations in their mineralogy and chemistry due to different deformation styles such as high-grade brittle deformation or high-grade ductile deformation (Figures 6h and i; zones C and D, respectively). Zone E always occurs at the margin of the arsenide mineralization and thereby forms the distal continuation of the zone D. Mineralogies and chemistries show a correlation between both zones. Most quantities of native Bi resides within as trails and veinlets within the gangue mineralizations, which occur as blackish colored regions (Figure 6j).

4.2.3 Grand Praz (GP)

Due to mining, the structural connection of the vein at GP to geotectonic models of Sartori (1990) and Steck (2008) is difficult to observe today. Gerlach (1873) and Huttenlocher (1925), however, recorded the vein geometry during the active mining period (Figure 4c), Meisser (1990) the mineralogy and mining sites. According to their descriptions, a mostly E-W-striking and 55-80° S-dipping vein crosscuts 15-20° N-dipping, S1 foliated muscovite-gneisses, but ore shoots were mostly observed where the vein crosscuts a meta-amphibolite layer (i.e. fahlbands; Figure 4c). The S1 foliation bends into a crenulation foliation parallel to the vein, however, this is more intensively evolved at the host rocks of the hanging wall and towards the veins. The 1-2 m thick carbonate vein contained up to 30 cm thick ore lenses in contact to fahlband areas with disseminated pyrite and arsenopyrite. The ore lenses occurred as mainly monomineralic aggregates of greyish (skutterudite) or reddish ore shoots (niccolite). No spatial correlation or any intergrowth was observed between the greyish and reddish ore shoots, neither today nor in the past. Since the vein at GP developed transversal to the main foliation, a post-Alpine age was suggested. The crenulation foliation, however, implies an at least syn-Alpine or older emplacement.

4.2.4 Collioux Inférieur (CI)

Compared to the other occurrences, the veins at Collioux Inférieur show very different geometric relationships to the host rocks as well as different mineralogies and gangue deformation textures. Up to 35 cm wide, massive quartz veins are strictly concordant to the main foliation S1 (Figure 4d). Foliation and veins are mostly horizontal with no preferred dip direction. The veins occur within paragneisses and chlorite-mica-schists and additionally pass through schist hosted fahlbands to the south. The proximity to the shear zone of the inverted limb of the Siviez-Mischabel Nappe (cf. Figure 3a) becomes apparent from the intensively sheared fahlbands or from the mylonitic character of shear zones intersecting the previous granoblastic vein quartz (cf. chapter 6.7 and 6.8). Relicts of siderite and dolomite reside within a fine-grained quartz matrix and are mostly displaced by iron oxides and –hydroxides (Figure 7a). Disseminated arsenopyrite occurs within quartz at which it mostly resides along up to cm-sized shear bands (Figure 7b). The last stage are up to 5 cm wide veinlets crosscutting the veins, which include fine-grained quartz, sericite and supergene erythrite (Figure 7c). Furthermore, Ansermet (2012) describes large quantities of scorodite, parasymplesite and pharmacosiderite.

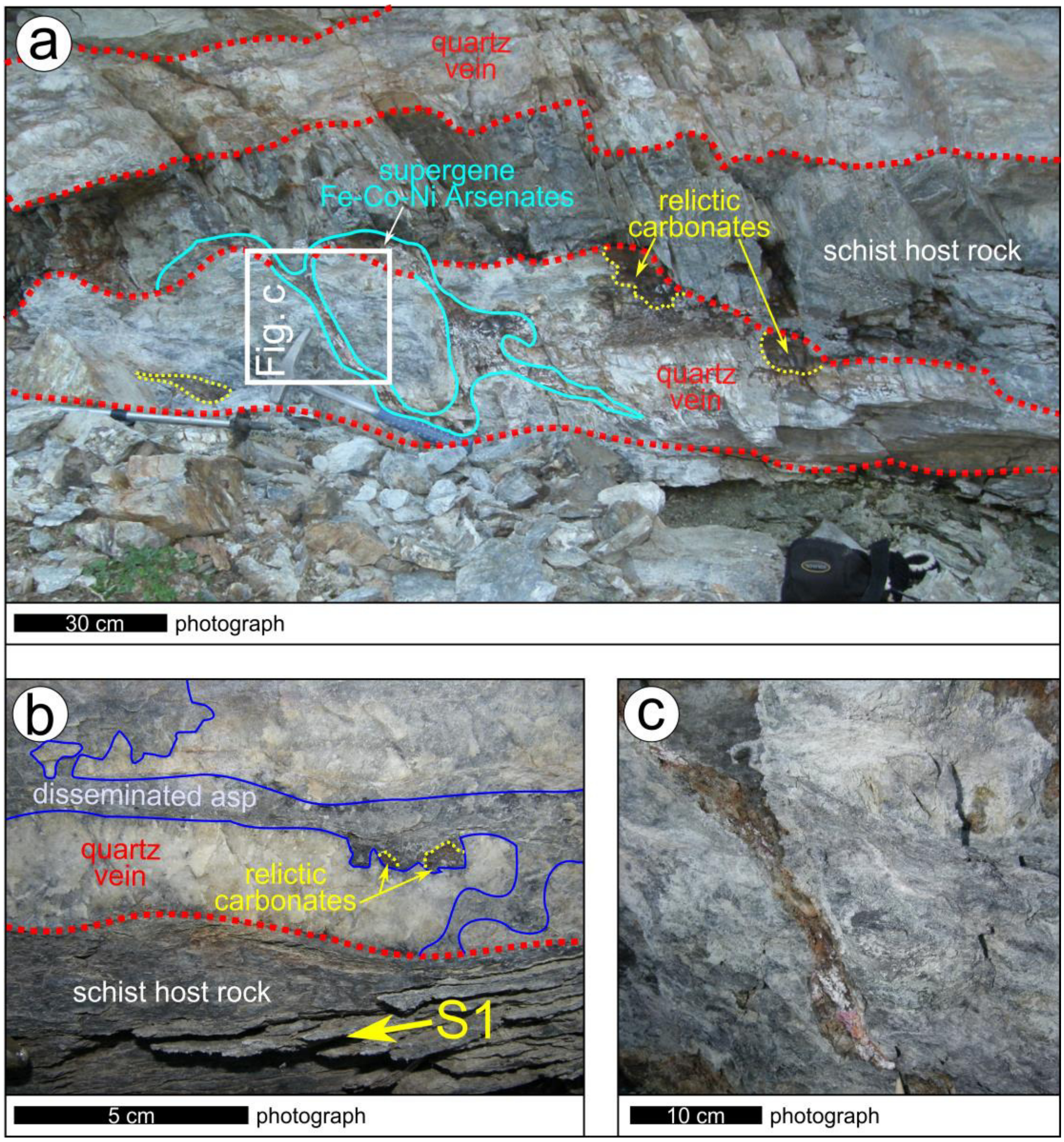

Figure 7: Photographs of different vein sections at Collioux Inférieur. (a) Quartz veins including relicts of carbonates. (b) Quartz vein intersected by shear bands of disseminated arsenopyrite. (c) Late stage formation of supergene weathering. For further information see text.

5 Analytical procedures

5.1 Mineral chemistry (electron microprobe analysis - EMPA)

The chemical composition of ore minerals (arsenides; sulfarsenides; sulfides) and carbonates was quantitatively determined using a JEOL JXA-8900RL electron microprobe equipped with 5 wavelength-dispersive spectrometers at the Fachbereich Geowissenschaften of the University of Tübingen, Germany. Analysis of the ore minerals was conducted using a focused beam, a current of 20 nA and an acceleration voltage of 25 kV. The carbonate analyses were done using a beam width of 5 µm, a current of 20 nA and an acceleration voltage of 20 kV. Natural and synthetic standards were used for calibration. Tables A3 and A4 (Appendix) report the standard materials, detection limits, and WDS configuration. For the ore mineral analysis, a peak overlap correction was applied for As *L*α/Sb *L*α and for S *K*α/Co *K*α lines. For the carbonate measurements, a correction was applied for As *L*α/Mg *K*α lines.

Matrix corrections for carbonate and ore mineral analyses were performed according to JEOL internal ϕρz and ZAF methods, respectively (Armstrong 1991). To improve the matrix correction of the carbonate analyses, carbon was additionally analyzed, but was not used for mineral formula calculation. Using the ZAF method, anomalously high analytical totals appeared for the tri- and diarsenides (mean values of 103.6 and 101.7 wt.%, respectively). These were carefully investigated and they do not relate to any other known interferences. The ZAF matrix correction, however, was nevertheless preferred since the ϕρz method resulted in even worse totals. Comparative measurements using the Cameca SX100 electron microprobe lab facilities at the University of Stuttgart, Germany, showed similar problems. Preliminary results using unpublished JEOL and CAMECA databases show that the above-mentioned problems relate to the uncertainty of mass absorption coefficient values.

Carbonate formula calculations of the calcites/siderites and ankerites/dolomites are based on one and two cation sites per formula unit, respectively. In both cases, CO_3 content is equimolar to the total moles of cations. Formulas of the arsenides and sulfarsenides are based on total atoms per formula unit (triarsenides: 4, diarsenides and sulfarsenides: 3, monoarsenides: 2).

5.2 U-Pb-age determination (LA-ICP-MS)

Uranium-lead (U-Pb) ages were obtained by laser ablation-inductively coupled plasma-mass spectrometry (LA-ICP-MS) at the Goethe University Frankfurt after the small scale isochrone method of Gerdes and Zeh (2006); Gerdes and Zeh (2009). Similar conditions were already applied for five-element veins by Burisch et al. (2017). Different carbonates, magnetite, Ni-Co-arsenides, -

sulfarsenides, chlorite, albite and annabergite were ablated in situ on polished thin sections from all deposits, whereas realizable U-concentrations were detected for the KB and GP samples only. Measurements were performed for co-precipitated mineral fractions, petrogenetically identified to be paragenetic.

A RESOlution laser ablation system (Australian Scientific Instruments) equipped with a 193 nm ArF high-pulse-energy excimer laser COMPexPro 102 (Coherent) and a two-volume ablation cell S155 (Laurin Technic), was coupled to an ELEMENT 2 sector field ICP-MS (Thermo Scientific). Each measurement was sequenced by a pre-ablation (removal of surface contaminants, 3 s), background acquisition (20 s), sample ablation (20 s) and washout (20 s). As reference, soda-lime glasses SRM-NIST 614 and 612 together with two in-house carbonate standards were used. For a static ablation, a spot size of 80 and 235 µm (depending on absolute U and Pb concentrations) and a fluence rate of < 1 J/cm² were used at a laser repetition rate of 5 Hz. This yields a depth penetration of about 0.6 µm/s for SRM-NIST 614 and an average ^{238}U sensitivity of 420 000 cps/µg g^{-1}. For line ablation, the standard error for U is about 1 % (SRM-NIST 612; spot size: 60 µm, depth penetration: 3 µm/s, repetition rate: 5 Hz and fluence rate: 1 J/cm²). Detection limits are ~ 0.1 and 0.04 ppb for ^{206}Pb and ^{238}U, respectively. Oxide formation was kept < 0.3 % (UO/U) during tuning the signal strength for its maximum sensitivity.

Prior the injection to the argon plasma, the ablation gas in the ablation atmosphere (helium stream, 0.6 L/min) was mixed in the ablation funnel with 0.7 L/min argon and 0.04 L/min nitrogen, passing a signal homogenization device (*The Squid*, Laurin Technic) to smooth out signal fluctuations due to fast washout characteristics and low laser repetition rates.

An in-house MS Excel© spread-sheet was used for raw data correction (Gerdes and Zeh 2006; Gerdes and Zeh 2009). Correction of mass bias (0.3 %) and for inter-element fractionation (~9 %) were applied for ^{207}Pb/^{206}Pb and ^{206}Pb/^{238}U ratios, respectively. This includes the sequence time drift over 12 h, using SRM-NIST 614. An additional matrix correction of 9% has been applied to the ^{206}Pb/^{238}U ratio for the carbonate samples. This value was determined at the beginning of each day of measurement using WC-1 carbonate reference material dated by TIMS (251 ± 2 Ma; E.T. Rasbury, pers. comm. 2014). Penetration-depth depending ^{206}Pb/^{238}U fractionation was below 3 % (20 s depth profiling, soda-lime glasses and WC-1), whereas no correction was applied for this. Over a measurement period of three days, WC-1 reproduces the common lead corrected ^{206}Pb/^{238}U ratio to 250.9±0.82 Ma (n = 24, MSWD = 0.74, 2σ = 1.7 %). Due to low Th contents in all carbonates (Th/U < 0.3) the common lead was calculated using the ^{208}Pb signal after subtracting the radiogenic ^{208}Pb appropriate to the detected Th signal and ^{206}Pb/^{238}U age (Millonig et al. 2012). Analyses of a secondary in-house standard (Zechstein dolomite from gypsum pit Tettenborn, Germany) show a lower intercept age of 255.6±3.0 Ma (n = 35, MSWD = 1.4), implying an accuracy and repeatability of the method of around 2 % or better. Data were plotted in the Tera-Wasserburg diagram and ages calculated as lower intercepts using Isoplot 3.71 (Ludwig 2012). All uncertainties are reported at the 2σ level.

5.3 Fluid inclusions (FI)

5.3.1 Microthermometry

Microthermometric analyses were performed using a Linkam THMS 600 stage at the Fachbereich Geowissenschaften, University of Tübingen. Double polished thick sections (100-300 µm) were produced from a cross-section through the mineralization to establish the relative chronological sequence of fluid inclusion assemblages (FIAs, Goldstein and Reynolds 1994). The observed fluid inclusions (FI) were classified into primary (p), pseudo-secondary (ps), isolated (iso) and clusters of inclusions (c; no geometrical relation to crystal surfaces or fractures). Each single FI was analyzed three times to identify the final dissolution temperature of ice (Tm_i), hydrohalite (Tm_{hh}), halite (Tm_{NaCl}) and the homogenization temperature (T_h). The database includes FI, for which triple analyses differ only less than 0.1°C for Tm_i and Tm_{hh} and less than 1°C for T_h. Synthetic H_2O, H_2O-NaCl and H_2O-CO_2 standards were used for calibration of the stage. Details of the FI nomenclature, refer to Walter et al. (2015).

Fluid inclusions with a strongly divergent behavior in salinity and T_h from a single trail were excluded, since this variability may indicate FI alteration by post-entrapment processes. No systematic variations within the assemblages could be recognized. Eutectic temperature T_e was observed around -52 °C and the salinity in the ternary NaCl-$CaCl_2$-H_2O system was calculated using Tm_i and Tm_{hh} pairs according to Steele-MacInnis et al. (2011). A pressure correction of T_h considering the method of Bodnar and Vityk (1994) was applied, assuming hydrostatic and lithostatic conditions (cf. chapter 8.2.1).

5.3.2 µ-Raman spectroscopy

To determine possible volatile phases, all FI generations were additionally analyzed at the Fachbereich Geowissenschaften, University of Tübingen, using a confocal Raman spectrometer Renishaw InVia Reflex. A laser wavelength of 532 nm and a measurement time of 10 s were used with a laser power between ~0.4-20 mW and 2-5 accumulations to improve each spectrogram. The used 100x Objective (Olympus MPlan), the numerical aperture of 0.9 and the opening angle of 128.3° result in a theoretical focus diameter of about 0.7 µm. For each FI, the focus was set on the gas phase, liquid phase and host mineral using the same measurement conditions and orientation. Due to the small size of the measured FI and the excitation of surrounding gas or liquid phases and host minerals, only mixed Raman spectra were achieved in the liquid, gas and host phases. For qualitative assignment, band shapes and wavenumber positions were compared to diverse literature data.

5.4 Stable Isotopes

Mineral separates were carefully handpicked, rinsed with ultrapure H_2O, dried at 80°C and finely powdered using an agar mortar. For carbon, oxygen and sulfur isotopic analysis, about 0.1 to 0.5 mg of fine-grained powder was used at the Geochemistry lab facilities Fachbereich Geowissenschaften, University of Tübingen.

To distinguish sources of sulfur during primary ore formation and Alpine processes, sulfides and sulfarsenides from the veins and fahlbands were used for S isotopic analysis using a NC 2500 connected to a Thermo Quest Delta + XL mass spectrometer. NBS 123 ($\delta^{34}S$ =17.1‰, relative to CDT), NBS 127 ($\delta^{34}S$ = 20.31‰, relative to CDT), IAEA-S-1 ($\delta^{34}S$ = -0.3‰, relative to CDT) and IAEA-S-3 ($\delta^{34}S$ = 21.7‰, relative to CDT) were used for calibration. The reproducibility of the measurements is better than ±0.3‰.

To investigate various origins of CO_2/HCO_3^- between different carbonate generations, carbon and oxygen isotope compositions were determined using a Gasbench II device connected with a Finnigan MAT 252 mass spectrometer via continuous flow from liberated CO_2 after reaction with H_3PO_4 (cf. Haßler et al. 2014 for details). Isotope ratios were calibrated using NBS18 ($\delta^{13}C$ = -5.00‰ and $\delta^{18}O$ = -22.96‰, relative to VPDB) and NBS19 ($\delta^{13}C$ = 1.95‰, $\delta^{18}O$ = -2.2‰, relative to VPDB). External reproducibility is better than ± 0.1‰ for $\delta^{13}C$ and $\delta^{18}O$. Oxygen isotopes were corrected using phosphoric acid fractionation factors of $\alpha_{CO2(ACID)–carbonate}$ = 1.008176, 1.009316, 1.009258 and 1.009078 for calcite, dolomite, ankerite and siderite, respectively.

5.5 Hydrogeochemical modelling

To evaluate the stability relations of arsenides and sulfarsenides in five-element veins, predominance diagrams were computed using The Geochemist’s Workbench (Version 11.0.6, Bethke and Yeakel 2015). Calculations of the systems Fe-As-S-H_2O and Ni-As-H_2O consistently used the thermodynamic thermoddem database of Blanc et al. (2012). For comparison to the system Co-As-H_2O, the LLNL database was used according to Johnson et al. (2000).

Mineral phases not included in the databases are the Ni-diarsenide rammelsbergite, the Co-/Ni-sulfarsenides cobaltite and gersdorffite, the triarsenide skutterudite and native bismuth. Within the log fO_2 vs pH space, predominance field sizes of the Fe- and Co-diarsenides löllingite and safflorite show the same size regarding the borders between the monoarsenides and native arsenic. Based on this fact, rammelsbergite was manually included, assuming similar sizes of the rammelsbergite, löllingite and safflorite predominance fields. The position of the rammelsbergite field was estimated by the combination of moving the invariant point between $NiAs_2$–$As(OH)_3$–NiAs along the $As(OH)_3$–NiAs equilibrium and assigning the predefined size of the rammelsbergite field to the native As–$As(OH)_3$ equilibrium. The latter estimates the invariant point of $NiAs_2$–$As(OH)_3$–native As. All slopes of the individual reactions between the solid phases $NiAs_2$, NiAs and native As to $As(OH)_{3(aq)}$ remained fixed during this procedure. The position and shape of the gersdorffite (NiAsS) predominance field was estimated between the phases NiAs/Ni_5As_2 and NiS/Ni_9S_8.

In addition to rammelsbergite and gersdorffite, no data is available for native Bi. Reaction 1 and 2, however, expect a higher O_2 and H^+ consumption for the reaction of chlorinated complexes to native Bi than for the reaction with native Ag.

$$AgCl_2^- + \frac{1}{2} H_2O \Leftrightarrow Ag^0 + 2 Cl^- + \frac{1}{4} O_2 + H^+ \qquad \text{(Reaction 1)}$$

$$BiCl_4^- + 1\frac{1}{2} H_2O \Leftrightarrow Bi^0 + 4 Cl^- + \frac{3}{4} O_2 + 3 H^+ \qquad \text{(Reaction 2)}$$

According to Markl et al. (2016), the expected Bi reaction should plot at lower fO_2 and higher pH. The exact position, however, is dependent on the salinity and Bi concentration, which is not possible to be estimated. The transition between skutterudite and safflorite was assumed according to Markl et al. (2016).

Arsenic and metal concentrations were used as described in Markl et al. (2016). The corresponding activities were recalculated based on their documented Ag, Co and As concentrations at temperatures of 200°C and pH 6-7 using the program code GSS implemented in The Geochemist's Workbench software package. Concentration of Fe and Ni were defined in similar range to Co, for Bi similar to Ag.

5.6 Micro X-ray diffraction (µXRD)

Micro X‑ray diffraction was used to characterize isotropic, Ni-dominated sulfarsenides with As/(As+S) ratios intermediate to common gersdorffite (NiAsS) and krutovite ($NiAs_2$). Measurements were performed on thin sections at the Fachbereich Geowissenschaften, University of Tübingen using a Bruker D8 Discover GADDS Θ-Θ micro diffractometer. A Co-anode with Kα radiation ($\lambda = 1.79$ Å) was used at 30 kV and 30 mA with a HOPG monochromator and monocapilarry optics of 500 µm with a 200 µm pinhole. Spectra were recorded using a Bruker VÅNTEC500 area detector system (Berthold et al. 2009). The incident angle was fixed to 15° and measurement time was set to 120 s. Detector frames were integrated between 5-70° 2Θ with a step size of 0.05° 2Θ.

5.7 Energy dispersive coupled scanning electron microscopy

Observations by optical light microscopy were additionally complemented by analyses using an energy dispersive coupled system (EDX) at a HITACHI TM3030 Plus scanning electron microscope (SEM) at the Fachbereich Geowissenschaften, University Tübingen. This method was used for differentiation of fine-grained gangue minerals, mineralogy of the host rock minerals and for the additional characterization of all phases involved during host rock alteration. If necessary for interpretation of the host rock alteration, rough estimates of chemical compositions include the expression EDX-SEM in the text (chapter 6.9).

6. Ore and gangue petrography

6.1 Differentiation between specific gangue and ore phases

Due to multi stage precipitation and remobilization during the Alpine Orogeny, the gangue and ore mineralizations represent complex systems of recurrent and syndetic replacements and recrystallization textures. In special cases, diverse stages can yield age differences of some hundreds million years although displaced on micro scale. Therefore, differentiation between individual but optically equal ore and gangue phases and their assignment to different stages is only possible by thorough and repeated crosschecking of optical and textural observations to different results (EMPA, U-Pb ages, CL and µXRD). For a better confirmability, the following will introduce which results were used to crosscheck and differentiate distinct phases. In addition, Table A2 (Appendix) lists all identified mineral generations, ordered after their temporal occurrence, including abbreviations used in other Figures and Tables, and occurrence within the different deposits KB, Pi, GPg and GPr.

Gangue minerals: The distinction between different siderite, dolomite and ankerite generations is possible due to combined observations of their crosscutting relationships, Fe-Mg-Mn-Ca chemistries (showing a progressive development; cf. chapter 7.1 and 8.1.2), U-Pb ages (cf. chapter 7.2 and 8.1.1) and the temporal offset of co-precipitated ore phases. Crosscutting relationships from early to late stages refer to chemical changes of the carbonates.

For quartz, the combination of different grain fabrics and cathodoluminescence colors reveal the subdivision of undisturbed, euhedral and concentric zoned aggregates with hydrothermal origin from others that show metamorphic structures with increasing dynamic recrystallization textures (cf. chapter 6.8).

Magnetite: Since optical and chemical properties do not differ between individual magnetite generations, their assignment to different stages is possible after comparing textural and relative ages with corresponding U-Pb ages (cf. 7.2 and 8.1.1).

Anisotropic arsenides and sulfarsenides: Differentiation between the anisotropic arsenides and sulfarsenides (löllingite, arsenopyrite, niccolite, rammelsbergite and safflorite) is possible by classical optical microscopy. Additionally, growth directions from early to late stages within single ore phases show progressive chemical changes of the ores (cf. chapter 7.1).

Isotropic arsenides: Identification of intergrowth relationships between isotropic triarsenides (skutterudite-group minerals) represents the most problematic issue. Chemical variations of studies skutterudites deviate to a restricted extend along a fixed Fe/Ni ratio of 1 and it is neither possible to determine relative crosscutting relationships by optical nor by electron microscopy. Temporal differentiation, however, was possible by comparing relative skutterudite intergrowth to other ore phases (i.e. arsenopyrite, gersdorffite, uraninite and albite), whose ages could be determined by U-Pb isotopes. As documented in chapters 7.1 and 7.2, comparison of chemical variations and U-Pb ages deviates early stage skutterudites (Co-dominated towards Fe-Ni-rich) from later stages (only Co-dominated).

Isotropic sulfarsenides: Due to optical microscopy of the isotropic sulfarsenides, it is possible to differ cobaltite (rose tint color) and gersdorffite-cobaltite solid solutions (faint grayish-rose to cream tint color) from krutovite and gersdorffite (pure white). Additionally, a general separation exists, since cobaltite occurs in different samples as the other sulfarsenides. On the mineralogical restriction of phases with the general formula $NiAs_xS_{x-1}$, krutovite ($2>x>1.5$) was distinguished from gersdorffite ($1.5>x>1$) based on Spiridonov and Chvileva (1996) by chemical As/(As+S) ratios >1.5 (EMPA analysis; cf. chapter 7.1) and optical reflectance >54% (reflected light oil immersion microscopy). Single aggregates that overlap these transitions further subdivide by µXRD analysis (cf. chapter 7.5). The temporal differentiation between gersdorffite I, gersdorffite II and the gersdorffite-cobaltite solid solutions was crosschecked by comparing U-Pb ages and chemical compositions.

6.2 Used nomenclature of chemically complex phases

Chemical compositions of observed arsenides and sulfarsenides in the Fe-Co-Ni-As-S space (niccolite, arsenopyrite, cobaltite, gersdorffite, krutovite, löllingite, rammelsbergite and skutterudite-group minerals) show a large variability regardless if it was possible to distinguish them by optical and electron microscopy. Especially the Ni-diarsenides and Ni-sulfarsenide deviate significantly from endmember composition with continuous transitions between their nominal compositions. Additionally, a strict and explicit characterization of the ores by powder X-ray diffraction was not possible due to µm-sized intergrowth of the phases. Therefore, mineral nomenclature after the guidelines of the international Mineral Association (IMA) was difficult. In this study, the ores with transitional compositions strictly named after the endmember, which reflect their dominating compositional component in the Fe-Co-Ni-As-S space. For the detailed differentiation between the Fe-Co-Ni-diarsenides ($[Fe,Co,Ni]As_2$) and -sulfarsenides ($[Fe,Co,Ni]AsS$), an equilateral triangular prism with edges of Fe, Co, Ni, As_2 and AsS was used for projection. Ore aggregates, which overlap these guidelines of the IMA, are either named after a single endmember if the chemical variability continuously evolves from one specific endmember composition or named after multiple endmembers if no dominated chemical evolution was found (e.g. gersdorffite II vs gersdorffite-cobaltite).

6.3 Generalized overview

Most microscopic observations coincide to Huttenlocher (1925), Hirschi (1939), Gilliéron (1946), Sartori and Della Valle (1986), Della Valle (1988) and Schafer (1996). The present work connects their observations with several additions and modern techniques to conclude a general paragenetic sequence for the Bi-Fe-Co-Ni-As-S-U mineralized siderite-dolomite-ankerite veins in the Swiss Penninic Alps. The localities Kaltenberg (KB), Pipji (PI) and Grand Praz (GP) are located about 7.2 km (horizontal) and 1.2 km (vertical) from each other, but microscopic and geochemical observations reveal general similarities among their mineral assemblages and evolution. The following chapters 6.4, 6.5 and 6.6 include their successive gangue and ore assemblages, respectively. The locality Collioux Inférieur (CI), however, represents an exception, since intensive silicification erased primary ore and gangue textures (cf. chapter 6.7). Additionally, chapter 6.8 presents the successive grades of deformation; and chapter 6.9 gives a short overview of the host-rock alteration.

The veins at KB show the most consistent ore and gangue mineralogy of all deposits and are (with minor additions from GP and PI) used to compile a generalized paragenetic sequence. Based on relative temporal positions, transition metal variations and subsidiary geochronology by radiogenic U-Pb isotopes, the complex evolution of the veins at KB can be subdivided into the stages I-VI, including the sub-stages Va and Vb (Figure 8):

Stage I	Massive, barren siderite (often present as relicts);
Stage II	Fe-Co stage of Fe-Co arsenides and sulfarsenides in dolomite, ankerite and minor siderite gangue;
Stage III	Sulfide stage of sulfides crosscutting stage II or as separate veins in quartz and calcite gangue (no Fe-Co-Ni arsenides);
Stage IV	Ni-Co stage of Ni-Co arsenides and sulfarsenides in ankerite and minor siderite gangue;
Stage V	Alpine stage and based on U-Pb ages subdivided into: V(a) In-situ Remobilization of stages II-IV (dissolution-reprecipitation); V(b) Co stage with euhedral safflorite, cobaltite and skutterudite; and
Stage VI	Hydrothermal overprint and supergene weathering.

Compared to KB, the veins at PI, GP and CI only show a subset of this full paragenetic succession, but (except the latter) reflect all stages including comparable mineralogical and textural features (cf. correlation matrix; bottom of Figure 8).

The paragenetic ore sequences of stages II (Fe-Co), IV (Ni-Co) and Vb (Co) show textural and paragenetic features typical of five-element veins, including native Bi, Fe-Co-Ni arsenides and sulfarsenides as open space fillings. Although native Ag is not present, the following uses the term five-element veins for observed assemblages. In addition to arsenides, sulfarsenides and sulfides, hematite and magnetite precipitation accompanies stages II-V. Either magnetite forms pseudomorphs after hematite or euhedral aggregates, which later resorbed by löllingite. Vein sections towards the selvedges and host rocks adjacent to the veins show increasing amounts of magnetite (Gilliéron 1946; Schafer 1996). All mineral descriptions and the classified temporal nomenclature of mineral phases with a multi-phase reoccurrence (e.g. gersdorffite I, II, III and IV) were adapted to the full paragenetic succession at KB. Note that, in the need of comparability, some mineral classes do not occur (or were not found by the author) in all deposits (e.g. paragenetic succession of GP misses löllingite I and begins with löllingite II).

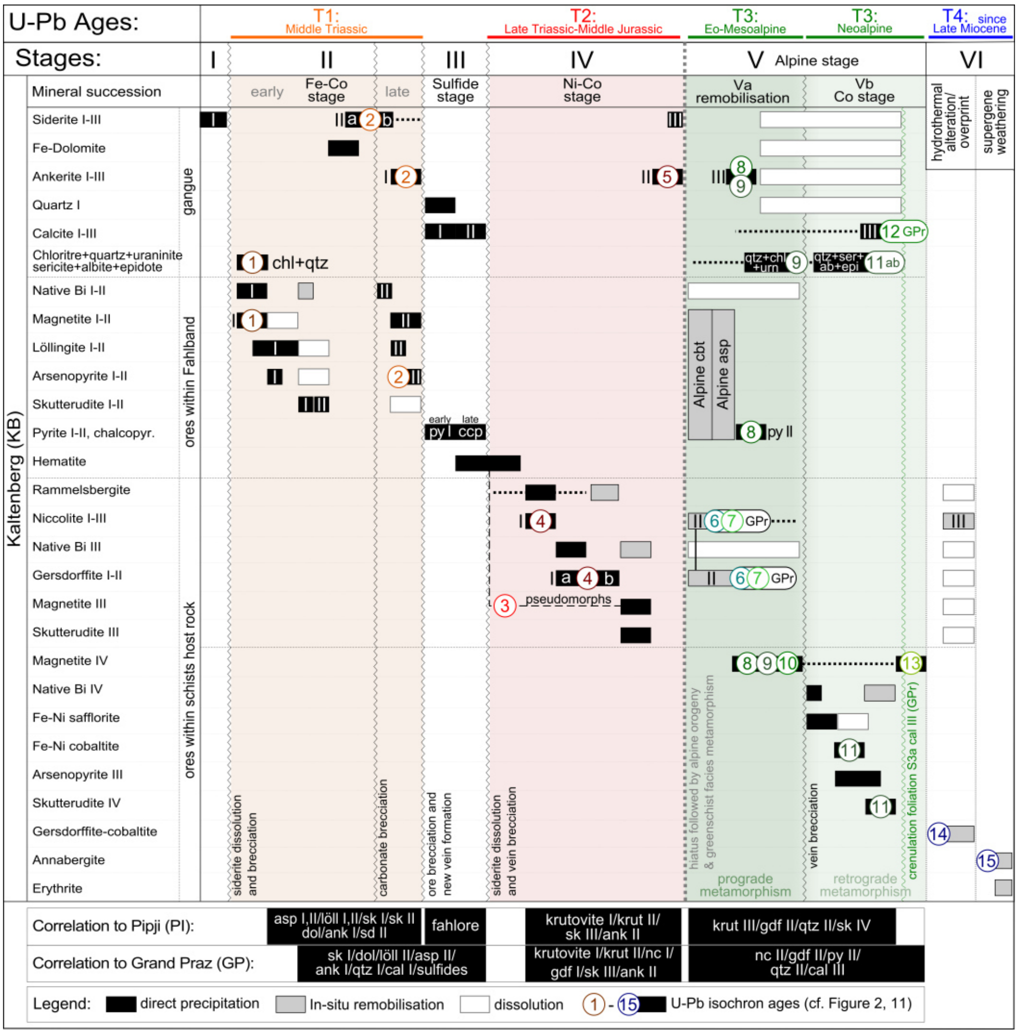

Figure 8: Simplified paragenetic sequence of the gangue and ore minerals from Kaltenberg. Black boxes at the bottom correspond to the correlation of the mineral succession of Kaltenberg to the deposits in Grand Praz and Pipji. For the detailed paragenetic sequences of Kaltenberg, Grand Praz and Pipji see Figure 10 and 25. Sequence includes the corresponding numbers of the isochrons, illustrated in Figure 2h. Note, Isochrons 6 and 7 were inferred from age determination from Grand Praz. Mineral abbreviations are py: pyrite, ccp: chalcopyrite, qtz: quartz, chl: chlorite, urn: uraninite, ser: sericite, ab: albite, epi: epidote.

6.4 Mineralogy Kaltenberg

6.4.1 Gangue minerals

Stage I: Gangue mineralogies show similar successions of all deposits. The first stage comprises pure, coarse-grained siderite I. Local occurrences of five-element assemblages (stages II, IV and Vb) show replacement features of this early (pre-ore) siderite I together with precipitation of magnetite (Figure 9a-b and 5e); elsewhere, siderite I stays unaffected where no arsenide and magnetite formation proceed (Figure 5d).

Stage II: Areas of siderite I dissolution show the precipitation of native Bi, arsenides and sulfarsenides within ankerite I (Figure 9c). Euhedral and concentric zoned Fe-dolomite and late siderite II overgrow siderite I and the early Fe-Co stage ores (i.e. löllingite I, arsenopyrite I and skutterudite I, II; Figure 9a). Ankerite I intersects and cements the previous carbonates during the latest phase of this stage (Figure 9a-d). Within ankerite I, repeated Fe-Co ore formation occurred (löllingite II, arsenopyrite II).

Stage III: Quartz I or early calcite I enclose early pyrite I, while later calcite II is associated with late chalcopyrite and/or hematite (quartz I: classified by blue to blue-green cathodoluminescence color; cf. Figure 9e). Mostly, sulfides occur as veinlets within the arsenides without gangue precipitation (Figure 9f).

Stage IV: Intensive dissolution of siderite I and accompanied post ore precipitation of ankerite II concerns vein sections including the Ni-Co ore stage IV (ank II; Figure 9g and h). Siderite I almost disappears and occurs as 1-10 µm sized relicts only (sd I, ank II; Figure 9i). Siderite III represents the last gangue of this stage, which encloses and replaces former ankerite II.

Stage Va: Minor ankerite III occurs as small veinlets crosscutting all previous carbonates and includes euhedral pyrite II. In addition, chlorite forms shear bands at the selvedges and intersects previous carbonates along their grain boundaries. Chlorite also contains minute uraninite crystals obvious by characteristic radiohalos (Hirschi 1939). At KB, quartz II crosscuts chlorite and the veins as single veinlets perpendicular to S1 or at interstitial regions between the boudinage (quartz II: classified by yellow to yellow-brown cathodoluminescence color, cf. Figure 9e and 5a-b).

Stage Vb: In contrast to the Fe-Co and Ni-Co stages, the ores of the Alpine Co stage Vb are in the equilibrium with albite or quartz replacing former carbonates (Figure 9j). Additionally, minor sericite and epidote can occur. As the last phase, calcite III replaces all previous carbonates (stages I-Va), albite and quartz.

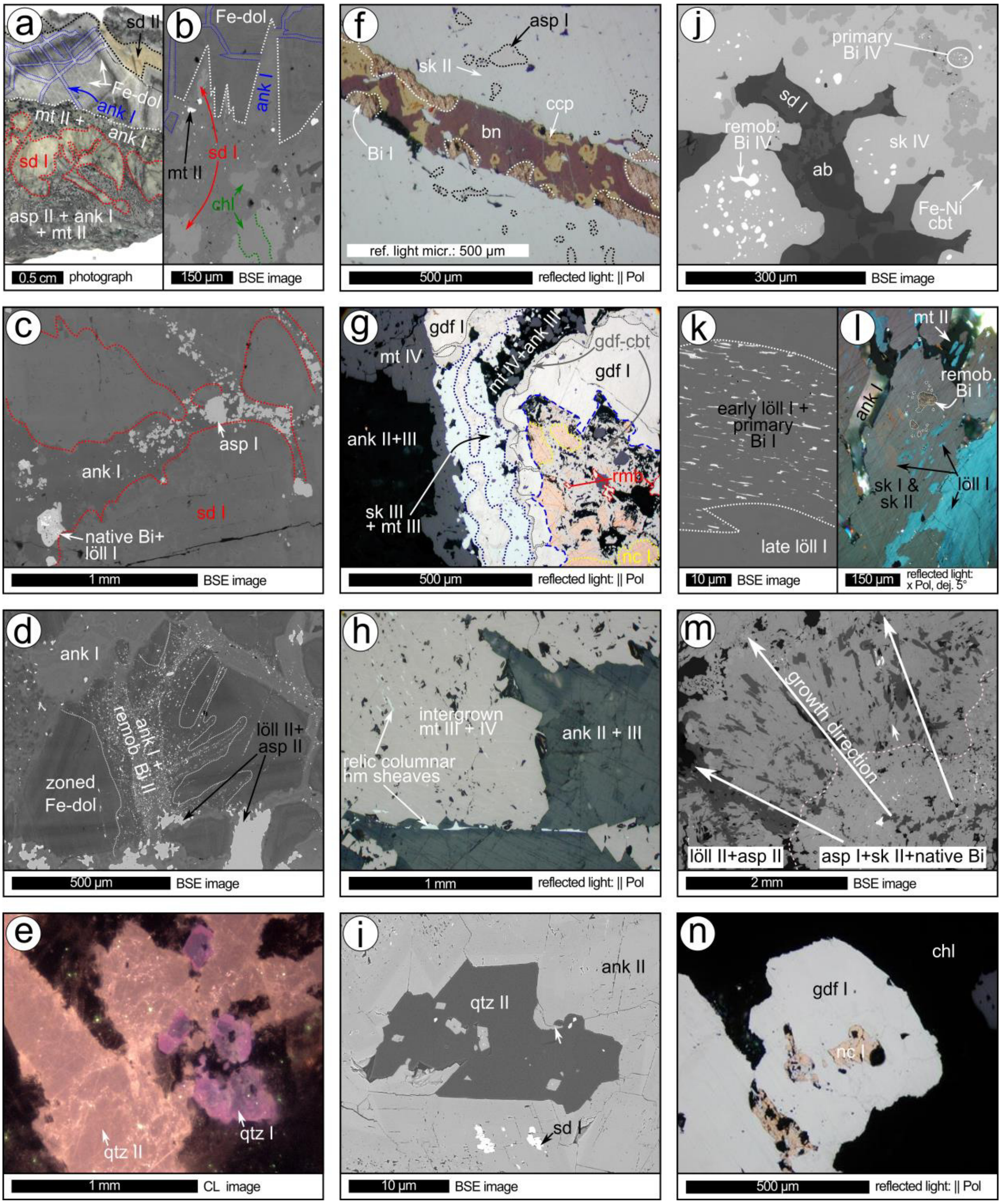

Figure 9: Mineral textures of the Kaltenberg mine samples. (a-d, k-m) Textural relationship of the ores from the Fe-Co stage, (e-f) of the sulfide stage, (g-i, n) of the Ni-Co stage, and (j) of the Alpine Co stage. For further explanations see text; for mineral abbreviations cf. Table A2 (Appendix).

6.4.2 Ore minerals

The Fe-Co and sulfide stages (II and III) are present in the middle level of vein 3 (near the sulfide-rich fahlband), the Ni-Co stage (IV) in their upper levels and the late Alpine Co stage (Vb) in vein 5 (both sericite-chlorite schists) (Figure 4a). Remobilization textures and concomitant neoformations of stage Va affect all previous stages and levels at KB. Most remobilization textures are present along the selvedges between the veins and host rocks or “intrude” preexisting ore aggregates from the selvedges into the vein.

Stage II (Five-element Fe-Co stage): In the early Fe-Co stage II, massive aggregates of radially aligned löllingite I crystals enclose glitter-like and sub-euhedral native Bi I, which afterwards are overgrown by skutterudite (Figure 9k-l). Some minor interspersed euhedral arsenopyrite I occur among the löllingites and skutterudites (Figure 9m). During the skutterudite formation, suppression of prior löllingite I and arsenopyrite I take place and remobilization of native Bi I leads to rounded, droplet-like aggregates (Figure 9l). The differentiation between skutterudite I and II is gradual and considers their early or late occurrence in the growth direction and their chemical evolution. Textures of the late Fe-Co stage II are similar to the previous ores, but occur additionally within brecciated dolomite, accompanied by late native Bi II, löllingite II, arsenopyrite II, magnetite II and ankerite I without any skutterudite precipitation (Figure 9d).

Stage III (Sulfide stage): The typical evolution from a native metal/arsenide stage to a sulfide precipitating system happened after the Fe-Co ore stage II. The sulfides mostly occur disseminated within the stage III gangue minerals, but also intersect the stage II Fe-Co arsenides and sulfarsenides along cracks (Figure 9f). Early pyrite I and later chalcopyrite occur at KB together with minor bismuthinite and bornite. Euhedral, tabular hematite is the latest ore phase of this stage.

Stage IV (Five-element Ni-Co stage): Gersdorffite I dominates stage IV, which enclosed and replaced early cores of rammelsbergite and niccolite I (Figure 9g). Rammelsbergite occurs prior to or/and after niccolite, or as relicts within gersdorffite I. According to their chemistry, gersdorffite includes early gersdorffite Ia and late gersdorffite Ib, whereas exclusively gersdorffite Ia includes dendritic and flitter like native Bi III. Younger skutterudite III and magnetite III enclose the former ore minerals; magnetite III forms pseudomorphs after euhedral, tabular hematite from the sulfide stage. Later, intensive dissolution and remobilization concern the arsenides and sulfarsenides of stage IV, especially niccolite, rammelsbergite and skutterudite (Figure 9g).

Stage Va (Eo-Mesoalpine in-situ remobilization): In vein sections hosted by schist host rocks (upper level, vein 3; Figure 4a), remobilization during stage Va lead either to a dissolution and reprecipitation replacement of the stage IV ores by variable Fe-Co-Ni sulfarsenides or neoformations of these aggregates within cavities. Due to the continuous chemical evolution of the ternary sulfarsenides outgoing from gersdorffite compositions towards higher Fe and Co, the various Ni-Co-

Fe sulfarsenides expressed as gersdorffite II (gdf II) in the following and in all Figures and Tables. This stage Va Ni-Co-Fe paragenesis is either restricted to stage IV ores that occurred within the marginal parts of the veins or within regions of the host rock, adjacent to the vein (cf. Figure 5a).

Within the fahlband host rocks, early Fe-cobaltite to late arsenopyrite occur as poikiloblastic and euhedral aggregates in direct vicinity to the veins at the lower level of vein 3 (cf. Figure 4a and 5h, Alpine cbt, Alpine asp). This stage Va Fe-Co paragenesis preferably grow along shear bands, crossing the preliminarily pure carbonate veins. Alpine cobaltite and arsenopyrite additionally replace the Fe-Co dominated ores of stage II, whereas gersdorffite II only present in the vicinity to the Ni-Co ores of stage IV.

Stage Vb (Neoalpine five-element Co stage): Following to the above-mentioned replacements due to dissolution and reprecipitation, Co-dominated ores precipitated with the typical textures of five-element veins within cavities. Euhedral Fe-Ni-rich cobaltite encloses primary native Bi IV and replaces relictic Fe-Ni-rich safflorite. The last formation is skutterudite IV, which encloses round droplets of native Bi (Figure 9j). Rounded native Bi droplets additionally occur as trail like aggregates, intersecting the previous gangue aggregates. In rare cases, skutterudite IV encloses some small grains of uraninite. Euhedral magnetite occurs in all generations of stage Va and Vb (cf. magnetite IV; Figure 8).

Stage VI (Late Alpine hydrothermal overprint and supergene weathering): As late Alpine hydrothermal overprint, aggregates of the gersdorffite-cobaltite solid solution affect and overprint most preliminary ore textures of the Ni-Co stage IV (gdf-cbt replacing gdf I and nc I; Figure 9g). Only aggregates entirely enclosed in chlorite stayed mostly unaffected by this late process (Figure 9n). Otherwise, niccolite I underwent intensive dissolution or recrystallized as myrmecitic intergrowths as niccolite III together with the gersdorffite-cobaltite solid solution (cf. Figure 8 and Figure 9g). Former euhedral grain boundaries of gersdorffite I towards skutterudite III are still recognizable. Note that niccolite II is only present at GP. U-Pb ages reveal that these late textures are independent from the primary ore formation (see chapter 7.2 and 8.1).

As supergene weathering products, erythrite and annabergite occur as pink and green bloom crusts at the mine walls, where Co- or Ni-dominated ores are present. Other areas show brownish colored iron-hydroxides. Within the thin sections, erythrite and annabergite are present in cavities.

6.5 Mineralogy Pipji

Although the mineralization of PI shows the most complex textures, the vein has never been mined and thus offers the best spatial relationship between consecutive ore stages and their correlation from primary precipitation to reworking phenomena during Alpine tectonic events. Observations on various textural and mineralogical characteristics (macroscopic and microscopic) show that different zones evolved. As illustrated in Figure 6, these zones are pre-defined as pristine Fe-Co ores (zone A); Ni-Co rich replacement ores (zone B); brittle ore brecciation along S2 direction (zone C); ores concerned by ductile deformation (zones D); and regions where neoformation of arsenide blasts occurred within Alpine gangue (zone E). These zones coincide with the temporal evolution of the vein. Figure 10a illustrates the paragenetic succession and related zones A-E.

Figure 10: Paragenetic sequences observed from (a) Pipji, (b) Grand Praz greyish ores and (c) Grand Praz reddish ores. For further explanations see text; for mineral abbreviations cf. Table A2 (Appendix).

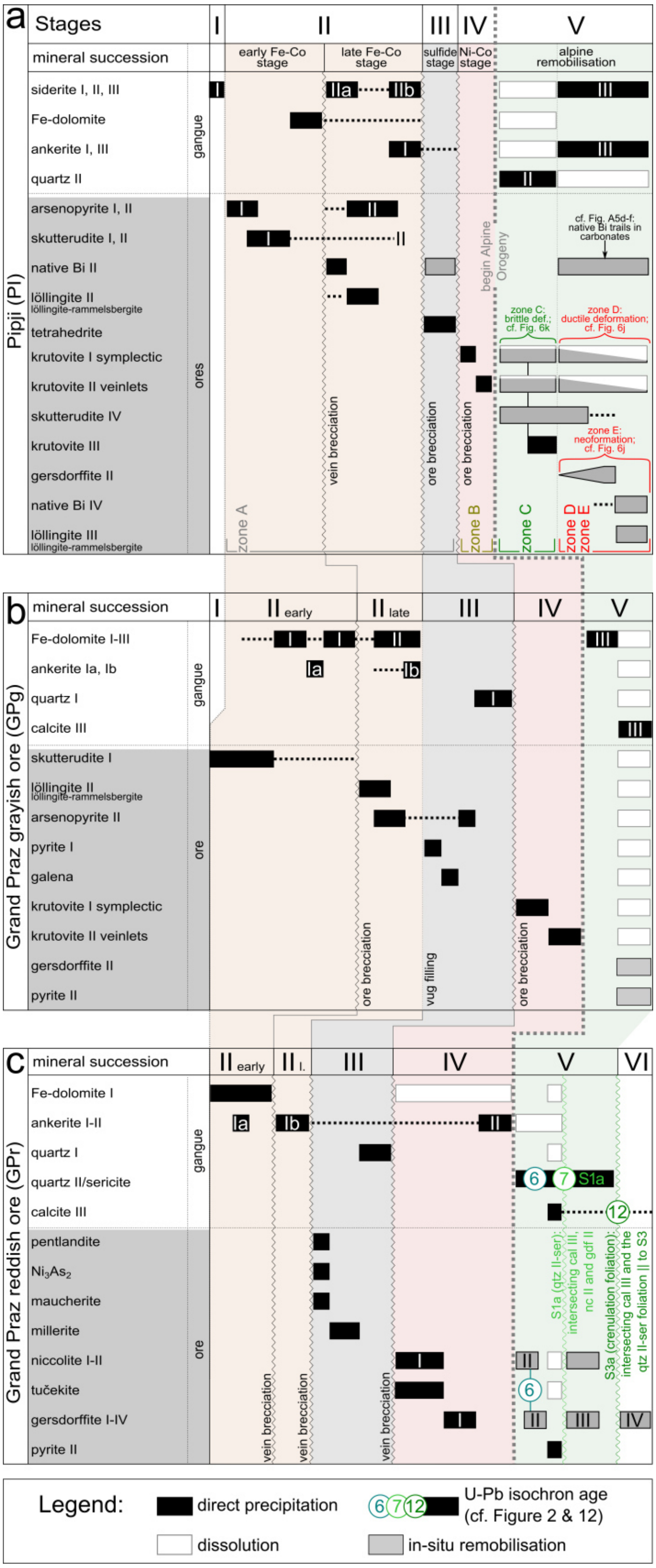

6.5.1 Definition of zones A-E

Zone A: Were no later alternation occurred in the primary and massive ores (Figure 6a, d-g: pristine Fe-Co ores), textural and mineralogical relationships are unambiguously identical to those of the Fe-Co ore stage of KB. Here mineralogical changes were limited during the Ni-Co stage IV and Alpine stage V. Additionally, changes due to intensive deformation, brecciation and metamorphic effects are minimal.

Zone B: First modifications of the pristine Fe-Co ores show chemical similarities to the ores of the Ni-Co stage IV at KB (cf. chapter 8.1.2). Compared to KB, the mineralogy is variable but similar to those at GPg (greyish ores; cf. Figure 10a and b). Here Ni-Co-rich ores infiltrated those of the pristine Fe-Co stage II along finger-like and irregular shaped reaction fronts (Figure 6a, d-g). In most cases, these contain arsenides and arsenic-rich sulfarsenides.

Zone C and D: In these zones, ore deformation occurs either as high-grade brittle or ductile deformation (cf. Figures 6h and i; zones C and D, respectively). Both zones gradually merge and therefore do not occur as distinct zones. Ore textures, mineralogy and composition are variable, depending on the style of deformation. Ni-Co ores that concerned by the brecciation in zone C often retain their pristine mineral intergrowth. Areas, which do not show brecciation, respond increasingly ductile. In zone D intensive deformation concerned primarily elongated crystal shapes. Unlike to zone B, sulfarsenides in zones C and D include more S-rich compositions.

Zone E: This zone often occurs adjacent to the ductile deformed areas (Figure 6i). Here ankerite and siderite replaced quartz that previously formed during brecciation in zone C. In addition to the dissolution of quartz, concentric blasts of sulfarsenides and arsenides occur. Compositionally, sulfarsenides and arsenides are identical to those of the ductile deformed areas of zone D (cf. chapter 8.1.2).

6.5.2 Gangue minerals

Fe-Co stage II: Siderite I, is overgrown by euhedral Fe-dolomite, and then intensively replaced by ore minerals (Figure 6c). Similar to KB, Fe-dolomite is abundant and intensively fractured, where the fragments are cemented by ankerite I. Oscillatory zoned siderite IIa towards IIb and late ankerite I occur in the pore spaces of the Fe-Co stage II ores (Figure 11a).

Sulfide stage III and Ni-Co stage IV: Ores of the sulfide stage III enclose euhedral ankerite I (Figure 11a). No gangue formation accompanies the in-situ Ni-Co stage IV formation within preexisting Fe-Co stage ores (zone B). Note that quartz I and ankerite II, which are abundant at KB, are completely lacking at PI (cf. Figure 8 and Figure 10).

Stage V: During the early stages of Alpine remobilization, brecciation of the massive ore aggregates occurred along the S2 direction, where the fractures are then cemented by quartz II (zone C). Quartz II replaces prior siderite, Fe-dolomite and ankerite generations. As the final stage, quartz II dissolution is accompanied by siderite III and ankerite III precipitation (zone D: Figure 11i). Besides these replacement features, Fe-dolomite consistently shows intensive formation of pressure twinning (cf. chapter 6.8).

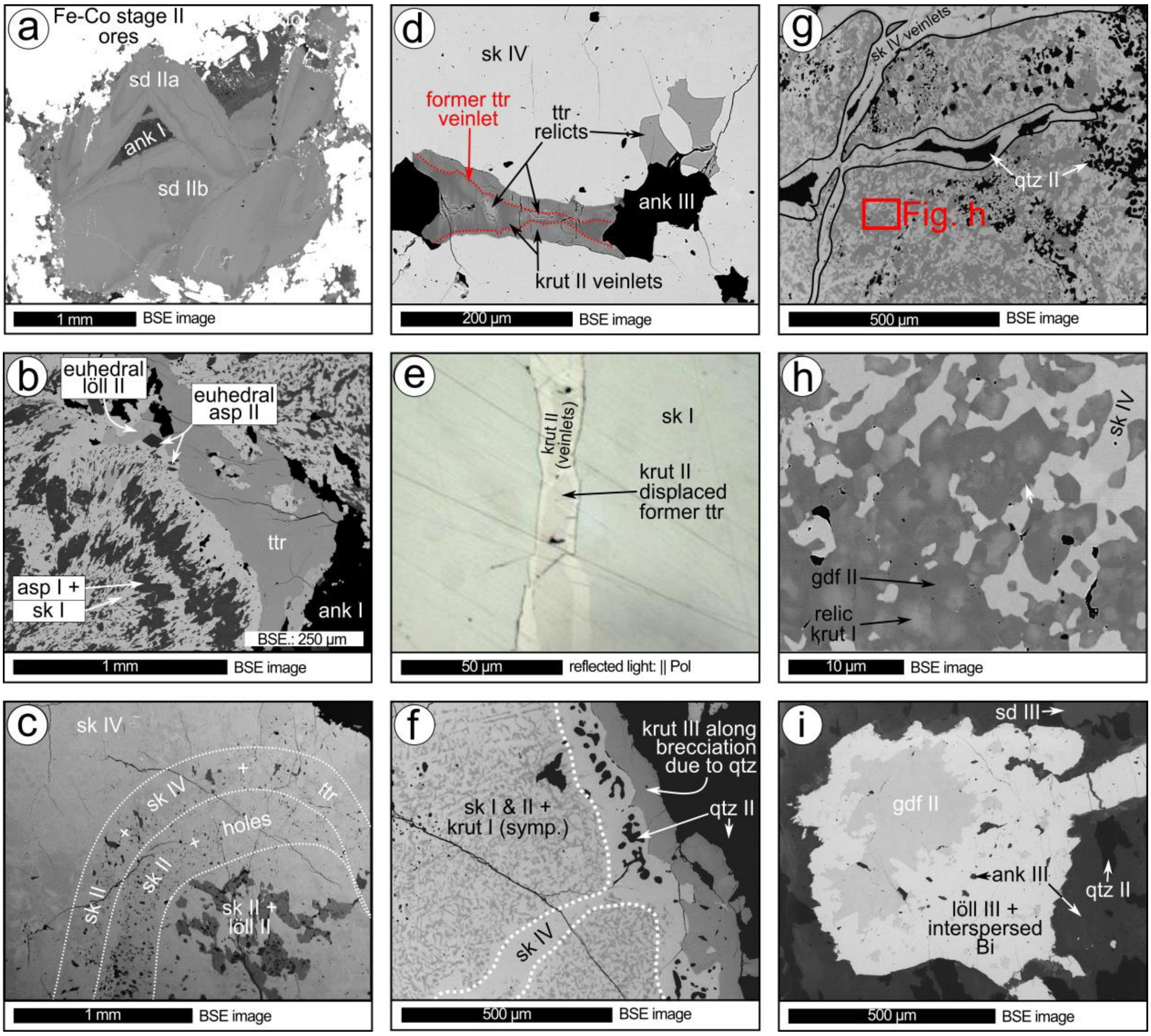

Figure 11: Mineral textures of the samples from Pipji. (a-e) Fe-Co stage at Pipji including minor effects of later modification. (f-h) Intensive formation of Ni-Co stage ores. (i) Neoformation of arsenide blasts within Alpine gangue For further explanations see text; for mineral abbreviations cf. Table A2 (Appendix).

6.5.3 Ore minerals

Transition from Fe-Co stage II to sulfide stage III (zone A): In detail, arsenopyrite I and skutterudite I are in intensive intergrowth during the initial stage, at which both show a rhythmic sequence between pure skutterudite and both together (Figure 11b). Within the remaining pore spaces, these aggregates are followed by euhedral löllingite II and arsenopyrite II. Skutterudite I encloses the euhedral arsenopyrite II and löllingite II aggregates, whereas skutterudite II displaced former löllingite II (Figure 11c). Tetrahedrite (i.e. the sulfide stage II) occurs within former pore spaces and overgrows the euhedral aggregates (Figure 11b). Additionally, tetrahedrite penetrated both skutterudite generations as up to 200 µm wide veinlets (Figure 11d). Most ores of this stage show intensive displacement by later ore stage (Figure 11c-d).

Ni-Co stage IV (zone B): Compared to KB, niccolite, rammelsbergite and gersdorffite do not occur at PI. Ni-dominated sulfarsenides (representing the transition between rammelsbergite and arsenian gersdorffite), however, occur as krutovite ($NiAs_{2-x}S_x$; $x<0.5$). Primary aggregates of this stage occur within skutterudite I or II either as a fine symplectic intergrowth of elongated krutovite I aggregates or a generation of krutovite II veinlets (Figure 11e-f). Due to intensive deformation, temporal relations between krutovite I and II are not obvious at PI. Crosscutting relationships at GP, however, indicate a displacement of early layers including symplectic krutovite I by the formation of late krutovite II veinlets (cf. chapter 6.6). Besides pure krutovite II veinlets, it additionally infiltrated prior tetrahedrite veinlets. Therefore, krutovite II is younger than tetrahedrite and indicate a temporally equal position as rammelsbergite and gersdorffite I of the Ni-Co stage IV at KB.

Alpine stage V (zones C-E): Major parts of the ores at PI altered during the Alpine Orogeny, at which brecciation and modifications by deformational textures replaced and destroyed many primary textures. In situ-replacements and neoformation occur as krutovite III, skutterudite IV, gersdorffite II, native Bi and löllingite III. Accompanied to brecciation (zone C: brittle deformation; Figure 6k), krutovite I and krutovite II were deformed to a minor extend and enclosed by a halo of early skutterudite IV with quartz II and late krutovite III (Figure 11f). Skutterudite IV infiltrates the previous ores along veinlets, leaving the textural relationship of the symplectic intergrown mostly unaffected. Intensive deformation of the symplectic intergrowth and in-situ replacement of skutterudite I, krutovite I and krutovite II by skutterudite IV, gersdorffite II and löllingite III occurs at regions where brecciation was restricted (zone D: ductile deformation; Figure 6j). The increased dissolution of skutterudite I and II coupled to concomitant recrystallization as skutterudite IV leaded to the formation of voids, quartz II precipitation and the dissolution of krutovite I (Figure 11g). Areas of high ductile deformation reveal that sulfur-rich gersdorffite II intensively replaces krutovite I (Figure 11h). Similarly, areas of zone E show the neoformation of early gersdorffite II cores surrounded by löllingite III with embedded, sub µm-sized native Bi (Figure 11i).

Besides these neoformations, all vein sections show intensive replacement and recrystallization of previous ores by skutterudite IV. Due to the isotopism, differentiation of the skutterudites is only possible by chemical analysis. In addition to skutterudite, native Bi shows very common textural evidence of ore deformation. Chapter 6.8 reports detailed information about deformation textures.

6.6 Mineralogy Grand Praz

Excessive mining at GP restricts petrographic observations to historic collection samples, at which temporal and spatial correlations of the host rocks and successive ore stages are limited. Nevertheless, greyish (GPg; Figure 12a-i) and reddish (GPr; Figure 12j-s) colored ore types can be distinguished, at which the mineralogy and chemistry resemble the Fe-Co ore stage II and the Ni-Co ore stage IV, respectively. Deformation textures, however, mostly restrict to the gangue carbonates and Alpine ore remobilization is more intensively developed at the reddish colored ore type. Figures 10b and 10c illustrate observed paragenetic successions of GPg and GPr, respectively.

6.6.1 Gangue minerals

Unlike to KB and PI, the gangue mineralization is less dominated by repeated ankeritisation and shows a dominance of early Fe-dolomites, ankeritisation and late calcite precipitation (Figure 12a and j). Generally, Fe-dolomites show yellowish-whitish and areas of intensive ankeritisation greyish-blackish colors. Calcite occurs as intermixtures of either pure white or (due to intersperse opaque phases) as blackish colored calcite. Both sample types show comparable mineralogic successions, although a higher grade of ankeritisation is present in the GPr samples than those in GPr. In addition, neither native Bi nor siderite is present.

Fe-Co stage II: The dominant gangue represents rhombohedral aggregates of cm-sized Fe-dolomite I, which includes several interlayers of ankerite Ia and encloses cm-sized aggregates of primarily pure skutterudite I (Figure 12a-c). At GPg a second Fe-dolomite II (that hosts euhedral aggregates of löllingite II) encloses the former aggregates. As the latest stage, ankerite Ib infiltrates the previous carbonates as a network of µm-sized veinlets (i.e. ankeritisation; cf. Figure 12b).

Sulfide stage III: The carbonates of the Fe-Co stage II form druses, filled with the sulfide stage mineralogy. This primordial gangue mineralization of the sulfide stage mostly disappeared due to its intensive dissolution and additional formation of calcite III during the Alpine stage. It is reasonable

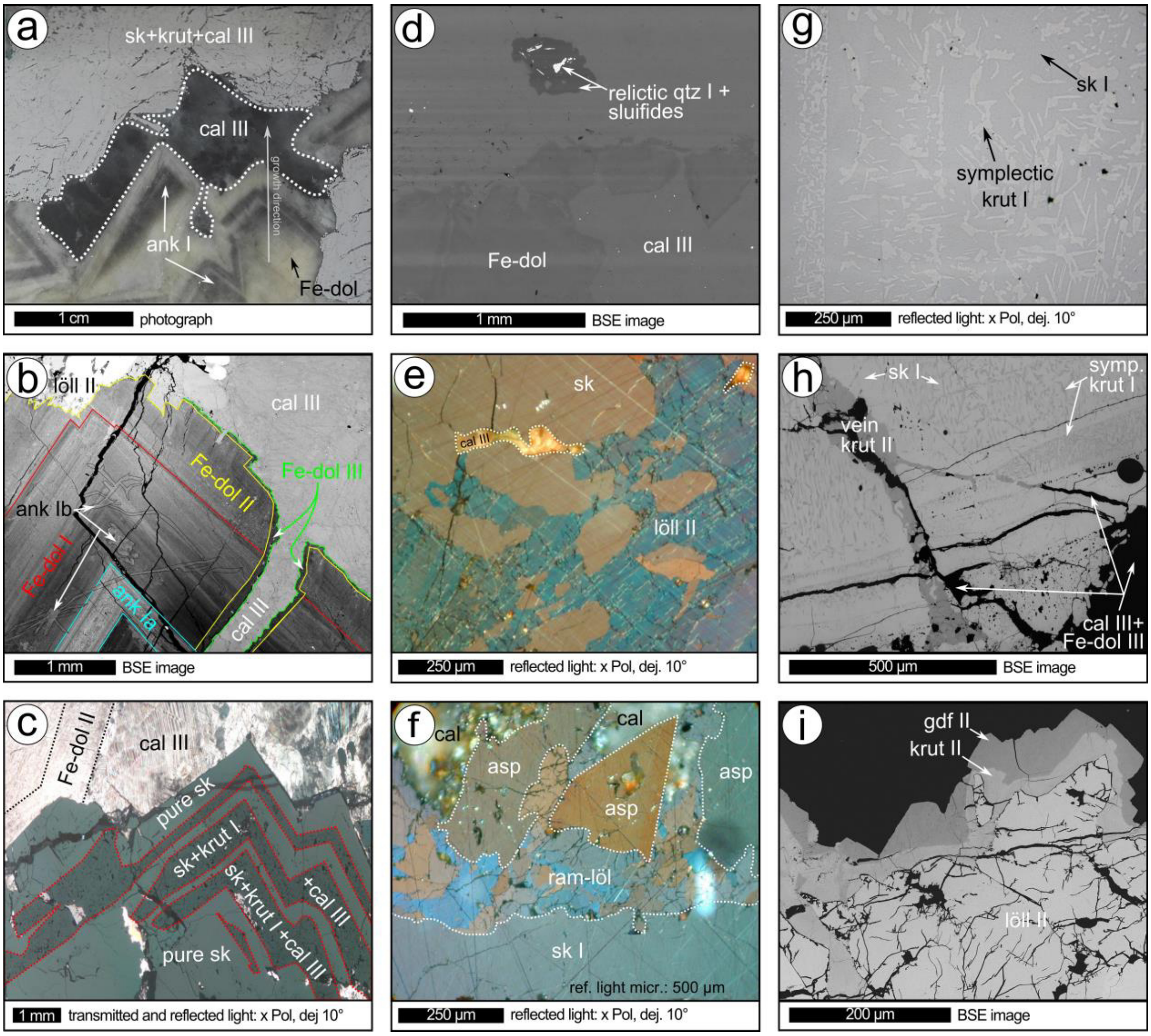

Figure 12a-i: Mineral textures of the samples from the greyish ores at Grand Praz (GPg). For further explanations see text; for mineral abbreviations cf. Table A2 (Appendix).

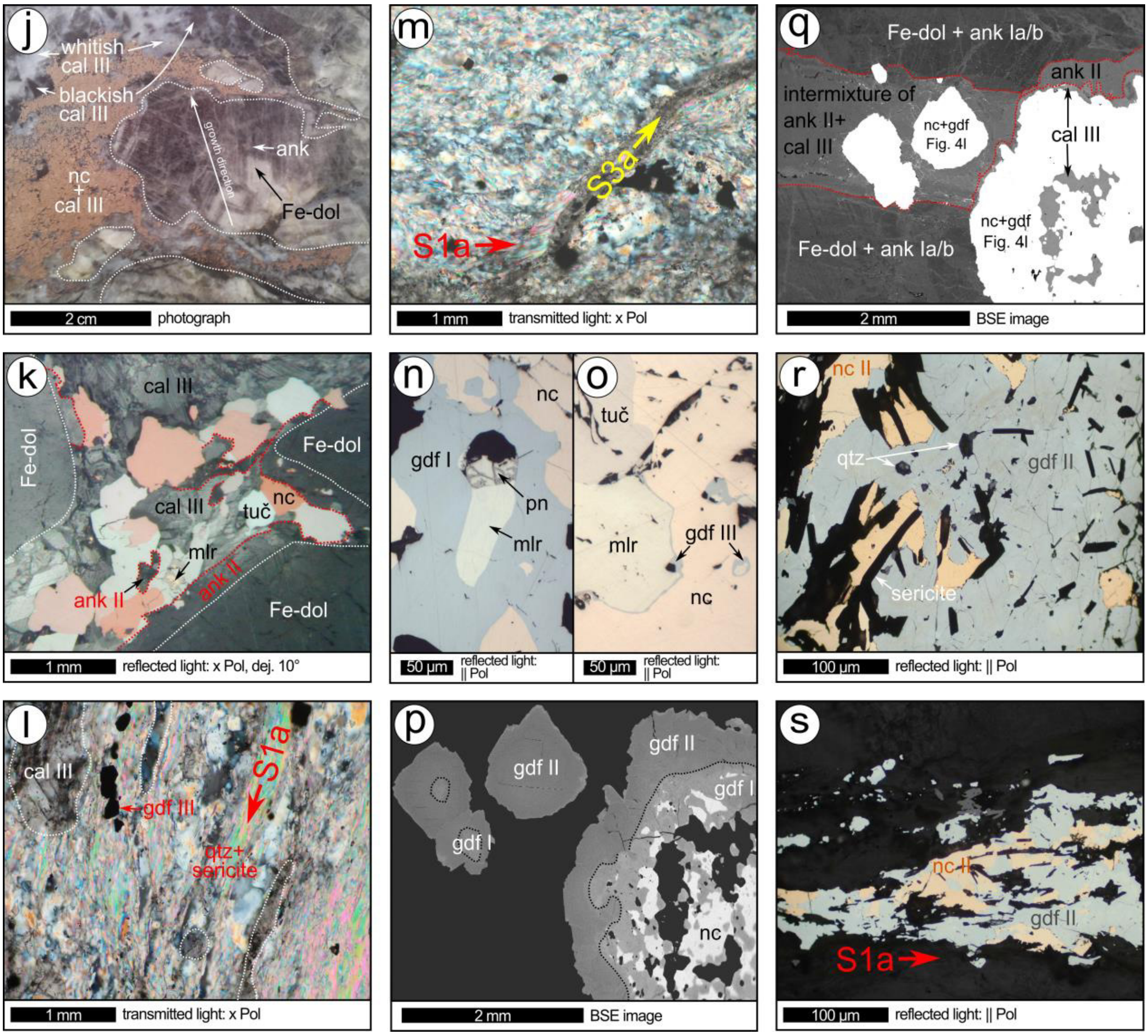

Figure 12j-s: Mineral textures of the samples from the reddish ores at Grand Praz (GPr). For further explanations see text; for mineral abbreviations cf. Table A2 (Appendix).

that quartz I was originally precipitated within the open spaces between Fe-dolomite, trapping the original sulfide stage ore mineralogy. Relicts of these ores, however, are present within relicts of quartz I (Figure 12d), which shows similar bluish-black cathodoluminescence colors as quartz I of the sulfide stage at KB. Calcite III precipitation, however, led to the dissolution of quartz I and the sulfides, leading to a large number of µm-sized single crystals of pyrite, galena and arsenopyrite.

Ni-Co stage IV: All gangue sections of the GPr ores show an intensive affectation by ankeritisation (Figure 12j). Similar to the pristine gangue paragenesis of the sulfide stage, the gangue mineralogy coprecipitated with the Ni-Co stage ores mostly disappeared. In some sections, however, relicts of ankerite II preserves the intensive gangue replacement by calcite III (Figure 12k). Where ankerite II relicts remained, it is reasonable that Fe-dolomite was fractured and open spaces were filled by ankerite II and the ore paragenesis. Ore formation, which is included in the Ni-Co stage at GPg, is not associated by specific gangue formation.

Stage V: Intense brecciation and displacement of previous gangue minerals by calcite III dominates the Alpine Stage V (Figure 12b and d). Besides this, Fe-dolomite III precipitates prior to calcite III at GPg (Figure 12b). Additionally, two foliations occur in the direct vicinity to the vein-host rock boundary, which (according to U-Pb ages; cf. chapter 7.2) either evolved before S1 or after S3 and therefore appointed as S1a and S3a, respectively. Foliation S1a includes sericite and quartz II with preferred orientation intersecting calcite III and S3a represents a crenulation foliation affecting calcite III, sericite and quartz II (Figure 10c; Figures 12l-m). In transmitted light, S3a is visible as a very fine-grained and often fibrous developed calcite that occurs as grayish and diffusive translucent aggregates.

6.6.2 Ore minerals

According to the main ore phases, the greyish ore (GPg) was identified as an intensive mixture of skutterudite, löllingite arsenopyrite and krutovite; the reddish ore (GPr) essentially as masses of niccolite and gersdorffite. Compared to KB and PI, main ore textures and the paragenetic successions show similarities of the GPg type ores to the Fe-Co stage II, and similarities of the GPr type to the Ni-Co stage IV. Both ore types include intermediate or previous sulfides (similar to the sulfide stage III at KB and PI) and affected by Alpine remobilization. The ores of GPr show intensive processes of reworking during Alpine stages and primary crystal intergrowth is masked by dissolution and reprecipitation. The ores of GPg stayed mostly unaffected, which benefits a more ordered identification of the successive transitions between the Fe-Co stage II, Ni-Co stage IV and late Alpine hydrothermal alteration.

Fe-Co stage II: Euhedral aggregates of skutterudite I dominate the ores of GPg which relate to the Fe-Co stage II (Figure 12a). Skutterudite I shows a periodic layering of pure skutterudite with layers of skutterudite I intergrown to krutovite I (Figure 12c). Note that krutovite I formed later during the Ni-Co stage. Identical to the Fe-Co stage II of KB, early löllingite II intensively displaces or overgrows skutterudite (Figure 12e-f). Successively to löllingite II, euhedral arsenopyrite II is present. No ore formation is obvious at ore aggregates of the GPr type during this stage. Neither as relicts nor as distinct phases.

Sulfide stage III: Due to intensive displacement of pristine sulfides by Alpine calcite III, the sulfide stage at the GPg type ores are not visible as their original textures. Finely dispersed arsenopyrite II, pyrite I and galena still represent the sulfide stage mineralogy to certain extent. Relicts of this stage are present within relicts of quartz I (Figure 12d). The sulfide stage within the GPr type ores is represented by mostly rounded and relic aggregates of pentlandite, maucherite, millerite and an unknown phase, which is analogous to haezlewoodite with a Ni_3As_2 stoichiometry (Figure 10c and Figures 12n-o).

Ni-Co stage IV: Similar to textures at PI, a symplectic intergrowth of skutterudite I and krutovite I evolves at the GPg type ores (Figure 12g). Additionally, late krutovite II occurs as veinlets crosscutting the alternating layers between skutterudite I and krutovite I (Figures 12h). Ore brecciation and additional formation of krutovite II favors the formation of symplectic krutovite I. Regions without brecciation remain as pure skutterudite I. Krutovite II additionally replaces löllingite II, what constrains its post-stage II formation (Figures 12i). Temporal relations to ores of the sulfide stage III are not present, but by the analogy of the krutovite II veinlets to PI, a post-stage III age can be expected.

The GPr type ores mostly consist of monomineralic niccolite I as massive ore aggregates (Figure 12j). Niccolite I develops equilibria like textures with 120° grain boundaries (cf. chapter 6.8). At the ore aggregates marginal parts, the equilibria like texture is accompanied by tučekite ($Ni_9Sb_2S_8$, tuč; Figure 12k, m). In some cases, gersdorffite I overgrow niccolite I and tučekite as corona-like disequilibrium textures (Figure 12p-q). In each case, these aggregates originally surrounded by ankerite II, which later was replaced by calcite III.

Alpine stage V: The ores of GPg show a restricted influence during this stage. Unlike textures in PI, the ores show no significant ductile deformation. The symplectic intergrowth between skutterudite I and krutovite I is crystallographically oriented and not disturbed. Layers including krutovite I, however, show a preferred displacement of krutovite by calcite III, leaving the above-mentioned layers of intergrown calcite III and skutterudite I (Figure 12c). Calcite III additionally displace the krutovite II veinlets (Figure 12h). In rare cases, gersdorffite II displaces former euhedral krutovite II aggregates that indicates a post-stage IV formation (Figure 12i).

The ores of the GPr type show more intensive and more complex remobilization textures. Niccolite I and tučekite mostly concerned by intensive displacement by calcite III (Figure 12k, p-q).

Former euhedral gersdorffite I additionally disappears by a concomitant in-situ replacement due to gersdorffite II (Figure 12p). Formation of pyrite II accompanies the precipitation of calcite III. Limited to the selvedges of the vein, late gersdorffite II with early niccolite II enclose µm-sized euhedral sericite and quartz II aggregates without preferred orientation (Figure 12r). Neither niccolite II nor gersdorffite II show a paragenetic relation to the niccolite I-tučekite-gersdorffite I mineralized parts of stage IV. Oppositely and accompanied by fine-grained sericite along foliation S1a, gersdorffite II and niccolite II show elongated grains and a successive orientation of former sericite and quartz II (Figure 12s). Regions affected by S1a additionally include euhedral and Fe-rich gersdorffite III, which additionally encloses pyrite II at regions where calcite III concerned by foliation S1a. Where niccolite I, tučekite and millerite are present, an additional generation of gersdorffite IV occurs narrowly restricted to the contact of niccolite and millerite, whereas the contact of niccolite I and tučekite resides unaffected (Figure 12o).

6.7 Mineralogy Collioux Inférieur

Although the vein at CI hosts abundant supergene weathering phases, microscopic observations display a very restricted mineralogy in respect to the primary gangue and ore stages. Unlike to PI, KB and GP, exclusively Alpine aged arsenopyrite III occurs as the single sulfarsenide. Arsenides lack at this locality and additionally Co and Ni are only present within an abundancy of secondary arsenates. Bleached and highly altered relicts of siderite or dolomite are present in coarse-grained quartz II (Figure 13a). Iron oxides/hydroxides and Fe-(Co-Ni) arsenates infiltrated the carbonates along their cleavage planes. Fine-grained quartz and muscovite percolates the prior coarse-grained quartz II along a network of shear bands. Restricted on these layers, euhedral and randomly distributed arsenopyrite occurs alongside (Figure 13b), but additionally occurs within cracks filled by aligned sheds of pure muscovite (Figure 13c). Some µm-mm sized veinlets of scorodite [$Fe^{3+}AsO_4 \cdot 2H_2O$] and Kolfanite [$Ca_2Fe_3^{3+}O_2(AsO_4)_3 \cdot 2H_2O$] -the latter reported by Ansermet (2012)- additionally crosscut the prior muscovite shear bands, at which they also infiltrate into the prior muscovite grain network (Figure X14d).

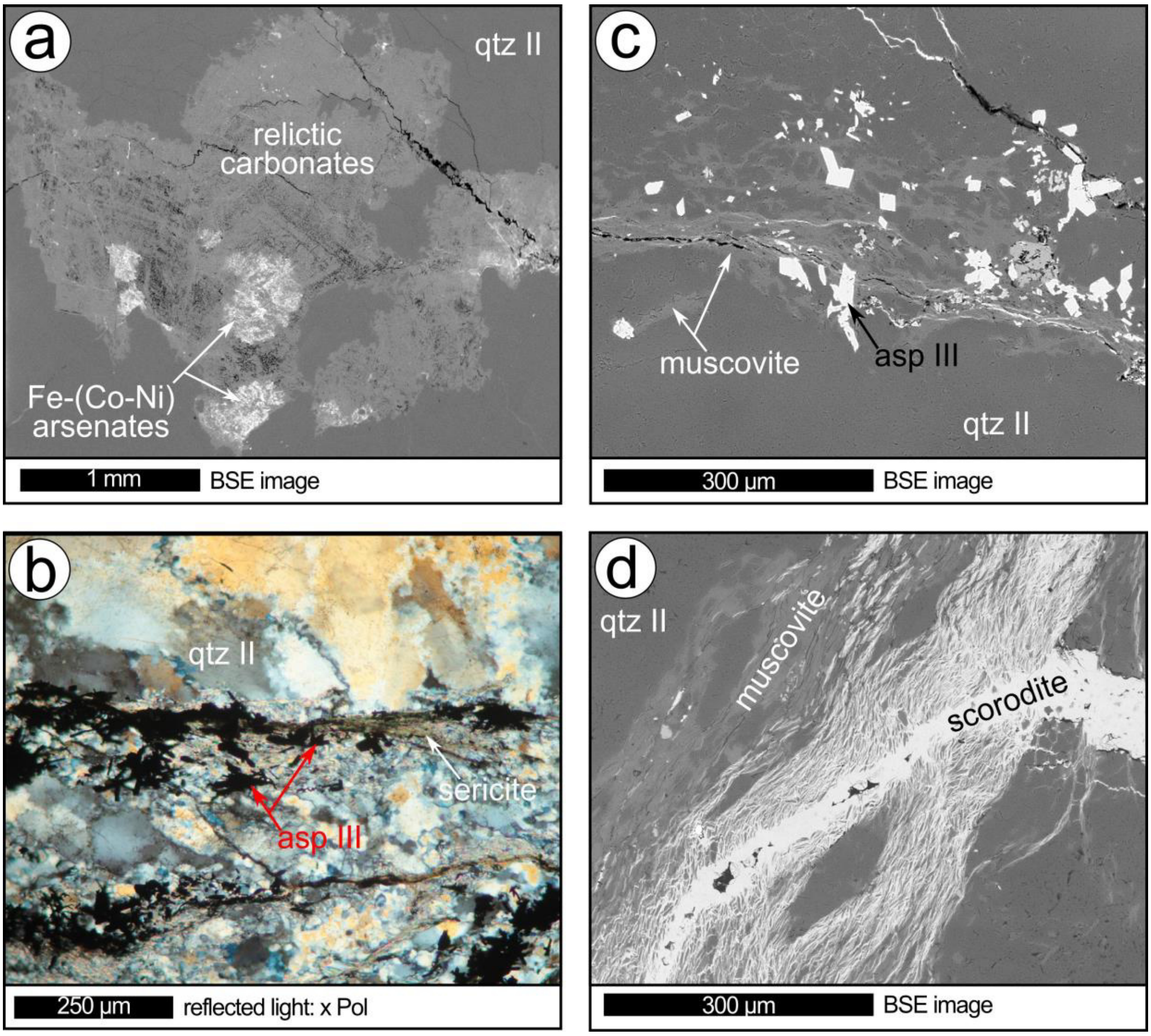

Figure 13: Mineral textures of the samples from Collioux Inférieur. For further explanations see text; for mineral abbreviations cf. Table A2 (Appendix).

6.8 Textures of deformation and metamorphic effects

Besides obvious deformation from vein-rock relationships (cf. chapter 4.2), several microscopic observations indicate that deformation of the gangue and ore phases happened after their precipitation. Some mineralizations additionally show a dynamic displacement of prior phases, and others show an intensive recrystallization. This chapter documents a condensed overview of these visible deformation textures that happened during the Alpine Orogeny and compares occurring deformation characters between the four vein systems. The textural notations for grain fabrics and their interpretation follow the descriptions of Passchier and Trouw (2005) and references therein.

6.8.1 Ore deformation and recrystallization

Firstly, ore deformation is visible from the arsenides due to the successive distortion of symplectic krutovite I (cf. Figures 11f-h and 12g-h). Additionally, formation of Alpine skutterudite IV favored the interruption of the formerly continuous krutovite II and tetrahedrite veinlets (Figure 14a). In such cases, skutterudite I and II recrystallized during the Alpine deformation leading to compositions of skutterudite IV. Areas where skutterudite recrystallisation occurs, show slightly bulged and blurry grain boundaries towards the veinlets (Figure 14b). Compositions surrounding relictic krutovite and tetrahedrite show those of skutterudite IV, relicts that reside within the veinlets were protected from this recrystallization and still show the former composition of primary skutterudite II. In addition to this, static recrystallization is indicated by grain fabrics of the tučekite-niccolite I paragenesis including 120° grain boundaries (Figure 14c).

The second index for a (probably ductile) deformation of the ores is the fact that native Bi only in rare cases reside within the arsenides. If native Bi occurs within the arsenides, however, euhedral and dendritic growth (which is very indicative for five-element veins) disappeared and mostly glitter-like aggregates remain (Figure 9k) or it resides as sub µm-sized fringes along different monomineralic or polymineralic grain boundaries (Figure 14d). Most quantities of native Bi moved from the arsenides into healed fractures of aligned 1-10 µm-sized droplets (Figure 14e), as up to mm-sized continuous veinlets (Figure 14f) or as the latest phase within druses covering euhedral quartz II, löllingite III, arsenopyrite III or albite (Figure 14g).

6.8.2 Gangue deformation and recrystallization

Without any exceptions, the above-mentioned late effects of native Bi infiltration concern all gangue minerals and all stages. Host minerals that surround native Bi do not show any radial crack formation due to typical volume expansion during the transition of native Bi from its liquid phase. Additionally, calcites and Fe-dolomites show intensive formation of pressure twinning. Regions of the

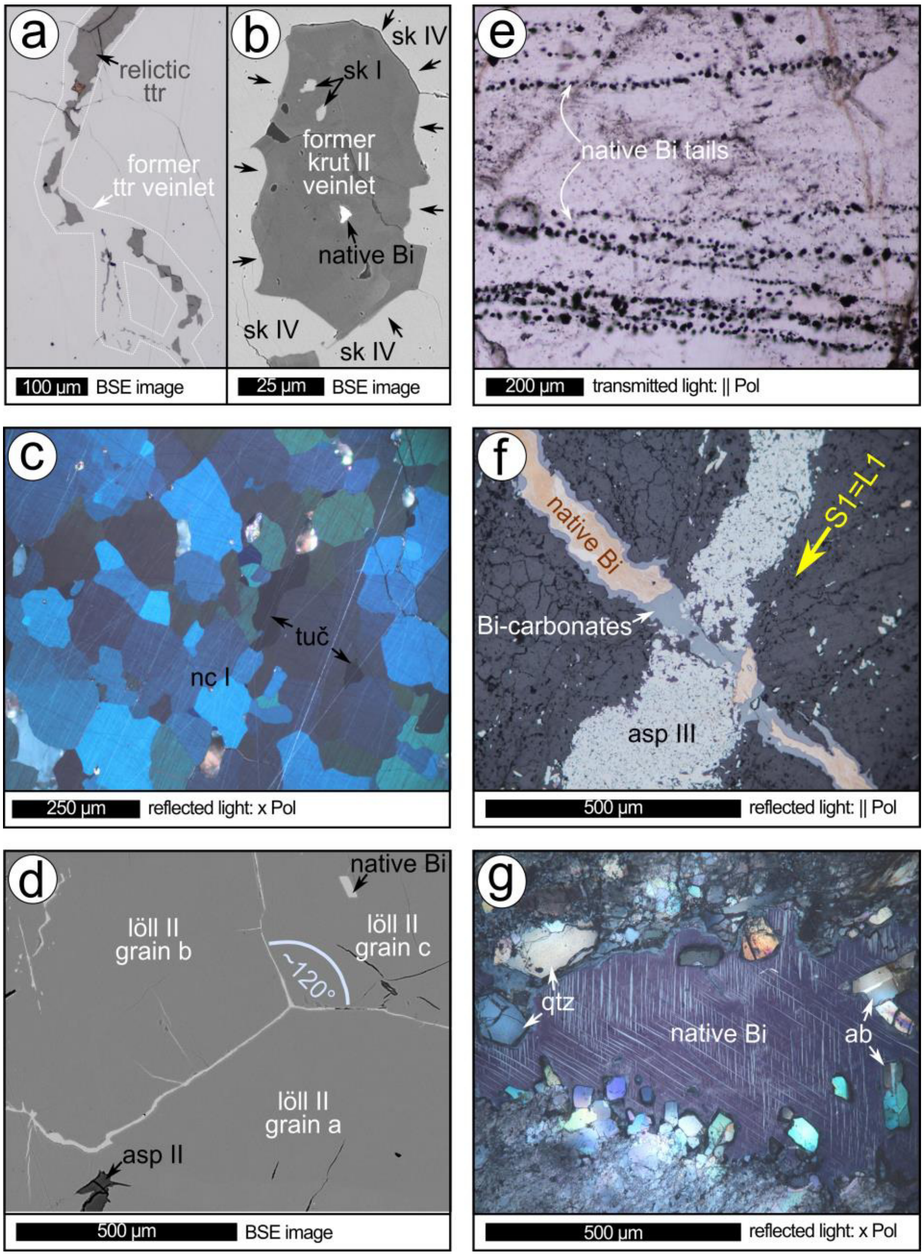

Figure 14: Deformation textures of the ore minerals. For further information see text.

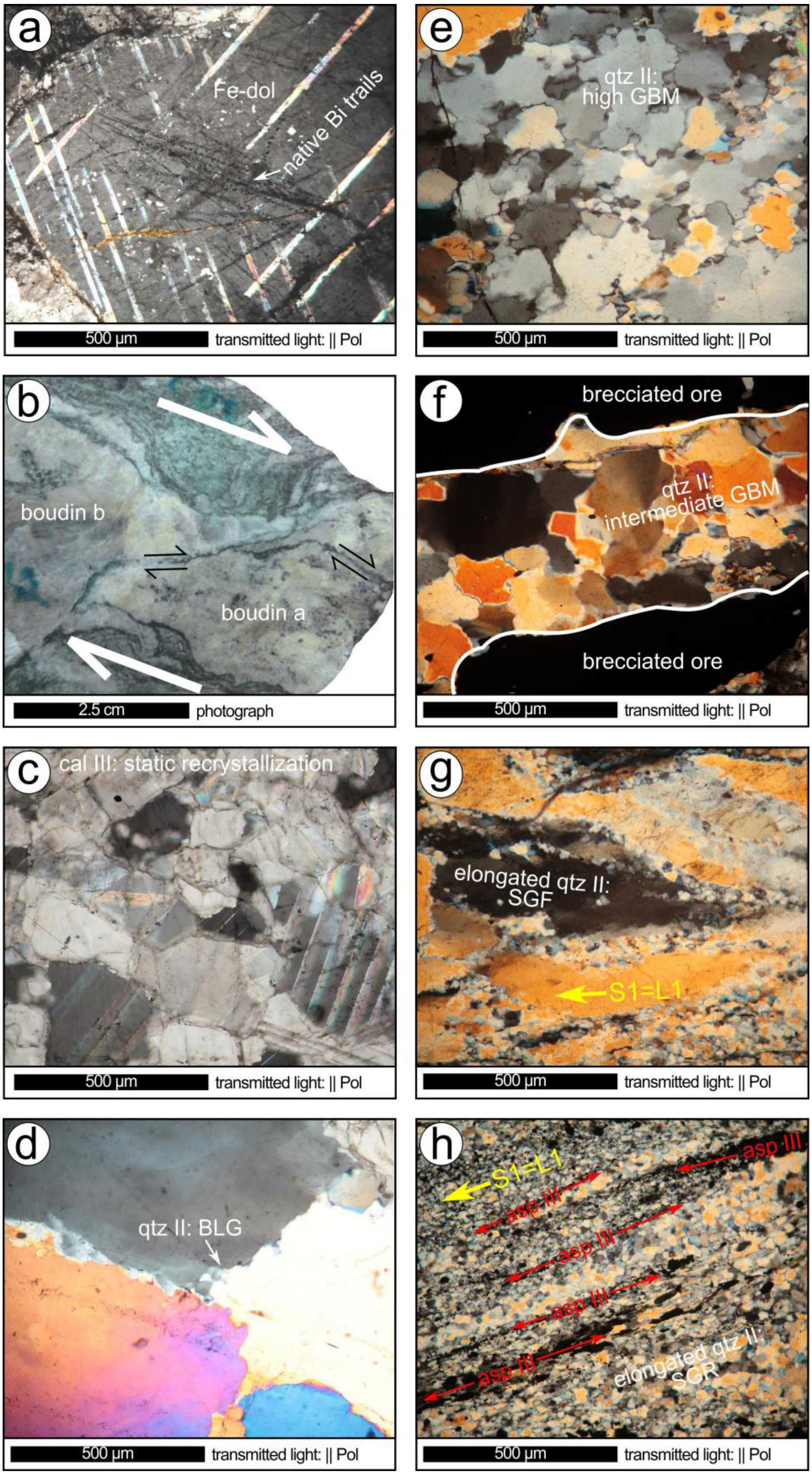

Figure 15: Deformation structures of the gangue minerals. (a) Pressure twinning of dolomite later healed due to the infiltration of native Bi trails. (b) backthrusting of two previously separated boudins. (c) foam texture of calcite III. (d-h) increasing strain within quartz II. For further information, see text.

Fe-dolomites, surrounding the native Bi droplet trails, however, show a recovery of the previously formed pressure twins in Fe-dolomite (Figure 15a).

Deformation of the carbonates mostly accommodated by the formation of boudins and folds obvious at KB and PI (Figures 4a-b; 5a-b). Individual boudins later got overthrusted and moved relatively to each other (Figure 15b). These extensive and compressive strains developed along the S1 foliation direction within veins perpendicular to the main stress vector. Single veins parallel to this vector reside unaffected (i.e. perpendicular to S1), which is most obvious at the vein of GP that does not show such effects (Figure 4b-c). Intensive deformation, however, is visible from deformation twinning of the gangue carbonates that compensated occurring strain (Figure 15a). Formation of polygonal calcite III that replaced older gangue or ore phases also indicate an at least static recrystallization at GP (Figure 15c). Additionally, foliations S1a and S3a affected sericite, quartz II, niccolite II, gersdorffite II and calcite III as S-C’-type shear bands at the transitional regions towards the host rocks (Figure 10c). Foliation S1a developed as the S direction, S3a corresponds to C’. This strain accommodation again developed alongside to the vein direction, but unlike to KB and PI this direction is perpendicular to the S1 foliation. It is speculative that this direction corresponds to the late Alpine S3 direction (cf. Figure 4c). At CI, Alpine deformation concerned the veins as mylonitic growth of quartz replaced primary phases and textures.

Quartz grain fabrics and its progressive irregularities of recrystallized grain boundaries additionally show a successive and increasing strain rate between the single occurrences. Relative increase of strain rates can be followed in Figure 15d-h, which analogously indicate correlation to experimental approaches of (Takahashi et al. 1998). According to Figure 1b and 3a, higher strain should be expected at CI and PI and followed by KB and lastly by GP, as they reside symmetrically across the recumbent fold of the Siviez-Mischabel Nappe. At GP, quartz only occurs within druses and intensively displaced by calcite III. Recrystallization of quartz is not visible but polygonal calcite III (within the veins) and evolution of foliations S1a and S3a (restricted to the selvedges) indicate a more static recrystallization and concerted deformation only along the margins of the vein. Quartz II precipitation is more intensive at KB and mostly crosscuts the veins perpendicular to the main foliation S1 and vein directions. Pressure shadows of the boudins additionally concerned by formation of quartz II (Figure 5a-b). In these regions, grain fabrics of quartz II prevailed under static conditions as indicated by coarse quartz with straight grain boundaries including low intensities of bulging recrystallization (Figure 15d: BLG). Quartz with interlobate granoblastic fabrics from more intensive grain boundary migration (GBM) and higher deformation rates, however, is present at regions, where intensive folding concerned the veins (Figure 15e: high GBM). At PI, quartz II consistently developed by GBM and deformation is therefore higher than in KB. Quartz II cementing the brecciated parts along S2 always shows polygonal granoblastic fabrics (Figure 15f: intermediate

GBM), where regions without brecciation also include interlobate granoblastic fabrics like in Figure 15e. This indicates lower strain occurring in the brecciated parts. The coarse-grained quartz at CI shows higher strain rates, which are visible due to exclusively interlobate granoblastic fabrics by BGL and additional elongated relicts of former quartz concerned by subgrain formation (SGF) at its margins (Figure 15g: SGF). The fine-grained shear bands (accommodating arsenopyrite III) show the highest strain rates. Here mylonitic textures occur as very fine-grained quartz with weak grain shape-preferred orientation due to subgrain rotation (SGR) during intensive dynamic recrystallization (Figure 15h: SGR).

6.9 Host rock alteration

Besides quartz and sericite, mostly pure chlorite occurs in the proximal host rocks at the direct contact to the veins. Where no chlorite is present (Figure 16a and b), abundant euhedral magnetite encloses tabular crystals showing transitions compositions between ilmenite, leached ilmenite and pseudorutile [$Fe^{2+}TiO_3$-$Fe^{3+}{}_2Ti_3O_9$ (EDX-SEM): cf. Mücke and Chaudhuri (1991) for nomenclature]. These crystals either enclose relicts of rutile [TiO_2] or include exsolution bodies of a Ti-hematite with Ti<6 mol% (EDX-SEM).

With increasing distance to the veins, the hornblende-epidote-albite-schists partly consist of monomineralic green hornblende [Rough formula of hornblende: $Na_{0.52}(Ca_{1.8}Na_{0.15}Fe_{0.05})_2(Mg_{2.3}Fe^{2+}{}_{1.65}Al_{0.85}Ti_{0.1}Fe^{3+}{}_{0.1})_5(Si_{6.5}Al_{1.5})_8O_{22}(OH)_2$ with a parasitic composition and low Fe^{3+} contents (EDX-SEM) (Oberti et al. 2012)]. Additionally, plagioclase is present within these rocks, but mostly relictic within saussuritic reaction halos (Figure 16c). Chlorite intensively displaces hornblende along its cleavage planes at regions where carbonate veinlets intersect these rocks (Figure 16d). Along with chlorite, epidote occurs where hornblende disappeared (Figure 16e). Additionally, intensive chloritisation of biotite developed besides the decay of hornblende (Figure 16f) [rough formula of chlorites: $(Mg_{2.5}Al_{1.5}Fe^{2+}{}_{1.7}Fe^{3+}{}_{0.25}Ti_{0.03}Mn_{0.02})_6(Si_3Al_1)_4O_{10}(OH)_8$ (EDX-SEM)]. Where hornblende disappeared, yellowish-brown leucoxene (translucent) is present that further enclosed by titanite and still show twinning lamellas common for rutile (Figure 16e). In rare cases, opaque phases are present instead of leucoxene that similarly represent $Fe^{2+}TiO_3$-$Fe^{3+}{}_2Ti_3O_9$ compositions as described previously. Relicts of rutile are still present within these Fe-Ti oxides. Leucoxene mostly appears without opaque relicts, where epidote is present.

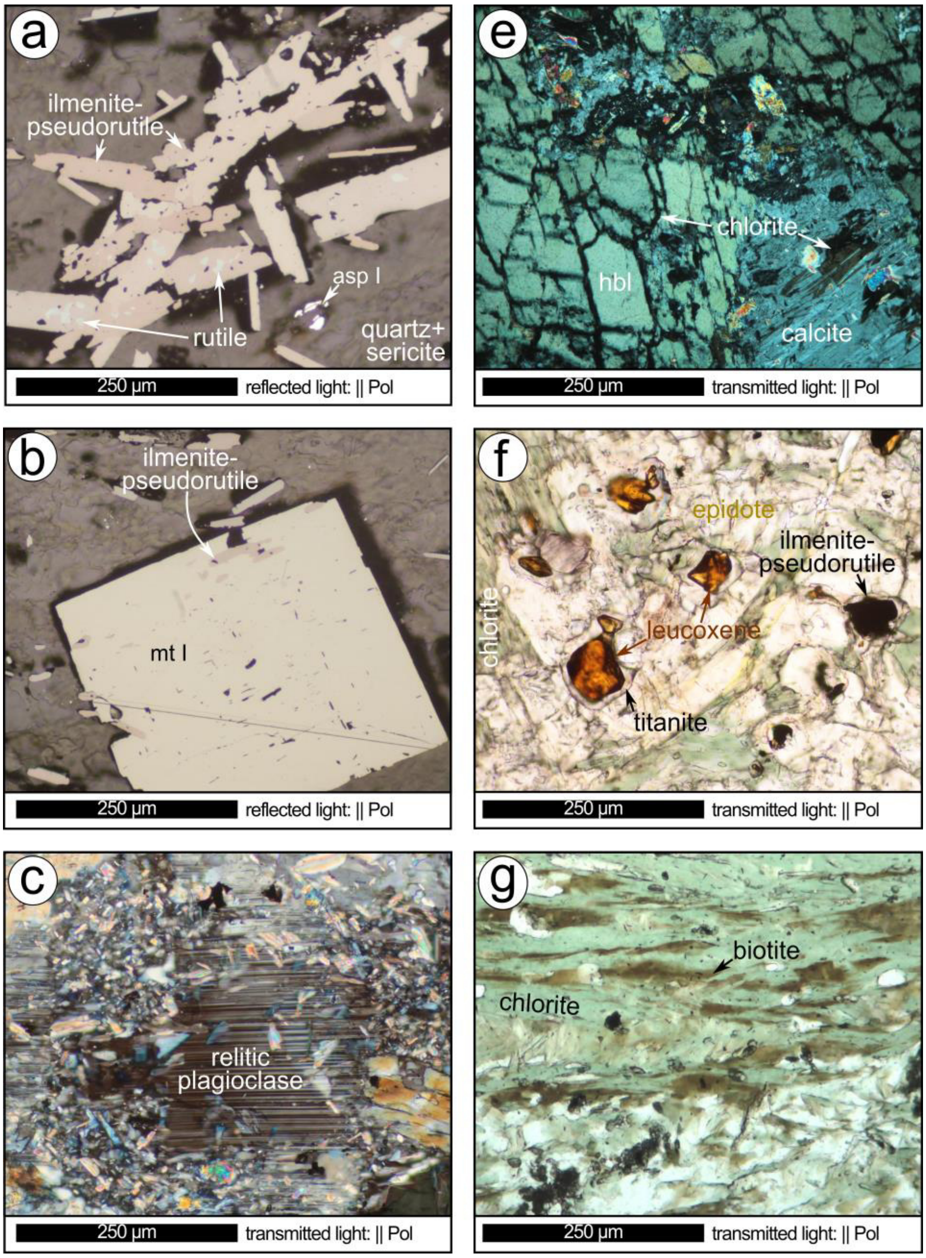

Figure 16: Host rock alteration along the five-element veins in the Penninic Alps. For further information, see text.

7. Results

7.1 Mineral chemistry (EMPA)

7.1.1 Carbonates

Representative chemical compositions of the carbonates are listed in Table 1. Table ES1 (electronic supplement) includes data of the single measurements of the carbonates. Figure 17a shows carbonate compositions at KB in the system (Fe+Mn)-Mg-Ca. Siderite compositions range from $Mg_{0.88}(Fe,Mn)_{1.12}CO_3$ to $Mg_{0.2}(Fe,Mn)_{1.8}CO_3$ (Ca < 1 mol%). Fe-dolomites and ankerites show a continuous solid solution between $Mg_{0.85}(Fe,Mn)_{0.2}Ca_{0.95}(CO_3)_2$ and $Mg_{0.25}(Fe,Mn)_{0.75}Ca_{1.0}(CO_3)_2$. The Fe-dolomites incorporate 1.5-3.2 mol% Fe, 6.5-8.5 mol% Mg, and 0.2-0.6 mol% Mn, the ankerites, however, range between 1.7-6.4 mol%, 2.1-6.5 mol% and 0.4-4.5 mol%, respectively. Mg contents are similar for siderites and the dolomites-ankerites. Calcites incorporate up to 1.5 mol% Fe, 2 mol% Mn and 0.85 mol% Mg.

Figure 17b shows calcites of KB, projected from Mg to the Fe-Mn-Ca system. Calcite I and calcite II precipitated during the sulfide stage III have an almost pure calcite composition, whereas late-stage calcite III reach Fe/(Ca+Fe) and Mn/(Ca+Mn) ratios of up to 0.08 and 0.1, respectively. Calcite III at GP shows similar compositions, but higher Fe contents than calcite III at KB.

Figure 17c shows carbonates from different mineralization stages of KB projected from Ca to the Fe-Mn-Mg system. Siderites range from 0.5 to 0.83 Fe# (Fe/[Fe+Mg+Mn]) and reach a maximum Mn# (Mn/[Fe+Mg+Mn]) of 0.36. The corresponding ankerites reveal Fe# between 0.14 and 0.65 and reach a maximum Mn# of 0.42. In both cases, the Mn# of siderites and ankerites increase continuously from 0.04 to 0.36 and 0.03 to 0.42, respectively. Fe#, however, first increase during stage II and then decrease during the following stage IV and V. Ankerite Ia directly replaced Fe-dolomite, ankerite Ib and siderite IIa replaced siderite I and siderite IIb represent open space fillings (cf. Figure 17c). Dolomites do not show high variability (Fe# of 0.14 to 0.35 and maximum Mn# of 0.07). Siderites, ankerites and dolomites at PI and GP show different absolute values of Fe, Mg and Mn, but comparable evolution trends as those at KB (cf. Figure A2).

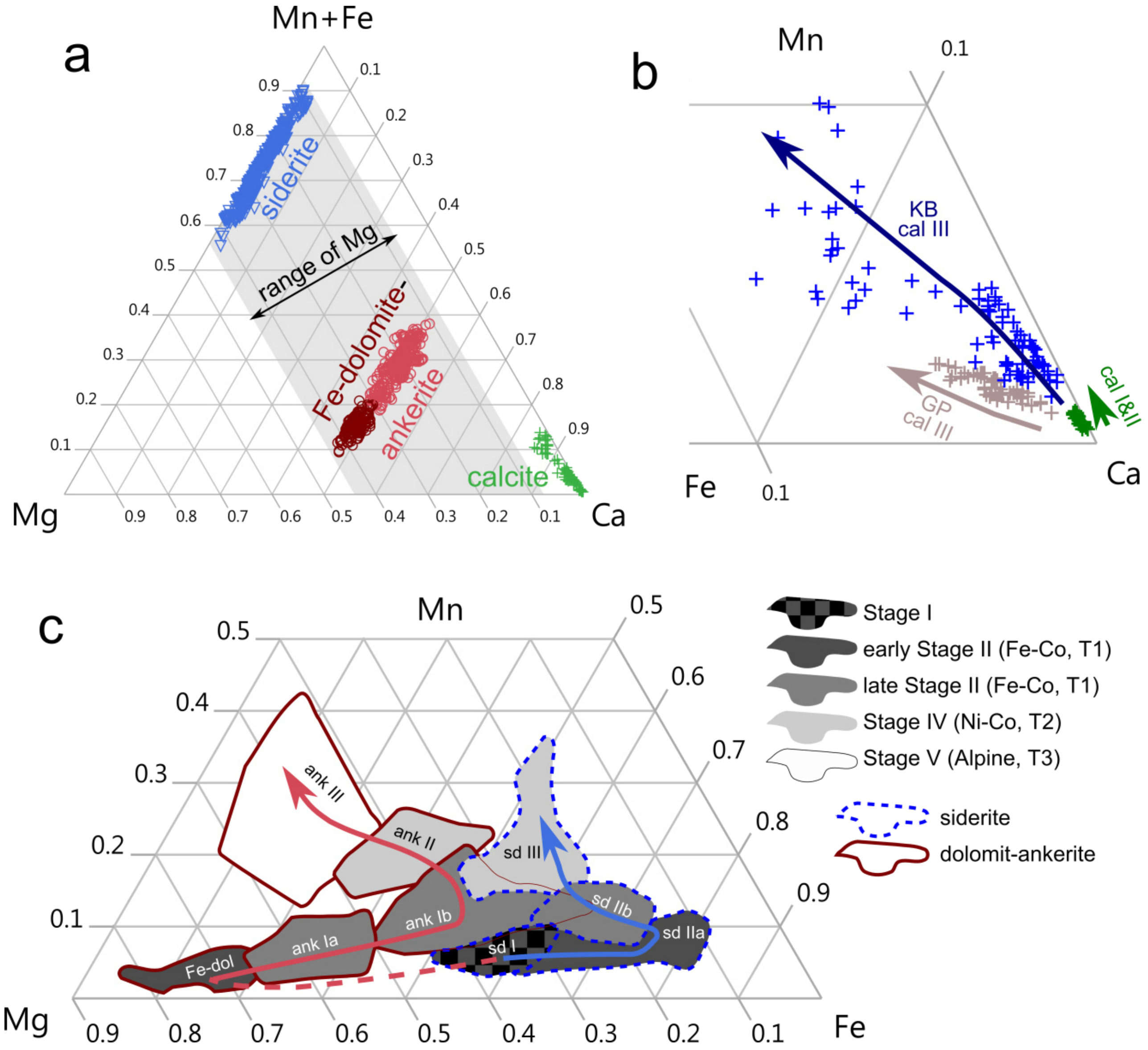

Figure 17: (a) Chemical composition of the carbonates from Grand Praz, Kaltenberg and Pipji. (b) Calcite chemistries of calcite I, II and III at Kaltenberg and calcite III at Grand Praz as the projection from Mg. (c) The chemical variance of the full range of siderite and ankerite generations, observed at Kaltenberg as the projection from Ca. Note, for siderites and ankerites Ca correspond to ~0 or ~1 formula units, respectively. Arrows indicate the temporal evolution of the chemistries. Carbonates of Grand Praz and Pipji only show a subset of this full carbonate evolution (cf. Figure 25). Corresponding stages at Grand Praz and Pipji given in Figure A2 (Appendix). For further explanation, see text.

Table 1: Representative chemical compositions of the presented carbonates in wt.%, XFe, XMg, XMn and XCa analyzed by electron microprobe.

location	GPg																		GPr		
generation	ank Ia*			ank Ib*			cal III			Fe-dol I*			Fe-dol II*			Fe-dol III*			ank Ia*		
N		10			5			45			55			17			20			6	
	min	mean	max	min	mean	max	min	mean	max	min	mean	max	min	mean	max	min	mean	max	min	mean	max
FeO	12.95	13.47	14.45	14.44	15.85	17.08	0.25	1.33	2.20	3.84	7.50	9.54	9.42	10.91	12.35	4.37	7.56	9.96	11.07	11.40	11.60
MgO	10.59	11.10	11.39	7.42	8.77	10.04	0.31	1.00	1.79	13.96	15.61	18.48	11.53	12.73	13.64	13.13	14.71	16.27	11.99	12.49	12.91
MnO	2.12	2.29	2.41	1.87	3.33	4.52	0.66	1.12	1.64	0.31	0.97	1.44	1.48	1.84	2.55	1.36	1.93	2.60	0.65	0.97	1.25
CaO	27.82	28.02	28.20	27.49	27.85	28.51	49.61	52.30	55.37	28.13	28.44	28.68	28.08	28.44	29.48	28.37	28.69	28.94	28.29	28.43	28.73
SrO	0.00	0.01	0.03	0.00	0.01	0.04	0.06	0.14	0.65	0.00	0.01	0.05	0.00	0.01	0.04	0.00	0.04	0.08	0.00	0.01	0.03
ZnO	0.00	0.01	0.03	0.00	0.02	0.04	0.00	0.00	0.04	0.00	0.01	0.07	0.00	0.01	0.05	0.00	0.01	0.07	0.00	0.01	0.03
BaO	0.00	0.00	0.02	0.00	0.01	0.02	0.00	0.01	0.05	0.00	0.01	0.04	0.00	0.01	0.04	0.00	0.00	0.02	0.00	0.01	0.04
SiO_2 [1]	0.00	0.00	0.01	0.00	0.00	0.02	0.00	0.00	0.03	0.00	0.00	0.04	0.00	0.00	0.02	0.00	0.00	0.04	0.00	0.00	0.00
As_2O_5 [2]	0.04	0.07	0.08	0.00	0.03	0.07	0.00	0.06	1.79	0.00	0.08	0.15	0.03	0.07	0.12	0.05	0.08	0.15	0.05	0.07	0.09
$CO_{2(calc)}$	43.56	43.78	43.96	42.80	43.22	43.54	41.67	43.71	44.79	44.02	44.57	45.12	43.60	44.05	44.30	44.03	44.43	44.79	43.32	43.54	44.02
Total	98.21	98.75	99.24	98.59	99.09	99.44	96.68	99.68	102.03	96.12	97.20	97.91	97.43	98.07	98.78	96.74	97.47	98.35	96.33	96.93	98.08
XFe	0.18	0.19	0.20	0.20	0.22	0.24	0.00	0.02	0.03	0.05	0.10	0.13	0.13	0.15	0.17	0.06	0.10	0.14	0.16	0.16	0.16
XMg	0.26	0.28	0.28	0.19	0.22	0.25	0.01	0.02	0.04	0.34	0.38	0.45	0.29	0.32	0.34	0.33	0.36	0.40	0.30	0.31	0.32
XMn	0.03	0.03	0.03	0.03	0.05	0.07	0.01	0.02	0.02	0.00	0.01	0.02	0.02	0.03	0.04	0.02	0.03	0.04	0.01	0.01	0.02
XCa	0.50	0.50	0.51	0.50	0.51	0.52	0.90	0.94	0.97	0.49	0.50	0.51	0.50	0.51	0.52	0.50	0.51	0.52	0.51	0.51	0.52

location	GPr												KB								
generation	ank Ib*			ank II*			cal III			Fe-dol*			ank Ia*			ank Ib*			ank II*		
N		27		31			15			21			55			123			236		
	min	mean	max	min	mean	max	min	mean	max	min	mean	max	min	mean	max	min	mean	max	min	mean	max
FeO	12.37	13.87	16.43	8.68	10.98	12.97	1.00	1.77	2.49	7.76	8.72	10.15	10.38	12.82	15.11	14.55	18.02	21.89	11.82	13.91	16.49
MgO	7.58	9.97	11.39	10.41	11.68	13.47	0.30	0.68	1.29	13.22	14.01	15.80	9.64	11.61	13.87	4.12	7.32	10.29	5.45	7.89	10.27
MnO	1.75	2.26	3.37	1.99	2.68	3.74	1.06	1.37	1.62	0.46	0.69	0.90	1.05	2.44	4.07	2.47	4.05	7.04	5.52	6.77	8.93
CaO	27.66	28.25	29.31	27.82	28.38	29.24	50.98	51.94	52.99	27.94	29.34	28.54	25.95	27.96	29.30	25.24	27.27	28.72	26.25	27.50	29.73
SrO	0.00	0.02	0.06	0.00	0.02	0.05	0.00	0.08	0.12	0.00	0.01	0.02	0.00	0.17	2.14	0.00	0.05	0.15	0.00	0.04	0.18
ZnO	0.00	0.01	0.05	0.00	0.01	0.04	0.00	0.01	0.05	0.00	0.01	0.04	0.00	0.01	0.06	0.00	0.01	0.07	0.00	0.01	0.05
BaO	0.00	0.01	0.03	0.00	0.00	0.02	0.00	0.00	0.02	0.00	0.01	0.03	0.00	0.00	0.03	0.00	0.00	0.05	0.00	0.00	0.05
SiO_2 [1]	0.00	0.00	0.00	0.00	0.00	0.01	0.00	0.00	0.01	0.00	0.01	0.09	0.00	0.00	0.05	0.00	0.00	0.21	0.00	0.01	0.42
As_2O_5 [2]	0.00	0.05	0.11	0.00	0.06	0.11	0.00	0.00	0.04	0.04	0.08	0.28	0.00	0.05	0.17	0.00	0.03	0.13	0.00	0.04	0.33
$CO_{2(calc)}$	42.14	42.97	43.51	42.86	43.43	44.06	43.07	43.47	43.94	43.45	44.03	44.54	42.86	44.06	45.99	42.05	42.97	44.20	41.79	42.95	44.05
Total	96.21	97.40	98.61	96.15	97.25	98.78	98.33	99.33	100.41	96.02	96.80	97.78	97.28	99.13	102.45	96.84	99.74	102.48	96.86	99.12	100.95
XFe	0.18	0.20	0.24	0.12	0.15	0.18	0.01	0.02	0.03	0.11	0.12	0.14	0.14	0.18	0.21	0.21	0.26	0.32	0.17	0.20	0.24
XMg	0.20	0.25	0.29	0.26	0.29	0.34	0.01	0.02	0.03	0.33	0.35	0.39	0.24	0.29	0.33	0.11	0.19	0.25	0.14	0.20	0.26
XMn	0.03	0.03	0.05	0.03	0.04	0.05	0.02	0.02	0.02	0.01	0.01	0.01	0.01	0.03	0.06	0.04	0.06	0.10	0.08	0.10	0.13
XCa	0.51	0.52	0.54	0.50	0.51	0.53	0.92	0.94	0.96	0.49	0.52	0.52	0.47	0.50	0.53	0.46	0.50	0.52	0.47	0.50	0.54

mineral abbreviations as in Table 1; N: number of measurements; [1, 2]measured as control to contamination; *low totals base on Ni and Co concentration of up to 4 wt.% (checked due to EDX measurements)

succession Table 1:

location	KB																				
generation	ank III*			cal I			cal II			cal III			Fe-dol*			sd I			sd IIb		
N	30			20			28			77			163			130			90		
	min	mean	max	min	mean	max	min	mean	max	min	mean	max	min	mean	max	min	mean	max	min	mean	max
FeO	5.84	9.86	12.68	0.04	0.10	0.15	0.03	0.12	0.19	0.12	1.46	5.14	5.62	9.60	12.02	35.13	40.72	42.82	40.89	44.90	48.32
MgO	8.11	10.36	12.51	0.02	0.07	0.11	0.00	0.08	0.15	0.08	0.49	1.68	13.00	15.27	17.95	10.43	13.05	16.71	5.23	7.71	10.87
MnO	4.95	7.63	15.43	0.28	0.39	0.65	0.39	0.51	0.63	0.94	2.73	7.16	0.58	1.49	2.39	2.62	4.54	6.29	5.14	7.08	10.04
CaO	24.86	27.43	29.16	53.51	54.86	55.32	53.95	54.70	55.44	46.14	51.24	54.10	27.65	28.23	28.91	0.09	1.18	2.64	0.24	0.82	1.94
SrO	0.03	0.12	0.29	0.00	0.12	0.29	0.00	0.13	0.31	0.00	0.15	0.45	0.00	0.01	0.06	0.00	0.01	0.07	0.00	0.01	0.04
ZnO	0.00	0.01	0.06	0.00	0.01	0.05	0.00	0.01	0.07	0.00	0.01	0.06	0.00	0.01	0.06	0.00	0.01	0.10	0.00	0.01	0.08
BaO	0.00	0.00	0.02	0.00	0.01	0.04	0.00	0.00	0.04	0.00	0.01	0.04	0.00	0.00	0.05	0.00	0.00	0.03	0.00	0.01	0.04
SiO_2 [1]	0.00	0.00	0.13	0.00	0.00	0.00	0.00	0.00	0.00	0.00	0.00	0.01	0.00	0.00	0.15	0.00	0.00	0.03	0.00	0.01	0.92
As_2O_5 [2]	0.00	0.04	0.12	0.00	0.00	0.00	0.00	0.00	0.00	0.00	0.00	0.04	0.00	0.07	0.28	0.00	0.08	0.33	0.00	0.04	1.04
$CO_{2(calc)}$	42.74	43.67	44.45	42.46	43.49	43.90	42.70	43.46	44.11	42.37	43.42	45.59	43.67	45.64	47.23	40.71	42.95	45.94	39.06	40.97	42.87
Total	96.99	99.12	100.44	96.72	99.06	99.99	97.22	99.01	100.46	96.84	99.52	105.16	96.23	100.33	103.33	96.04	102.55	108.70	97.29	101.58	104.32
XFe	0.08	0.14	0.18	0.00	0.00	0.00	0.00	0.00	0.00	0.00	0.02	0.07	0.08	0.13	0.16	0.50	0.58	0.62	0.60	0.67	0.73
XMg	0.21	0.26	0.31	0.00	0.00	0.00	0.00	0.00	0.00	0.00	0.01	0.04	0.32	0.37	0.42	0.27	0.33	0.42	0.14	0.21	0.28
XMn	0.07	0.11	0.22	0.00	0.01	0.01	0.01	0.01	0.01	0.01	0.04	0.10	0.01	0.02	0.03	0.04	0.07	0.09	0.08	0.11	0.15
XCa	0.46	0.49	0.53	0.99	0.99	0.99	0.98	0.99	0.99	0.84	0.93	0.98	0.47	0.49	0.52	0.00	0.02	0.05	0.00	0.02	0.04

location	KB						PI														
generation	sd IIa			sd III			ank I*			ank III			Fe-dol*			sd I			sd II		
N	186			43			160			19			153			17			219		
FeO	min	mean	max	min	mean	max	min	mean	max	min	mean	max	min	mean	max	min	mean	max	min	mean	max
MgO	41.41	45.59	52.21	31.94	37.72	42.00	14.51	19.09	23.07	17.08	18.79	21.29	6.50	9.81	14.23	35.36	41.42	44.20	44.19	48.07	53.37
MnO	3.32	8.68	13.41	5.50	8.43	13.44	3.25	6.62	9.90	4.13	5.80	6.64	9.95	13.52	16.88	9.70	11.74	16.55	2.64	5.62	9.24
CaO	2.81	5.45	8.78	10.04	13.84	22.74	2.37	3.95	5.28	5.13	6.07	6.84	0.46	2.22	3.80	3.80	4.70	5.54	3.95	6.25	8.50
SrO	0.18	0.73	1.72	0.24	0.82	1.41	26.00	27.07	27.97	26.21	26.76	27.23	27.23	28.38	29.95	0.06	0.60	1.55	0.06	0.89	2.02
ZnO	0.00	0.01	0.05	0.00	0.01	0.04	0.00	0.07	0.20	0.03	0.08	0.14	0.00	0.02	0.16	0.00	0.01	0.03	0.00	0.01	0.05
BaO	0.00	0.02	0.08	0.00	0.01	0.06	0.00	0.01	0.06	0.00	0.01	0.05	0.00	0.01	0.07	0.00	0.01	0.05	0.00	0.01	0.07
SiO_2 [1]	0.00	0.00	0.04	0.00	0.00	0.03	0.00	0.00	0.05	0.00	0.01	0.04	0.00	0.00	0.04	0.00	0.00	0.02	0.00	0.00	0.04
As_2O_5 [2]	0.00	0.02	2.26	0.00	0.01	0.25	0.00	0.00	0.41	0.00	0.00	0.00	0.00	0.02	1.01	0.00	0.00	0.04	0.00	0.01	1.74
$CO_{2(calc)}$	0.00	0.08	3.29	0.00	0.05	0.14	0.00	0.04	0.25	0.00	0.12	1.31	0.00	0.09	1.21	0.05	0.10	0.25	0.00	0.05	0.19
Total	38.95	41.38	43.72	40.29	41.54	43.54	41.01	42.66	44.18	41.90	42.65	43.36	42.62	44.44	45.85	40.80	41.59	42.72	38.75	40.17	41.62
XFe	0.60	0.68	0.81	0.47	0.56	0.63	0.21	0.27	0.34	0.25	0.27	0.31	0.09	0.14	0.20	0.51	0.61	0.66	0.67	0.73	0.82
XMg	0.09	0.23	0.34	0.15	0.22	0.34	0.08	0.17	0.25	0.11	0.15	0.17	0.26	0.33	0.41	0.26	0.31	0.43	0.07	0.15	0.24
XMn	0.04	0.08	0.13	0.14	0.21	0.35	0.03	0.06	0.08	0.08	0.09	0.10	0.01	0.03	0.05	0.06	0.07	0.08	0.06	0.10	0.13
XCa	0.00	0.01	0.03	0.00	0.02	0.03	0.48	0.50	0.52	0.49	0.49	0.51	0.48	0.50	0.53	0.00	0.01	0.03	0.00	0.02	0.04

mineral abbreviations as in Table 1; N: number of measurements; [1, 2]measured as control to contamination; *low totals base on Ni and Co concentration of up to 4 wt.% (checked due to EDX measurements)

7.1.2 Bi-Co-Ni-Fe-As-S-(U) mineralized ores (stages II, IV and Vb)

Representative chemical compositions of the arsenides are listed in Table 2. Table ES2 (electronic supplement) includes data of the single measurements of the arsenides and sulfarsenides. Figures 18a-f show the chemical compositions of all mono-, di-, tri- and sulfarsenides according to the occupancy of Fe, Co and Ni on the cation site in molar ratios. Detailed correlations of As and S are given in Figure 19. The amount of arsenic incorporated by the particular generations of sulfarsenides are also noted in Figure 18 as arsenic per formula unit (As.pfu).

Fe-Co stage II (Figure 18a): Skutterudites at KB show a fixed Fe:Ni ratio of 1:1 and a large range of Co# from 0.9-0.35 (Co#: Co/[Fe+Co+Ni]). Skutterudite I shows a higher Co concentration than skutterudite II. At PI, skutterudite ranges from 0.78-0.25 Co# with slightly various Fe/Ni ratios between 1.5 and 0.66. A lower range of cobalt developed for the skutterudites from GPg with 0.73-0.55 Co# and similar Fe/Ni ratios as in PI. A clear differentiation between skutterudite I and II similar to KB, however, was not possible due to blurry textures and intensive remobilization of the ores.

Along their growth zonations, löllingites and arsenopyrites evolve from Co-rich over Fe-dominated to more Ni-rich compositions along their growth zonations. The composition of löllingite I (early Fe-Co stage) changes from an intermediate Fe# of ≳0.5 and Ni# of 0.07 (first ores) towards higher Fe and Ni compositions reaching a mean Fe# of 0.7 and Ni# of 0.18 (last ores) (Fe#: Fe/[Fe+Co+Ni], Ni#: Ni/[Fe+Co+Ni]). Löllingite II (late Fe-Co stage) shows higher Ni contents than löllingite I, whereas cobalt stays at ~0.1 Co# with rising Ni# of up to 0.25 at KB, 0.27-0.42 at PI and ~0.35 at GPg. Arsenopyrites from the localities KB and PI show a smaller, but comparable variability from Co- over Fe- to Ni-rich compositions. No relevant Ni concentrations are observed for arsenopyrite I, but increasing Fe# from 0.85 to 1 at KB and 0.7 to 1 at PI (early Fe-Co stage). Arsenopyrite II, however, shows increasing Ni and Co contents reaching ~0.05 Ni# and ~0.05 Co# for both localities (late Fe-Co stage). The arsenopyrites' arsenic content ranges from 1.1-0.9 atoms per formula unit without any correlation to their temporal occurrence or Fe-Co-Ni signatures.

Ni-Co stage IV (Figure 18b, c and f): Niccolite and rammelsbergite from KB ranges from 0.0 to 0.15 Co# and 0.06 to 0.21 Co#, respectively (iron always <0.01 Fe#), those of GPr, however, are nearly pure stoichiometric niccolite and rammelsbergite. Skutterudite III at KB is rich in cobalt (0.92-0.78 Co#) and has a Ni:Fe ratio ≥ 1. Gersdorffite I shows a high arsenic content of 1.8-1.3 atoms per formula unit (cf. Figure 18b, f and Figure 19c, d). High arsenic correlates with Ni-rich compositions. Those of KB show two different branches, ranging from the signature of niccolite and rammelsbergite to either more Co-rich (up to ~0.3 Co#) or more Fe-rich compositions (up to ~0.12 Fe# at 0.1Co#). At GPr, gersdorffite I similarly ranges from the pure Ni endmember to iron- and cobalt-bearing zones, reaching up to 0.08 Fe# and 0.1 Co#.

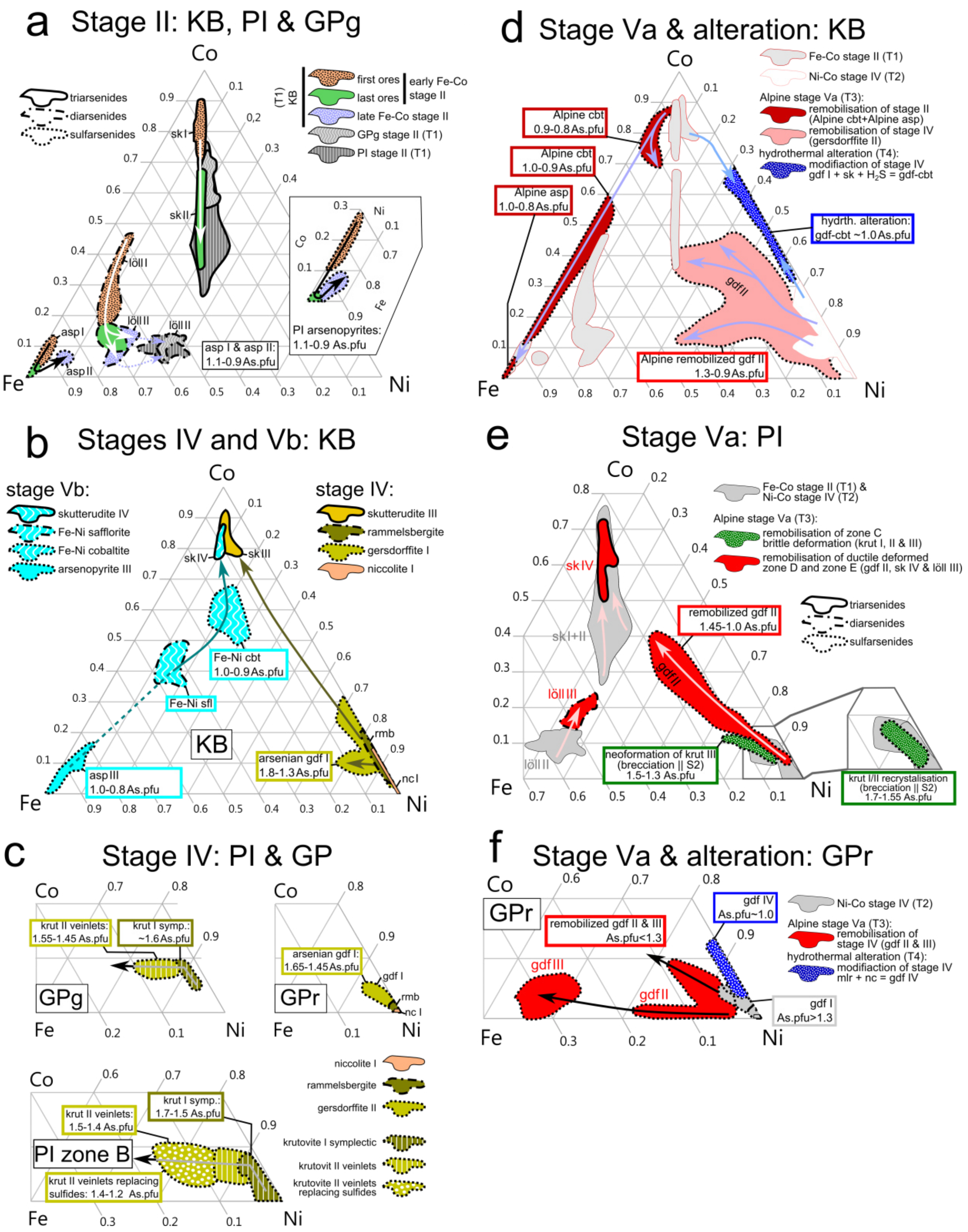

Figure 18: Chemical composition and evolution of the arsenides and sulfarsenides. (a) Ores of the Fe-Co stage II at KB, PI and GPg. (b) Ores of the Ni-Co stage IV and Co stage Vb at KB. (c) Ores of the Ni-Co stage IV at GP and PI. Note that krutovite I and II show similar trends between GPg (greyish ores) and PI (zone A), whereas niccolite, rammelsbergite and gersdorffite I at GPr (reddish ores) are similar to those at KB (cf. Figure 18b) (d) The Alpine redistribution at KB during stage Va in red and during hydrothermal alteration in blue. Note that in-situ remobilization chemistries of stage Va are different, depending on which ore stage was remobilized. (e) Evolution of the ores at PI during stage Va. Ni-Co pre-enriched ores of zone A (krutovites I and II) either recrystallized along brecciation || S2 including neoformation of krutovite III (zone B; krutovites I, II and III, green colored) or concerned by intensive neoformation of gersdorffite II, löllingite III and skutterudite IV (red colored). (f) redistribution at GPr (reddish ores) during stage Va in red and during hydrothermal alteration in blue. (a)-(f) all temporal stages and mineral generation correspond to those illustrated in Figure 8 and 25. Arrows indicate the temporal evolution of the chemistries.

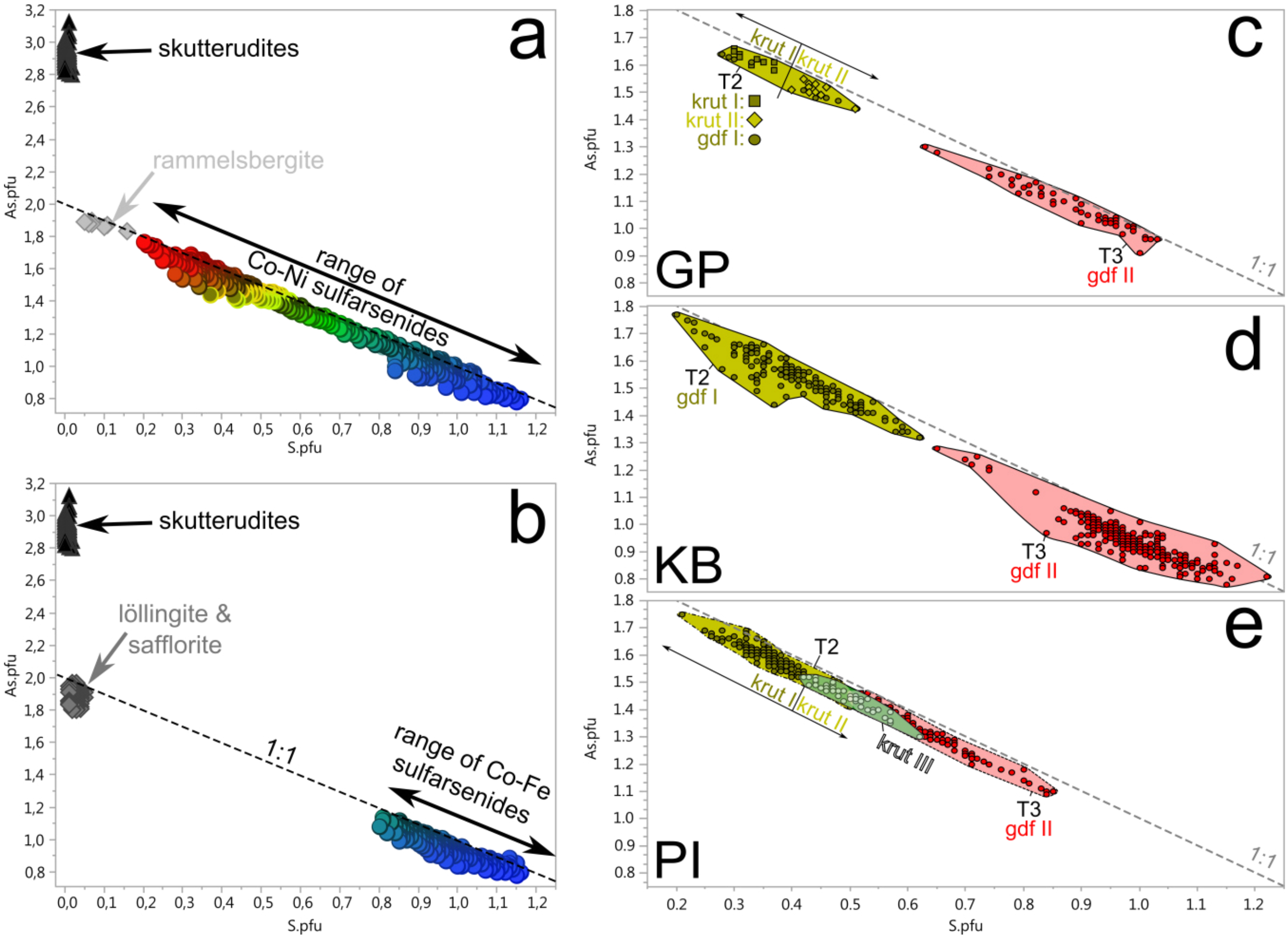

Figure 19: (a) As per formula unit vs. S per formula unit of the skutterudites. diarsenides and sulfarsenides at KB, Pi, and GP in (a) and (b). Formula was standardized as cations equal to 1. (a) highlighted the full range of the observed Co-Ni sulfarsenides. (b) those of the Co-Fe sulfarsenides. Despite nearly S free diarsenides. relic rammelsbergite at Kaltenberg shows increased S amounts. (c), (d) and (e) different sulfarsenide generations of primary ore formation during T2 (krut I/II; gdf I in red) and its secondary remobilization during T3 (gdf II in green) at GP, KB and PI, respectively.

Table 2: Representative chemical compositions of the presented mono-. di-. tri- and sulfarsenides as wt.% and atoms per formula unit analyzed by electron microprobe.

location	KB			PI			KB			KB			PI			KB			KB		
stage	T1: Fe-Co stage			T1: Fe-Co stage			T1: Fe-Co stage			T1: Fe-Co stage			T1: Fe-Co stage			T1: Fe-Co stage			T1: Fe-Co stage		
mineral	asp I			asp I			löll I*			sk I			sk I & sk II			sk II*			asp II		
N	50			44			30			33			242			5			12		
	min	mean	max	min	mean	max	min	mean	max	min	mean	max	min	mean	max	min	mean	max	min	mean	max
Fe	29.6	32.6	35.4	23.9	30.1	35.1	13.5	18.7	20.8	1.3	2.1	3.0	2.4	4.7	7.6	3.5	5.3	6.7	28.4	29.4	30.3
Co	0.0	2.1	4.6	0.0	3.8	9.8	2.9	6.6	13.5	15.6	17.8	19.0	5.7	11.9	17.1	7.7	10.7	14.3	1.8	2.3	2.7
Ni	bdl	0.2	0.9	0.0	0.6	1.7	2.0	3.7	6.8	1.1	1.7	2.8	2.2	5.1	8.3	3.5	5.3	6.8	2.2	2.8	3.4
Bi	bdl	0.0	0.3	bdl	0.1	0.3	bdl	0.2	0.5	bdl	0.1	0.3	bdl	0.1	8.8	bdl	0.1	0.4	bdl	0.1	0.5
Ag	bdl	0.0	0.1	bdl	0.0	0.0	bdl	0.0	0.1	bdl	0.0	0.1	bdl	0.0	0.1	bdl	bdl	bdl	bdl	0.0	0.1
Pb	bdl	0.0	0.1	bdl	0.0	0.1	bdl	bdl	bdl	bdl	0.0	0.2	bdl	0.0	0.3	bdl	0.0	0.1	bdl	0.0	0.1
Cu	bdl	0.0	0.1	bdl	0.0	0.5	bdl	bdl	bdl	bdl	0.0	0.1	bdl	0.0	1.6	bdl	bdl	bdl	bdl	bdl	bdl
Zn	bdl	0.0	0.1	bdl	0.0	0.0	bdl	0.0	0.1	bdl	0.0	0.1	bdl	0.0	0.0	bdl	0.0	0.1	bdl	0.0	0.1
As	39.6	45.8	48.4	44.6	47.9	50.0	68.2	69.8	70.4	77.5	79.8	81.4	72.0	81.6	83.6	77.7	77.9	78.4	47.4	49.7	51.9
S	16.3	18.5	22.1	16.1	17.7	20.2	0.2	0.5	1.5	bdl	0.1	0.2	bdl	0.0	0.4	0.1	0.1	0.2	15.7	16.5	17.2
Sb	bdl	0.1	1.2	bdl	0.1	0.3	bdl	0.1	0.5	bdl	bdl	bdl	bdl	0.0	0.0	bdl	bdl	bdl	bdl	0.0	0.0
Se	0.1	0.2	0.4	0.1	0.2	0.3	0.3	0.4	0.5	0.1	0.3	0.6	0.1	0.3	0.4	0.4	0.5	0.5	0.2	0.3	0.4
Hg	bdl	0.0	0.1	bdl	0.0	0.1	bdl	bdl	bdl	bdl	0.0	0.1	bdl	0.0	0.1	bdl	bdl	bdl	bdl	bdl	bdl
total	98.8	99.6	100.3	99.9	100.5	101.3	100*	100*	100*	100.0	102.0	104.1	101.4	103.8	106.8	100*	100*	100*	100.0	101.3	102.9
∑ formula unit	3			3			3			4			4			4			3		
Fe.p.f.u.	0.88	0.96	1.04	0.72	0.89	1.02	0.50	0.69	0.76	0.06	0.10	0.15	0.12	0.23	0.37	0.18	0.27	0.34	0.84	0.88	0.91
Co.p.f.u.	0.00	0.06	0.13	0.00	0.11	0.28	0.10	0.23	0.47	0.75	0.84	0.92	0.26	0.55	0.79	0.37	0.51	0.69	0.05	0.07	0.08
Ni.p.f.u.	0.00	0.01	0.02	0.00	0.02	0.05	0.07	0.13	0.24	0.05	0.08	0.14	0.10	0.24	0.38	0.17	0.25	0.33	0.06	0.08	0.10
As.p.f.u.	0.85	1.01	1.09	0.96	1.06	1.13	1.85	1.91	1.93	2.92	2.95	2.97	2.83	2.97	2.99	2.93	2.94	2.95	1.06	1.11	1.15
S.p.f.u.	0.86	0.95	1.11	0.85	0.92	1.02	0.01	0.03	0.09	0.00	0.01	0.02	0.00	0.00	0.03	0.01	0.01	0.01	0.82	0.86	0.90

location	PI			GPg			KB			PI			GPr			KB			KB		
stage	T1: Fe-Co stage			T1: Fe-Co stage			T1: Fe-Co stage			T1: Fe-Co stage			T2: Ni-Co stage			T2: Ni-Co stage			T2: Ni-Co stage		
mineral	asp II			löll II			löll II			löll II			gdf I			gdf Ia			gdf Ib		
N	15			10			23			81			8			121			47		
	min	mean	max	min	mean	max	min	mean	max	min	mean	max	min	mean	max	min	mean	max	min	mean	max
Fe	28.6	30.6	33.1	14.2	15.3	16.5	17.5	19.3	21.8	14.3	15.8	17.8	0.2	0.5	0.9	bdl	0.5	3.8	0.1	0.5	1.6
Co	0.2	2.0	4.2	1.7	3.3	4.0	1.0	3.1	4.5	1.4	2.8	3.8	0.6	1.0	1.4	0.9	4.1	6.6	4.1	7.2	9.8
Ni	0.9	1.8	3.0	9.7	10.3	11.5	4.6	6.3	8.3	8.2	10.3	12.5	29.5	29.7	29.9	24.2	26.5	30.0	22.3	24.4	27.3
Bi	bdl	0.0	0.2	bdl	0.0	0.1	bdl	0.2	0.6	bdl	0.0	0.4	bdl	bdl	bdl	bdl	0.0	0.6	bdl	0.0	0.1
Ag	bdl	0.0	0.0	bdl	0.0	0.0	bdl	0.0	0.1	bdl	0.0	0.1	bdl	0.0	0.0	bdl	0.0	0.1	bdl	0.0	0.0
Pb	bdl	bdl	bdl	bdl	0.0	0.1	bdl	0.0	0.1	bdl	0.0	0.2	bdl	0.0	0.1	bdl	0.0	0.2	bdl	0.0	0.1
Cu	bdl	0.2	1.4	bdl	0.0	0.1	bdl	0.0	0.1	bdl	0.1	0.7	bdl	0.0	0.1	bdl	0.0	0.1	bdl	0.0	0.1
Zn	bdl	0.0	0.0	bdl	0.0	0.0	bdl	0.0	0.1	bdl	0.0	0.0	bdl	bdl	bdl	bdl	0.0	0.0	bdl	0.0	0.0
As	46.8	48.3	50.0	71.0	71.4	71.8	69.6	70.9	73.1	70.6	72.2	74.1	59.4	62.0	64.4	59.4	62.6	67.1	55.2	58.7	60.5
S	16.4	17.5	18.5	0.4	0.6	0.8	0.1	0.4	0.8	0.3	0.5	0.9	4.7	6.4	8.2	3.2	6.3	8.4	7.8	9.0	11.0
Sb	bdl	0.1	0.3	bdl	0.0	0.0	bdl	0.0	0.2	bdl	0.1	0.2	0.1	0.1	0.2	bdl	0.0	0.1	bdl	0.0	0.0
Se	0.1	0.2	0.3	0.1	0.3	0.4	0.3	0.4	0.5	0.1	0.3	0.4	0.2	0.3	0.4	0.2	0.3	0.4	0.2	0.3	0.4
Hg	bdl	0.0	0.1	bdl	0.0	0.1	bdl	bdl	bdl	bdl	0.0	0.1	bdl	0.0	0.1	bdl	0.0	0.1	bdl	0.0	0.1
total	100.1	100.8	102.2	100.6	101.3	101.6	100.0	100.8	102.9	100.8	102.0	104.0	99.4	100.1	101.8	98.9	100.4	102.8	99.1	100.1	101.5
∑ formula unit	3			3			3			3			3			3			3		
Fe.p.f.u.	0.85	0.91	0.97	0.52	0.55	0.60	0.64	0.70	0.80	0.52	0.57	0.64	0.01	0.02	0.03	0.00	0.02	0.13	0.00	0.02	0.05
Co.p.f.u.	0.00	0.06	0.12	0.06	0.11	0.14	0.04	0.11	0.16	0.05	0.09	0.13	0.02	0.03	0.05	0.03	0.13	0.21	0.13	0.23	0.31
Ni.p.f.u.	0.03	0.05	0.08	0.33	0.36	0.40	0.16	0.22	0.29	0.28	0.35	0.43	0.95	0.97	1.00	0.78	0.87	0.99	0.70	0.77	0.88
As.p.f.u.	1.02	1.07	1.11	1.92	1.93	1.95	1.90	1.93	1.96	1.92	1.94	1.96	1.49	1.59	1.68	1.48	1.60	1.78	1.35	1.46	1.52
S.p.f.u.	0.85	0.90	0.94	0.02	0.04	0.05	0.01	0.03	0.05	0.02	0.03	0.05	0.29	0.38	0.48	0.20	0.38	0.49	0.46	0.52	0.63

N: number of measurements; bdl: below detection limit; Fe./Co./Ni./As./S.p.f.u.: atoms per formula unit; *measurements using Cameca SX100, where As calculated as difference to 100 wt%

Succession Table 2:

location	GPg			PI			GPg			PI			PI			GPr			KB		
stage	T2: Ni-Co stage			T2: Ni-Co stage			T2: Ni-Co stage			T2: Ni-Co stage			T2: Ni-Co stage			T2: Ni-Co stage			T2: Ni-Co stage		
mineral	krut I			krut I			krut II			krut II			krut II (sulfides)			nc I			nc I		
N	11			60			10			33			19			21			5		
	min	mean	max	min	mean	max	min	mean	max	min	mean	max	min	mean	max	min	mean	max	min	mean	max
Fe	0.5	0.6	0.8	0.2	0.7	1.8	1.2	1.6	2.8	0.4	1.5	2.3	1.9	3.4	4.5	bdl	0.0	0.0	bdl	0.0	0.0
Co	1.5	2.1	2.6	0.1	1.3	2.4	2.2	2.5	2.7	1.2	1.9	2.7	1.2	2.4	3.5	bdl	0.0	0.1	0.0	0.0	0.0
Ni	26.7	27.6	28.6	23.9	28.9	30.6	26.2	27.0	27.8	27.0	28.1	28.9	24.7	26.9	28.8	43.8	44.4	45.3	44.2	45.0	45.3
Bi	bdl	0.0	0.1	bdl	0.4	21.1	bdl	0.0	0.2	bdl	0.0	0.2	bdl	0.0	0.3	bdl	0.0	0.1	bdl	0.0	0.1
Ag	bdl	0.0	0.0	bdl	0.0	0.1	bdl	0.0	0.1	bdl	0.0	0.1	bdl	0.0	0.0	bdl	0.0	0.0	bdl	0.0	0.0
Pb	bdl	0.0	0.1	bdl	0.0	0.2	bdl	bdl	bdl	bdl	0.0	0.1	bdl	0.0	0.1	bdl	0.0	0.1	bdl	bdl	bdl
Cu	bdl	0.0	0.1	bdl	0.0	0.2	bdl	0.0	0.1	bdl	0.0	0.1	bdl	0.0	0.1	bdl	0.0	0.1	bdl	0.0	0.1
Zn	bdl	0.0	0.0	bdl	0.0	0.0	bdl	0.0	0.0	bdl	0.0	0.0	bdl	0.0	0.0	bdl	0.0	0.0	bdl	0.0	0.0
As	61.8	62.9	63.9	52.2	62.9	65.4	58.4	60.2	61.1	58.2	60.5	61.5	53.6	57.0	60.0	50.6	52.2	52.8	52.7	53.0	53.1
S	4.9	5.5	6.2	4.1	5.9	7.6	6.9	7.5	8.8	6.8	7.6	8.8	8.5	10.4	13.2	0.2	0.4	0.8	0.2	0.4	0.6
Sb	0.0	0.1	0.1	0.1	0.2	0.3	0.0	0.1	0.1	0.1	0.2	0.3	0.1	0.2	0.3	1.2	1.5	2.0	0.9	1.0	1.0
Se	0.2	0.3	0.4	0.2	0.3	0.4	0.2	0.3	0.4	0.2	0.3	0.5	0.2	0.3	0.4	0.2	0.3	0.3	0.3	0.3	0.4
Hg	bdl	0.0	0.0	bdl	0.0	0.1	bdl	0.0	0.1	bdl	0.0	0.1	bdl	0.0	0.1	bdl	0.0	0.0	bdl	0.0	0.1
total	98.5	99.2	100.0	98.8	100.6	105.2	98.3	99.3	100.9	99.3	100.2	101.8	99.4	100.6	101.9	98.2	98.9	100.1	98.9	99.7	100.2
∑ formula unit	3			3			3			3			3			2			2		
Fe.p.f.u.	0.02	0.02	0.03	0.01	0.02	0.06	0.04	0.06	0.09	0.01	0.05	0.08	0.06	0.11	0.14	0.00	0.00	0.00	0.00	0.00	0.00
Co.p.f.u.	0.05	0.07	0.09	0.00	0.04	0.08	0.07	0.08	0.09	0.04	0.06	0.09	0.04	0.07	0.11	0.00	0.00	0.00	0.00	0.00	0.00
Ni.p.f.u.	0.89	0.92	0.95	0.87	0.95	1.01	0.84	0.88	0.90	0.87	0.90	0.94	0.77	0.83	0.89	1.01	1.02	1.03	1.02	1.02	1.03
As.p.f.u.	1.60	1.64	1.68	1.48	1.62	1.72	1.46	1.53	1.56	1.45	1.52	1.56	1.26	1.38	1.48	0.91	0.94	0.95	0.94	0.94	0.96
S.p.f.u.	0.30	0.34	0.38	0.25	0.35	0.44	0.41	0.45	0.52	0.40	0.45	0.51	0.49	0.59	0.72	0.01	0.02	0.03	0.01	0.02	0.02

location	GPr			KB			KB			KB			KB			KB			KB		
stage	T2: Ni-Co stage			T2: Ni-Co stage			T2: Ni-Co stage			T3: alpine stage			T3: alpine stage			T3: alpine stage			T3: alpine stage		
mineral	rmb			rmb			sk III			asp III (rem.)			cbt I (rem.)			cbt II (rem.)			Fe-Ni cbt		
N	3			9			47			179			29			24			24		
	min	mean	max	min	mean	max	min	mean	max	min	mean	max	min	mean	max	min	mean	max	min	mean	max
Fe	0.0	0.0	0.0	0.0	0.1	0.2	0.5	1.2	2.1	28.5	34.5	52.3	2.8	6.5	8.3	14.6	26.7	31.3	4.6	6.5	9.2
Co	0.1	0.2	0.3	1.7	3.9	6.1	17.6	19.3	20.3	0.0	0.8	5.9	25.2	29.5	32.2	4.4	8.1	22.5	17.9	20.8	24.2
Ni	28.6	28.8	28.9	23.0	25.2	27.4	1.0	1.6	3.8	bdl	0.2	2.1	0.2	1.3	3.5	0.0	0.5	1.8	6.1	8.8	11.2
Bi	bdl	bdl	bdl	bdl	0.0	0.1	bdl	0.0	0.2	bdl	0.0	0.2	bdl	0.0	0.2	bdl	0.0	0.1	bdl	0.0	0.2
Ag	bdl	bdl	bdl	bdl	bdl	bdl	bdl	0.0	0.1	bdl	0.0	0.1	bdl	0.0	0.0	bdl	0.0	0.1	bdl	0.0	0.1
Pb	bdl	0.1	0.2	bdl	0.0	0.2	bdl	0.0	0.4	bdl	0.0	6.1	bdl	bdl	bdl	bdl	bdl	bdl	bdl	bdl	bdl
Cu	bdl	0.0	0.1	bdl	0.0	0.1	bdl	0.0	0.1	bdl	0.0	0.1	bdl	0.0	0.5	bdl	0.0	0.1	bdl	0.0	0.1
Zn	bdl	0.0	0.0	bdl	0.0	0.0	bdl	0.0	0.0	bdl	0.0	0.0	bdl	0.0	0.0	bdl	0.0	0.0	bdl	0.0	0.0
As	70.9	71.0	71.2	68.3	70.0	71.0	79.7	81.4	82.1	35.9	44.2	59.3	37.8	40.4	42.6	42.2	45.5	48.7	44.4	45.2	47.2
S	0.3	0.3	0.3	0.8	1.3	2.6	bdl	0.1	1.4	17.5	20.3	30.3	20.3	22.3	23.7	17.0	19.0	21.8	17.5	18.6	19.3
Sb	0.1	0.2	0.2	bdl	0.0	0.1	bdl	bdl	bdl	bdl	0.0	0.6	bdl	bdl	bdl	bdl	0.0	0.1	bdl	0.0	0.0
Se	0.2	0.3	0.4	0.3	0.3	0.4	0.2	0.3	0.4	0.1	0.2	0.3	0.1	0.2	0.2	0.1	0.2	0.3	0.1	0.2	0.2
Hg	bdl	bdl	bdl	bdl	0.0	0.1	bdl	0.0	0.1	bdl	0.0	0.1	bdl	0.0	0.1	bdl	0.0	0.0	bdl	0.0	0.1
total	100.6	100.9	101.2	100.7	101.1	101.8	103.3	103.9	105.0	97.2	100.3	142.8	96.9	100.1	102.4	99.4	100.0	101.5	99.5	100.2	102.7
∑ formula unit	3			3			4			3			3			3			3		
Fe.p.f.u.	0.00	0.00	0.00	0.00	0.00	0.01	0.02	0.06	0.10	0.82	1.00	1.05	0.08	0.18	0.24	0.43	0.79	0.90	0.14	0.19	0.27
Co.p.f.u.	0.00	0.01	0.01	0.06	0.13	0.21	0.81	0.89	0.94	0.00	0.02	0.16	0.69	0.80	0.89	0.12	0.23	0.62	0.50	0.59	0.69
Ni.p.f.u.	1.01	1.01	1.01	0.80	0.87	0.95	0.05	0.07	0.17	0.00	0.01	0.06	0.01	0.03	0.10	0.00	0.01	0.05	0.17	0.25	0.32
As.p.f.u.	1.95	1.95	1.95	1.83	1.90	1.92	2.81	2.96	2.98	0.80	0.95	1.07	0.80	0.86	0.92	0.90	1.00	1.08	0.97	1.00	1.06
S.p.f.u.	0.02	0.02	0.02	0.05	0.08	0.16	0.00	0.01	0.12	0.91	1.02	1.21	1.02	1.11	1.18	0.89	0.97	1.08	0.92	0.96	0.99

N: number of measurements; bdl: below detection limit; Fe./Co./Ni./As./S.p.f.u.: atoms per formula unit; *measurements using Cameca SX100, where As calculated as difference to 100 wt%

Succession Table 2:

location	KB			GPr			KB			Pl			GPr			Pl			Pl		
stage	T3: alpine stage			T3: alpine stage			T3: alpine stage			T3: alpine stage			T3: alpine stage			T3: alpine stage			T3: alpine stage		
mineral	Fe-Ni sfl			gdf II			gdf II			gdf II			gdf IV			krut I/II remob.			löll III		
N	7			47			52			102			6			24			57		
	min	mean	max	min	mean	max	min	mean	max	min	mean	max	min	mean	max	min	mean	max	min	mean	max
Fe	10.2	12.6	14.2	0.7	2.1	5.6	0.2	5.5	14.4	2.1	3.6	7.3	8.2	9.9	11.5	0.4	1.4	2.4	11.6	13.4	15.5
Co	10.8	12.3	14.7	0.2	0.8	3.0	0.1	8.1	16.8	3.3	5.9	14.1	0.0	1.2	2.3	1.5	3.2	4.5	3.7	5.1	6.9
Ni	3.3	4.7	6.5	28.7	31.4	33.7	10.9	21.7	33.3	15.3	23.2	26.2	23.0	24.2	25.5	25.0	26.6	28.4	9.6	10.4	11.3
Bi	bdl	0.0	0.1	bdl	0.0	0.1	bdl	0.0	0.2	bdl	0.0	0.2	bdl	0.0	0.1	bdl	0.0	0.1	bdl	0.0	0.1
Ag	bdl	0.0	0.1	bdl	0.0	0.1	bdl	0.0	0.1	bdl	0.0	0.1	bdl	bdl	bdl	bdl	0.0	0.0	bdl	0.0	0.1
Pb	bdl	0.0	0.2	bdl	bdl	bdl	bdl	0.0	0.2	bdl	0.0	0.1	bdl	bdl	bdl	bdl	0.0	0.1	bdl	0.0	0.2
Cu	bdl	0.0	0.1	bdl	0.0	0.1	bdl	0.0	0.1	bdl	0.0	0.2	bdl	0.0	0.1	bdl	0.0	0.1	bdl	0.0	0.2
Zn	bdl	bdl	bdl	bdl	0.0	0.0	bdl	0.0	0.0	bdl	0.0	0.0	bdl	0.0	0.0	bdl	0.0	0.0	bdl	0.0	0.0
As	70.7	71.9	72.9	44.3	47.9	54.9	41.8	45.7	54.7	48.7	55.7	59.4	43.4	43.9	44.9	58.1	61.3	67.1	71.1	72.1	72.9
S	0.4	0.5	0.6	11.5	16.7	19.2	12.0	18.3	20.9	8.6	11.2	16.2	19.0	19.7	20.3	3.5	7.2	9.2	0.3	0.4	0.7
Sb	bdl	0.2	0.6	0.1	0.4	2.2	bdl	0.0	0.3	bdl	0.1	0.3	bdl	0.0	0.1	0.0	0.1	0.1	bdl	0.0	0.1
Se	0.2	0.3	0.3	0.2	0.2	0.4	0.1	0.2	0.3	0.1	0.3	0.5	0.2	0.2	0.3	0.2	0.3	0.4	0.1	0.3	0.4
Hg	bdl	0.0	0.1	bdl	0.0	0.1	bdl	0.0	0.1	bdl	0.0	0.1	bdl	0.0	0.1	bdl	0.0	0.1	bdl	0.0	0.1
total	101.8	102.5	103.1	98.9	99.7	100.5	97.8	99.7	102.8	99.0	100.2	101.2	98.4	99.3	100.6	99.3	100.2	101.3	101.0	101.9	102.7
∑ formula unit	3			3			3			3			3			3			3		
Fe.p.f.u.	0.37	0.45	0.51	0.02	0.07	0.17	0.01	0.16	0.42	0.07	0.12	0.22	0.24	0.29	0.33	0.01	0.05	0.08	0.42	0.48	0.56
Co.p.f.u.	0.37	0.42	0.50	0.00	0.02	0.09	0.00	0.23	0.48	0.10	0.18	0.41	0.00	0.03	0.06	0.05	0.10	0.14	0.13	0.18	0.24
Ni.p.f.u.	0.11	0.16	0.22	0.82	0.92	0.97	0.30	0.62	0.95	0.44	0.72	0.83	0.65	0.68	0.72	0.80	0.86	0.94	0.33	0.36	0.39
As.p.f.u.	1.90	1.93	1.94	0.99	1.10	1.32	0.92	1.02	1.31	1.11	1.35	1.48	0.94	0.97	0.99	1.44	1.56	1.76	1.93	1.95	1.96
S.p.f.u.	0.03	0.03	0.04	0.65	0.89	0.99	0.67	0.95	1.06	0.50	0.63	0.86	0.99	1.02	1.03	0.21	0.42	0.53	0.02	0.03	0.05

location	GPr			KB			GPg			KB			Pl			KB			GPr		
stage	T3: alpine stage			T3: alpine stage			T3: alpine stage			T3: alpine stage			T3: alpine stage			T4: alteration			T4: alteration		
mineral	nc II			nc II			sk IV			sk IV			sk IV			cbt-gdf (myrmecitic)			gdf III		
N	19			23			22			12			86			60			20		
	min	mean	max	min	mean	max	min	mean	max	min	mean	max	min	mean	max	min	mean	max	min	mean	max
Fe	bdl	0.0	0.3	bdl	0.0	0.1	2.7	3.5	4.4	1.3	2.0	2.6	2.3	3.7	5.1	0.2	0.5	1.6	0.1	0.2	0.3
Co	bdl	0.0	0.1	0.0	0.1	0.5	12.4	14.1	15.9	17.1	17.9	18.6	11.0	13.8	16.7	11.3	20.1	23.8	1.5	2.5	4.2
Ni	43.8	44.3	45.2	43.4	44.2	44.9	3.1	4.1	5.4	1.5	1.9	2.4	2.6	4.2	5.4	10.9	14.8	23.2	30.7	32.5	33.9
Bi	bdl	0.0	0.1	bdl	0.0	0.1	bdl	0.0	0.1	bdl	0.0	0.1	bdl	0.0	0.1	bdl	0.0	0.3	bdl	0.0	0.1
Ag	bdl	0.0	0.0	bdl	0.0	0.1	bdl	0.0	0.1	bdl	0.0	0.1	bdl	0.0	0.1	bdl	0.0	0.1	bdl	0.0	0.1
Pb	bdl	0.1	0.2	bdl	0.0	0.1	bdl	0.0	0.2	bdl	0.0	0.1	bdl	0.0	0.2	bdl	bdl	bdl	bdl	bdl	bdl
Cu	bdl	0.0	0.1	bdl	0.0	0.1	bdl	0.0	0.1	bdl	bdl	bdl	bdl	0.0	0.1	bdl	0.0	0.1	bdl	0.0	0.1
Zn	bdl	0.0	0.0	bdl	0.0	0.0	bdl	0.0	0.0	bdl	0.0	0.0	bdl	0.0	0.0	bdl	0.0	0.0	bdl	0.0	0.1
As	53.6	54.0	54.4	53.0	53.5	54.0	80.3	81.2	81.9	80.7	81.1	81.7	80.7	81.8	83.4	44.8	46.7	48.0	41.3	41.9	43.0
S	bdl	0.0	0.1	0.0	0.1	0.2	bdl	0.0	0.0	0.0	0.1	0.4	bdl	0.0	0.1	15.9	17.4	18.6	18.6	18.9	19.3
Sb	0.2	0.3	0.7	0.1	0.1	0.2	bdl	0.0	0.0	bdl	bdl	bdl	bdl	0.0	0.0	bdl	0.0	0.1	2.1	2.8	3.4
Se	0.2	0.3	0.4	0.2	0.3	0.4	0.2	0.2	0.4	0.2	0.3	0.4	0.1	0.2	0.4	0.1	0.2	0.3	0.2	0.2	0.3
Hg	bdl	0.0	0.1	bdl	0.0	0.1	bdl	0.0	0.1	bdl	0.0	0.1	bdl	0.0	0.1	bdl	0.0	0.1	bdl	0.0	0.1
total	98.4	99.2	100.1	97.8	98.5	99.5	102.3	103.3	104.1	102.6	103.4	105.8	102.5	103.9	105.9	98.6	99.8	101.0	97.4	99.0	100.2
∑ formula unit	2			2			4			4			4			3			3		
Fe.p.f.u.	0.00	0.00	0.01	0.00	0.00	0.00	0.13	0.17	0.22	0.07	0.10	0.13	0.11	0.18	0.25	0.01	0.02	0.05	0.00	0.00	0.01
Co.p.f.u.	0.00	0.00	0.00	0.00	0.00	0.01	0.58	0.66	0.74	0.79	0.83	0.87	0.51	0.64	0.78	0.33	0.58	0.68	0.04	0.07	0.12
Ni.p.f.u.	1.01	1.02	1.03	1.01	1.02	1.03	0.14	0.19	0.25	0.07	0.09	0.11	0.12	0.19	0.25	0.32	0.43	0.67	0.88	0.94	0.97
As.p.f.u.	0.96	0.97	0.98	0.96	0.97	0.97	2.95	2.97	2.98	2.90	2.96	2.98	2.96	2.97	3.00	1.01	1.06	1.11	0.93	0.95	0.96
S.p.f.u.	0.00	0.00	0.00	0.00	0.00	0.01	0.00	0.00	0.00	0.00	0.01	0.03	0.00	0.00	0.01	0.86	0.92	0.97	0.99	1.00	1.01

N: number of measurements; bdl: below detection limit; Fe./Co./Ni./As./S.p.f.u.: atoms per formula unit; *measurements using Cameca SX100, where As calculated as difference to 100 wt%

Krutovites ($NiAs_{2-x}S_x$; 0.6>x>0.2) originate exclusively from the Ni-Co stages IV at PI and GPg, respectively (Figure 18c). At both localities, symplectic krutovite I shows Ni-rich compositions with variable Co# (PI: 0.0-0.1 Co#; GPg: 0.05-0.1 Co#) but with a mostly fixed Fe/Ni ratio (PI: 0.05; GPg: 0.03). The compositions of the krutovite II veinlets, crosscutting the previous ores, show variable and higher Fe contents at fixed Co/Ni ratios. Krutovite II reaches 0.1 Fe# and, if replacing sulfides such as tetrahedrite, up to 0.16 Fe#. The concentration of arsenic decreases successively from krutovite I to krutovite II (Figure 19c, e). At PI, krutovite I shows 1.7-1.5, krutovite II 1.5-1.4 and krutovite II replacing sulfides 1.4-1.2 As per formula unit. Symplectic krutovite I of GPg has ~1.6 As, krutovite II ranges from 1.55 to 1.45 As per formula unit.

Alpine Co stage Vb (Figure 18b): The Co stage at KB includes Fe-Ni safflorite (0.50-0.65 Fe#; 0.10-0.23 Ni#) and Fe-Ni cobaltite (0.12-0.26 Fe#; 0.16-0.33 Ni#). Skutterudite IV shows comparable Co concentrations as skutterudite III from the Ni-Co stage, but tends to slightly more Fe-dominated compositions. In contrast to the arsenian gersdorffite I (Ni-Co stage), Fe-Ni cobaltite and arsenopyrite III show only 1.0-0.9 and 1.0-0.8 As per formula unit, respectively.

7.1.3 Ore remobilization and hydrothermal alteration (stages Va and VI)

Alpine remobilization stage Va (Figure 18a): Sulfarsenides formed during the remobilization of previous ores generally include lower arsenic/sulfur ratios than their precursor phases (gdf II, remobilized krut I and krut III; cf. Figures 18d-f and 19c-e). For example, gersdorffite II of stage Va at KB incorporates 1.3-0.8 As apfu, which remobilized/replaced gersdorffite I from the Ni-Co stage IV with 1.8-1.3 As (Figure 19d). In addition to this enrichment in sulfur, the Fe-Co-Ni ratios evolve to higher Co and Fe following different branches towards the Fe-Ni safflorite, Fe-Ni cobaltite and arsenopyrite compositions of the following Co stage Vb (Figure 18d). Contemporaneously with this rising Co and Fe of gersdorffite II, arsenic commonly decreases from 1.3 to 0.8 As. Similar effects of increasing sulfur, iron and cobalt are observed at PI and GP (Figure 18e and f, respectively). Where the symplectic intergrowth of skutterudite and krutovite I was modified and destroyed by deformational textures, higher sulfur is present in krutovite I (1.65-1.4 As; relic krut I, Figure 11g-h) than in the unaffected textures (1.7-1.5 As; symplectic krut I, Figure 11f). With further sulfur increase, gersdorffite II incorporated 1.45-1.0 As and tends from the krutovite I signature towards higher Fe and Co of up to 0.16 Fe# and 0.4 Co#. Concomitant to this, skutterudite IV restricts to higher cobalt compositions with 0.5-0.78 Co# than previous skutterudite I and II (down to 0.27 Co#); co-precipitated löllingite III incorporates higher Co/Fe ratios than löllingite II.

The disseminated cobaltite and arsenopyrite from the lower level of vein 3 show a different trend (Figure 18d; named as Alpine cbt and Alpine asp). Early cobaltite enclosing pyrite has 0.9-0.7 Co# and 0.8-0.9 As. This generation additionally tends to slightly higher Ni contents of up to 0.1 Ni#

and towards the composition of the Fe-Ni cobaltite from the following Co stage Vb. In the further succession, however, cobaltites evolve to more Fe-rich and S-poor compositions (0.6-0.1 Co#; 0.9-1.0 As) and end up with arsenopyrite (Co# < 0.07; 0.8-1.0 As).

The gersdorffite-cobaltite solid solution of the hydrothermal alteration stage at KB shows Fe# < 0.05 and a range of 0.3-0.7 Ni# at a fixed stoichiometric As/S ratio of 1 (Figure 18f). At GPr, gersdorffite III grains between niccolite and millerite similarly show the same As/S stoichiometric ratio and Co# up to 0.14.

7.2 U-Pb data (LA-ICP-MS)

The different carbonate generations and various ore samples from all three mineralizations were tested for their U and Pb concentrations. Only a few proved to be suitable with μ values ($^{238}U/^{204}Pb$) > 1. These were used to construct isochrons in the Tera-Wasserburg diagram. An age determination for PI was not possible due to dispersed native Bi, which caused tailing effects at the detector of ^{209}Bi on ^{207}Pb. The individual ages of the single and multi-mineral isochrons are shown in Table 3 with regards to their initial $^{207}Pb/^{206}Pb$ ratio ($^{207}Pb/^{206}Pb_i$), MSWD, ranges of U and Pb contents and ratios of $^{238}U/^{206}Pb$ and $^{207}Pb/^{206}Pb$. Table 4 shows ranges of U and Pb contents and $^{238}U/^{206}Pb$ and $^{207}Pb/^{206}Pb$ ratios of the distinct mineral aggregates. Table ES3 (electronic supplement) includes single raw data and standard errors. Each isochrone represents U-Pb data from paragenetic mineral associations (cf. Figure 8). An overview of all Tera-Wasserburg isochrons is given in Figure 20, the detailed single isochrons including the distinct mineral phases in Figures 21a-l and the sample localities in Figure A1 (Appendix). The following section reports only isochrone ages which are based on detailed textural observations of texturally stable mineral assemblages.

At Kaltenberg, isochrons were gained for magnetites and associated host rock alteration products from the early Fe-Co stage II (magnetite I), the gangue assemblage including arsenopyrite from the late Fe-Co stage II (siderite II, ankerite I, arsenopyrite II), and for the assemblage of the remobilization stage (ankerite III, magnetite IV, pyrite II) of samples SK80/81/82. The samples come from the lower to middle level of KB vein 3 (transition of the fahlband and the sericite-chlorite-schists). Isochrone ages are 235.6±6.7 Ma, 233±10 Ma and 48.3±5.5 Ma (Figure 20a; Isochrons 1, 2 and 8, respectively).

At the upper level of KB vein 3, samples SK170/171 were analyzed. Magnetites (magnetite III, pseudomorph after hematite), arsenides and sulfarsenides (niccolite I, gersdorffite I) have comparable isochrone ages of 189±31 Ma and 182±26 Ma, whereas magnetite IV (euhedral overgrowing magnetite III) has an age of 33.2±8.8 Ma (Figure 20b; Isochrons 3, 4 and 10, respectively). Gangue minerals of these samples (Figure 20c) gave ages of 171.3±5.8 Ma (ankerite II; Isochrone 5) and 39.94±0.86 Ma (ankerite III, magnetite IV, quartz II, uraninite and chlorite;

Isochrone 9). Where aggregates of the hydrothermal overprint (gersdorffite-cobaltite solid solution) infiltrate the primary niccolite I + gdf I assemblage, isochrons show a rejuvenation to 5.8±1.1 Ma (Figure 20b; Isochrone 14). Supergene weathering occurred at least since 2.46±0.23 Ma (annabergite; Isochrone 15).

Co-dominated ores and paragenetic albite in sample SK75 from KB vein 5 show an isochrone age of 28.2±1.1 Ma (Isochrone 11; Figure 20b).

Samples SK134/136 from the reddish ores of GPr include aggregates of niccolite II and gersdorffite II, both finely intergrown with sericite and quartz. Mixed isochrone ages accumulate either at 71.1±1.4 Ma where niccolite II and gersdorffite II overgrow randomly oriented sericite and quartz along the selvedges (Figure 20d; Isochrone 6), or at 44.6±1.5 Ma where a second generation of sericite and quartz replace and crosscut the ores along the S1 foliation (Figure 20d; Isochrone 7). Calcite III related to the crenulation foliation S3a shows an age of 27.3±1.8 Ma (Figure 20d; Isochrone 12).

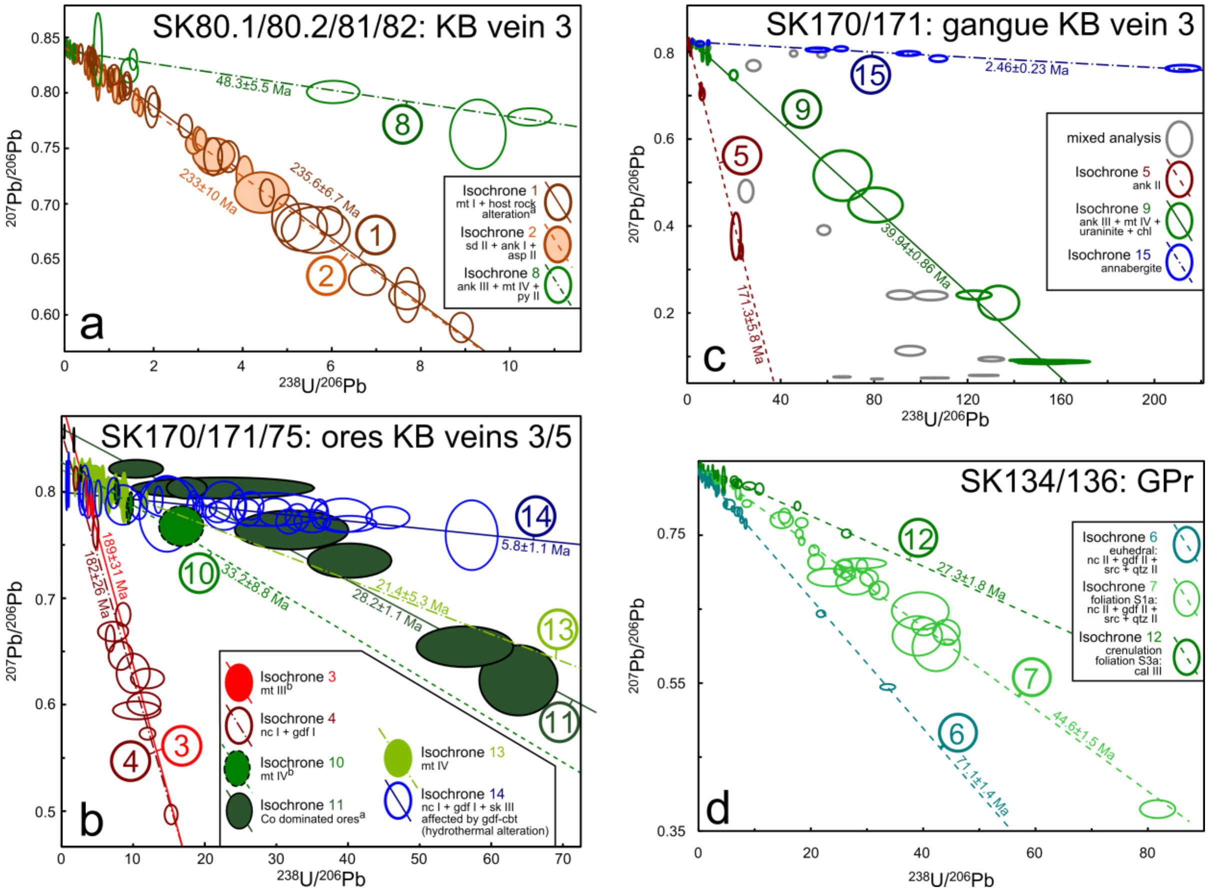

Figure 20: Thera-Wasserburg diagrams showing $^{207}Pb/^{206}Pb$ versus $^{238}U/^{206}Pb$. For the comparison to Figures 2h and 8, Isochrons 1-15 of the different single- and multi-mineral isochrons are marked and color-coded. (a) Samples SK80.1/80.2/81/82, middle/lower level KB vein 3. (b) Ni-Co ores and magnetite of SK170/171, upper level KB vein 3 and SK75, upper level KB vein 5. (c) Gangue paragenesis of samples SK170/171, upper level KB vein 3. (d) SK134/136, GPr. All data-point error ellipses illustrated as 2σ. [a]for paragenetic mineral fractions see Figure 21a and f. [b]calculated by maximum and minimum ages of errochrone ages see Figure 21e.

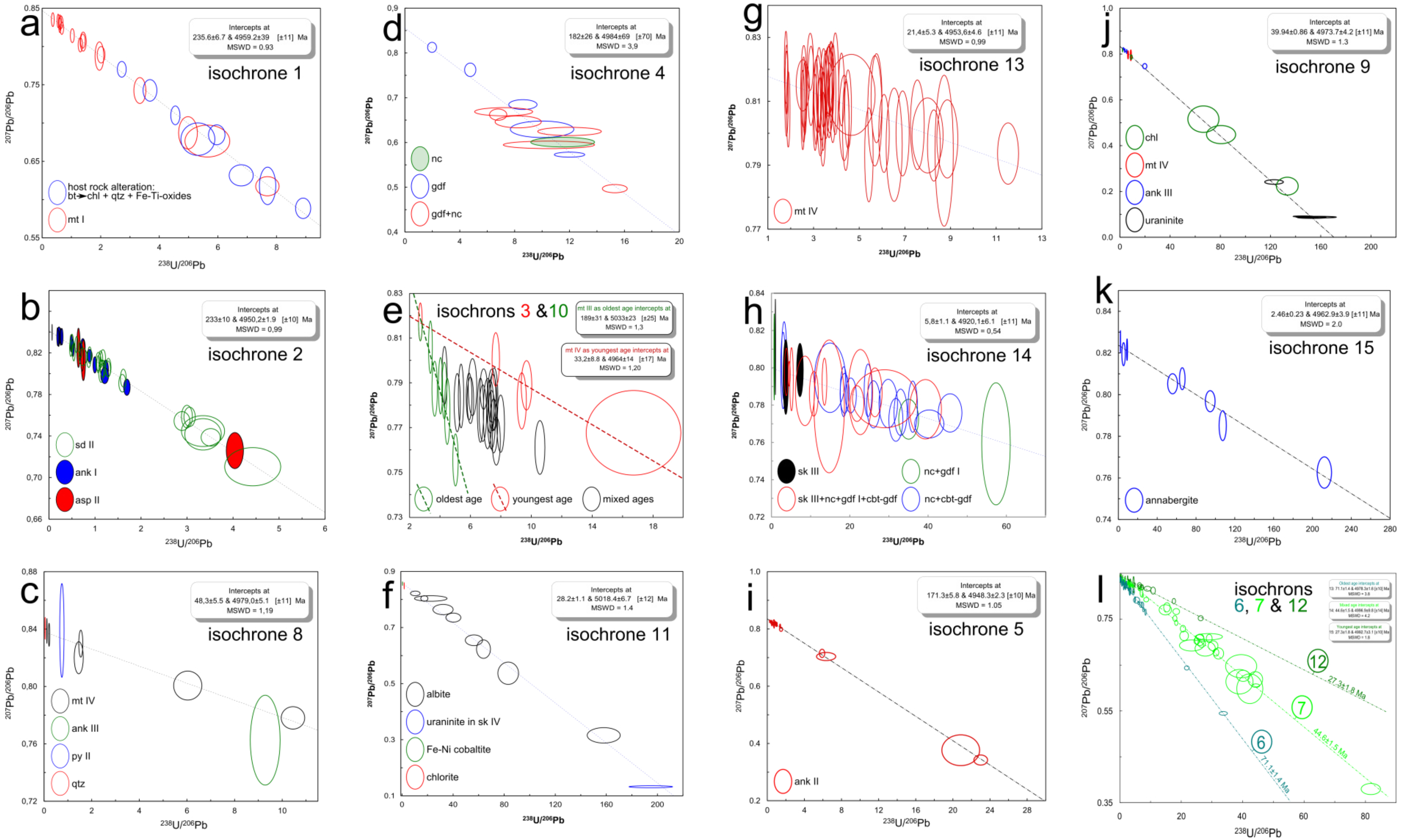

Figure 21: Thera-Wasserburg diagram showing ^{207}Pb/^{206}Pb versus ^{238}U/^{206}Pb of isochrons 1-15 measured in-situ at samples from Kaltenberg and Grand Praz.

Table 3: U-Pb data from KB as single and multi-mineral isochrons 1-15, including their isochrone ages, initial $^{207}Pb/^{206}Pb$ ratios ($^{207}Pb/^{206}Pb_i$) and mean square weighted deviation (MSWD) of the fits. Concentrations of U, Pb and the $^{238}U/^{206}Pb$, $^{207}Pb/^{206}Pb$ ratios are given as min, mean and max values, respectively. In addition, corresponding ore stages, sample localities, paragenesis of the single/multi-mineral isochrones and number of measurements (N) are given. Numeration of the isochrones correspond to those in Figure 2 and 8. U-Pb data of distinct minerals are given in Table 4..

Ore stage	Sample locality	Paragenesis	Isochrone number	N	Isochrone age [Ma]	$\frac{^{207}Pb}{^{206}Pb_i}$	MSWD	U [mg/kg]			Pb [mg/kg]			$^{238}U/^{206}Pb$			$^{207}Pb/^{206}Pb$		
								min	**mean**	**max**	**min**	**mean**	**max**	**min**	**mean**	**max**	**min**	**mean**	**max**
Stage II	KB middle level	mt II+bt+chl+qtz	1	24	235.6±6.7	0.8469	0.93	0.23	2.17	14.9	0.32	2.12	6.46	0.37	3.33	8.91	0.59	0.75	0.84
Stage II	KB middle level	sd II+ank I+asp II	2	45	233±10	0.8414	0.99	0.17	4.26	22.7	0.51	11.3	19.6	0.07	1.29	4.43	0.71	0.80	0.84
Stage IV	KB upper level	mt III[a]	3	7	189±31	0.8863	1.30	0.29	0.48	1.25	0.22	0.49	1.62	2.71	3.94	5.02	0.76	0.79	0.82
Stage IV	KB upper level	nc I +gdf I	4	12	182±26	0.8558	3.90	0.33	4.75	25.1	0.43	1.82	9.19	1.98	9.07	15.3	0.50	0.65	0.81
Stage IV	KB upper level	ank II	5	21	171.3±5.8	0.8333	1.05	0.29	1.31	7.48	0.11	3.49	17.3	0.25	3.29	23.0	0.34	0.76	0.83
Stage V(a)	GPr selvedges	nc II+gdf II+ser+qtz	6	25	71.1±1.4	0.8400	3.80	0.34	2.35	21.0	0.34	1.19	8.93	0.34	4.54	33.7	0.54	0.80	0.84
Stage V(a).	GPr selvedges	as Isochrone 6	7	97	44.6±1.5	0.8482	4.20	0.06	6.52	43.7	0.13	3.49	20.1	0.01	11.0	81.8	0.38	0.78	0.84
Stage V(b)	KB middle level	ank III+mt IV+py II+qtz	8	9	48.3±5.5	0.8380	1.19	0.37	5.20	22.6	1.19	41.3	267	0.05	3.32	10.5	0.76	0.82	0.84
Stage V(b)	KB upper level	ank III+mt IV+urn+chl	9	17	39.94±0.86	0.8340	1.30	0.52	723	4027	0.28	7.21	31.0	2.14	63.0	158	0.09	0.53	0.82
Stage V(b)	KB upper level	mt IV[b]	10	5	33.2±8.8	0.8276	1.20	0.67	1.53	3.61	0.30	0.66	1.62	2.71	9.23	16.7	0.77	0.79	0.82
Stage V(b)	KB vein 5	ab+urn+chl+Fe-Ni cbt	11	12	28.2±1.1	0.8593	1.40	0.32	141	911	0.66	3.20	8.32	0.41	56.8	195	0.13	0.66	0.86
Stage V(a).	GPr selvedges	cal III	12	16	27.3±1.8	0.8438	1.80	0.16	2.91	10.8	0.40	1.09	4.37	0.06	6.81	26.4	0.75	0.82	0.85
Stage V(b	KB upper level	mt IV	13	46	21.4±5.3	0.8203	0.99	0.13	0.42	1.40	0.20	0.33	1.22	1.79	4.36	11.5	0.79	0.81	0.82
weathering	KB upper level	mixtures with cbt-gdf	14	32	5.8±1.1	0.7996	0.54	0.06	6.59	42.2	0.16	1.01	4.09	0.70	20.3	57.3	0.76	0.79	0.81
weathering	KB upper level	anb	15	8	2.46±0.23	0.8238	2.00	1.93	126	333	3.16	6.14	11.0	2.17	69.1	212	0.76	0.80	0.83

[a]maximum age, [b]minimum age, mt: magnetite, bt: biotite, chl: chlorite, qtz: quartz, sd: siderite, ank: ankerite, asp: arsenopyrite, nc: niccolite, gdf: gersdorffite, ser: sericite, py: pyrite, urn: uraninite, ab: albite, cbt: cobaltite, cal: calcite, anb: annabergite

Table 4: U-Pb data of the distinct minerals of Table 3, including number of measurements (N), corresponding isochrone ages, U, Pb concentrations and the $^{238}U/^{206}Pb$, $^{207}Pb/^{206}Pb$ ratios as min, mean and max values, respectively. Note that mixed measurements indicated as mixed. Samples and isochrons numeration according to Table 3.

Mineral	**Sample**	**Isochrones**	**N**	**Isochrone ages**	**U [mg/kg]**			**Pb [mg/kg]**			**$^{238}U/^{206}Pb$**			**$^{207}Pb/^{206}Pb$**		
					min	**mean**	**max**	**min**	**mean**	**max**	**min**	**mean**	**max**	**min**	**mean**	**max**
sd II	SK80.1, 80.2	2	26	233±10 Ma	1.02	5.97	22.7	7.15	11.5	15.9	0.48	1.64	4.43	0.71	0.79	0.83
ank I	SK80.1, 80.2	2	15	233±10 Ma	0.25	2.09	5.79	8.73	12.5	17.8	0.07	0.61	1.69	0.79	0.82	0.84
ank II	SK170, 171	5	21	171.3±5.8 Ma	0.29	1.31	7.48	0.11	3.49	17.3	0.25	3.29	23.0	0.34	0.76	0.83
ank III	SK81, 170	8, 9	6	48.3±5.5, 39.94±0.86 Ma	1.98	11.8	58.4	1.59	9.08	35.8	2.71	7.50	19.8	0.75	0.80	0.82
mt II	SK81	1	17	235.6±6.7 Ma	0.23	2.39	14.9	0.32	2.64	6.46	0.37	2.41	7.69	0.62	0.77	0.84
mt III, IV (mixed)	SK170, 171	3, 10	31	189±31, 33.2±8.8 Ma	0.29	0.76	3.61	0.22	0.41	1.62	2.71	6.61	16.7	0.76	0.78	0.82
mt IV	SK81, 170, 171	8, 9, 13	54	48.3±5.5, 39.94±0.86, 21.4±5.3 Ma	0.13	1.17	22.6	0.20	1.02	10.8	0.12	4.36	11.5	0.78	0.81	0.84
ab	SK75	11	9	28.2±1.1 Ma	6.25	136	911	1.84	3.21	8.32	10.4	53.8	158	0.32	0.67	0.82
bt, chl, qtz (mixed)	SK81	1	7	235.6±6.7 Ma	0.47	1.64	4.16	0.42	0.87	1.32	2.72	5.55	8.91	0.59	0.68	0.77
chl	SK170, 75	9, 11	6	39.94±0.86, 28.2±1.1 Ma	0.32	66.3	237	0.66	1.83	2.86	1.72	48.9	133	0.22	0.61	0.85
qtz	SK82	8	1	48.3±5.5 Ma		0.39			29.6			0.05			0.84	
asp II	SK80.2	2	4	233±10 Ma	0.17	1.28	4.04	0.51	5.48	19.6	0.64	1.54	4.04	0.73	0.79	0.83
py II	SK82	8	1	48.3±5.5 Ma		0.90			267			0.75			0.84	
urn	SK170, 75	9, 11	6	39.94±0.86, 28.2±1.1 Ma	470	2050	4027	3.07	16.0	31.0	123	154	195	0.09	0.12	0.24
Fe-Ni cbt	SK75	11	1	28.2±1.1 Ma		0.65			5.83			0.41			0.86	
nc I	SK170	4	1	182±26 Ma		1.49			0.53			11.5			0.60	
gdf I	SK170	4	5	182±26 Ma	0.33	7.97	25.1	0.57	3.00	9.19	1.98	7.47	12.0	0.57	0.69	0.81
gdf I, nc I (mixed)	SK170, 171	4	9	182±26 Ma	0.10	3.53	11.4	0.29	0.92	1.69	0.70	17.0	57.3	0.50	0.67	0.81
sk III, cbt-gdf (mixed)	SK171	14	3	5.8±1.1 Ma	0.06	0.37	0.59	0.21	0.27	0.33	0.99	3.97	7.27	0.80	0.80	0.81
nc I, gdf I, cbt-gdf (mixed)	SK171	14	12	5.8±1.1 Ma	0.63	2.56	9.98	0.16	0.68	2.55	3.78	16.7	39.3	0.78	0.79	0.80
nc III, cbt-gdf (mixed)	SK171	14	14	5.8±1.1 Ma	0.33	11.6	42.2	0.29	1.52	4.09	2.98	24.7	45.6	0.77	0.78	0.80
anb	SK170	15	8	2.46±0.23 Ma	1.93	126	333	3.16	6.14	11.0	2.17	69.1	212	0.76	0.80	0.83
nc II, gdf II, ser (mixed)	SK134, 136	6, 7	25	71.1±1.4, 44.6±1.5 Ma	0.06	4.71	43.7	0.13	2.29	20.1	0.01	8.89	81.8	0.38	0.80	0.85
cal III (foliation S3)	SK134, 136	12	113	27.3±1.8 Ma	0.16	2.91	10.8	0.40	1.09	4.37	0.06	6.81	26.4	0.75	0.82	0.85

mineral abbreviations as in Table 1

7.3 Fluid inclusions (FI)

7.3.1 Microthermometry

Fluid inclusions (FI) were analyzed in siderite, Fe-dolomite, ankerite, calcite, and quartz. The size of the fluid inclusions ranges from 3 to 10 µm in siderite, dolomite and ankerite; 5 to 80 µm in calcite and quartz. Unambiguous phase transitions were only observed in FIs > 5 µm. It was possible to analyze Fe-dolomite I, ankerite I and calcite III from GP; Fe-dolomite, ankerite I and quartz II from PI; and Fe-dolomite, siderite II and III, calcite I, II and III and quartz II from KB.

Fluid inclusions show a filling degree of ~0.9 (liquid/vapor). First eutectic melting occurs consistently at -52 °C. It was not possible to freeze fluid inclusions within siderite I even after mounting the samples inside liquid nitrogen. Table ES4 (electronic supplement) shows all observed phase transitions of the melting temperature of ice (Tm_i), hydrohalite (Tm_{hh}), and halite (Tm_{NaCl}), uncorrected homogenization temperatures (T_h), calculated weight fractions of NaCl and $CaCl_2$, corresponding salinities and Ca/(Ca+Na) ratios. No clathrates were observed in any of the different FIAs. Due to their small size and micro-scaled intergrowth of the carbonate generations, a determination of bromine from the FIs was not possible. The diverse FIAs show a wide range of T_h between 179 and 307 °C, salinities from 13.4 to 35.3 wt.% (NaCl+$CaCl_2$) and molar Ca/(Ca+Na) ratios from ~0 to 0.5 (cf. Table 5).

FIAs of the carbonates (precipitated during the Fe-Co stage at KB) show a tendency to lower T_h and salinities (200-220 °C; 20.3-23.6 wt.% NaCl+$CaCl_2$) than those from PI and GP (220-286 °C; 32-35.3 wt.% NaCl+$CaCl_2$). FIAs of siderite III from KB, however, show similar T_h and Ca/(Ca+Na) ratios as Fe-dolomite from PI and GP (249-262 °C; 0.9-0.17), but their salinity is similar to those of siderite II from KB (~22.4 wt.% NaCl+$CaCl_2$). In addition, FIAs of the Fe-Co stage at KB show lower Ca/(Ca+Na) ratios (0-0.14) than those at PI and GP (0.11-0.26). Corresponding to the Ni-Co stage at KB, siderite III shows T_h between 249 and 262 °C, salinities of ~22.4 wt.% (NaCl+$CaCl_2$) and Ca/(Ca+Na) ratios from 0.09 to 0.17. They are in a range similar to Fe-dolomite and ankerite I at GP and PI. At each deposit, Alpine quartz II shows higher T_h (PI: ~300°C; KB: ~273°C) and Ca/(Ca+Na) ratios (PI: ~23.7; KB: ~17.1), but lower salinities (PI: ~0.44; KB: ~0.23) compared to the carbonates of the Fe-Co and Ni-Co stage.

Fe-dolomite of GP, PI and KB represents the first gangue stage after Fe-Co-Ni arsenide and sulfarsenide precipitation with T_h of 264-286, 229-241 and 214-220 °C, salinities of 34-35.3, 32.1-33.3 and 20.3-21.2 wt.% NaCl+$CaCl_2$, and Ca/(Ca+Na) ratios of 0.18-0.22, 0.11-0.12 and ~0, respectively. The following stages of ankerite I at GP and PI and siderite II at KB show slightly decreasing T_h to around 245, 222 and 206 °C, but increasing Ca/(Ca+Na) ratios of 0.23, 0.24 and 0.08, respectively. Compared to the FIAs of the earlier carbonates, constant salinities of 33 wt.% NaCl+$CaCl_2$ are

Table 5: Condensed overview of observed homogenization temperatures (Th), corrected formation temperatures of maximum pressure estimation ($T_{P\text{-max.corr}}$), calculated wt. fraction $NaCl+CaCl_2$, and corresponding Ca/(Ca+Na) ratios. All variables are givens as min, mean and max values. The correlation of Ca_{excess} and $Na_{deficit}$ given as $\Delta Ca_{excess}/\Delta Na_{deficit}$ and corresponding R². Note that simple halite dissolution brine do not show a $\Delta Ca_{excess}/\Delta Na_{deficit}$ correlation which correspond to plagioclase albitisation reactions between a factor of 1 and 2 (SK126; Fe-dol).

						T_h [°C]			$T_{P\text{-max,corr}}$ [°C]			$NaCl+CaCl_2$ [wt.%]			Ca/(Ca+Na) []			$\Delta Ca_{excess}/\Delta Na_{deficit}$
sample	location	stage	host	inclusion type	N	min	mean	max	min	mean	max	min	mean	max	min	mean	max	
SK113b	GPg	II	Fe-dol I	H_2O-NaCl-$CaCl_2$-(CO_2)	12	264	272	286	280	288	303	34.0	34.8	35.3	0.18	0.20	0.22	1.61 (R²: 0,9884)
SK113b	GPg	II	ank I	H_2O-NaCl-$CaCl_2$-(CO_2)	15	234	245	253	272	284	293	32.0	32.5	33.2	0.22	0.23	0.26	1.59 (R²: 0.9931)
SK113b	GPg	V(b)	cal III	H_2O-NaCl-$CaCl_2$	4	190	194	200	274	278	286	29.9	30.0	30.3	0.08	0.12	0.15	1.54 (R²: 0.9996)
SK42.2	PI	II	Fe-dol	H_2O-NaCl-$CaCl_2$-(CO_2)	8	229	240	251	237	246	249	32.1	32.6	33.3	0.11	0.11	0.12	1.72 (R²: 0.96)
SK42.2	PI	II	ank I	H_2O-NaCl-$CaCl_2$-(CO_2)	4	220	222	225	240	242	245	32.6	33.0	33.3	0.23	0.24	0.25	1.60 (R²: 0.9912)
SK42.2	PI	V(b)	qtz II	H_2O-NaCl-$CaCl_2$	9	289	301	307	407	423	433	22.9	23.7	24.2	0.38	0.44	0.50	1.46 (R²: 0.9949)
SK126	KB	II	Fe-dol	H_2O-NaCl-$CaCl_2$-(CO_2)	3	214	218	220	220	223	226	20.3	20.6	21.2	0.00	0.00	0.00	0.22 (R²: 1; N=3)
SK126	KB	II	sd II	H_2O-NaCl-$CaCl_2$-(CO_2)	7	200	206	220	214	220	235	23.0	23.3	23.6	0.05	0.08	0.14	1.51 (R²: 0.9987)
SK90	KB	III	cal I	H_2O-NaCl-$CaCl_2$	32	204	213	221	218	227	236	17.7	19.6	20.7	0.16	0.28	0.38	1.60 (R²: 0.9964)
SK90	KB	III	cal II	H_2O-NaCl-$CaCl_2$	23	179	196	208	192	209	222	20.4	21.0	21.6	0.29	0.35	0.39	1.59 (R²: 0.9965)
SK107	KB	IV	sd III	H_2O-NaCl-$CaCl_2$-(CO_2)	16	249	256	262	260	268	274	22.0	22.4	22.8	0.09	0.12	0.17	1.47 (R²: 0.9975)
SK126	KB	V(b)	qtz II	H_2O-NaCl-$CaCl_2$	10	269	273	280	384	389	400	16.9	17.1	17.4	0.20	0.23	0.28	1.57 (R²: 0.998)
SK92	KB	V(b)	cal III_a	H_2O-NaCl-$CaCl_2$	7	224	232	240	317	328	338	22.0	22.8	23.1	0.20	0.22	0.23	1.50 (R²: 0.9703)
SK92	KB	V(b)	cal III_b	H_2O-NaCl-$CaCl_2$	8	218	222	227	313	319	326	15.3	15.5	15.8	0.17	0.19	0.21	1.49 (R²: 0.9895)
SK92	KB	V(b)	cal III_c	H_2O-NaCl-$CaCl_2$	8	195	201	206	283	291	298	13.4	14.3	15.0	0.00	0.03	0.06	1.47 (R²: 0.9689)
SK92	KB	V(b)	cal III_d	H_2O-NaCl-$CaCl_2$	5	194	200	204	277	284	290	24.4	24.6	24.9	0.35	0.38	0.42	1.53 (R²: 0.9974)
SK92	KB	V(b)	cal III_e	H_2O-NaCl-$CaCl_2$	8	183	186	190	263	268	273	19.6	19.9	20.3	0.25	0.28	0.30	1.40 (R²: 0.9935)
SK92	KB	V(b)	cal III_f	H_2O-NaCl-$CaCl_2$	8	182	185	190	262	266	272	24.6	24.8	25.0	0.22	0.24	0.27	1.57 (R²: 0.9997)

mineral abbreviations as Table 1

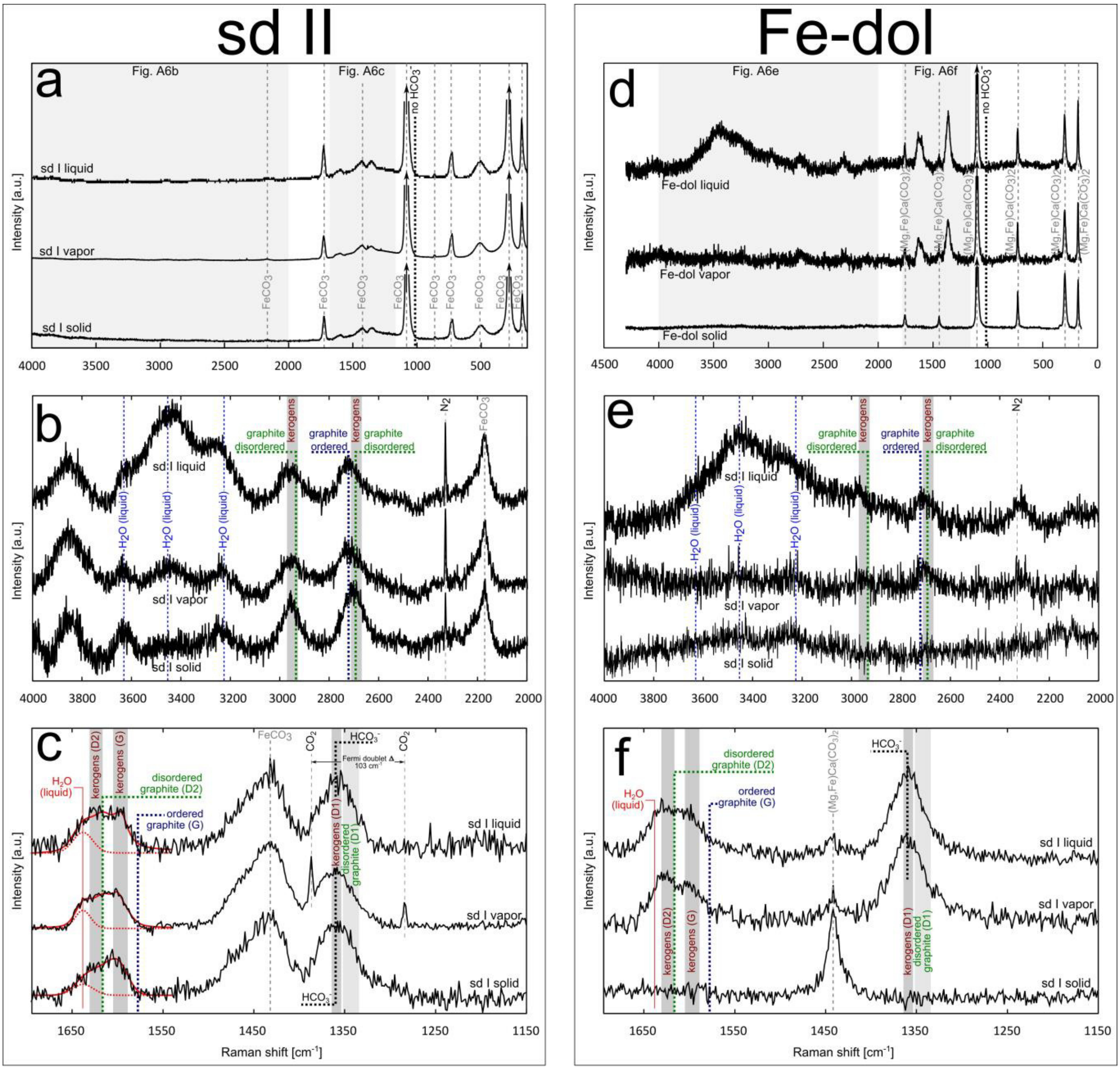

Figure 22: Representative micro Raman spectrographs of sd I (a)-(c) and Fe-Dol (b)-(f). In each figure, measurements of the liquid, vapor and solid phase are given in the upper, middle and lower spectra, respectively. Detailed Raman bands at wavenumbers of 4500-2000 and 1700-1200 cm-1 are shown in (b)-(e) and (c)-(f), respectively. For detailed description of the species, see text.

observed for ankerite I at PI, a decrease to 32.5 wt.% for ankerite I at GP and an increase to 23.3 wt.% for siderite II at KB.

Calcite from the sulfide stage (only present at KB and following siderite II), shows a further increase of the Ca/(Ca+Na) ratio from 0.16 to 0.38 in calcite I but a later, temperature-dependent decrease to 0.29 in calcite II. For calcite I, T_h stays nearly constant compared to earlier Fe-dolomite and siderite II, but decreases towards ~180 °C for calcite II. Generally, calcite I shows slightly lower salinities (~19.6 wt.%) than calcite II (~21 wt.%). FIAs in quartz II and calcite III show a wide spread, but separate groups emerge in their mean T_h, Ca/(Ca+Na) ratios and salinities. For details, see Figure A3 (Appendix).

7.3.2 µ-Raman spectroscopy

According to Raman results, FI of all calcite generations and quartz II (sulfide stage III and Alpine stage Vb) host no other volatiles than H_2O. In contrast, 32 FIs trapped by siderite II, Fe-dolomite, ankerite I and ankerite II (Fe-Co stage II and Ni-Co stage IV; five-element stages), show the results reported in Figure 22a-f. Besides the characteristic Raman bands for H_2O, siderite, ankerite and dolomite (Figure 22a/b and d/e), additional features occur at wavenumbers of ~3100-2600 cm^{-1} and ~1650-1250 cm^{-1} (Figure 22b/e and c/f, respectively). In these regions, broad but distinct bands arise at ~2960 cm^{-1}, ~2700 cm^{-1}, ~1360 cm^{-1}, and a broad feature with different bands at 1670-1560 cm^{-1}. In parts, also the solid phase includes these additional Raman active bands. The observed N_2 band may be due to air between objective and sample. Besides these, no other volatile species (like H_2, H_2S, SO_2 or CO) were detected, which are reported by conventional Raman spectroscopy literature for fluid inclusions (e.g. Frezzotti et al. 2012). Chapter 8.5 includes the detailed discussion of the characteristic Raman active features occurring at wavenumbers of ~3100-2600 cm^{-1} and ~1650-1250 cm^{-1} that reveal kerogen material within the FIs and host minerals.

7.4 Stable Isotopes

7.4.1 Sulfur: Sulfides and Sulfarsenides

Sulfur isotope compositions are reported as $\delta^{34}S_{(CDT)}$-values in Figure 23 and Table 6. Fahlband pyrites show exclusively negative $\delta^{34}S$-values between -20.8‰ and -12.4‰, while the sulfarsenides and sulfides of the Fe-Co stage II and successive sulfide stage III consistently show positive values from +4.6‰ to +18.1‰. The first occurring sulfarsenide shows the heaviest sulfur isotopes (arsenopyrite I: +18.1‰), whereas isotopes in the sulfide stage successively decrease over early pyrite I (py I: +13.5‰ and +11.7‰) to late chalcopyrite (ccp: +4.6‰ and +6‰). Undeformed symplectic krutovite I shows higher values (-1.3‰; Ni-Co stage IV) than deformed krutovite from

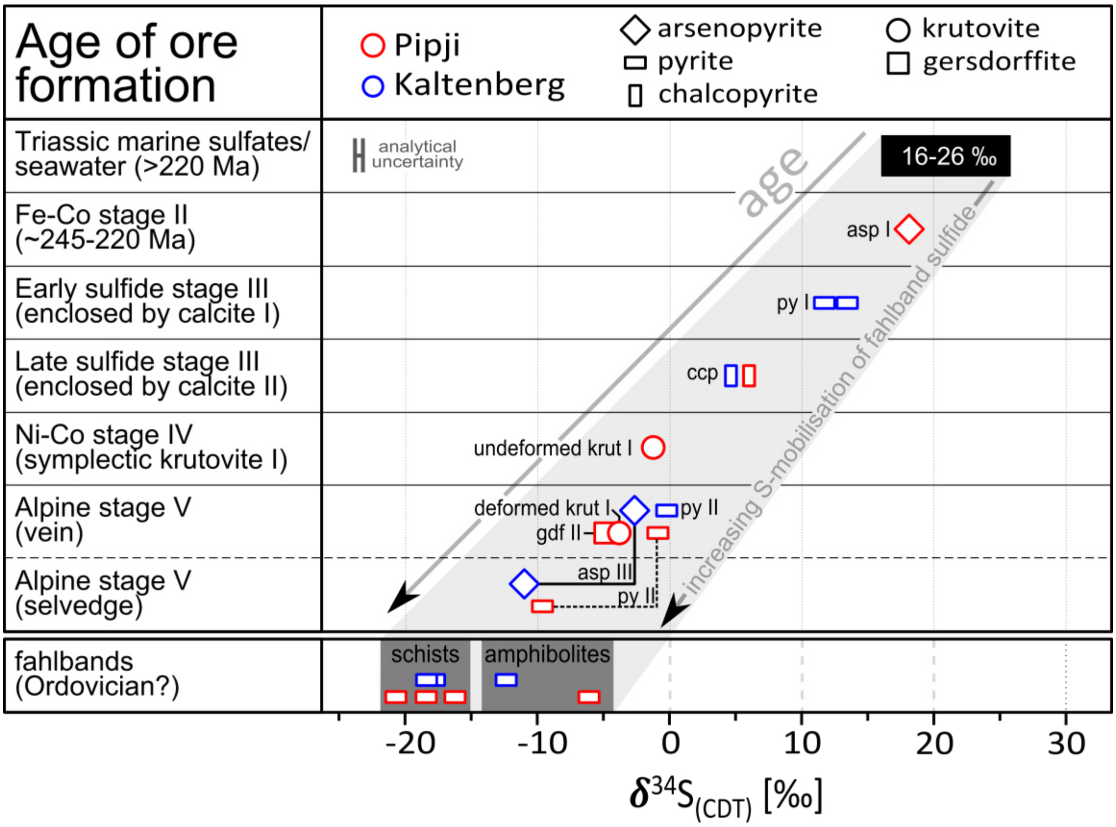

Figure 23: S-isotopic illustration of the sulfarsenides and sulfides from the deposits Kaltenberg and Pipji. Isotopic signatures during the Fe-Co stage reflect a quantitative reduction of Triassic-Jurassic seawater derived sulfates. With further paragenetic succession, S-isotopes evolve to signatures towards Ordovician sulfides from the Fahlbands.

stressed vein sections (-3.9‰; Alpine stage V). Gersdorffite II, arsenopyrite III and pyrite II, which precipitated during the Alpine stage V, have values between -11‰ and -0.23‰. Texturally Alpine pyrite II and arsenopyrite III from the selvages between the vein and the fahlband contact show lighter and nearly similar isotopic signatures as the fahlband pyrites (Figure 23). Kaltenberg and Pipji show similar isotope systematics.

Table 6: S-isotopic composition of sulfides and sulfarsenides. Analytical uncertainty is 0.3‰

Stage	Mineral	Sample	$\delta^{34}S_{(CDT)}$[‰]	Locality
Ordovician fahlbands	Fahlband pyrite	SK101	-12.41	Kaltenberg
	Fahlband pyrite	SK100	-17.82	
	Fahlband pyrite	SK138	-18.44	
	Fahlband pyrite	SK32	-20.77	Pipji
	Fahlband pyrite	SK83	-16.29	
	Fahlband pyrite	SK30	-18.47	
Fe-Co stage II	arsenopyrite I	SK103	18.11	Kaltenberg
sulfide stage III	pyrite I	SK90	11.72	Kaltenberg
	pyrite I	SK139	13.45	
	chalcopyrite	SK91	4.62	
	chalcopyrite	SK115	5.99	Pipji
Alpine stage V	pyrite II (displacement pyrite I)	SK119	-0.23	Kaltenberg
	arsenopyrite III	SK138	-2.65	
	arsenopyrite III	SK138	-11.03	
	pyrite II	SK36	-0.91	Pipji
	pyrite II	SK140	-6.13	
	pyrite II	SK36	-9.63	
	gersdorffite II	SK41	-1.28	
	gersdorffite II	SK41	-4.92	
	gersdorffite II	SK41	-3.85	

7.4.2 Oxygen and Carbon: Carbonates

Table 7 and Figure 24 report oxygen and carbon isotope compositions of the carbonates as $\delta^{13}C_{(VPDB)}$ and $\delta^{18}O_{(VSMOW)}$-values from KB, PI and GP. Analysis of distinct mineral separates indicate the isotopic signatures of the carbonates, precipitated during the barren siderite stage I (siderite I), Fe-Co stage II (Fe-dolomite, ankerite I and siderite II), sulfide stage III (calcite I and II) and Ni-Co stage (ankerite II and siderite III). Figure 24a shows the carbonate evolution at KB and Figure 24b compares the results of KB to PI and GP. Figure 24a and c-f illustrate the temporal and spatial relationship the oxygen and carbon isotope compositions during carbonate precipitation, dissolution and mixing of different reservoirs.

At KB, barren siderite I represents narrow $\delta^{13}C$ and $\delta^{18}O$ mean values of about -6.3‰ and +13.3‰, respectively. Similarly, siderite I at PI represents narrow $\delta^{13}C$ values (~-5.8‰) but with slightly more variable $\delta^{18}O$ (~+13.9 to +14.4‰). Carbonates of the following Fe-Co stage II, which are barren for arsenides/sulfarsenides and did not interact with prior siderite I (precipitated underneath the fahlbands at KB; Figure 24d), show a decreasing C-O isotopes evolution from earliest dolomites ($\delta^{13}C$: -3.6‰; $\delta^{18}O$: +16.3‰) to latest ankerites I ($\delta^{13}C$: -6.2‰; $\delta^{18}O$: +11‰). With successive age, carbonates that replace siderite I and host Fe-Co stage II arsenides/sulfarsenides, show increasing

δ^{18}O between +11.4‰ (Fe-dolomite) and +12.6‰ (siderite II). This C-O correlation represents a flat incline as δ^{13}C compositions remain almost constant at -6.2±0.07‰ [1σ]. This reflects intermediate signatures between prior barren ankerite I and barren siderite I. Although no barren dolomites and ankerites are present in PI and no barren siderite I in GP, similar flat C-O isotope correlations evolved during their Fe-Co stage II carbonate precipitation. They include a successive δ^{18}O increase (PI: +12.2‰ to +13.5‰, GP: 12.8‰ to +16.1‰) at constant δ^{13}C (PI: -5.8±0.02‰, GP: -4.8±0.22‰; both [1σ]). At PI, this stage again represents similar δ^{13}C values as those of siderite I. In contrast to the flat incline during the mineralized Fe-Co stage II, isotopic C-O signatures of the sulfide stage III and Ni-Co stage IV carbonates show steep correlations. From early calcite I to the late calcite II the δ^{13}C compositions range between -6‰ and -7.35‰, whereas the δ^{18}O values remain constant (+12±0.08‰ [1σ]). Similarly, ankerite II and siderite III show a steep slope of the δ^{18}O and δ^{13}C values from +12‰ and -6.5‰ towards +11.7‰ and -7.4‰, respectively.

Table 7: C- and O-isotopic compositions of carbonates. Analytical uncertainty is 0.1‰

Stage	Mineral	Sample	$\delta^{13}C_{(VPDB)}$[‰]	$\delta^{18}O_{(VSMOW)}$[‰]	Locality
stage I (barren siderite)	siderite I	SK105	-6,24	13,19	Kaltenberg
		SK127	-6,30	13,48	
		SK36.4	-5,77	14,17	Pipji
		SK37	-5,68	14,40	
		SK42.2	-5,77	13,91	
		SK42.2	-5,86	13,87	
barren stage II (carbonates below fahlband)	barren Fe-dolomite (early)	SK119	-5,03	13,19	Kaltenberg
		SK139	-4,69	14,19	
		SK96.2	-5,06	12,99	
		SK97	-3,58	16,29	
	barren ankerite I (late)	SK119	-5,62	12,20	
		SK96.2	-6,23	11,10	
		SK97	-6,11	10,98	
Fe-Co stage II (carbonates replacing siderite I)	Fe-dolomite	SK103	-6,29	11,37	Kaltenberg
		SK127	-6,14	11,55	
	ankerite I	SK127	-6,30	11,80	
	siderite II	SK103	-6,26	12,52	
		SK127	-6,18	12,77	
	Fe-dolomite	SK42.2	-5,76	12,25	Pipji
	ankerite I	SK36.4	-5,74	12,99	
		SK42.3	-5,77	12,74	
	siderite II	SK42.3	-5,78	13,50	
	Fe-dolomite I	SK112.1	-4,74	16,09	Grand Praz
		SK112.2	-5,01	15,73	
		SK113	-4,78	13,15	
		SK114	-5,25	12,76	
	ankerite I	SK112.1	-4,57	15,70	
		SK112.2	-4,80	15,39	
		SK113	-4,60	13,28	
		SK114	-4,82	14,42	
sulfide stage III	calcite I	SK119	-6,02	12,05	Kaltenberg
		SK119	-6,09	12,10	
		SK92	-6,74	11,90	
	calcite II	SK90	-7,34	12,04	
		SK91	-7,27	11,97	
Ni-Co stage IV	ankerite II	SK86	-7,44	11,68	
		SK106	-6,47	12,02	
	siderite III	SK107	-7,41	11,63	

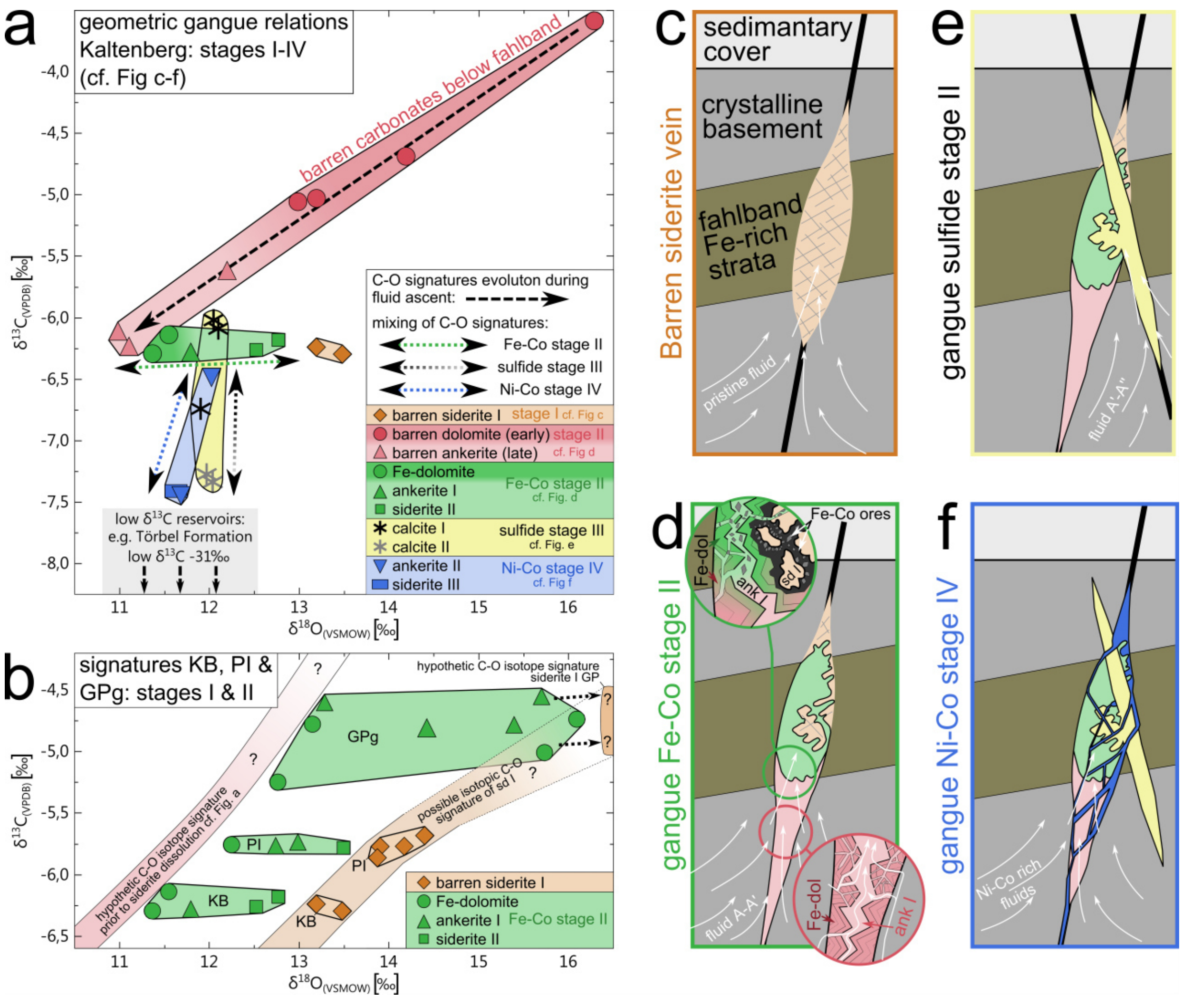

Figure 24: S-isotopic composition of gangue carbonates from Kaltenberg in (a) and compared to Pipji and Grand Praz in (b). Sketches in (c-f) show the spatial and temporal evolution of carbonates during successive displacements of siderite I by later stages.

$\delta^{18}O$ between +11.4‰ (Fe-dolomite) and +12.6‰ (siderite II). This C-O correlation represents a flat incline as $\delta^{13}C$ compositions remain almost constant at -6.2±0.07‰ [1σ]. This reflects intermediate signatures between prior barren ankerite I and barren siderite I. Although no barren dolomites and ankerites are present in PI and no barren siderite I in GP, similar flat C-O isotope correlations evolved during their Fe-Co stage II carbonate precipitation. They include a successive $\delta^{18}O$ increase (PI: +12.2‰ to +13.5‰, GP: 12.8‰ to +16.1‰) at constant $\delta^{13}C$ (PI: -5.8±0.02‰, GP: -4.8±0.22‰; both [1σ]). At PI, this stage again represents similar $\delta^{13}C$ values as those of siderite I. In contrast to the flat incline during the mineralized Fe-Co stage II, isotopic C-O signatures of the sulfide stage III and Ni-Co stage IV carbonates show steep correlations. From early calcite I to the late calcite II the $\delta^{13}C$ compositions range between -6‰ and -7.35‰, whereas the $\delta^{18}O$ values remain constant (+12±0.08‰ [1σ]). Similarly, ankerite II and siderite III show a steep slope of the $\delta^{18}O$ and $\delta^{13}C$ values from +12‰ and -6.5‰ towards +11.7‰ and -7.4‰, respectively.

7.5 µ-X-Ray diffraction (µXRD)

Figure A4 (cf. Appendix) reports µ-resolved X-ray diffraction patterns of the Ni-dominated sulfarsenides to separate unusual arsenian gersdorffites from common krutovites (cf. chapter 6.1). Arsenian gersdorffites (gdf I: $NiAs_xS_{1-x}$, 1.8>x>1.35) show single reflexes at identical diffraction angles as gersdorffites with a common formula of $NiAs_{1.23}A_{0.77}$ (Bayliss 1968). The krutovites, however, show a reflex splitting, either obvious as peak shoulder towards lower diffraction angles (e.g. ~45° 2Θ) or as complete reflex shifts (e.g. ~41° 2Θ). If reflex splitting occurs, one component shifts to lower diffraction angles and towards those of krutovite with a common formula of $NiAs_2$ (Munson 1968). The other component shifts to higher diffraction angles, which are common for Ni-dominated sulfarsenides with higher Fe and Co contents (Bayliss 1982). All measured spots included Ni-dominated sulfarsenides in intensive intergrowth to skutterudite. Skutterudite reflexes fit to those reported by Mandel and Donohue (1971).

8. The Penninic occurrences: Discussion

8.1 From Triassic to present: multi-stage evolution and Alpine overprint

8.1.1 Ages of primary ore formation and Alpine remobilization

In-situ U-Pb dating of unconventional low-U minerals is of increasing interest for dating geologic processes (Rasbury and Cole 2006; Gerdes and Zeh 2009; Rasbury and Cole 2009; Millonig et al. 2012; Ring and Gerdes 2016). Recently, Burisch et al. (2017) showed that this approach reveals robust formation ages for five-element veins by dating associated gangue minerals. While their primary arsenides were sensitive to isotopic exchange reactions and therefore not suitable for age determination, the present study shows that gangue carbonates give comparable ages as cogenetic multi- and single-mineral isochrone ages including arsenides, sulfarsenides, magnetite, sericite, chlorite, albite and uraninite. Thus, it is possible to unravel a complex and long-lasting history of mineralization, deformation, remobilization and tectonic evolution from the studied samples.

Isochrone ages of cogenetic gangue and ore minerals accumulate four discrete mineralization intervals (Figure 2h), namely:

- T1: Middle Triassic (~243-223 Ma);
- T2: Late Triassic to Middle Jurassic (~220-156 Ma);
- T3: Late Cretaceous to early Miocene (~73-16 Ma); and
- T4: late Miocene to Pliocene (~6.9-2.2 Ma).

The summary of the isochrone ages in Figure 25 illustrates the host rock alteration processes and successive formation of distinct mineral assemblages at these times. According to isochrons 1 and 2, formation of the Fe-Co ores (stage II) occurred during T1 at the Middle Triassic (235.6±6.7 and 233±10 Ma; Figure 2h). Reaction textures indicate that possibly arsenic-rich hydrothermal fluids interacted with preexisting siderite (stage I), host rock biotite and plagioclase. In this case, isochrone 1 reflects the formation of magnetite from siderite together with paragenetic Fe-Ti-oxides, chlorite and quartz as alteration of host rock biotite and hornblende. Where epidote occurs during this stage, rutile is the present Ti-mineral (corresponding for the (Fe)-Ti-oxides). Here, Fe^{3+} was compensated by epidote and not available for the precipitation of Fe^{3+}-Ti-oxides such as pseudorutile. Isochrone 2, however, records the formation ages of ankerite and arsenopyrite combining arsenic-rich fluids with Fe available due to siderite dissolution and Mg and Ca available due to biotite, hornblende and plagioclase alteration. After the Variscan orogeny (Figure 26a), slab-rollback of the Paleo-Tethys and

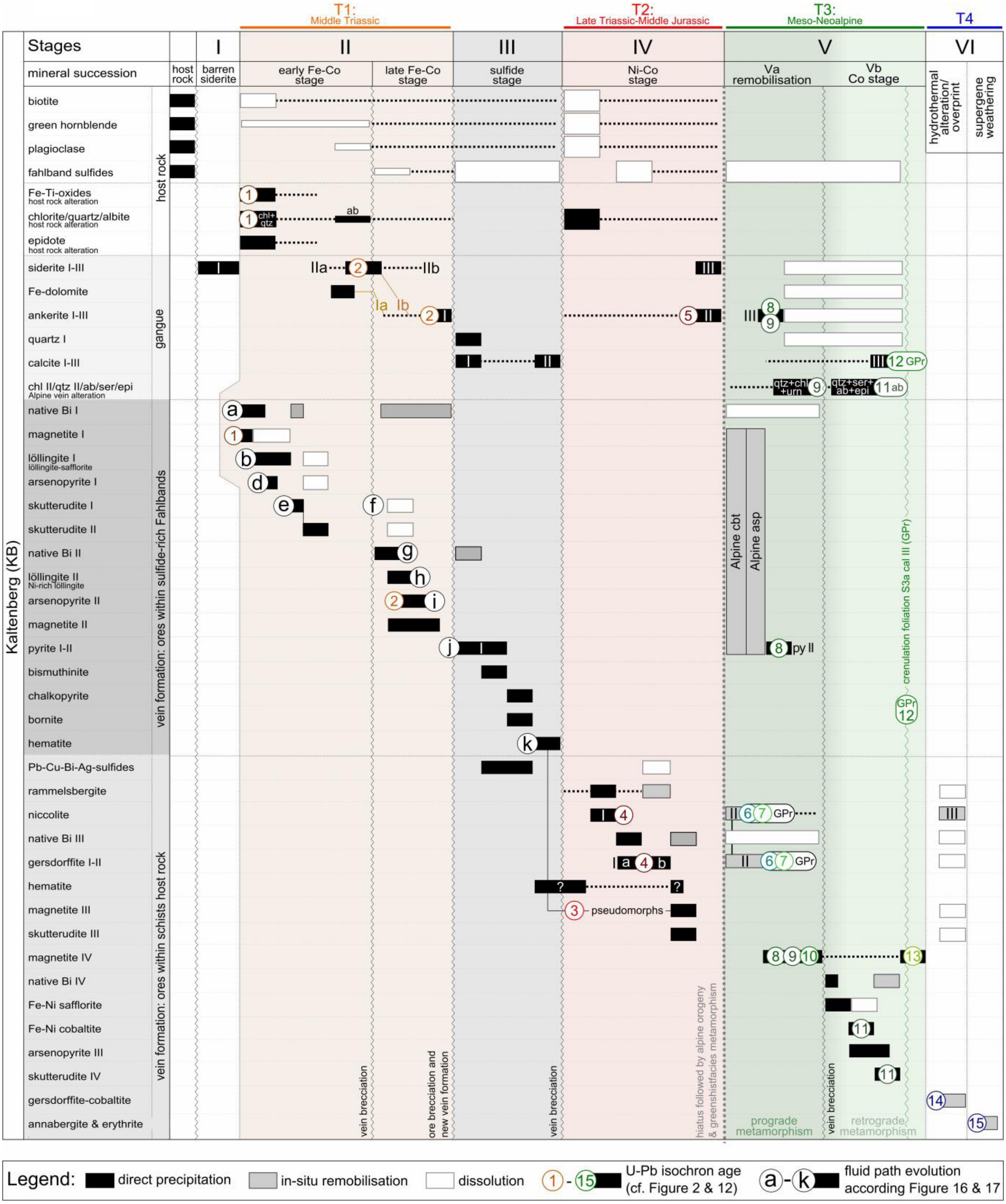

Figure 25: Detailed paragenetic succession at Kaltenberg. Letters a-k correspond to the successive steps during ore formation. Each step is considered in Figures 32-33.

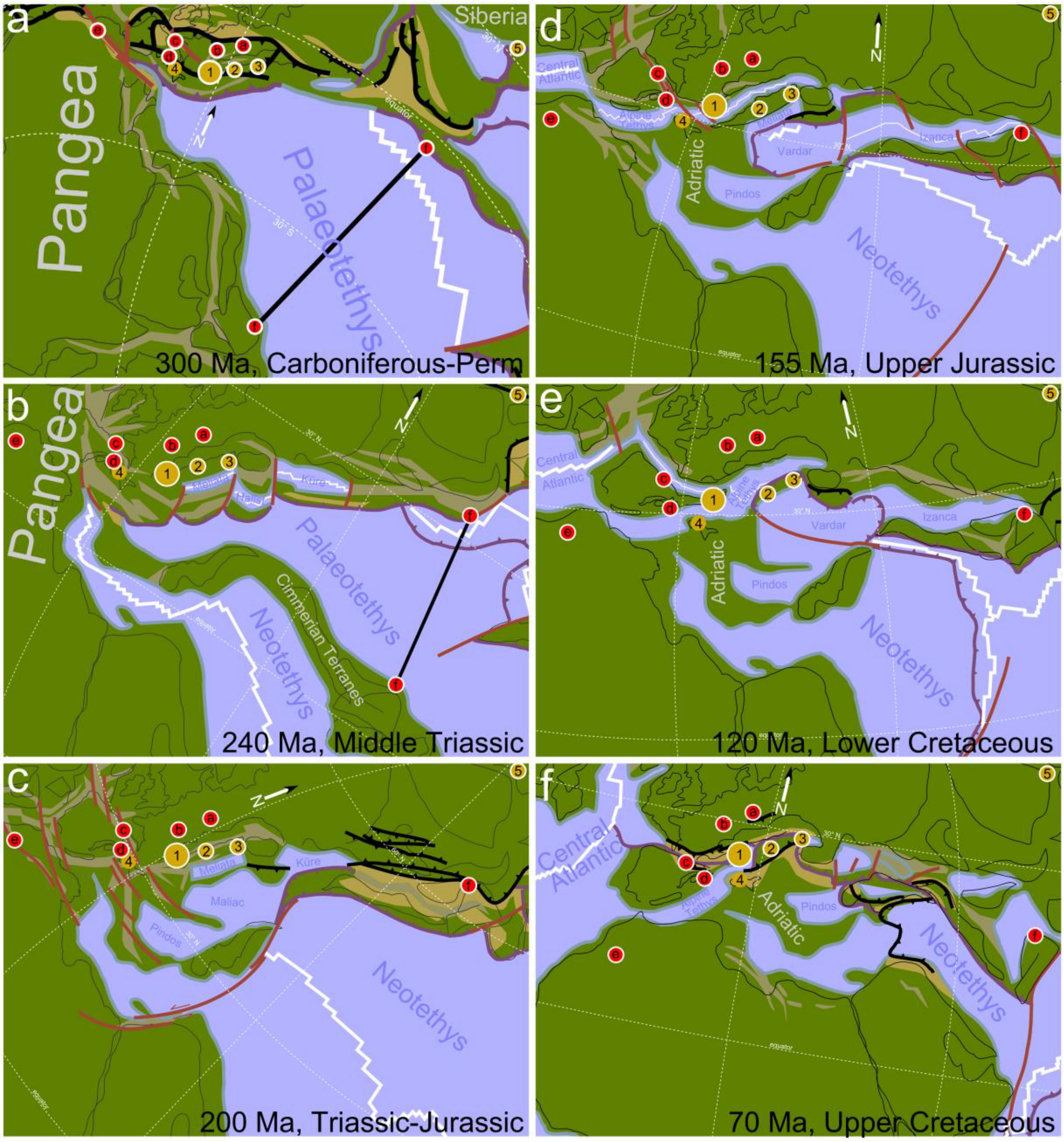

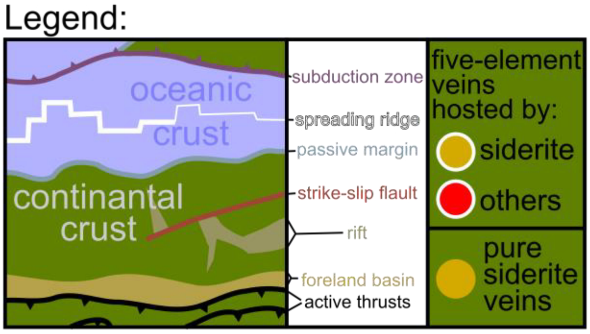

Figure 26: Paleotectonic reconstruction from 300-70 Ma before present. Districts including five-element vein formation are illustrated as circles (hosted by abundant siderite: yellow; no abundant siderite: red). 1: Wester Alps, 2: Niedere Tauern, 3: Western Carpathians, 4: Southern Alps, 5: Altai Mountains, a: Erzgebirge, b: Schwarzwald and Odenwald, c: Pyrenees, d: Sardinia, e: Bou Azzer and f: Anarak.

back-arc spreading initiated the Meliata Ocean rift (Figure 26b-c: 240-200 Ma). This consequently resulted in the ore formation during stage II due to the tectonic collapse and Triassic subsidence of the northern Variscan to Penninic domains (cf. T1 in Figure 2; Ziegler and Stampfli 2001; Stampfli et al. 2002; Stampfli and Borel 2002).

Following the (unfortunately un-datable) sulfide stage III, the Ni-Co ore stage IV formed during the Late Triassic to Middle Jurassic (182±26, 189±31 and 171.3±5.8 Ma; isochrons 3-5; Figure 2h). The primary ore and gangue minerals reflect a common and robust formation age. As illustrated in Figure 26d-e, this probably indicates the stress regime during initial rift structure formation of the Alpine Tethys (Upper Penninic ocean) and Lower Penninic ocean spreading as a far-field effect of the Neo-Tethys slab rollback and Central Atlantic spreading (cf. T2 in Figure 2; Ziegler and Stampfli 2001; Stampfli et al. 2002; Stampfli and Borel 2002).

The tectonic settings (T1 and T2) may have affected subsidence-related exhumation/decompression of the Penninic basement rocks and, thus, may have mobilized fluids according to the model by Staude et al. (2009). Burisch et al. (2017) already linked five-element veins in the Odenwald Variscan basement to the North Atlantic opening at about ~174 Ma. Additionally, other European five-element occurrences show similar Jurassic ages (Romer and Schneider 2010; Staude et al. 2012b). As the Siviez-Mischabel nappe was part of a pre-Alpine, Variscan basement, the tectonic conditions obviously favored the precipitation of five-element veins in Central Europe at that time. Therefore, the breakup of the Alpine Tethys in the Jurassic could have caused a number of other occurrences with similar mineralogies that previously situated along its rift shoulders (Figure 27). Today many of these occurrences can be found either displaced from their original position next to the rift or included into the Pyrenean, Alpine and Carpathian Orogeny. Note that no magmatic activity is known in this time from the SM nappe (Thélin et al. 1993; Sartori et al. 2006). Interestingly, hydrothermal activity and alteration observed from the (Helvetic) Central Aare Granite or the (Northern Penninic) Lengenbach Pb-Zn-As-Tl-Ba-deposit (which are today about 60 and 30 km away from the veins considered here) yield similar ages of 230±8 or 185±17 Ma, respectively (Schaltegger 1990; Knill 1995; Hofmann and Knill 1996). This supports pervasive fluid flow and hydrothermal alteration in both, the circum-Penninic basement rocks (as already suggested by Schaltegger and Gebauer (1999)) and the observed five-element veins in the Turtmanntal and the Val d’Anniviers.

The Alpine ages of T3 show the most complex relations. The isotopic U-Pb signature of magnetite IV shows a large and overlapping trend ranging from Eocene to Lower Miocene ages (~54-16 Ma; isochrons 8, 9, 10 and 13; Figure 2h). Therefore, the magnetite ages remarkably reflect the long lasting tectonic activity during Alpine processes. They cannot, however, be used to distinguish between the remobilization textures during stage Va and formation of the Co ore stage Vb. In addition, the Alpine remobilization assemblage of gersdorffite II, niccolite II, sericite and quartz II

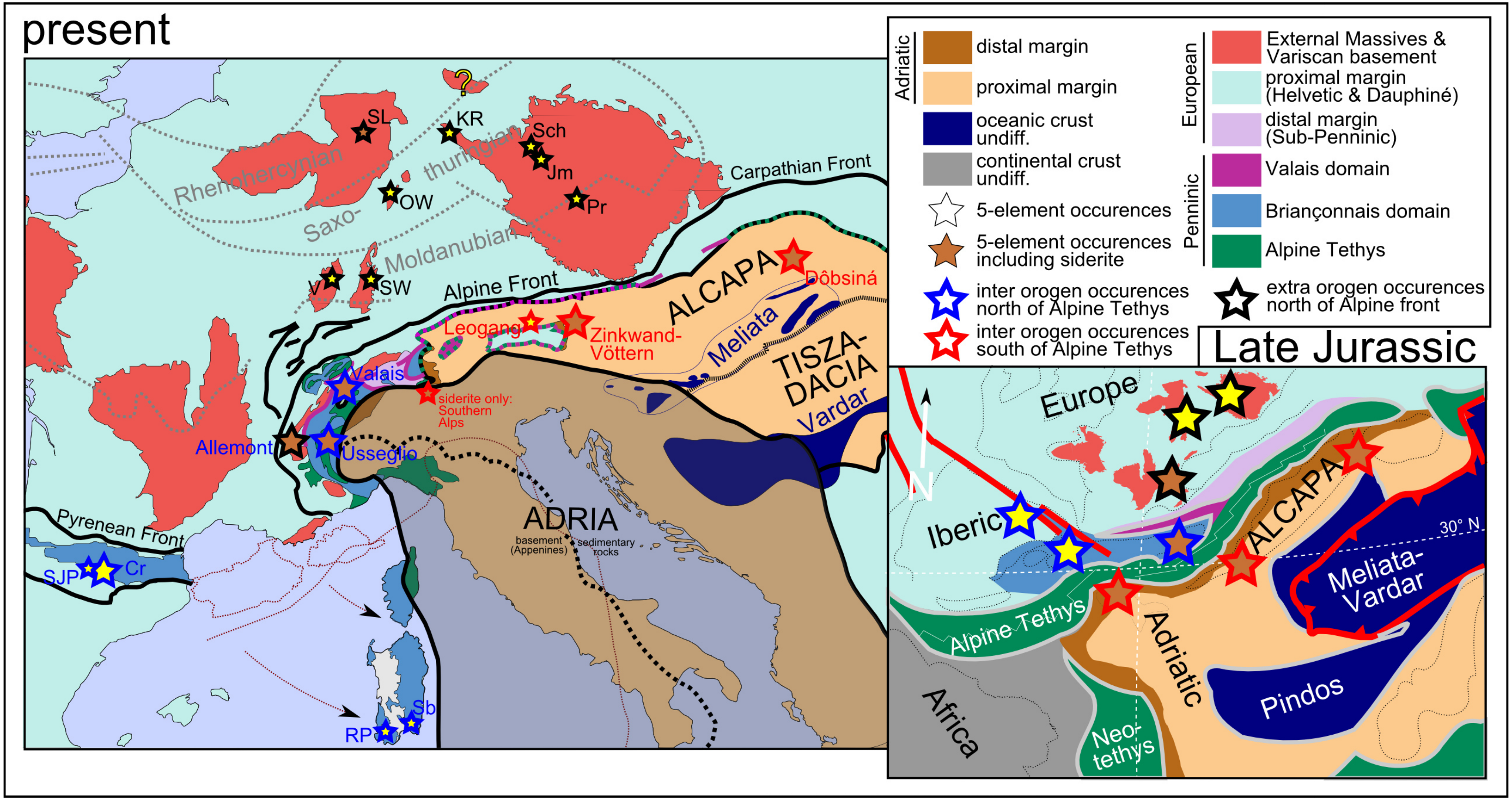

Figure 27: Present day and Late Jurassic Paleotectonic reconstruction after Stampfli et al. (2002) including the todays and former positions of five-element occurrences in Central Europe. During the Late Jurassic the shown occurrences positioned along the Alpine Tethys Rift.

shows either Upper Cretaceous or Middle Eocene ages (isochrons 6 and 7; Figure 2h). As inferred from their ages and structural relationships (they formed prior to or during the foliation S1a; cf. Figure 10c), remobilization of the Triassic to Jurassic deposits occurred at least since the subduction of the Upper Penninic ocean at ~71 Ma and continued until ~45 Ma. Hence, the latter age that corresponds to formation of the S1a foliation at GP predates the S1 foliation of the Siviez-Mischabel Nappe about 4 Ma (cf. muscovite S1 foliation Ar-Ar age: 41-36 Ma; Markley et al. 1998). Consequently, ores affected by the foliation S1a indicate that deformation already happened before those of the muscovite S1 foliation. Including the formation age of Alpine magnetite, ankerite, chlorite and uraninite (isochrone 9), remobilization of the Triassic to Jurassic ores happened as a first-order process by compressive overthrusting, tectonic nappe formation and metamorphism. These processes were related to the subduction of the Upper and Lower Penninic oceans and the collision of the Middle Penninic microcontinent with the European margin and its under-thrusting to the Adriatic plate (Figure 2 and 26f, ~75-30 Ma; cf. Escher et al. 1997). Note, that remobilization during this compressive phase was restricted to in-situ replacement textures of T1 and T2 ores, favored along ductile deformation structures such as the selvages between the veins and host rocks.

In contrast, the Alpine five-element Co stage Vb (isochrone 11) and the crenulation foliation of calcite along S3a (isochrone 12) show the change from a compressive to a transtensional strike slip regime during the Late Oligocene to early Miocene (Figure 2e-h, D1/D2 to D3). Textural observations of this stage show dendritic native Bi, safflorite, cobaltite and skutterudite in albite and quartz gangue, which crosscut the former carbonate veins in open space fillings. The extensional component reported by Sartori (1990) enhanced rock permeability and resulting fluid mobilization promoted the Neoalpine five-element stage. Necessary movements followed as dextral transtensional strike-slip, backfolding and lateral escape tectonics due to movements of the Insubric Indenter or additionally tangential stretching and bending of the Western Alpine arc by the progressing counterclockwise West Mediterranean subduction rollback (Mancktelow 1985; Maurer et al. 1997; Rosenbaum et al. 2002; Sue and Tricart 2002; Champagnac et al. 2006; Hinsbergen et al. 2014). Isochrons 11-13 (28.2±1.1 to 21.4±5.3 Ma) agree well with ages documented for late alpine extension with an onset of the ductile Simplon shear zone and begin of brittle extension between ~32-18 Ma (Steck 2008). Progressive deformation is also known form strike-slip deformation from other regions in the Alps (Katschberg-, Brenner-, Turbe- and Simplon Fault; <32 to <28 Ma) or the adjacent European Cenozoic Rift System (Limagne-, Bresse-Rhone-, Oberrhein- and Bonndorf-Bodensee Graben; 34-18 Ma) as a result of the West Mediterranean subduction rollback and development of the Western Alpine Arc (Bergerat 1987; Nievergelt et al. 1996; Rosenbaum et al. 2002; Schumacher 2002; Glodny et al. 2008; Ring and Gerdes 2016).

With respect to peak metamorphism in the Siviez-Mischabel nappe (~38 Ma; Escher et al. 1997), the ages of the ore remobilization during stage Va must be considered as prograde, those of the following stage Vb as retrograde processes during the Alpine orogenic cycle. Retrograde quartz II and calcite III must have formed after chlorite formation (isochrone 9: 39.94±0.86 Ma; quartz II crosscuts chlorite) but prior to the crenulation foliation S3a within calcite III (isochrone 12: 27.3±1.8 Ma; calcite III replaced quartz II). The FI temperatures of both mineral assemblages (cf. chapter 5.3) also preserve this retrograde process, accompanied by uplift and cooling.

During T4, formation of gersdorffite-cobaltite (hydrothermal overprint; isochrone 14, 5.8±1.1 Ma, Figure 2h) is related to low temperature hydrothermal fluids (<120-70°C; apatite fission-track: 7.2-13.4 Ma; Seward and Mancktelow 1994), possibly mobilized by post-obductional processes and the Rhone-Simplon fault. The intense overprint of the earlier ores by late gersdorffite-cobaltite solid solutions affected earlier ages (Figure 9g). A primary age information of the Ni-Co stage IV, however, was retained in regions where chlorite enclosed this assemblage entirely and protected it from the influence of late gersdorffite-cobaltite precipitation (Figure 9n). As supergene oxidation product of the Ni-arsenides/-sulfarsenides, annabergite shows ages similarly correlating to the Rhone-Simplon fault system (supergene weathering; isochrone 15, 2.46±0.23 Ma).

8.1.2 Mineralogical, chemical and structural evolution

The chemical characterization, deformation textures and related U-Pb ages, suggest that all investigated mineralizations have a pre-Alpine origin (T1 and T2) and were in parts remobilized during the Alpine orogeny (T3). The following chapters will discuss the correlation of the occurrences found at PI, KB, GP and CI.

8.1.2.1 Correlation of mineralogical and chemical aspects

Similarities between KB, PI, GPg and GPr are the chemical evolution of the gangue and ore phases (Figure 18), and their similar/identical mineralogical and textural age sucessions (cf. Figure 25 and Figure 10). The correlation box at the bottom of Figure 8 additionally summarizes a brief overview of these mineralogical and textural.

The first similarity among the different deposits is the relationship between the different carbonates (ankerite I–III, siderite I–III and Fe-dolomite). The three ankerite stages at KB formed during T1, T2 and T3 and are distinguished by their Mg-Fe-Mn contents (cf. Figure 2h, Figure 8 and Figure 17c). Ankerites at PI, GPr and GPg only represent a subset of the KB stages and, together with Fe-dolomite, show different absolute Mg-Fe-Mn concentrations. However, they show the same Fe and Mn enrichment of ankerite I relative to Fe-dolomite and the evolution of ankerite II to increasing Mn and decreasing Fe relative to ankerite I (cf. Figure 17c and Figure A2).

The second connection is the compositional evolution of the tri-, di- and sulfarsenides with respect of their Fe-Co-Ni signatures. Figure 18a compares ores precipitated during the Fe-Co stage II (T1). It is obvious that arsenopyrites and löllingites developed from Co-rich to more Fe-rich compositions (early Fe-Co stage II; arsenopyrite I, löllingite I); later, Ni and Co increased again (late Fe-Co stage II; arsenopyrite II, löllingite II). In addition, skutterudites show comparable Fe-Co-Ni ratios with decreasing Co but constant Fe/Ni ratios from skutterudite I to skutterudite II. At KB and PI both skutterudites can be diversified since skutterudite II displaces earlier löllingite I and arsenopyrite I and therefore adopt their Fe contents. At GP, however, no displacement of previous löllingite and arsenopyrite happened and therefore skutterudites represent exclusively Co-dominated compositions.

In the transition to the Ni-Co stage IV ores are even higher in Ni (cf. Figures 18b-c). Gersdorffites Ia and Ib show similar Fe-Co-Ni signatures to krutovite I and II and especially high arsenic contents of the sulfarsenides (cf. Figure 19c-e). Similar to krutovites, arsenic in gersdorffite I is particularly high, ranging from 1.8-1.3 As/(As+S). Early aggregates with higher As are Ni-rich (rammelsbergite, gersdorffite Ia, krutovite I) and were overgrown or replaced by As-poorer and Fe-Co-richer compositions (gersdorffite Ib, krutovite II). Ni-rich fluids may either infiltrated the Fe-Co stage II ores, which affected the formation of symplectic krutovite I and krutovite II veinlets in GPg and PI or precipitated the succession from niccolite I over rammelsbergite to gersdorffite I at KB and GPr. According to the U-Pb ages, this process started during the Jurassic (stage IV) and possibly happened again during the remobilization (stage Va).

During the in-situ ore replacement, chemical Fe-Co-Ni compositions governed by the compositions of the primary ores. For example, gersdorffite II shows Ni-rich compositions while replacing the Ni-dominated ores of stage IV, whereas Alpine cobaltite and arsenopyrite are Fe-Co dominated as they replace the Fe-Co ores of stage II (Figure 18d). All remobilized ores, however, show a tendency towards more Fe- and Co-rich compositions (Figures 18d-f). As illustrated in Figure 19c-e, these Fe-Co-dominated sulfarsenides of the Alpine stage Va (T3 gersdorffite II, krut III;) reach higher sulfur concentrations than those of the Ni-Co stage IV (T2 gersdorffite I, krut I, krut II). This may relate to an enhanced mobilization of sulfur from the sulfide-rich fahlbands during the onset of the Alpine deformation (cf. chapter 7.4.2). The development towards more ternary Fe-Co-Ni compositions can be explained by additional input of Fe from the Fahlband pyrites as well as the equilibration and remobilization of all previously precipitated ores.

Obviously, the overall transition and temporal evolution of the hydrothermal system evolved from a (i) primary Fe-Co dominance towards (ii) its overprint by Ni-rich chemistries and (iii) successive equilibration during Alpine metamorphism to ternary Fe-Co-Ni compositions. This relationship and successive change in chemistries is most visible at the spatially coherent but mineralogically and texturally different ore types of zones A-E at PI (cf. Figure 6a-j and Figure A5).

In addition to this and as described above, skutterudites of the Fe-Co stage at KB and PI show comparable Fe-Co-Ni ratios with decreasing Co but constant Fe:Ni ratios of 1:1 from skutterudite I to II. Skutterudites from GPg and skutterudite IV from PI show such persistent Fe/Ni ratios as well, but rather do not gain comparable high Fe and Ni concentrations compared to KB and PI. Revealing primarily equal enriched Fe and Ni contents, however, a subsequent Co increase resulted either due to the exsolution of symplectic krut I at GPg during stage IV (Figure 18c) or due to an additional dissolution and reprecipitation as skutterudite IV and co-precipitation of gersdorffite II and löllingite III at PI (Figure 18e). According to the loss of Ni, what obviously can be projected from skutterudite II to the Ni component, remnant skutterudite should effectively be enhanced in both, Fe and Co. Similarly, the displacement of arsenopyrite and löllingite by skutterudite should lead to Fe:Ni ratios of >1:1. This, however, does not coincide with the chemistries from the studied skutterudites. Nonetheless, this variation of Co by a fixed Fe:Ni ratio of 1:1 are similar to natural skutterudites observed by Gervilla et al. (2012) from Bou Azzer and the solid-solution for synthetic skutterudite observed by Roseboom (1962). To maintain the skutterudite structure, total cations of Co-Fe-Ni have to be trivalent and all six, non-bonded d-electrons must achieve complete spin-pairing in their t_2g orbitals. Since Fe^{3+} or Ni^{3+} cannot fully spin-pair its five or seven non-bonded d-electrons, a coupled replacement of two Co^{3+} by one Fe^{2+} and one Ni^{4+} accompanies changing Co concentrations to complement a complete spin-pairing in their t_2g orbitals and lead to constant Fe:Ni ratio of 1:1 (Nickel 1970; Schumer et al. 2017).

8.1.2.2 Timing and effects of deformation and metamorphism

Due to their boudinage structures and folds along D2 structures, Schafer (1996) assigned the formation of the carbonate veins at KB as pre- to syn-D1 or even as pre-Alpine (Figure 4a). In contrast, Sartori and Della Valle (1986) suggested that the PI vein emplaced post-D2 to syn-D3, as the veins are discordant to S1 and lack folds and boudinage structures (Figure 4b). Own field observations at PI, however, suggest a pre-D1 emplacement, as the NS-striking vein shows an intensive boudinage along S2 and the ores are brecciated along the S1 and S2 direction (Figure 4b and Figure 6a, d). For the vein at GP, descriptions of Huttenlocher (1925) again appear to reveal a post-D1/-D2 emplacement as the vein crosscuts the host rocks discordant to S1. This foliation, however, turns into the S-C’ foliations S1a and S3a contoured alongside the vein boundary (Figure 4c). Unfortunately, Sartori (1990) did not observe any D2 or D3 deformation structures in the host rocks at GP (cf. Figure 3). These relative age relationships are not comparable between the different occurrences and it is not possible to reveal which tectonic and metamorphic events affected the primary mineralogy at each time.

U-Pb ages of the stage Va remobilization at GP, however, firstly occurred as the neoformation of gersdorffite II and niccolite II and later in their deformation along the S1a foliation (Figure 2h isochrons 6 and 7). Therefore, ore deformation and remobilization at GP happened between ~70 and ~45 Ma, which represents the beginning nappe formation during Eoalpine and Mesoalpine collisional tectonics (Escher et al. 1997). In analogy to KB, the formation of krutovite, gersdorffite I and niccolite I should predate both ages and it is likely that the primary Fe-Co stage II and Ni-Co stage IV at GP and PI also developed during the Jurassic (cf. Figure 2h). Hence, our new age data are in agreement with the structural observations. In addition, Pb-Pb model ages of different ores from the SM nappe imply a pre-Alpine formation between 300 and 150 Ma (Zingg 1989). These investigations include most fahlbands, carbonate-hosted galena veins (not investigated in the present contribution) and the five-element veins at KB. Vice versa, the remobilization of the primary mineralogy during stage Va at PI and KB most likely correspond to the ages represented by isochrons 6 and 7 found at GP (cf. Figure 18d-f: Alpine cobaltite and arsenopyrite, gersdorffite II-III, löllingite III and skutterudite IV). According to tectonometamorphic conditions at this time (Seward and Mancktelow 1994; Escher et al. 1997; Markley et al. 1998; Steck 2008), prograde metamorphism during continent-continent collision affected the remobilization of Triassic and Jurassic ores to a great extend (cf. Figure 2h, Figure 25 and Figure 10). Since the emplacement of the Siviez-Mischabel Nappe succeeded as a symmetrically developed recumbent fold, remobilization effects reported in chapter 6.8 attained a higher grade at regions near to the two different shear zones of the inverted and normal limbs (cf. Figures 1b and 3a). As consequence, the occurrence at CI shows the highest remobilization and deformation grades. It is likely that most primary ores were dissolved during Alpine processes and exclusively Alpine arsenopyrite precipitated within mylonitic quartz. At PI, remobilization and deformation mostly happened due to the ore and gangue brecciation, recrystallization of skutterudite, disruption of tetrahedrite and krutovite veinlets and most obviously from the distorted symplectic intergrowth. At GP, which resides within the central parts, virtually no deformation happened to the ores as the symplectic intergrowth and the continuation of the veinlets stayed unaffected. This increasing deformation and remobilization is also visible from changing quartz grain fabrics between the different occurrences (Figure 15).

The later developed alongside crenulation foliation S3a that concerned foliation S1a, calcite III, quartz II, sericite, gersdorffite II and niccolite II can be interpreted as consequence of the D3 deformation, since the U-Pb age of this C′ foliation with ~27 Ma directly corresponds to the D3 deformation in the SM nappe (cf. Figure 2h; isochrone 12). At this time, tectonometamorphic conditions changed from a compressive continent-continent collision and prograde metamorphism towards dextral strike slip tectonics and lateral extrusion of the Western Alps accompanied by retrograde metamorphism. During this time, accommodated extension favored open fractures, which filled by metamorphic fluid in equilibrium to pristine ore, gangue and host rocks mineralogies. Consequently, and unlike to the in-situ remobilization during stage Va, the euhedral crystals of the Co stage Va ores precipitated within open veins from this retrograde fluid (Figure 2h; isochrone 11).

Besides these prograde and retrograde metamorphic effects, isochrons 14 and 15 document processes of hydrothermal alteration and supergene weathering of the ores (Figure 2h). The tectonometamorphic conditions of these ages correspond to brittle deformation during post-Alpine orogenic collapse (Steck 2008). This transition from ductile to brittle deformation is visible from expected temperatures and textural relationships between dolomite twinning and its successive recovery along native Bi trails (Figure 15a). Twinning of dolomite exclusively forms at temperatures >300°C (Barber and Wenk 2001), which represents temperatures during ductile deformation at an approximate age of greenschist facies peak metamorphism in the Siviez-Mischabel Nappe (~38 Ma; Escher et al. 1997). Temperatures of Alpine quartz II easily exceeded those needed for dolomite twinning (Table 5: 430°C). As a result, dolomites show a recovery of the pressure twins along the trails of droplet-like native Bi aggregates what indicates some kind of annealing effects after its twinning. The temperature of native Bi emplacement and associated annealing, however, cannot be derived from heterogeneous solidification temperatures of its common low-pressure polymorph Bi(I) at ~267±3°C (retrograde metamorphism at ~130 MPa) [cf. Bridgman (1935) for Bi phase nomenclature]. Feuerbacher (1989) and Oxtoby (1992) showed that metastable solidification of metals by homogeneous nucleation is more important to form droplet-like aggregates than a heterogeneous formation. Slow cooling of dispersed, fine liquid Bi droplets within fluids leads to undercooling of the liquid-solid transition (Yoon et al. 1986). Experiments showed that first nucleation of the metastable high-pressure polymorph Bi(II) as 1-20 µm-sized droplets occurs at 175±5°C through cooling (130 MPa). Rather than the nucleation of a euhedral low-pressure polymorph Bi(I) at temperatures of ~267±3°C (130 MPa) this represents textures and conditions which can be attributed to the studied samples. Native Bi droplets along trails therefore precipitated during retrograde metamorphism and cooling below 175°C. The precipitation as the high-pressure polymorph Bi(II) additionally supports the fact that no congelifraction happened during the solidification of native Bi droplets. Otherwise, formation of Bi(I) would have formed radial cracks within the host minerals due to volume expansion during solidification from its liquid phase. In order to this, dolomites developed pressure twins during prograde metamorphism (upper greenschist facies conditions), later cracked and sealed with twin-free Fe-dolomite including native Bi droplets during retrograde metamorphism (175°C). According to cooling rates of the Siviez-Mischabel Nappe (Markley et al. 1998), this coagulation of native Bi happened at a time of ~17-18 Ma what coincides to the brittle-ductile transition observed by Steck (2008) at an age of ~18 Ma (cf. Figure2h). Most native Bi disappeared from the arsenides and today resides as large quantities either at the trails or as relictic sub µm-sized fringes along the arsenide grain boundaries. Changing temperature and plasticity expect the following processes of native Bi transport. Firstly, metamorphic heating affected melting and mobilization of primary native Bi aggregates. Later intensive deformation "squeezed" the ores and consequently native Bi was pressed out from its original position within the arsenides. Re-precipitation finally occurred during slow, retrograde cooling and along brittle fractured trails within the gangue minerals.

According to the new U-Pb ages at KB and GP and the observation on the native Bi trails, the following scenario describes the Triassic to post-Alpine tectonics:

1. Primary and pre-Alpine ore formation due to rift-induced extensive tectonics during the Meliata and Alpine Tethys Rifts, which represents the cause for the first accumulation of Bi-Co-Ni-Fe-As-S-(U) (Fe-Co stage II and Ni-Co stage IV)
2. Syn-Alpine in-situ remobilization and deformation during European-Adriatic continent-continent collision (stage Va; i.e. prograde metamorphism)
3. Late-Alpine processes causing formation of new veinlets including five-element mineralogies and native Bi remobilization due to lateral extrusion of the Western Alpine arc (stage Vb; i.e. retrograde metamorphism)
4. Post-Alpine processes leading to hydrothermal alteration and supergene weathering during brittle extension, orogenic collapse and erosion of the Alps.

8.2 The fluids: physico-chemical conditions, source and evolution

In order to reconstruct the source of the ore forming fluids and their evolution from the Middle Triassic (T1: Fe-Co stage II) to Early Miocene (T3: Alpine stage V) processes, FI temperatures and chemistries of carbonates and quartz as well as isotope signatures of the carbonates were used from the successive gangue sections. These reconstructions restrict on observations at Grand Praz, Kaltenberg and Pipji, since primary gangue aggregates at Collioux Inférieur did not persisted Alpine deformation and silification.

8.2.1 Pressure and temperature conditions

Total overburden in the Triassic (T1) and Jurassic (T2) was calculated according to the sedimentary thickness reconstructed by Wissing and Pfiffner (2003) plus today's vertical distance of the deposits to the basement-cover unconformity. Since this is a Cretaceous reconstruction, basement stretch during Jurassic-Cretaceous rifting was backcalculated using a maximum stretching factor of 1.1 (Stampfli et al. 1998). Thinning or thickening during Alpine tectonics are not considered due to lack of information. Therefore, the deposits GP, KB and PI originally located approximately 0.6-2.4 km and 0.8-2.6 km below ancient sea floor levels and water columns can be estimated to 10 m and up to 500 m during T1 and T2, respectively (Stampfli et al. 1998). In order to perform pressure correction for the homogenization temperatures T_h during extensional tectonic settings, it is reasonable to assume initial hydrostatic fluid pressures, which later became lithostatic due to sealing of the fluid paths (Munz et al. 2002). Therefore, hydrostatic pressures were expected for the euhedral and initial gangue carbonates Fe-dolomite and siderite III; lithostatic conditions for ankerites, and calcites, which replace previous gangue minerals and sealed the remaining cavities. Pressure corrections for the formation temperatures were estimated considering variable sedimentary basin thickness and differences in depth (cf. Figure 28). Estimated minimum-maximum pressures (hydrostatic/lithostatic) during the Fe-Co stage II (T1) at GP, KB and PI were 24-25/61-64 MPa, 7-10/17-26 MPa and 12-13/31-34 MPa MPa, respectively. During the Ni-Co stage IV (T2), a minimum-maximum pressure of 14-18 MPa can be assumed at KB (hydrostatic). According to their relative ages (~40-30 Ma), lithostatic pressures of ~105-160 MPa are assumed for alpine calcite III and quartz II (T3) from inferred depths of 4-6 km (Stampfli et al. 1998). For correction of formation temperature calculations, used in Table 5 and Figure 29a, the maximum pressure estimates were used ($T_{P\text{-max.corr}}$). Furtheron, only the corrected temperatures are used in the discussion.

Fluid inclusions in the first precipitating carbonate (Fe-dolomite) following the ore formation during the Fe-Co stage II (T1) shows mean pressure-corrected formation temperatures at KB, PI and GP of 225°C, 245°C and 290°C, respectively (Figure 29a). Since the textural and mineralogical features

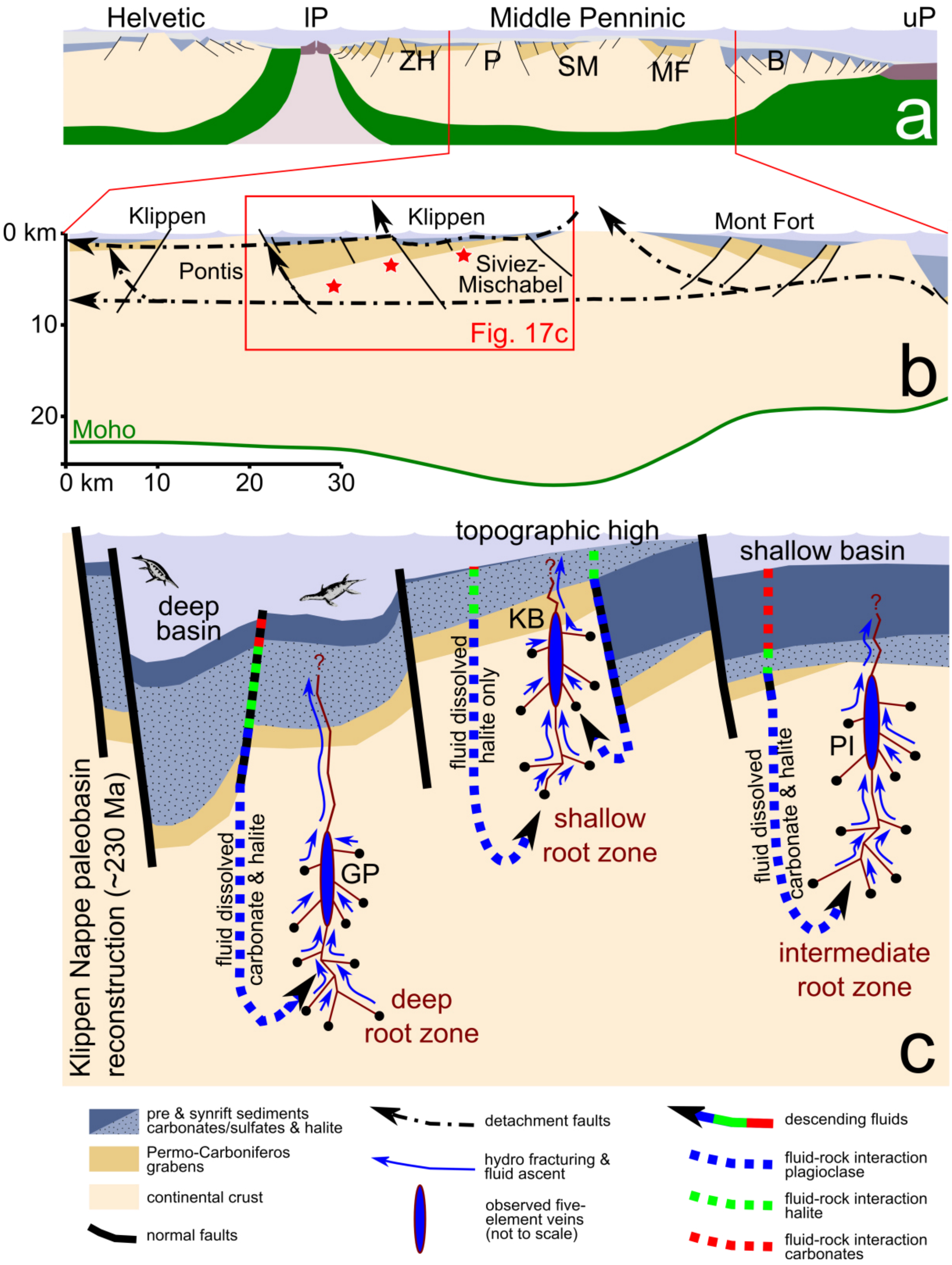

Figure 28: (a)-(b) Middle Triassic paleotectonic reconstruction of the Middle Penninic micro-continent and its present day Alpine nappe stratification after Stampfli et al. (1998). LP: Lower Penninic, UP: Upper Penninic, ZH: Zone Houillière, P: Pontis, SM: Siviez-Mischabel, MF: Mont Fort, B: Brèche. (c) Paleobasin reconstruction of the Klippen Nappe after Wissing and Pfiffner (2003), which overlaid the Siviez-Mischabel Nappe at the Middle Triassic. Descending fluids penetrated carbonates and evaporites at Grand Praz and Pipji, whereas carbonates missed above Kaltenberg due to evolved fault systems and topographic height. At Kaltenberg, fluid descent may be attributed by the nearby fault system.

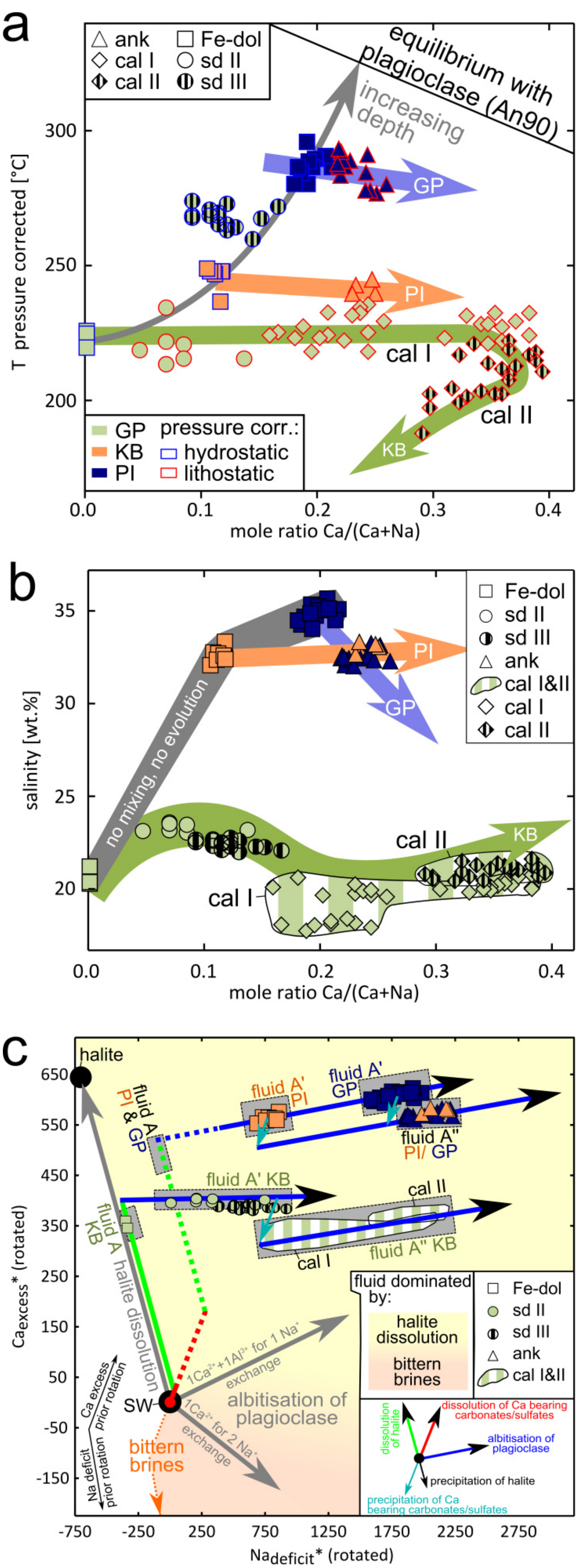

Figure 29: (a) Fluid data as T_h vs molar Ca/(Ca+Na) ratio and (b) salinity (wt.% NaCl+$CaCl_2$) vs molar Ca/(Ca+Na) ratio. (c) Presentation of the Ca_{excess} vs $Na_{deficit}$ plot calculated by formula 1 and 2 in Davisson and Criss (1996). For a better resolution, Ca_{excess} and $Na_{deficit}$ were rotated using $Na_{deficit}$*=$Na_{deficit}$·cos(56.3°)+Ca_{excess}·sin(56.3°) and Ca_{excess}*=Ca_{excess}·cos(56.3°)-$Na_{deficit}$·sin(56.3°). Original direction of the Ca_{excess}- and $Na_{deficit}$-axis are shown in the lower left. Black dots indicate seawater (SW) and halite compositions, orange arrow indicates the evolution during evaporation towards bittern brines. Lower right insect illustrates other fluid evolution directions during fluid-mineral interactions and mineral precipitations.

of the different deposits are similar, apparently temperature did not control ore precipitation. Simply mixing a hot basinal and cool sedimentary brine in variable amounts to explain the different temperatures is unlikely due to the lack of a straight mixing line between the different Fe-dolomite generations in temperature and salinity vs Ca/(Ca+Na) diagrams (Figure 29a and b). Therefore, differences in pressure-corrected temperatures during primary ore formation (Fe-dolomite, Fe-Co stage II) need a more detailed consideration in the light of paleogeographic reconstruction and observed salinities and Ca/(Ca+Na) ratios (cf. chapter 8.2.2). Interestingly, gangue formation temperatures at GP exceeded the melting point of native Bi. This may explain the lack of native Bi at GP.

If a primary hydrostatic fluid flow path was sealed during the formation of siderite II (Fe-Co stage II) and calcite I (early sulfide stage III) at KB, the hydrothermal fluids resided at similar temperatures. Towards late calcite II, however, fluids slightly cooled during successive carbonate, pyrite and chalcopyrite precipitation (mean temperatures calcite I: 230°C; calcite II: 210°C). The transition from Fe-dolomite to ankerite I at PI and GP similarly shows negligible cooling (calculated <5°C, hence within uncertainty) of the initial fluids (ankerite I mean temperatures PI: 240°C; GP: 285°C). Fluid inclusions trapped during the Ni-Co stage IV (T2; siderite III: 270°C), however, reached higher temperatures than those during the previous stages II and III (Figure 29a). Based on comparable salinities and Ca/(Ca+Na) ratios between siderite II and siderite III, similar fluid sources can be assumed for the formation of Fe-Co stage II and Ni-Co stage IV.

Based on the formation temperatures and the stratigraphic position of the three deposits, the variations in fluid composition during precipitation were probably caused by the different depth of the root zones and the resulting downward flux distances of the fluids (Figure 28). Greater depth resulted in higher temperatures of the fluids and longer percolation distances allowing for stronger interaction with the surrounding rocks. In case of plagioclase albitisation reactions, the Ca and Na signature of the FIs at KB, PI and GP also documents their different depths of formation (cf. chapter 8.2.2). This temperature effect is best preserved in the initial carbonate stages (Fe-dolomite) (grey arrow in Figure 29a). As PI effectively resides at similar depth as KB, not only the stratigraphic position of the deposit, but also additional fluid paths such as normal faults control the migration (and thereby, the reaction) time of a fluid. Indeed, the normal fault illustrated in Figure 28 next to KB is no interpretation, but can be found in the field today (Figure 3) and also appears in the detailed reconstructions of the Klippen nappe on top of the SM nappe (Wissing and Pfiffner 2002; Wissing and Pfiffner 2003).

Fluid inclusion compositions in the Alpine quartz II and calcite III (T3; stage Vb) indicate complex mixing processes of different metamorphic or sedimentary fluids (cf. Appendix: Figure A3). If lithostatic pressures of ~105-160 MPa are assumed from inferred depths of 4-6 km (Stampfli et al.

1998), formation temperatures of Alpine quartz II and calcite III (430-380°C and 340-260°C, respectively) and their relative ages (~40-30 Ma) fit well to the retrograde cooling temperatures and ages compiled by Markley et al. (1998) (~440-240°C from 40-30 Ma). This again indicates the retrograde metamorphism during stage Vb whereas ore remobilization during stage Va was related to prograde metamorphism.

8.2.2 Fluid source and evolution by fluid-rock interactions

During stage II ore precipitation and the successive transition to the sulfide stage III, constant temperatures in the paragenetic sequence can be assumed from Fe-dolomite to ankerite I (GP and PI) and from Fe-dolomite over siderite II to calcite I (KB; Figure 29a). This is accompanied by an increase of the Ca/(Ca+Na) ratios, although absolute salinity does not show any systematic evolution (Figure 29b). This does not exclude interaction of multi component systems, but simple mixing of two fluid endmembers (with different temperatures and Na-Ca-Cl compositions) or simple cooling of the fluids do not constrain fluid evolution and ore precipitation of the investigated occurrences at Grand Praz, Kaltenberg and Pipji. Aspects in following chapters indicate that fluid mixing was not a plausible process for fluid evolution and ore formation in this hydrothermal system. Rather than these processes, Ca_{excess} vs $Na_{deficit}$ correlations (chapter 8.2.2.1) and C-O isotope signatures (chapter 8.2.2.2) reveal that fluids from a single source equilibrated to diversely composed cover rock lithologies during fluid descent and successively interacted with preexisting siderite veins and adjacent basement rocks.

8.2.2.1 The Ca_{excess} vs $Na_{deficit}$: primary source and evolution during fluid descent

While large quantities of Ca-bearing carbonates are precipitated, a continuous increase of the Ca/(Ca+Na) ratios implies a constant influx of calcium or a concomitant depletion of sodium during precipitation. To distinguish different fluid-rock-interactions such as albitisation of plagioclase, halite, Ca-sulfate/-carbonate precipitation or dissolution, the approach of the Ca_{excess} vs $Na_{deficit}$ was used. This systematic was introduced by Davisson and Criss (1996) and applied to basinal fluid signatures. Calculations therein normalize molar Ca and Na values to seawater composition; different slopes in the Ca_{excess} vs $Na_{deficit}$ diagrams then indicate different seawater-rock-interactions and evaporation sequences fluid signatures. Figure 29c indicates a fluid evolution by carbonate, sulfate and halite dissolution and different albitisation reactions of plagioclase, either exchanging one Ca+Al of plagioclase for one Na+Si [$\Delta Ca_{excess}/\Delta Na_{deficit}=2$] (Merino 1975) or simply one Ca for two Na [$\Delta Ca_{excess}/\Delta Na_{deficit}=1$] (Helgeson 1974). Note that data were rotated for better representation and expressed as $Ca_{excess}*$ and $Na_{deficit}*$ (cf. caption Figure 29). All of the observed FIAs plot on individual but straight correlation lines (Figure 29c) and range from 1.4-1.72 $\Delta Ca_{excess}/\Delta Na_{deficit}$ (Table 5), indicating a strong effect of plagioclase alteration in all stages of fluid evolution combining both above mentioned exchange reactions. Again, the very first gangue precipitates of the Fe-Co stage II do not lie on a single correlation line, excluding simple mixing processes or a single fluid batch to be responsible for the fluid compositions of all three deposits (Fe-dolomites; Figure 29c). Therefore, different fluid paths and histories can be expected for the hydrothermal systems at PI and GP compared to KB.

To explain the controlling factors for the different fluid signatures trapped by Fe-dolomite using the hydrothermal fluid flow model of Bons et al. (2014), one can consider the locations of GP, KB and PI in relation to the paleotectonic setting of the SM basement and the overlying sedimentary paleobasins of the Klippen Nappe during the Fe-Co stage II (Figure 28a-c). At that time, half graben-induced topography resulted in thickness variations of the pre-/synrift carbonates; a topographic high around KB probably resulted in less evolved carbonate platforms (Wissing and Pfiffner 2002; Wissing and Pfiffner 2003). In such settings, high salinity brines form du to mineral hydration reactions in the basement (Gleeson et al. 2003; Stober and Bucher 2004; Bucher and Stober 2010). These desiccation processes at depth cause continuing descent of chemically evolving fluids (Bons and Gomez-Rivas 2013). However, it seems unlikely that desiccation processes alone (i.e., passive Cl enrichment by hydration reactions) caused the high salinity populations with > 23 wt.% (Figure 29b), since highly saline fluids >18 wt.% require external Cl sources (Burisch et al. 2016). Observed Ca_{excess}*-$Na_{deficit}$* values do not involve any signatures within the range between bittern brines and fluid-plagioclase interactions (Figure 29c: orange colored region). This excludes the involvement of modified bittern brines, which are typical fluid sources in many upper crustal rocks (Bottomley et al. 1994; Gleeson and Yardley 2002; Bejaoui et al. 2014; Bons et al. 2014; Walter et al. 2016).

The Ca_{excess}*-$Na_{deficit}$* signatures, salinities, temperatures and S-isotopes, propose the following, general two step fluid migration scenario (Figure 28c and 29c):

1. Sedimentary brines evolved during carbonate, sulfate and halite dissolution within the 0.3-1.3 km thick cover rocks (carbonates above evaporates).
2. Fluids descended (i.e., were sucked) into the basement where additional desiccation and plagioclase albitisation happened at 0.6-1.2 km (KB), 1.1-1.3 (PI) and 2.2-2.6 km (GP) depth. This further increased salinities and Ca_{excess}*-$Na_{deficit}$* signatures, respectively.

Due to an increased fluid flow along fault zones at KB, primary fluids stayed mostly unaffected against desiccation and it was possible to preserve the almost “pure” halite dissolution brine in the FIs of Fe-dolomite [fluid A] (Figure 28c and 29c; green bold line). This early fluid signature most likely correlate to interaction with evaporitic units of the Klippen nappe, which in turn may indicate very thin (if any) carbonate sediments at the topographic high above KB. The dissolution of Ca-carbonates and/or Ca-sulfates would additionally increase the Ca_{excess} of the evolving fluid A (Figure 29c; red bold line); the higher effect for the fluids at PI and GP compared to KB again indicates thicker carbonate platforms in the regions above PI and GP (Figure 29c; red dashed line). Similar to the Ca_{excess}*-$Na_{deficit}$* signatures, elevated $\delta^{34}S_{(CDT)}$-values of arsenopyrite I from the Fe-Co stage II against the following stages (Figure 23) indicate an origin of sulfur either from seawater or from Triassic aged marine sulfates (Kampschulte and Strauss 2004). Similarly, Robinson and Ohmoto (1973) suggested that sulfur of the ore-forming fluids originated from seawater or evaporitic sulfates at the five-element veins of Great Bear Lake, Canada.

With further fluid descent through the SM basement, fluid evolution of fluid A at all deposits followed similar pathways (cf. Figure 28c and 29c). Plagioclase albitisation was the controlling factor on the successive Ca_{excess}*-$Na_{deficit}$* signatures, trapped by Fe-dolomite at PI and GP or siderite II at KB [fluids A'] (Figure 29c; blue bold line). Reaction of plagioclase produced coupled changes of Ca_{excess} and $Na_{deficit}$. Similar to the formation temperatures, the stepwise increase in Ca_{excess} and $Na_{deficit}$ from KB to PI to GP indicate the increasing depth of mineralization and more extended fluid pathways illustrated in Figure 28c.

Lastly, fluid evolution within the hydrothermal veins and during gangue precipitation changed the fluid composition again [fluid A''], rendering it different from the earlier evolution lines [fluid A'], although still interaction with plagioclase was involved. The abrupt shift to exclusively lower Ca_{excess} values results from the precipitation of large amounts of Ca-bearing carbonates like Fe-dolomite, ankerite and calcite.

8.2.2.2 Oxygen and carbon isotope signatures: evolution during fluid-siderite interaction

The evolution from fluid A to fluids A' and A'' links the initial ore precipitation to an intensive and prolonged dissolution of siderite and co-precipitation of Fe-dolomite, ankerite I and siderite II (Figure 8). Siderite dissolution or precipitation does not affect the previously described Ca-Na systematics and therefore it is not possible to reconstruct any fluid-siderite interaction from FI studies. Oxygen and carbon isotopic compositions of involved carbonates, however, are able to track processes that were essential during ore and gangue precipitation. From geometric relationships at KB and corresponding isotopic signatures it is possible to elaborate processes that happened during initial crack opening, pristine siderite brecciation and carbonate precipitation temporary prior and during fluid-siderite interaction (Figure 24a, c-d).

Prior to ore formation and siderite dissolution, barren dolomites together with late ankerites I show a coupled and linear decrease of the $\delta^{18}O$ and $\delta^{13}C$ values from vein sections below the fahlband (Figure 24d; red region). In this region, no siderite was present and no primary ore formation happened. Note that disseminated cobaltite and arsenopyrite formed during Alpine tectonics only. Early dolomite includes the highest and ankerite I the lowest $\delta^{18}O$ and $\delta^{13}C$ values, at which both specify a gradient of -0.49 $\Delta(\delta^{13}C)/\Delta(\delta^{18}O)$ (Figure 24a; red region). Five-element veins from the Odenwald that formed due to reduction by methane do not show any gradients of the $\delta^{18}O$ and $\delta^{13}C$ values (Burisch et al. 2017). In addition, hydrothermal vein type deposits including base metal sulfides formed during fluid mixing show higher $\Delta(\delta^{13}C)/\Delta(\delta^{18}O)$ of +1.5-1.65 (Zheng and Hoefs 1993; Schwinn et al. 2006). Such scenarios seem to be unlike for the formation of the veins in the Penninic Alps. Carbonates from other five-element veins, however, show similar positive gradients ranging from 0.56-0.66 $\Delta(\delta^{13}C)/\Delta(\delta^{18}O)$ (Schwinn et al. 2006; Staude et al. 2007; Staude et al. 2012a). Staude et al. (2012a) showed that concomitant O and C changes of primary and remobilized carbonates involve temperature changes and fluid interaction with graphite or other forms of reduced carbon. Constant temperatures during gangue precipitation of the observed samples, however, speak against it. In combination to fluid mixing calculations of Zheng and Hoefs (1993) and Schwinn et al. (2006), Staude et al. (2012a) revealed a fluid mixing of hot, CO_2 dominated basement fluids (low $\delta^{18}O$ and $\delta^{13}C$) with relatively colder and HCO_3^- dominated sedimentary aquifers (high $\delta^{18}O$ and $\delta^{13}C$). Temperature controlled isotope fractionation (O'Neil et al. 1969; Truesdell 1974; Golyshev et al. 1981) and examples from fluid inclusions of natural samples (Staude et al. 2012a), however, show that (depending on the temperature range) temperature differences of two mixing fluids result in too high temperature gradients between succeeding formation of primary carbonates (~50-150°C for both $\delta^{18}O$ and $\delta^{13}C$). Such temperature changes are not obvious for any gangue sequence in all occurrences in the Penninic Alps (cf. Figure 29a; maximum gradient Fe-dol→ank I: 30°C). In order to these mixing models, earliest carbonate precipitation at the highest temperatures would result in the lowest $\delta^{18}O$ and $\delta^{13}C$ values. Unlike, the Pennine deposits show, a slight drop in temperatures and a vice versa trend, as the earliest carbonates include the highest $\delta^{18}O$ and $\delta^{13}C$ values. Therefore, mixing of two fluids with high temperature gradients at which the carbon source in the initial stages mostly dominated by relatively light $\delta^{13}C$ signatures (e.g. methane or graphite) can be excluded for the formation of the veins in the Penninic Alps. A similar five-element vein system, showing comparable $\Delta(\delta^{13}C)/\Delta(\delta^{18}O)$ ratios with equal gradient direction (-0.35) during constant temperatures is represented at the Terra mine, Great Bear Lake Ontario Robinson and Badham (1974). According to C-O-S isotopes and rather than fluid mixing, they suggest that fluids with a high oxidation potential derived from seawater or sedimentary brines at which seawater sulfate indicates to be the source of sulfur and cover rock limestones the source of carbon. Analogously, this is the most likely scenario that influenced fluids prior to ore formation at the Penninic veins.

Gangue carbonates that host arsenides and sulfarsenides show comparable carbon and oxygen isotope evolutions at KB, PI and GP (green color: Figure 24a, b). As indicated above, the descending (near surface) fluids had a high oxidation potential and therefore were in large disequilibrium with the siderites. Concomitant to the decay of siderite, $\delta^{18}O$ values of Fe-dolomite, ankerite I and siderite II shift continuously towards heavier isotopic compositions of pristine siderite I. It is reasonable that dissolving siderite successively affected aqueous CO_2 and HCO_3^- of the ore forming fluids. As illustrated in Figure 24a, the Fe-Co stage II carbonates (green; i.e they displaced siderite) represent transitional $\delta^{18}O$ and $\delta^{13}C$ values intermediate to the barren carbonates below the fahlband (red) and the pristine siderite veins (brown). Again, an involvement of relatively negative $\delta^{13}C$ signatures that indicate significant amounts of carbon from isotopic lighter hydrocarbons or graphite during ore formation (Staude et al. 2012a; Markl et al. 2016; Burisch et al. 2017) is not obvious from this change in $\delta^{18}O$ at constant $\delta^{13}C$.

Carbonates, which originate from the following sulfide stage III and Ni-Co stage, however, show more negative carbon $\delta^{13}C$ signatures (yellow and blue color: Figure 24a). The adjacent host rocks, though, do not contain any graphitic rocks or carbonaceous matter. Representative reservoirs, influencing more negative $\delta^{13}C$ signatures, could be found at the kerogen bearing Törbel Formation ($\delta^{13}C$: ~-31‰) between the polymetamorphic basement and Permotriassic cover rocks of the overturned limb of the Siviez-Mischabel nappe found in the Mattertal (Genier et al. 2008). Additionally, decreasing $\delta^{13}C$ could happened self-induced, since reduced fluid conditions by siderite dissolution and magnetite formation would inevitably result in the very reduced conditions. Therefore, reduced carbon species such as CH_4 or kerogen could be formed from residual CO_2 formed during the initial stage of the hydrothermal system.

Based on the geometric relationships and associated isotope values, it can be concluded that the siderite vein formation was preferentially bound to the fahlband strata (Figure 24c). Brecciation and infiltration by the ascending fluid A' can be observed in a later stage. No siderite was present below the fahlbands where precipitated Fe-dolomites and ankerites reflect a continuous and undisturbed fluid development (red area Figure 24d). Where the source fluid intersected the pristine siderite, its dissolution caused the primary ore precipitation and an increased adoption of its isotopic carbon and oxygen signature into Fe-dolomite and ankerite I (Fe-Co stage II, green area Figure 24d). The hydrothermal system further shifted towards the sulfide stage III (fluid A'-A'') and later was repeatedly activated during the Ni-Co stage. In both cases, infiltration and penetration of the previous veins caused the re-deposition of pre-existing ores (sulfide stage III and Ni-Co stage IV; Figure 24e, f). Reduced carbon species (with lower $\delta^{13}C$) may have played a major role in these subsequent phases than previously.

8.3 The element sources: metals, arsenic and sulfur

As already illustrated for the Triassic ores in Figures 28c and 29c, a single descending fluid (fluid A) is sufficient to explain different temperatures, salinities, Ca- and Na-contents at various places in its flow path, due to host rock equilibration with the evaporites and carbonates of the Klippen Nappe, with plagioclase of the SM basement and carbonate precipitation after ore formation. The following will discuss the possible sources of the metals, arsenic and sulfur as well as the influence of the fahlband host rocks and its sulfides.

8.3.1 Transition metals and arsenic

Most studies suggested the fahlbands as main source of arsenic, sulfur and iron (Sartori and Della Valle 1986; Della Valle 1992; Schafer 1996), although our observations prove that most sulfides show only minor evidence of dissolution and neither Ni nor Co were considered. In addition, the Alpine Orogeny at greenschist facies conditions concealed original textures and possibly compositions of the original fahlband lithology. Although the fahlbands gain low Ni and Co today (e.g. amphibolite at GP: 54 ppm Ni and 27 ppm Co; Della Valle 1992), mass calculations indicate realistic volumes of ~$0.26 \cdot 10^{-3}$ km³ and ~$0.29 \cdot 10^{-3}$ km³, which would be sufficient for the amount of Ni and Co ores at GP, respectively (280 t with 14 wt.% Ni and 8 wt.% Co). Most likely, descending fluids leached Ni and Co during post-Variscan aged retrograde hydration reactions from the fahlbands. Since dissolution of siderite occurred at the same time as the ore precipitation, Fe most likely stems from siderite. Other basic rocks of the SM nappe like metagabbros or serpentinites, however, could represent other possible Ni and Co sources. In addition, Burisch et al. (2016) show that at least Ni and As can also be leached from biotite in ordinary crystalline rocks such as granites and gneisses at $T > 180°C$ and $P > 0.9$ MPa. Since Permian rhyolites of the Monte Leone Nappe show a pre-enrichment of As, Ni and Co, in the vicinity of the Penninic-hosted Lengenbach deposit (Binntal, Switzerland; Knill 1995; Hofmann and Knill 1996), the Randa Granite and corresponding rhyolites analogously may also be considered as source of these elements (intruded into the SM basement 269±2 Ma; Bussy et al. 1996).

8.3.2 Sulfur and the importance of the fahlbands

Della Valle (1992) and Schafer (1996) suggested the mobilization of fahlband-hosted sulfides as the source for sulfur influx during the sulfarsenide formation. Field observations, however, show only minor evidence of pyrite dissolution in the direct vicinity to the veins (e.g. Figure 5f). In addition, sulfarsenide precipitation is limited especially during the Fe-Co stage II, where arsenopyrite I only occurs as small layers within the massive löllingite I aggregates. The following demonstrates that sulfur, cobalt and nickel mobilization from the fahlbands was primarily of minor importance during the early Fe-Co stage II but increasingly influenced the hydrothermal system towards the late Fe-Co stage II, in the Ni-Co stage IV and the Alpine stages.

Inferred from arsenic contents of arsenopyrite I (~31-32 mol% As) in equilibrium with löllingite I at temperatures around 225°C, only very low sulfur activities (log a H_2S: -4 to -5) are necessary to stabilize arsenopyrite in the Fe-Co stage II (Kretschmar and Scott 1976). This very low sulfidation state (Einaudi et al. 2003) implies that mobilization of sulfides was not significant during the Fe-Co stage II and explains why no major sulfide dissolution textures are observed in the fahlbands. In addition, the sulfur isotope data imply sulfur derivation from Triassic to Jurassic evaporitic sequences and/or seawater compositions (arsenopyrite I, Figure 23). Sulfate dissolution from Triassic to Jurassic evaporites of the Klippen nappe (and later reduction during siderite I dissolution) is the most coherent sulfur source for small amounts of sulfarsenides during the Fe-Co stage II. High Fe concentrations necessary to precipitate large amounts of löllingite I, however, were mobilized in situ from siderite I dissolution and not from the fahlband pyrite, indicating an independent source of iron and sulfur in this early stage. Large quantities of skutterudite and increasing Ni contents in arsenopyrite II and löllingite II imply higher Co and Ni concentrations in the subsequent fluid. If siderite dissolution was considerably faster than fluid-host rock interaction (i.e. desiccation and hydration reactions), this would be an explanation for the fact that Fe dominates the Triassic ores (Fe-Co stage II), while Ni dominates the Jurassic stage (Ni-Co stage IV).

In addition, sulfur isotopes show this temporal offset of the element mobilization from the fahlbands. According to converging sulfur isotopes towards the fahlband signature (pyrite I and chalcopyrite, sulfide stage III; Table 6 and Figure 23) and the coupled influx of sulfur, iron and nickel, an increased mobilization of the fahlbands happened successively after the Fe-Co stage II leading to the precipitation of gersdorffite I and magnetite III (Ni-Co stage IV; Figure 9g). In the further evolution, remobilized sulfarsenides of the Alpine stage Va (T3 gersdorffite II, krutovite III; Figure 19c-e) reach even higher sulfur concentrations than those of the Ni-Co stage IV (T2 gersdorffite I, krutovite I, krutovite II), which were related to a further enhanced mobilization of sulfur from the sulfide-rich fahlbands during the onset of the Alpine deformation. Again, sulfur isotope data of remobilized sulfarsenides and sulfides in Table 6 and Figure 23 (gersdorffite II, pyrite II and arsenopyrite III) support this hypothesis. In contrast, the initial vein stages II and III show sulfur isotope values indicative of heavier sulfur sources (Fe-Co stage II: arsenopyrite I; sulfide stage III: pyrite I, chalcopyrite) such as Triassic-Jurassic seawater-derived sulfates.

8.4 Fluid volatiles: are there hydrocarbons involved?

Analogously to other five-element veins and related systems (Kerrich et al. 1986; Essarraj et al. 2005; Essarraj et al. 2016; Levresse et al. 2016; Markl et al. 2016; Burisch et al. 2017; Essarraj et al. 2017), fluid reduction by hydrocarbon influx could also be a potent process for ore precipitation at the Penninic occurrences. Although sulfide stage III and Ni-Co stage IV carbonates show successively decreasing δ^{13}C-values at fixed δ^{18}O, an influence of isotopically light carbon such as hydrocarbons cannot be generally assumed. On the one hand, ore formation during the initial Fe-Co stage II does not show comparable C-O evolutions and on the other hand isotopically lighter carbon could also originate from other reservoirs besides classical hydrocarbons like methane. Nearby examples of such material within the Siviez-Mischabel Nappe are e.g. reported by Genier et al. (2008) as kerogens from the Törbel Formation (δ^{13}C: ~-31‰).

Raman spectroscopy of the FIs indicate that involvement of acyclic saturated hydrocarbons (C_nH_{2n+2}) was unlikely during ore formation. The species of interest occur as broad but distinct Raman active bands at ~2960 cm^{-1}, ~2700 cm^{-1}, ~1360 cm^{-1}, and a broad feature with different bands at 1670-1560 cm^{-1} (Figures 22b/e and c/f, respectively). These results require a detailed discussion, as conventional Raman spectroscopy literature for fluid inclusions does not report these specific vibrations (e.g. Frezzotti et al. 2012). The band combination may be assigned to different carbonaceous materials (CM), ranging from poorly ordered kerogen material over disordered to more ordered graphite (Wopenka and Pasteris 1993). Although the asymmetric band at 2700 cm^{-1} shows a tendency to be more ordered graphite material in the liquid and vapor phases (e.g. Figure 22b/e), the observed bands at 1360 cm^{-1} and 1670-1560 cm^{-1} occur at higher wavenumbers than ordered (G) and even disordered (D1 and D2) bands reported for graphite (Figure 22c/f). Therefore, ordered and disordered graphite is unlikely and all band features at ~2960 cm^{-1}, ~2700 cm^{-1}, ~1360 cm^{-1} and 1670-1560 cm^{-1} resemble mostly those known from kerogens (Beyssac et al. 2002a; Beyssac et al. 2002b; Huang et al. 2010). As can be seen in Figure 22b and c, in parts also the solid phase includes this kerogen material. Note, the 1360 cm^{-1} band region may interfere with HCO_3^-, but the lack of its strong C-OH stretching mode at ~1017 cm^{-1} excludes this species (Figures 22a/d). In some rare cases, bands at ~1385 cm^{-1} and ~1285 cm^{-1} indicate CO_2 in the vapor phase. but this species is mostly masked by the fluorescence at ~1360 cm^{-1} and has only low densities of <0.2 g/cm³ (cf. Figure 22c Fermi doublet Δ: 103 cm-1; Frezzotti et al. 2012). Although the degradation of CO_2-CH_4 inclusions to H_2O-C (graphite) reported by Burke (2001) may proceed, presented data excludes the presence of CH_4 and other hydrocarbons from frequencies at 3100-2600 cm^{-1} and due to the low probability of this reaction in such low density CO_2-bearing inclusions. Besides the two broad kerogen bands at ~2960 cm^{-1} and ~2700 cm^{-1}, additional Raman active vibrations were detected as broad features including maximum intensities at 3065 cm^{-1}, 2960 cm^{-1}, 2930 cm^{-1} and 2875 cm^{-1} (Figure 30a). Although methane, ethane and propane (C_nH_{2n+2}; n=1-3) occur at similar wavenumbers, such species can be excluded in this study since comparison to resin material reveals intensive fluorescence effects of unsaturated and aromatic hydrocarbons (cf. Figure 30b: Raman bands of Superglue and Körapox epoxy resin). Whereas other works, such as Li (2017), inaccurately refer species with similar band shapes and wavenumbers to CH_4 and C_2H_6 (Figure 30b), no interpretation was made about FIs showing such features in this work. Since pre-ore siderite I does not host kerogen material while all successive carbonates include such species after dissolution of siderite I (Fe-dolomite, siderite II-III and ankerite I-II), kerogens possess a more important influence on ore precipitation of five-element veins. Previous works already considered such carbon species like a C-H-O containing solid phase at Kongsberg (Neumann 1944) or other carbon-rich lithologies (e.g. Kissin 1992; Staude et al. 2012b). If either the influx of kerogen triggered the ore formation at the Penninic occurrences or kerogens eventually formed during siderite dissolution together with the ore stages will be the discussion in following chapter 8.5.

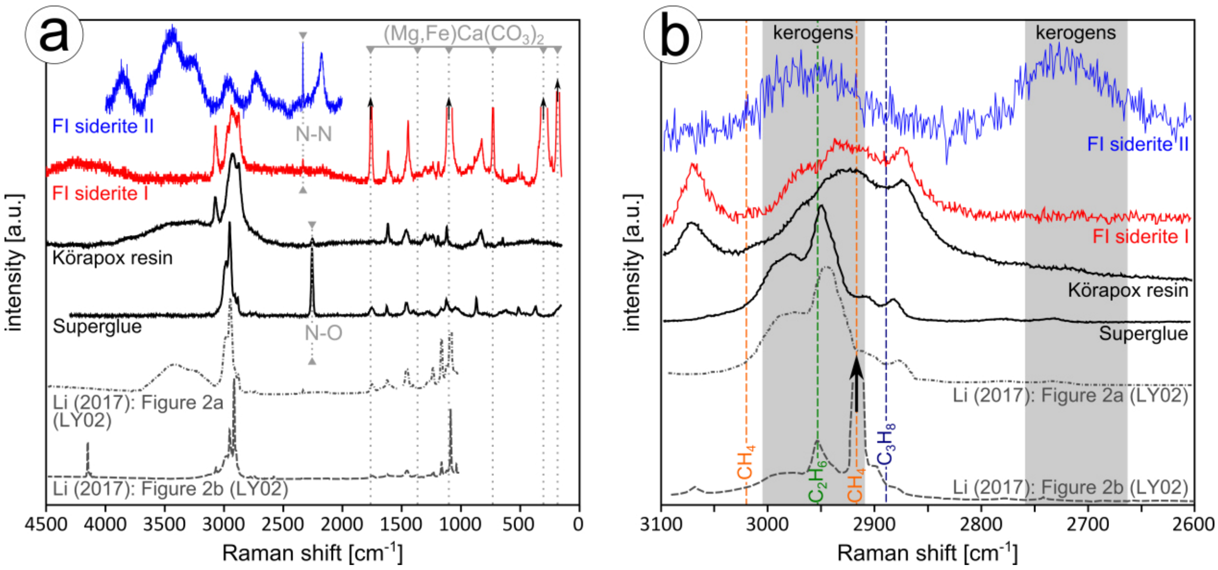

Figure 30: (a) Representative Raman spectra, which occurred during analysis of FIs hosted by siderite I (red) and siderite II (blue). For correlation with other substances, preparation resins (this study: Körapox and Superglue) and spectra of hydrocarbons from Li (2017) are additionally shown. (b) spectral range between 2600-3100 cm^{-1} show Raman active bands of siderite II at region common for kerogens (cf. Figure 22). No hydrocarbons were detected during measurements. Note that artefacts due to preparation resin fluorescence occur at similar wavenumbers. For further information, see text.

8.5 The ore precipitation trigger: fluid reduction

8.5.1 Siderite dissolution

Theoretical calculations combined with textural and mineralogical observations and the data from Raman spectroscopy reveal that the redox reactions between highly saline water such as fluid A and stage I siderite is a viable mechanism for five-element ore precipitation in the Valais. Other processes such as hydrocarbon influx, postmagmatic high T reactions (involving CO_2, H_2O and metal oxides), retrograde metamorphism (involving carbonate-graphite bearing rocks), carbonate methanation (at preexisting H_2 fluids) or Fischer-Tropsch catalysis (by group VIII transition metals and related oxides) (Holloway 1984; Giggenbach 1997; Yoshida et al. 1999; McCollom 2003; Etiope and Sherwood Lollar 2013) appear unlikely for various reasons (e. g., lack of magmatic activity, pre-Alpine ages, lack of graphite and hydrocarbons).

Experimental siderite-water interactions by Milesi et al. (2015) showed siderite dissolution at 200-300°C and 50 MPa, producing magnetite and carbonaceous matter (CM) like kerogens. Calculations at 200°C for fluid compositions previously in equilibrium with siderite, magnetite and CM at 100°C show an oversaturation of magnetite and CM, following a two-step process according to Reactions 3 and 4 (Milesi et al. 2016):

$$3FeCO_3 + H_2O \Leftrightarrow Fe_3O_4 + 3CO_2 + H_2 \qquad \text{(Reaction 3)}$$

$$CO_2 + 2H_2 \Leftrightarrow C\ \text{(CM; i.e. kerogen)} + 2H_2O \qquad \text{(Reaction 4)}$$

Raman spectroscopy (Figure 22) proved that such kerogen material is present in the FIAs and the solid phases of Fe-dolomite, siderite II and ankerite I, II, but not in the earlier stage I generation of siderite I. Textures reveal an intensive dissolution of siderite I and reprecipitation of Fe-dolomite, siderite II or ankerite I-III together with magnetite and interspersed kerogen (e.g. Figures 9a, b, d, g, h). In addition, massive Fe-Co-Ni ores and magnetite are present where intensive replacement of siderite I happened (Figure 5e), but remained barren where siderite I was unaffected (Figure 5d). Hence, ore precipitation occurred due to simple fluid-siderite interaction, where a previous fluid was modified by fluid-rock interactions in the cover and basement rocks (cf. chapter 8.2) during which it had gained necessary metal, arsenic and sulfur concentrations (cf. chapter 8.3). Ore formation from these pre-enriched fluids occurred due to crustal extension and concomitant decompression, where the pore fluid pressure exceeded the host rock pressure, resulting in fluid-filled fracture meshes (Staude et al. 2009; Bons et al. 2014). These mobilized fluids propagated towards the preexisting siderite veins and, according to combined Reaction 4, reaction of the fluids with siderite triggered ore formation due to siderite dissolution, oxidation of ferrous iron (precipitation as magnetite) and concomitant reduction of the metals, As and S.

$6FeCO_3 + 5H_2O + As(OH)_{3(aq)} \Leftrightarrow 2Fe_3O_4 + 6HCO_3^{-}{}_{(aq)} + 7H^+ + As^-$ (Reaction 4)

8.5.2 Host rock alteration

Besides the dissolution of siderite and accompanied oxidation of ferrous iron, additional fluid-rock interaction within the adjacent host-rocks may have supported fluid reduction. Such a gradual decrease of the oxygen fugacity through reaction with Fe^{2+}-minerals such as biotite, hornblende and pyroxene is already reported by Robinson and Ohmoto (1973) from the five-element vein system at Echo Bay, Canada. Host rock alteration at the occurrences of the Valais Alps similarly shows chloritisation reactions displacing ferrous biotite and hornblende (cf. Figures 16e, g; Reactions 5 and 6):

$2K(Fe,Mg)_3AlSi_3O_{10}(OH)_2 + 4H^+$

$\Leftrightarrow (Fe,Mg)_5Al_2Si_3O_{10}(OH)_8 + 3SiO_2 + 0.5Fe^{2+} + 0.5Mg^{2+} + 2K^+$ (Reaction 5)

$NaCa_2Al_3Mg_4Si_6O_{22}(OH)_2 + 9.2H^+$

$\Leftrightarrow 2.4H_2O + Na^+ + 2Ca^{2+} + 0.8Mg_5Al_2Si_3O_{10}(OH)_8 + 1.4Al^{3+} + 3.6SiO_2$ (Reaction 6)

Observed chlorite compositions, however, only contain low Fe^{3+} contents and therefore both reactions do not represent an effective process for supported fluid reduction. Most likely, redox processes within the host rocks, directly adjacent to the veins, were favored due to the co-precipitation of ilmenite ($Fe^{2+}TiO_3$), its immediate transition towards pseudorutile ($Fe^{3+}{}_2Ti_3O_9$) and further enclosement by magnetite. As chlorite does not include Ti, excessive amounts that originate from biotite and hornblende chloritisation precipitated as rutile. With increasing distance to the veins, excess Ti precipitated as rutile (TiO_2) and is later displaced by leucoxene. During hornblende breakdown (Reaction 7), no pseudorutile or magnetite occurred due to Fe^{3+} compensation by epidote ($Ca_2Fe^{3+}Al_2Si_3O_{12}OH$). This reaction may additionally have favored Fe^{2+} to Fe^{3+} oxidation and concomitant fluid reduction.

$NaCa_2Al_3Mg_4Si_6O_{22}(OH)_2 + 4.1H_2O + 0.6Al^{3+} + Fe^{2+} + 0.25O_2$

$\Leftrightarrow Na^+ + Ca_2Fe^{3+}Al_2Si_3O_{12}OH + 0.8Mg_5Al_2Si_3O_{10}(OH)_8 + 0.6SiO_2 + 2.8H^+$ (Reaction 7)

$^{207}Pb/^{206}Pb$ vs $^{238}U/^{206}Pb$ ratios of the host rock alteration paragenesis plot together with magnetite I along Triassic ages (isochrone 1: biotite → chlorite + quartz + pseudorutile; Figure 21a). Reduction of the fluids due to the co-precipitation of Fe-To-oxides therefore favored the ore precipitation at least during the Fe-Co stage II, whereas the age of epidote formation remains unclear.

8.6 The physico-chemical and thermodynamic control on ore formation

8.6.1 General thermodynamic control on five-element vein formation

Calculated thermodynamic predominance diagrams of the systems Fe-As-S-H_2O, Co-As-H_2O and Ni-As-H_2O show the effects of changing arsenic concentrations (Figures 31a-c), metal concentrations (Figures 31d-f) and temperatures (Figures 31g-i) on the corresponding phase relations in the log fO_2 vs pH space. In each system, native As occurs at the lowest pH and is followed with increasing pH by the corresponding diarsenides (löllingite, safflorite and rammelsbergite) and monoarsenides (westerveldite, modderite and niccolite). With regard to pH values most relevant for hydrothermal fluids (pH ~4 to 8), diarsenides are more stable than monoarsenides at higher fO_2. Arsenopyrite as the Fe-sulfarsenide has its predominant stability field at the highest oxygen fugacity and is located between native As and löllingite. Even at low sulfur contents and at relevant pH values (4-8), arsenopyrite is the dominant solid phase in equilibrium with $As(OH)_3$. Under different conditions, however, more basic fluids produce löllingite (pH>8), more acid fluids native As (pH<4). Although no reliable thermodynamic data are available for gersdorffite and cobaltite, their predominance relations should be similar to those of arsenopyrite. In addition, no consistent data are available for skutterudite. According to Reaction 8 and the valence state of Co, the predominance of skutterudite ($Co^{3+}As_3$) is expected to be at lower pH and higher fO_2 than safflorite ($Co^{2+}As_2$), i. e., somewhere between safflorite and native As like illustrated in Figure 32 (Markl et al. 2016). One can expect that temperature, metal and arsenic content may affect the skutterudite stability in the same way as safflorite.

$$Co^{3+}As_3 + 0.5H_2O \Leftrightarrow Co^{2+}As_2 + As^- + H^+ + 0.25O_2 \quad \text{(Reaction 8)}$$

If the Fe-, Co- and Ni-systems are compared, it is obvious that the Ni minerals are stable at the highest fO_2, followed by the Co minerals and finally by the Fe minerals (with decreasing fO_2). Note that the used metal activities reflect identical concentrations in fluids in the pH range of 4-8 (Figures 31d-f). Elevated arsenic contents (Figures 31a-c) and increasing temperatures (Figures 31g-i) shift the borders between $As(OH)_{3(aq)}$ and the native As, diarsenides and monoarsenides fields to higher fO_2. The transitions between native As and diarsenides or diarsenides and monoarsenides remain at the same position during changing arsenic contents but shift to lower pH values upon metal and temperature increase. With elevated arsenic concentrations, predominance transitions between native As or the arsenides to aqueous $As(OH)_3$ shift to higher fO_2. Therefore, higher arsenic concentrations increase the possibility to precipitate five-element veins.

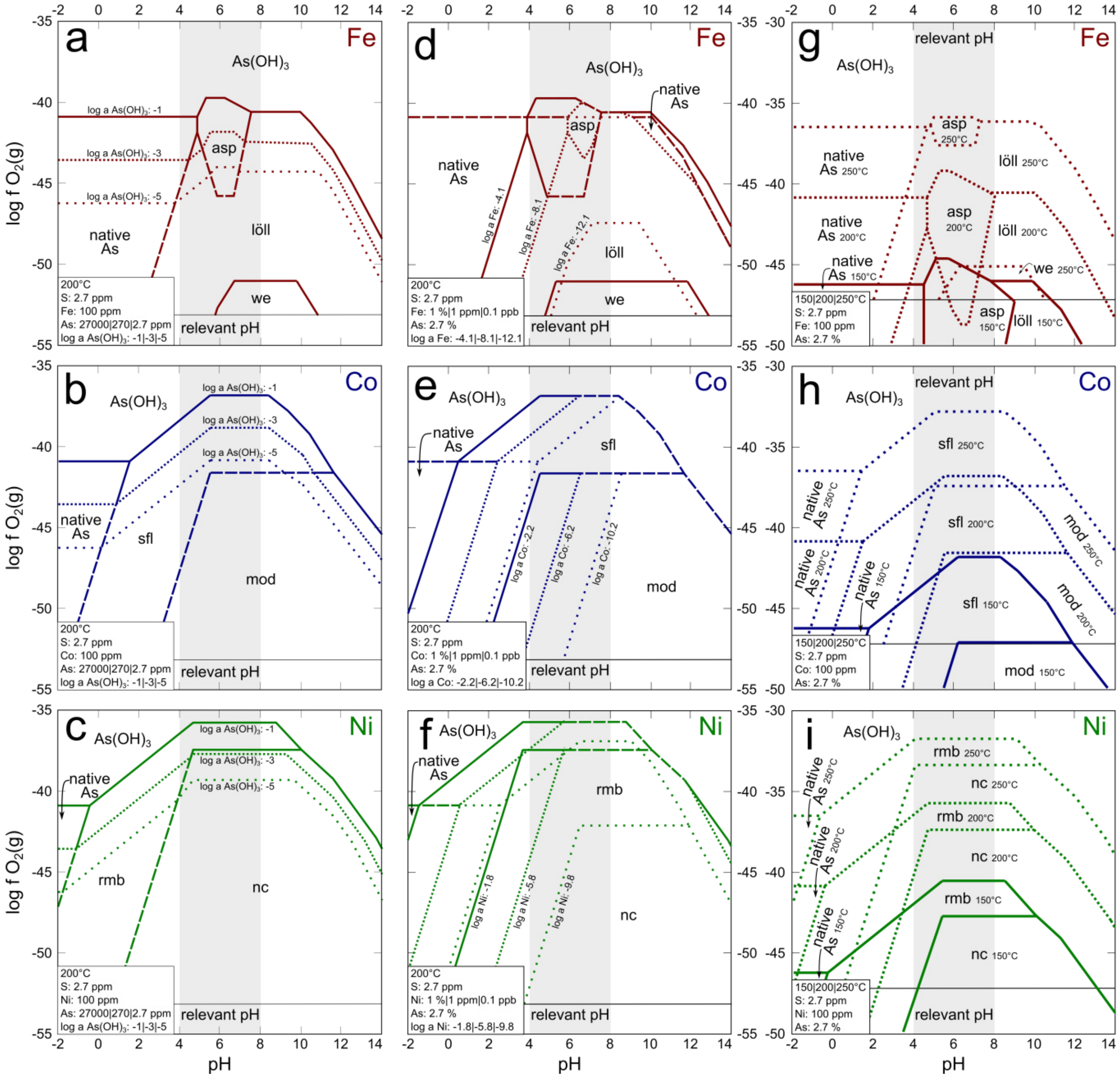

Figure 31: Predominance diagrams log fO$_2$ vs pH for the systems Fe-As-S-H$_2$O, Co-As-H$_2$O and Ni-As-H$_2$O, calculated with the software package Geochemist Workbench. (a)-(c) Different concentrations of arsenic, (d)-(f) Fe/Co/Ni metal contents, and (g)-(i) different temperatures. Note that obvious temperature effects on the predominance fields as a function of fO$_2$ are not representative for of the effective redox potential, since diagrams (g-i) are not corrected for the temperature effect on fO$_2$. Thermodynamic data used for (a), (d), (g), (c), (f) and (i): thermoddem (Blanc et al. 2012); (b), (e) and (h): LLNL (thermo) (Johnson et al. 2000). Predominance of rammelsbergite inferred from phase relations similar to the Fe and Co systems (cf. chapter 5.5). asp: arsenopyrite, löll: löllingite, we: westerveldite, sfl: safflorite, mod: modderite, rmb: rammelsbergite, nc: niccolite.

At highest fO_2, the diarsenides' predominance fields develop as roof-like fields on top of the monoarsenides due to kinks of the monoarsenide-diarsenide and diarsenide-$As(OH)_{3(aq)}$ equilibrium. These kinks depend on the Ni-/Co-/Fe-chloride to Ni-/Co-/Fe-oxide transition and occur at decreasing pH values from the Fe system over Co to Ni (e.g. Figure 31a-c; Fe: pH 6.7, Co: pH 5.7 and Ni: pH 4.7). With decreasing arsenic concentration, these roofs decrease in size due to the stable position of the mono- to diarsenide and metal-chloride to metal-oxide transition, but variable transition from $As(OH)_3$ to the diarsenides. Due to relations between variable and fixed phase transitions, this effect is more pronounced for the Ni- than the Co-system, and again for the Co- than Fe-system. With decreasing arsenic concentrations in the fluid, rammelsbergite stability disappears between niccolite and $As(OH)_3$ in the relevant pH range (Figure 31c; log a $As(OH)_3$: -3 and -5), whereas the Fe- and Co-diarsenides remain stable (Figure 31a, b). As a consequence, it is possible to reach the niccolite stability field by reducing fO_2 without precipitating major amounts of rammelsbergite. For the Fe- and Co-system, this is either completely unrealistic for Fe (Figure 31a) or rarely achieved at very high and unrealistic pH values for Co (Figure 31b pH>11.5). This may explain the very rare natural occurrence of westerveldite (4 known localities worldwide) and modderite (3 localities) in contrast to the very common occurrence of niccolite (642 localities) (Mindat.org 2017).

As illustrated in Figures 31d-f, fluctuating metal concentrations of Fe, Co and Ni shift the predominance fields towards higher pH and lower fO_2 values. Merely the highest possible fO_2 of the arsenides and native As predominance fields in the Fe and Co systems stay almost unaffected. The field of rammelsbergite, however, shifts to lower fO_2, if Ni concentrations reach very low activities (Figure 31f; log a Ni^{2+}: -9.8).

In conclusion, temperature and arsenic contents do not explain the observed (relative) mineralogical differences in the Fe-, Co- and Ni-systems, except for the disappearance of rammelsbergite in favor of niccolite at very low arsenic contents. Rather, differences in the quantity and availability of Fe, Co or Ni govern the dominance of the different mineral phases. Since the presented predominance diagrams only deal with endmember compositions (which in natural environments only occur to a certain degree), note that these thermodynamic modeling results are only the best approach to the problem possible at the time being – but not the final solution.

As a general conclusion, a simple decrease of fO_2 would inevitably result in the succession from Ni- over Co- to Fe-dominated ores. However, such simple relations cannot describe the chemical and mineralogical evolution of the Valais five-element deposits, which show an evolution from Co- over Fe- to more Ni-rich compositions. Following chapter 8.6.2 addresses the main redox process by siderite dissolution and iron oxidation present in the Valais deposits and their controversial Fe-Co-Ni evolution.

8.6.2 Evolution of arsenides, sulfarsenides and their Fe-Co-Ni signatures

For the Fe-Co stage II, letters (a-k) in the detailed paragenetic sequence of Figure 25 links the temporal evolution of the ore precipitation to the modeled fluid path in Figures 32 and 33. Fluid evolution leading to ore precipitation of the Ni-Co stage IV is compared to the previous stage in Figure 34. In both stages, the dissolution of siderite and the resulting redox processes results in a decrease of fO_2. If the fluid path enters distinct predominance fields, precipitation starts and the fluid path will evolve along slopes towards lower pH and fO_2, defined according to the different precipitation Reactions 9-11.

$2BiCl_4^- + 3H_2O \Leftrightarrow 2Bi^0 + 8Cl^- + 1.5O_2 + 6H^+$ (Reaction 9)

$(Fe,Co,Ni)^{2+} + 2As(OH)_3 \Leftrightarrow (Fe,Co,Ni)As_2 + 2H_2O + 2O_2 + 2H^+$ (Reaction 10)

$Co^{3+} + 3As(OH)_3 \Leftrightarrow CoAs_3 + 3H_2O + 3O_2 + 3H^+$ (Reaction 11)

Metal, sulfur and arsenic activities decrease during ore precipitation and finally, Reactions 9-11 will stop. This will lead to further decreasing fO_2 at constant pH (Figures 32-18). The following will discuss the evolution of respective fluid paths and phase precipitation in stages II and IV.

Middle Triassic Fe-Co stage II (Figure 32 and 33): The Fe-Co stage II ores formed during T1 in close proximity to the pyrite-bearing fahlband (Figure 4a), and they formed as a result of the dissolution of siderite. Therefore, it is reasonable to assume Fe^{2+} to be more abundant than Ni^{2+} and Co^{2+} (several thousand ppm to wt.%). Ni and Co, in contrast, were probably of minor importance, but dissolved $As(OH)_3$ was present in excess. Figure 32a shows these initial predominance relations between löllingite and safflorite, whereas rammelsbergite is critically undersaturated. Due to the Fe dominance, the löllingite field plots at fO_2 values very close to safflorite. Otherwise, if similar Fe and Co concentrations prevail, the löllingite field would appear at very low fO_2 (cf. Figure 31).

With the onset of siderite dissolution, activities of Fe^{2+}, CO_2, HCO_3^-, and $Fe[(CO_3)_2]^{2-}$ increase. With precipitation of hematite and magnetite, fO_2 starts to decrease until the fluid reaches the native Bi field, which precipitates in (a). With further evolution, the fluid path hits the safflorite stability field and minor amounts of Co-rich löllingite precipitate (b). Due to the low concentration of Co and the proximity to the löllingite stability field, the system immediately evolves towards more Fe-rich compositions (c) (cf. löll I; Figure 18a). During the early Fe-Co stage II, hematite and magnetite are the dominant co-precipitated Fe-oxides (Figure 33a). Later, they are resorbed due to further siderite dissolution and concomitant high HCO_3^- activities (Figure 33b). Since most magnetite resides in the selvedges and within the adjacent host rocks, it seems plausible, that Fe was stabilized by $Fe[(CO_3)_2]^{2-}$ in the fluid which migrated to the margins of the veins, where low carbonate activities favored magnetite formation. The high H^+ activities due to ore precipitation (Reaction 9-11), preclude

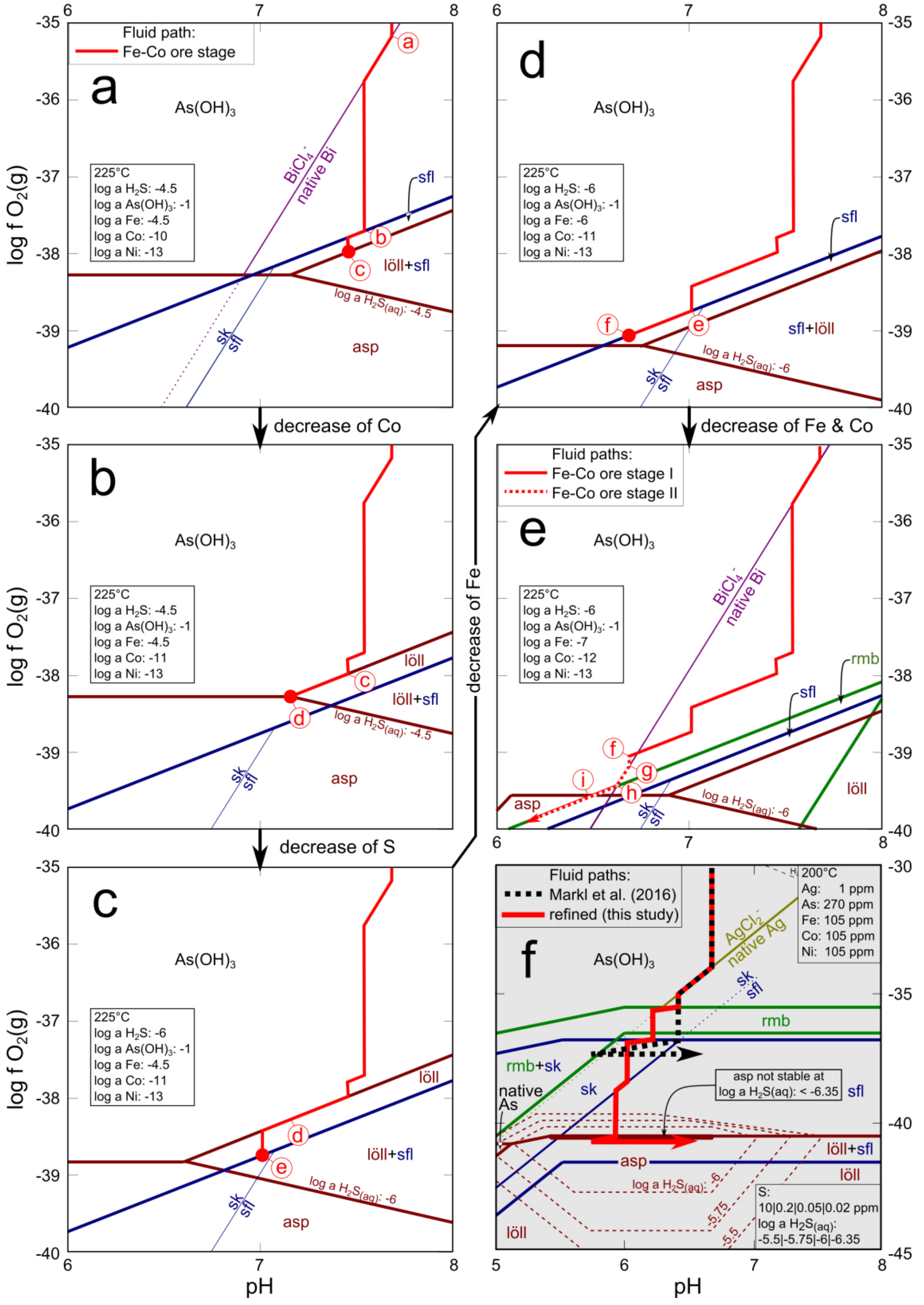

Figure 32: Combined predominance diagrams log fO₂ vs pH for the systems Fe-As-S-H₂O, Co-As-H₂O and Ni-As-H₂O. (a)-(e) Fluid path evolution fitted for the paragenetic succession of the Fe-Co ore stage II of KB with changing activities of Fe, Co, Ni, As and S during ore precipitation (for further information see text). Letters of the illustrated Fluid path correspond to those in the detailed paragenetic sequence of Figure 25. (f) Evolution of common five-element veins with "normal" succession of rmb-sk-sfl-löll (according to ores from the Odenwald, Markl et al. 2016; Burisch et al. 2017). (a)-(e) Illustrate an initial system dominated by Fe as main metalloid species, (f) a system with exactly the same amounts of Fe, Ni and Co in the initial fluid. Thermodynamic data and mineral abbreviations as Figure 31. sk: skutterudite. Note that the sk-sfl transition is only hypothetic due to Reaction 11 after Markl et al. (2016).

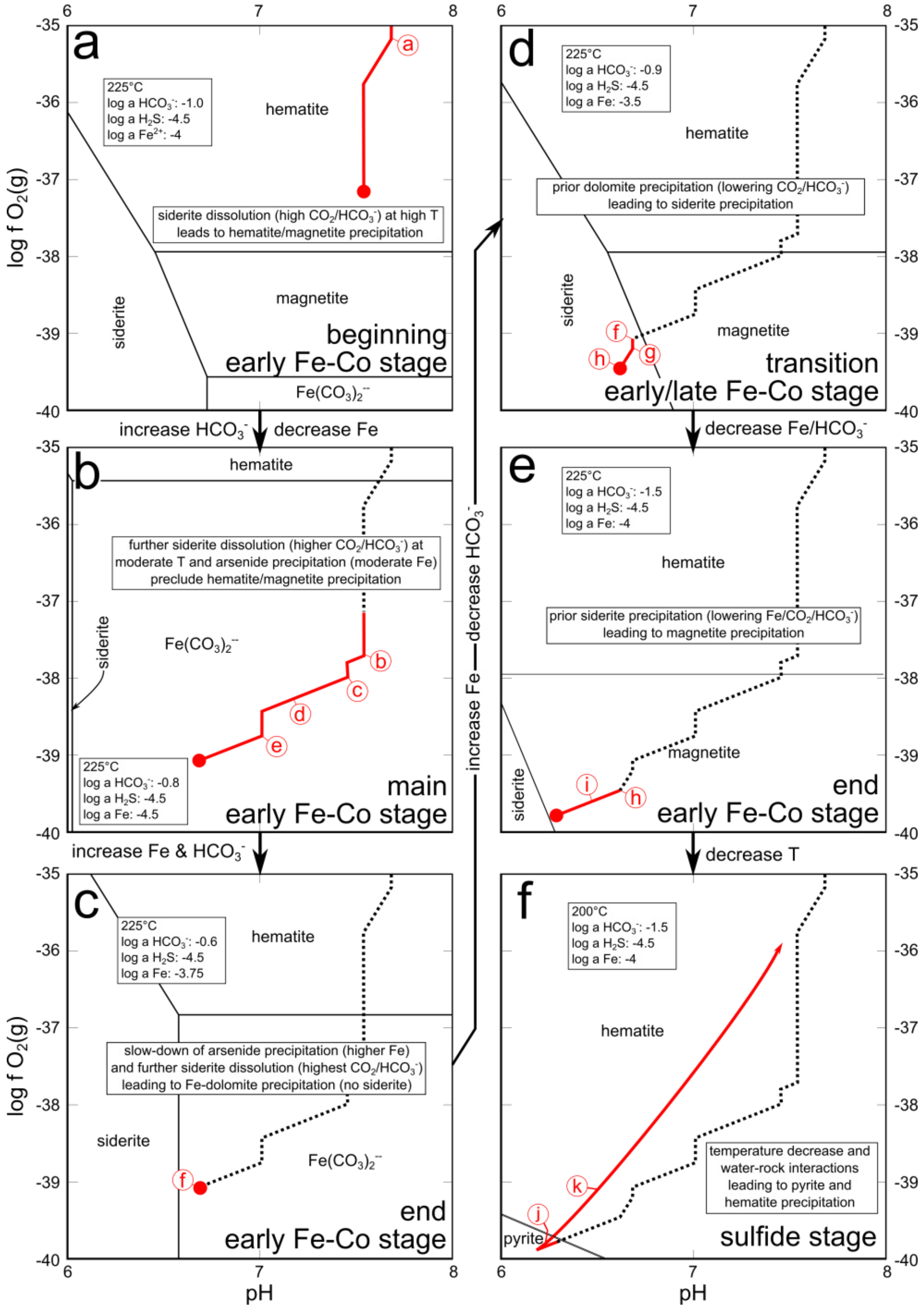

Figure 33: Predominance diagram log fO$_2$ vs pH for the system Fe-S-HCO$_3^-$-H$_2$O at 225 °C (a)-(c) and 200 °C (d). Illustrated fluid path similar to Figure 32a-e. Note changing activities of Fe, HCO$_3^-$ and H$_2$S in (a)-(f) fitted for the paragenetic succession of the Fe-Co ore stage II of KB. Letters of the illustrated Fluid path correspond to those in the detailed paragenetic sequence of Figure 25. (a) Beginning Fe-Co stage II: siderite dissolution starts and Fe-oxides precipitated. (b) Early Fe-Co stage II: high siderite dissolution rates and Fe-arsenide/-sulfarsenide precipitation lead to high HCO$_3^-$ and low Fe activities. Precluded Fe-oxide precipitation and support the resorption of early magnetite. (c) End of early Fe-Co stage II: slow-down of Fe-arsenide/-sulfarsenide precipitation and further siderite dissolution increases the Fe and HCO$_3^-$ activities. Aqueous Fe(CO$_3$)$_2^{2-}$ precludes siderite precipitation and results in dolomite formation. (d) Transition early to the late Fe-Co stage II (step f): reduced HCO$_3^-$ and enriched Fe^{2+} activities (dolomite formation) led to intermediate siderite precipitation. (e) End of late Fe-Co stage II: decreased Fe^{2+} and HCO$_3^-$ activities (siderite precipitation) led to magnetite precipitation. (f) Sulfide stage: decrease of temperature (see FI data) and rock buffered pH and fO$_2$ increase shifts the system into the sulfide stage with early pyrite and late hematite. Thermodynamic data and mineral abbreviations as Figure 31.

carbonate precipitation during this stage in spite of siderite dissolution (b-e) (cf. Markl et al. 2016). Depending on the prevailing sulfur concentrations, arsenopyrite begins to precipitate until step (d) (Figure 32b). Small amounts of interspersed arsenopyrite I as layer-like aggregates within the massive löllingite I growth zonation possibly record pulses of elevated sulfur activities, discussed in chapter 8.3.2. After the precipitation of arsenopyrite and the concomitant decrease of sulfur, fO_2 still decreases and reaches the skutterudite stability field in (e) (Figure 32c). Note, that the skutterudite-safflorite transition is only plotted qualitatively at this position as previously explained. Whether skutterudite or safflorite precipitates significantly depends on pH. During the transition from the early to the late Fe-Co stage II, arsenide precipitation slows down possibly due to the depletion of arsenic and/or the metals. Consequently, this stop of arsenide precipitation and continued siderite dissolution lead to increasing Fe^{2+} and HCO_3^- activities and precipitation of Fe-dolomite and ankerite (Figure 33c, d and Figure 25), as the saturation of ankerite and dolomite exceeds the one of siderite at temperatures >150°C (Bénézeth et al. 2013). Fe, Mg and Ca necessary for the precipitation of dolomite or ankerite (Reaction 12), stems from the interaction of the hydrothermal fluids with the host rocks (biotite: chloritisation Reaction 5; plagioclase: albitisation Reaction 13).

$$2HCO_3^- + Ca^{2+} + 0.5Mg^{2+} + 0.5Fe^{2+} \Leftrightarrow Ca(Mg,Fe)(CO_3)_2 + 2H^+ \qquad \text{(Reaction 12)}$$

$$CaAl_2Si_2O_8 + 2Na^+ + 4SiO_2(aq) \Leftrightarrow 2NaAlSi_3O_8 + Ca^{2+} \qquad \text{(Reaction 13)}$$

At the begin of this transition, high activities of HCO_3^- and complexation of aqueous $Fe[(CO_3)_2]^{2-}$ suppress siderite precipitation, but later, after the precipitation of Fe-dolomite, decreasing HCO_3^- activities lead to the precipitation of late-stage siderite II (f in Figure 33c, d). Initiated by an additional fluid batch, indicated by intensive brecciation of Fe-dolomite (Figure 9d), lead to precipitation of ankerite I. At the same time, the late Fe-Co stage II begins to precipitate native Bi II (g), löllingite II (h) and arsenopyrite II (i) (Figure 32d/e). The newly formed aggregates of löllingite II and arsenopyrite II may reach higher Ni concentrations than löllingite I and arsenopyrite I due to increased Ni influx from the host rocks during progressive fluid-rock interaction (cf. löll I/II and asp I/II; Figure 18a). As the concomitant carbonate precipitation and new fluid batches in this stage depletes the fluid in HCO_3^- again, magnetite co-precipitates along with löllingite II and arsenopyrite II (Figure 33e). Still later, temperature decreases and lead to the precipitation of pyrite (j). Subsequent water-rock interaction and adjustment of fO_2 and pH to original conditions lead to the formation of hematite (k) (Figure 33 f).

Late Triassic to Middle Jurassic Ni-Co stage IV (Figure 34): Similar processes of siderite dissolution, simultaneous fO_2 reduction and fluctuating amounts of sulfide, Co and Ni mobilization from the fahlbands induce the formation of the Ni-Co stage IV during T2. High gangue/ore ratios, however, indicate lower concentrations of Fe, Co, Ni and As (note different log a $As(OH)_3$ in Figure 32 and 34: -1 and -3, respectively). This may imply that the stage IV fluids were affected by increased fluid-rock interaction compared to the fluids from the Fe-Co stage II and sulfide stage III. Due to precipitation of pyrite and chalcopyrite during the sulfide stage III, consequential Fe concentration during stage IV should be some orders of magnitude lower than in stage II. In addition, the lack of Fe-arsenides/-sulfarsenides imply this lesser importance of Fe. In order to this, Fe, Co and Ni concentrations were assumed to be in the same range during the Ni-Co stage IV (Figure 34a; log a Fe^{2+}, Co^{2+} and Ni^{2+}: -8). Rammelsbergite and niccolite were formed from diluted fluids with similar Fe, Co and Ni concentrations during initial fluid reduction (Figure 34a). Later, the influx of Fe and S due to mobilization of pyrite from the fahlband favored the formation of gersdorffite together with late skutterudite and magnetite, finally enclosed by siderite and ankerite (Figure 34b).

The relevant fluid path for this model setup first reaches the native Bi stability followed by the precipitation of rammelsbergite (Figure 34a). Due to low As concentration, the rammelsbergite stability field is very narrow between niccolite and $As(OH)_3$; accordingly, the fluid quickly moves into the niccolite stability field. With further precipitation of niccolite, however, rammelsbergite re-appears and encapsulates niccolite (cf. Figure 8a). Low-As fluids will either produce niccolite-dominated ore deposits instead of rammelsbergite or lead to the alternating precipitation of rammelsbergite and niccolite. High HCO_3^- concentrations due to the dissolution of carbonates preclude hematite and magnetite formation at these low metal contents.

In most textures observed from the Valais deposits, however, gersdorffite replaced most of these rammelsbergite generations and shows very high and non-stoichiometric arsenic concentrations (cf. gersdorffite I, Figure 19d). This late occurrence of gersdorffite is expected based on the inferred predominance field between NiS and NiAs or Ni_5As_2 and Ni_9S_8 (Figure 34b, log a H_2S: -5). The fahlband and mobilization of pyrite could represent the source of sulfur since deposits far from sulfide-bearing strata do not show gersdorffite. The continuous shift to higher sulfur contents of gersdorffite I additionally represents this successive increase of the sulfur activity. Since pyrite dissolution connects excess S to a concomitant Fe influx, fahlband mobilization immediately will result in the destabilization of aqueous Fe-complexes (e.g. $Fe[CO_3]_3^{3-}$, $FeCO_{3(aq)}$ and $FeOH^-$) and formation of hematite, magnetite and siderite at the end of the Ni-Co stage IV (Figure 34b, log a Fe^{2+}: -5.25). Representing the latest ores in this stage, precipitation of magnetite III is coupled to skutterudite III and both followed by ankerite II or siderite III (cf. Figure 9g and 7). Since the arsenide predominance fields of the Co-system are situated at lower fO_2 than those of the Ni-system, again skutterudite III forms the last ore phase of the Ni-Co stage IV (cf. Figure 34b and Figure 9g). The presence of Fe-oxides and -carbonates instead of Fe-arsenides and -sulfarsenides implies that redox potential was not sufficient to reach their predominance fields at much lower fO_2.

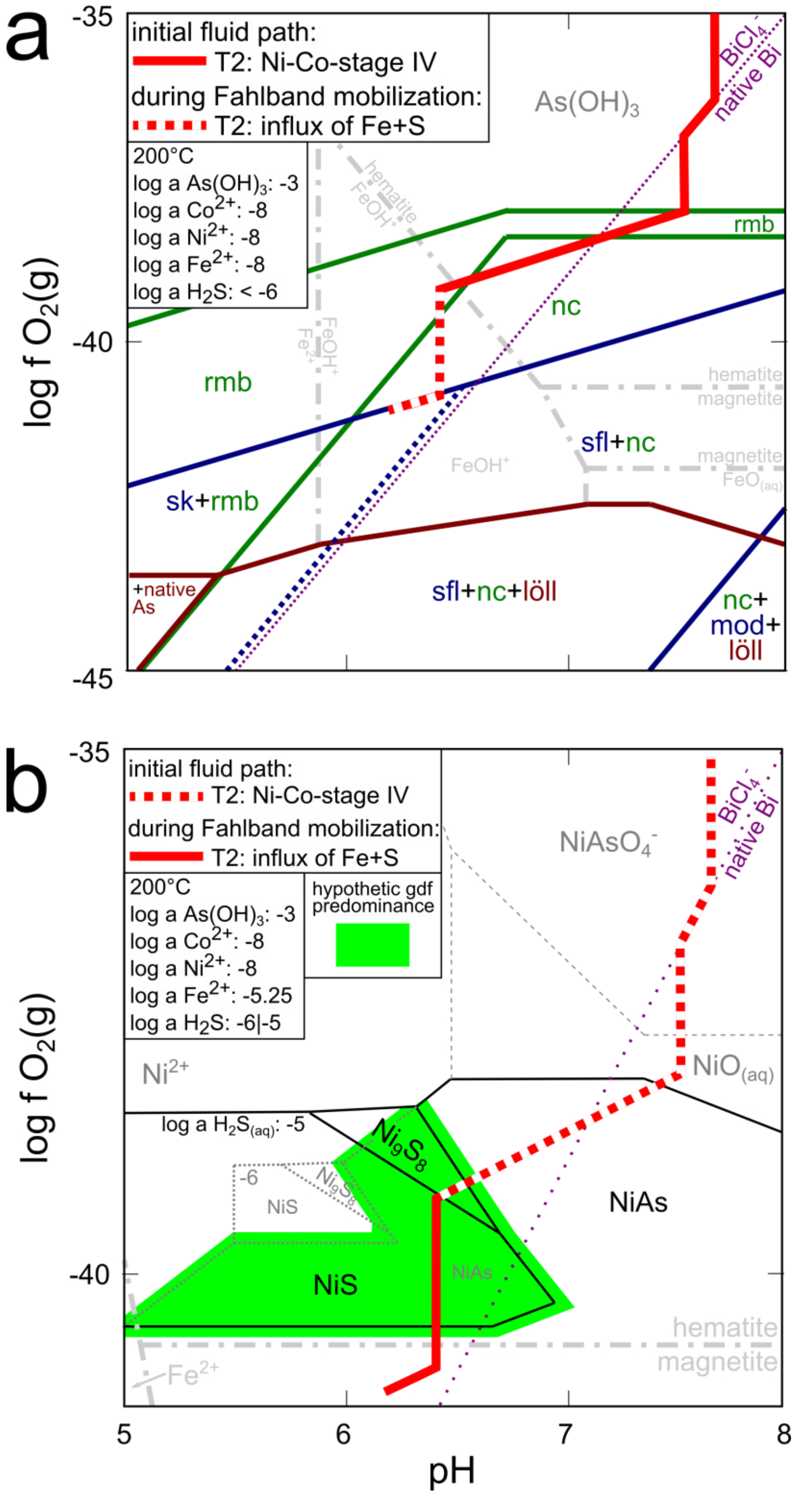

Figure 34: (a) Predominance diagram log fO₂ vs pH for the system Ni/Co-As-H₂O and (b) Ni-As-S-H₂O. (a) The hypothetic fluid path of the Ni-Co stage IV at KB (red path) is compared to those of the Fe-Co stage II (dotted path). In contrast to Figure 32a-e the Ni^{2+} activity is overrunning those of Co^{2+} and Fe^{2+}, and the As concentration is chosen to simulate low water-rock ratios. For gersdorffite, no thermodynamic data are present, but (b) shows the hypothetic position of its predominance as intermediate phase between Ni_9S_8 and Ni_5As_2, Ni_9S_8 and NiAs or NiS and NiAs. (a) Resembles the mineral succession rmb-nc-rmb-native Bi-sk and (b) rmb-nc-rmb & gdf-native Bi & gdf-sk.

9. The Penninic occurrences: comparison to other five-element veins

9.1 Re-classification of arsenide-dominated five element veins

Comparing the hydrochemical and mineralogical trends of the Alpine deposits to similar arsenide-dominated five-element veins worldwide, a complex mineralogical relationship between mono-, di- and triarsenides and their Fe-Co-Ni signatures can be observed. Markl et al. (2016) distinguished between native Ag/Bi-dominated, arsenide-dominated and native As-dominated veins. Following their arguments, slightly different pH values during the continuous fO_2 decrease and ore formation lead to these different vein types. Predominance diagrams of the present study agree with this suggestion as Figure 31 shows that native As is more stable at low pH and arsenides gain a stability to even lower fO_2 at intermediate pH. Furthermore, Figure 32a and b illustrate that native Bi or native Ag precipitation increases continuously to higher fO_2 at higher pH. The following will evaluate the previous classification compared to the predominance diagrams presented in Figure 31 and will discuss in what way fluid composition governs the precipitated arsenides (mono-, di- or triarsenides) and their chemical succession in Fe-Co-Ni space.

The modified model in Figure 32f refines the fluid path proposed for the arsenide-dominated veins of the Odenwald/Germany (Markl et al. 2016; Burisch et al. 2017). In general, a paragenetic sequence of native Ag/Bi ⇨ rammelsbergite ⇨ skutterudite ⇨ safflorite/löllingite was observed, which easily can be explained by equal activities of Fe, Co and Ni in the fluid and a continuous fO_2 decrease. In this case, the Ni phases precipitate at the highest fO_2, followed by the Co and the Fe phases upon fO_2 decrease. The precipitation of arsenides leads to a simultaneous decrease in pH and since the stability of skutterudite is at lower pH than safflorite, the initial pH is essential in determining whether skutterudite precipitates prior to safflorite or vice versa. Therefore, the refined model does not invoke a pH change to more basic conditions to drive the fluid path from the triarsenide to the diarsenide (Markl et al. 2016).

Since skutterudite always occurs as the latest phase in the Valais five-element veins, the present study expects a higher initial pH and lower redox potential for the Valais than for the Odenwald deposits. Therefore, the redox potential is consumed prior the predominance of safflorite is reached. This perfectly fits with the different reduction mechanisms invoked: the redox process via siderite dissolution at Valais (Reaction 14 and 15) has a lower redox potential, consumes H^+ and results in higher pH values than the reduction due to methane influx (Reaction 16 and 17), which was proposed for the Odenwald veins. This higher pH also results from lower H^+/HCO_3^- ratios in Reaction 13 (siderite: $H^+/HCO_3^- = 1.67$) compared to Reaction 15 (methane: $H^+/HCO_3^- = 9$):

$9FeCO_3 + 2BiCl_4^- + 12H_2O \Leftrightarrow 3Fe_3O_4 + 2Bi + 8Cl^- + 9HCO_3^- + 15H^+$ (Reaction 14)

$FeCO_3 + 2H^+ + \frac{1}{4}O_2 \Leftrightarrow Fe^{3+} + HCO_3^- + \frac{1}{2}H_2O$ (Reaction 15)

$0.75CH_4 + 2BiCl_4^- + 2.25H_2O \Leftrightarrow 2Bi + 8Cl^- + 0.75HCO_3^- + 6.75H^+$ (Reaction 16)

$CH_4 + 2O_2 \Leftrightarrow H_2O + HCO_3^- + H^+$ (Reaction 17)

This refined model (based on equal Fe, Co and Ni concentrations) also reproduces the observed continuous evolution of the diarsenides in the Odenwald, evolving from Ni- to Co- and finally Fe-rich compositions. In contrast, fluids at KB must have been dominated by Fe to explain the succession of the Valais diarsenides from Co- to Fe- to Ni-rich. In other words: Co-rich löllingite (i.e. sfl/löll) formed prior to skutterudite and Ni-rich löllingite or rammelsbergite in the Valais deposits due to siderite dissolution, while methane influx in the Odenwald veins resulted in the inverse order.

Different types of the ores from Bou Azzer (Morocco) (Ahmed et al. 2009; Gervilla et al. 2012) show paragenetic sequences and Fe-Co-Ni chemistries as the Fe-Co stage II and Ni-Co stage IV of this work and as the Ni-Co-Fe-dominated veins of the Odenwald (Burisch et al. 2017). Specifically, Fe-Co-dominated veins from Bou Azzer (safflorite-löllingite) show comparable compositions as the löllingites of our Middle Triassic Fe-Co stage II (Figure A6a, Appendix), while Ni-Co-Fe-dominated veins at Bou Azzer show trends comparable to the deposits at the Odenwald (Figure A6b). Concerning Ni-Co-dominated ores, the authors reported a decrease in arsenic during a concomitant Co enrichment within arsenian gersdorffite, which replaced niccolite and rammelsbergite (Bouabdellah et al. 2016) (Figure A6a). This corroborates the observations from our samples, and also resembles paragenetic sequences observed at Schneeberg, Saxony/Germany and Bieber, Spessart/Germany which are characterized by a distinct evolution and a dominance of niccolite (Ni-monoarsenide) and rammelsbergite (Ni-diarsenide) (Wagner and Lorenz 2002; Lipp and Flach 2003b). Generally, the paragenetic sucessions follow either:

(i) native metals → rammelsbergite → niccolite/skutterudite → rammelsbergite+ skutterudite → safflorite → sulfarsenides or

(ii) native metals → niccolite → rammelsbergite → skutterudite → rammelsbergite → safflorite.

In some cases, rammelsbergite precipitates prior to and after niccolite formation, in other cases, however, the first rammelsbergite stage is lacking. As demonstrated above, fluid/rock ratios play an important role to form Ni-Co instead of Ni-Co-Fe ores. Fluids with elevated concentrations of arsenic will lead to the precipitation of sucessions like our Fe-Co stage II or those reported from the Odenwald (cf. Figure 32). Less As in the fluid will reduce the diarsenide stability fields at pH values of

~4 to 10 (Figure 31a-c). The greatest effect occurs in the Ni-rich system and affects the stability of rammelsbergite, but changes are also visible in the Co system. Therefore, low arsenic concentrations favor the precipitation of niccolite, but rammelsbergite can occur in smaller amounts prior to and after niccolite formation as demonstrated in Figure 34a. The löllingite stability in the Fe system is affected by low As concentration, but the occurrence of the Fe-monoarsenide westerveldite at very low fO_2 seems unlikely in hydrothermal systems.

Their different mineral associations and their Fe-Co-Ni evolution of the di- and sulfarsenides suggest a further subdivision of arsenide-dominated five element veins into the following classes (Table 8 and Figure A6a, b):

1. Fe-Co arsenide-dominated ores:
   diarsenide succession: Fe→Co→Ni; examples: Fe-Co stage II, Valais (this study); Co-Fe ores, Bou Azzer (Gervilla et al. 2012).
2. Ni-Co arsenide-dominated ores:
   diarsenide succession: Ni→Co; presence of sulfur; examples: Ni-Co stage IV, Valais (this study); Co-Ni ores, Bou Azzer (Ahmed et al. 2009); Bi-Co-Ni-formation, Schneeberg/Saxony (Lipp and Flach 2003b).
3. Ni-Co-Fe arsenide-dominate ores:
   diarsenide succession: Ni→Co→Fe; examples: Ni ores, Bou Azzer (Gervilla et al. 2012); Ag-/Bi-Ni-Co-Fe-As veins, Odenwald (Burisch et al. 2017).

Table 8: Revised classification of arsenide-dominated five-element veins from observations of this work and references.

Subclass	Fluids	Evolution
1. Fe-Co arsenides	- Fe-dominated fluids - high arsenic - intermediate pH (4-8)	[2]Minor native Ag/Bi encapsulated by arsenides. Under-saturation of niccolite and diarsenide evolution from safflorite to löllingite and late rammelsbergite component with a restriction to löllingite compositions. [Diarsenide evolution: Co ⇨ Fe ⇨ Ni]
2. Ni-Co arsenides	- equal Fe-, Co- and Ni- concentration - low arsenic - intermediate pH (4-8) - higher sulfur than other subclasses	[2, 3, 4]Minor native Ag/Bi encapsulated by arsenides. Supersaturation of niccolite and evolution from rammelsbergite to safflorite. If sulfur is present, arsenian gersdorffite or krutovite supersede diarsenides. Sulfarsenide evolution from Ni- to Co-dominated compositions and increasing sulfur contents. High pH and low arsenic favors niccolite over rammelsbergite. [Di-/sulfarsenide evolution: Ni ⇨ Co & As ⇨ S]
3. Ni-Co-Fe arsenides	- equal Fe-, Co- and Ni- concentration - high arsenic - intermediate pH (4-8)	[1, 2]Minor native Ag/Bi encapsulated by arsenides. Under-saturation of niccolite and diarsenide evolution from rammelsbergite over high safflorite component towards löllingite. [Diarsenide evolution: Ni ⇨ Co ⇨ Fe]

[1]Burisch et al. (2017); [2]Ahmed et al. (2009), Gervilla et al. (2012) and Bouabdellah et al. (2016);
[3]Wagner and Lorenz (2002); [4]Lipp and Flach (2003a)

9.2 Future research

The sub-classification of arsenide-dominated five element mineralizations in chapter 9.1 bases on the mineralogy and Fe-Co-Ni systematics from the Valais (Switzerland), Bou Azzer (Morocco) as well as the Odenwald, Schneeberg and Bieber (Germany). Mineralogies of these arsenide-dominated five-element veins directly reflect the physico-chemical conditions of precipitation. To extend this arsenide-dominated classification to worldwide five-element veins and understand the physico-chemical conditions (i.e. including arsenide-dominated, native As-dominated and native Ag/Bi-dominated), however, a further comprehensive literature review about paragenetic sequences and detailed chemical evolutions in the Fe-Co-Ni, As-S and Ag-Bi spaces are necessary. Especially well investigated high grade deposits such as Cobalt-Gowganda, Great Bear Lake and Thunder Bay (Canada), Kongsberg (Norway), Jáchymov (Czech Republic) and well investigated low grade occurrences such as Wittichen and Wenzel (Schwarzwald, Germany), Dobšiná (Carpathians, Slovakia), San Juan de Plan and Crescencia (Pyrenees, Spain) must additionally be considered in future works.

Although the thermodynamic model calculations in chapter 8.7 explain the frequently occurring mineralogical shifts between mono-, di- and triarsenides as well as the Ni→Co→Fe transition due to simple fluid reduction, this work focuses almost entirely on the Law of Mass Action, neglecting the need for mass balance. Therefore, quantitative models are not possible without robust thermodynamic data of all mineral species (i.e. triarsenides, Ni-diarsenides, Co-Ni-sulfarsenides and native Bi). Additionally, the most problematic consequence due to the lack of thermodynamic data is that several reactions of aqueous-aqueous species redistribution and aqueous-solid equilibria run simultaneously and are therefore not considered by the approach of distinct reaction paths of single reactions. For the calculation of “real” fluid evolution paths, however, a complete and consistent thermodynamic database comprising the whole and complex Na-Ca-Cl-Fe-Co-Ni-Bi-Ag-As-S-HCO_3^--H_2O system is necessary. In addition, more details about differences in the physico-chemical conditions, caused by the diversity of reducing agents such as siderite, hydrocarbons, graphite or even H_2S fluids, and more knowledge about the present metal and arsenic concentrations within the fluids will help to understand these fascinating hydrothermal systems in detail.

In spite of these limitations, this work presents the first (but still very simplified) model approach how the observed mineral successions may have been formed while concentrations (and therefore activities) successively modify during ore precipitation. A more detailed approach that considers the above mentioned problems, however, is proposed by Scharrer et al. (in. prep.).

10. Summary and Conclusion

The various Bi-Co-Ni-Fe-As-S-(U) occurrences in the Middle Penninic rocks of the Valais part of the Alps are typical examples of five-element veins according to ore mineralogy, geotectonic setting and formation conditions. The deposits at Kaltenberg, Grand Praz and Pipji show a comparable chemical and mineralogical evolution, similar fluid sources and formation ages.

The ore content of the carbonate-hosted deposits initially formed during water-rock interaction of descending fluids with preexisting siderite veins. During the further evolution of the hydrothermal system, Ni, Co and S were mobilized from the adjacent sulfide-rich strata of layered schists and amphibolites. Siderite dissolution at temperatures of 200-300°C and oxidation of Fe^{2+} to Fe^{3+} triggered the redox process required for the formation of native bismuth and arsenides. The accompanied precipitation of hematite and magnetite confirms the potential of Fe^{2+} minerals such as siderite to cause five-element vein formation besides other reducing agents like hydrocarbons, which were proposed by Markl et al. (2016). Additionally chloritisation of biotite and co-precipitation of Fe^{3+}-bearing Fe-Ti-oxides favored this fluid reduction via fluid-host rock interaction. Raman spectroscopy results of fluid inclusions do not support the presence of hydrocarbons in these Alpine five-element veins. Therefore, it is reasonable that fluids in disequilibrium with siderite and other redox-active Fe-minerals can cause fO_2 shifts, which cause the combined formation of arsenides, sulfarsenides and Fe-oxides.

Mineral textures and U-Pb ages constrain a primary five-element vein formation of löllingite-skutterudite-carbonate-dominated veins during the Middle Triassic (Fe-Co stage II; ~233±10 Ma), niccolite-gersdorffite-skutterudite-carbonate-dominated veins during the Late Triassic to Middle Jurassic (Ni-Co stage IV; ~188±32 Ma) and a remobilization stage of safflorite-cobaltite-skutterudite-albite-dominated veins during the Late Oligocene to Early Miocene (Co stage Vb; ~11.7±6.6 Ma). The ages of the Fe-Co and Ni-Co stages relate to crustal thinning caused by the breakup of the Alpine Tethys and are consistent with pervasive hydrothermal fluid flow and host rock alteration in other Alpine (Helvetic and Penninic) and European continental regions. The similarity of these ages to the formation age of five-element veins in the Odenwald, Schwarzwald and Erzgebirge (Germany), reveal that interaction of fluids, whose origin and migration depend on the tectonic conditions, favored the precipitation of five-element veins in Central Europe. Tectonic conditions influenced by the Alpine Tethys rift indicate favored conditions in the framework of the specific geochemical and mineralogical environment of the region at this time.

The Late Oligocene to Early Miocene remobilization of the Triassic to Jurassic ores (stage Va) and the metal reprecipitation in later Co ores (stage Vb) is related to Alpine processes. The formation of recrystallized gersdorffite II and niccolite II occurred during the compressive first-order processes of overthrusting, tectonic nappe formation and metamorphism due to the consequent subduction of the Upper Penninic ocean, collision of the Middle Penninic microcontinent and its under-thrusting under the Adriatic plate (~71-44.5 Ma). The Alpine five-element Co-ore precipitation and formation of native Bi as droplet-like trails within the gangue mineralogy, however, happened due to enhanced rock permeability and fluid mobilization as a second-order effect of the reversion from ductile compression to brittle transtensional strike-slip tectonics. Late Alpine lateral escape tectonics due to movements of the Insubric Indenter and tangential stretch within the Western Alpine arc by the progressing West Mediterranean subduction rollback obviously favored Alpine ore formation in this part of the orogeny.

Fluid inclusion microthermometric data records how fluids descended through the cover and basement rocks overlying the deposits at Kaltenberg, Grand Praz and Pipji during the Middle Triassic to Middle Jurassic, thereby being chemically modified. The fluids then interacted with preexisting siderite, showing highly variable entrapment temperatures (200-286°C), salinities (20-35 wt% $CaCl_2$+NaCl) and Ca-Na ratios (0-0.26 Ca/[Ca+Na]) during five-element ore precipitation. Differences in temperature and Ca_{excess} to $Na_{deficit}$ signatures, correlate with different migration paths, depths and fluid-rock interaction intensity. Importantly, only a single fluid is necessary to understand the formation of each deposit. This fluid gained temperature, salinity, Ca-Na-signature and metal content on its descent from the ocean through sediments to its final precipitation as five-element veins by the disequilibrium with reducing siderite.

Sulfur isotope values of the ores reveal the involvement of different sources of sulfur. Sulfate dissolution from Triassic evaporites acted as primary source during fluid descent. Further, a quantitative reduction of sulfate and precipitation as sulfarsenides yield isotopic signatures comparable to Triassic evaporites for the Fe-Co stage II. Very low sulfate concentrations in the fluids are supported by increased As/S ratios of the sulfarsenides and their rare occurrence compared to the large quantities of di- and triarsenides. As the hydrothermal system evolved over the sulfide stage III and Ni-Co stage IV towards the remobilization related to the Alpine orogeny, sulfur isotopic signatures changed towards $\delta^{34}S$ values of the sulfide-rich fahlbands. Stronger involvement of these fahlbands affected previously precipitated five-element veins by the reprecipitation of sulfur-dominated sulfarsenides.

Nevertheless, future work needs a better understanding of thermodynamic parameters to establish detailed and “real” fluid evolution paths including consistent and quantitative models of five-element ore precipitation.

As a very last remark of this work that should contribute to future works –dealing with natural hydrothermal systems that yield very variable mineralogies but originate from comparable processes– the author wants to advise the reader to a famous suggestion of Schrödinger (1985) (in german):

"…verschiedene Ansichten über denselben Gegenstand … müssten, anstatt den Gegensatz zu unterscheiden, die verschiedenen Seiten zu einem Gesamtbild zusammensetzen – ohne Kompromiß, durch welchen … vornherein unwahre Aussagen entstehen …".

11. References

Ahmed AH, Arai S, Ikenne M (2009) Mineralogy and Paragenesis of the Co-Ni Arsenide Ores of Bou Azzer, Anti-Atlas, Morocco Economic Geology 104:249-266

Andrews A (1986) Silver vein deposits: summary of recent research Canadian Journal of Earth Sciences 23:1460-1462

Andrews A, Masliwec A, Morris W, Owsiacki L, York D (1986a) The silver deposits at Cobalt and Gowganda, Ontario. II: An experiment in age determinations employing radiometric and paleomagnetic measurements Canadian Journal of Earth Sciences 23:1507-1518

Andrews A, Owsiacki L, Kerrich R, Strong D (1986b) The silver deposits at Cobalt and Gowganda, Ontario. I: Geology, petrography, and whole-rock geochemistry Canadian Journal of Earth Sciences 23:1480-1506

Ansermet S (2012) Mines et minéraux du Valais - II. Anniviers et Tourtemagne. Porte-Plumes, Ayer

Armstrong JT (1991) Quantitative elemental analysis of individual microparticles with electron beam instruments. In: Heinrich KFJ, Newbury DE (eds) Electron probe quantitation. Springer, pp 261-315

Barber DJ, Wenk HR (2001) Slip and dislocation behaviour in dolomite European Journal of Mineralogy 13:221-243

Bastin ES (1939) The nickel-cobalt-native silver ore type Economic Geology 34:1-40

Bayliss P (1968) Crystal Structure of Disordered Gersdorffite Am Mineral 53:290-293

Bayliss P (1982) A further crystal structure refinement of gersdorffite Am Mineral 67:1058-1064

Bejaoui J, Bouhlel S, Sellami A, Braham A (2014) Geology, mineralogy and fluid inclusion study of Oued Jebs Pb–Zn–Sr deposit; comparison with the Bou Grine deposit (diapirs zone, Tunisian atlas) Arabian Journal of Geosciences 7:2483-2497

Bénézeth P, Stefánsson A, Gautier Q, Schott J (2013) Mineral solubility and aqueous speciation under hydrothermal conditions to 300 C–the carbonate system as an example Reviews in Mineralogy and Geochemistry 76:81-133

Bergemann C et al. (2017) Th-Pb ion probe dating of zoned hydrothermal monazite and its implications for repeated shear zone activity: An example from the Central Alps, Switzerland Tectonics 36:671-689

Bergerat F (1987) Stress fields in the European platform at the time of Africa-Eurasia collision Tectonics 6:99-132

Berry LG (1971) The Silver-arsenide Deposits of the Cobalt-Gowganda Region, Ontario The Canadian Mineralogist 11:1-429

Berthold C, Bjeoumikhov A, Brügemann L (2009) Fast XRD2 Microdiffraction with Focusing X-Ray Microlenses Particle & Particle Systems Characterization 26:107-111

Bethke CM, Yeakel S (2015) GWB Essentials Guide vol 11. The Geochemist's Workbench®. Aqueous Solutions LLC, Champaign, IL

Beyssac O, Goffé B, Chopin C, Rouzaud J (2002a) Raman spectra of carbonaceous material in metasediments: a new geothermometer Journal of metamorphic Geology 20:859-871

Beyssac O, Rouzaud J-N, Goffé B, Brunet F, Chopin C (2002b) Graphitization in a high-pressure, low-temperature metamorphic gradient: a Raman microspectroscopy and HRTEM study Contributions to Mineralogy and Petrology 143:19-31

Biju-Duval B, Dercourt J, Le Pichon X (1977) From the Tethys ocean to the Mediterranean seas: a plate tectonic model of the evolution of the western Alpine system. In: Biju-Duval B, Montadert L (eds) International Symposium on the Structural History of the Mediterranean Basins, Split 1976. Technip., Paris, pp 143-164

Blanc P, Lassin A, Piantone P, Azaroual M, Jacquemet N, Fabbri A, Gaucher EC (2012) Thermoddem: A geochemical database focused on low temperature water/rock interactions and waste materials Applied Geochemistry 27:2107-2116

Bodnar JB, Vityk MO (1994) Interpretation of Microthermometric data for H_2O-NaCl fluid inclusions. Fluid Inclusion in Minerals: Methods and Applications. Virginia Tech, Blacksburg, VA

Bons PD, Fusswinkel T, Gomez-Rivas E, Markl G, Wagner T, Walter B (2014) Fluid mixing from below in unconformity-related hydrothermal ore deposits Geology 42:1035-1038

Bons PD, Gomez-Rivas E (2013) Gravitational fractionation of isotopes and dissolved components as a first-order process in crustal fluids Economic Geology 108:1195-1201

Bottomley DJ, Gregoire DC, Raven KG (1994) Saline ground waters and brines in the Canadian Shield: geochemical and isotopic evidence for a residual evaporite brine component Geochimica et Cosmochimica Acta 58:1483-1498

Bouabdellah M, Maacha L, Levresse G, Saddiqi O (2016) The Bou Azzer Co–Ni–Fe–As (±Au±Ag) District of Central Anti-Atlas (Morocco): A Long-Lived Late Hercynian to Triassic Magmatic-Hydrothermal to Low-Sulphidation Epithermal System. In: Mineral Deposits of North Africa. Springer, pp 229-247

Boyle R, Dass A (1971) The origin of the native silver veins at Cobalt, Ontario. In: Berry L (ed) The silver-arsenide deposits of the Cobalt-Gowganda region, Ontario, vol The Canadian Mineralogist 11. vol 1. pp 414-429

Bridgman P (1935) Polymorphism, principally of the elements, up to 50,000 kg/cm 2 Physical Review 48:893

Bucher K, Stober I (2010) Fluids in the upper continental crust Geofluids 10:241-253

Bugge A (1931) Gammel og ny geologi ved Kongsberg sölvverk Norsk Geologisk Tidsskrift 12:123

Burisch M, Gerdes A, Walter BF, Neumann U, Fettel M, Markl G (2017) Methane and the origin of five-element veins: Mineralogy, age, fluid inclusion chemistry and ore forming processes in the Odenwald, SW Germany Ore Geology Reviews 81:42-61

Burisch M, Marks MA, Nowak M, Markl G (2016) The effect of temperature and cataclastic deformation on the composition of upper crustal fluids—An experimental approach Chemical Geology 433:24-35

Burke EA (2001) Raman microspectrometry of fluid inclusions Lithos 55:139-158

Bussy F, Sartori M, Thélin P (1996) U-Pb zircon dating in the middle Penninic basement of the Western Alps (Valais, Switzerland) Swiss Bulletin of Mineralogy and Petrology 76:81–84

Castelli D, Giorza A, Rossetti P, Piana F, Clerico F (2011) Le mineralizzazioni a siderite e arseniuri di cobalto-ferro-nichel del vallone di Arnàs (Usseglio, valli di Lanzo). In: Rossi M, Porticelli F, Gattiglia A (eds) Terre rosse, pietre verdi e blu cobalto. Miniere a Usseglio. Prima raccolta di studi. Museo civico alpino "Arnaldo Tazzetti, pp 21-36

Champagnac J-D, Sue C, Delacou B, Tricart P, Allanic C, Burkhard M (2006) Miocene lateral extrusion in the inner western Alps revealed by dynamic fault analysis Tectonics 25

Changkakoti A, Morton R (1986) Electron microprobe analyses of native silver and associated arsenides from the Great Bear Lake silver deposits, Northwest Territories, Canada Canadian Journal of Earth Sciences 23:1470-1479

Changkakoti A, Morton R, Gray J, Yonge C (1986) Oxygen, hydrogen, and carbon isotopic studies of the Great Bear Lake silver deposits, Northwest Territories Canadian Journal of Earth Sciences 23:1463-1469

Cheilletz A, Levresse G, Gasquet D, Azizi-Samir M, Zyadi R, Archibald DA, Farrar E (2002) The giant Imiter silver deposit: Neoproterozoic epithermal mineralization in the Anti-Atlas, Morocco Mineralium Deposita 37:772-781

Clavel M (1963) Contribution à l'étude métallogénique de la région d'Allemont (Massif de Belledonne-Isère)-Alpes françaises. Université de Nancy

Conte A, Cuccuru S, Naitza S, Oggiano G, Secchi F, Tocco S Into the depth of the Arburèse vein system: arsenide-sulfide evolution in the Ni-Co ores. In: 2nd European Mineralogical Conference, 2016. pp 601-601

Davisson ML, Criss RE (1996) Na-Ca-Cl relations in basinal fluids Geochimica et Cosmochimica Acta 60:2743-2752

Della Valle G (1988) Contribution à l'interprétation métallogénique des fahlbandes et des veines polymétalliques du Val d'Anniviers et du Val de Tourtemagne (Valais). Lausanne

Della Valle G (1992) Les fahlbandes et les veines polymétalliques du Val d'Anniviers et du Val de Tourtmagne (Zone pennique, Valais) Materiaux pour la Geologie de la Suisse, Serie Geotechnique 81:1-62

Einaudi MT, Hedenquist JW, Inan EE (2003) Sulfidation state of fluids in active and extinct hydrothermal systems: transitions from porphyry to epithermal environments Special Publication-Society of Economic Geologists 10:285-314

Escher A, Hunziker J, Marthaler M, Masson H, Sartori M, Steck A (1997) Geologic framework and structural evolution of the western Swiss-Italian Alps Deep structure of the Swiss Alps: results of NRP 20:205-221

Essarraj S, Boiron M-C, Cathelineau M, Banks DA, Benharref M (2005) Penetration of surface-evaporated brines into the Proterozoic basement and deposition of Co and Ag at Bou Azzer (Morocco): Evidence from fluid inclusions Journal of African Earth Sciences 41:25-39

Essarraj S, Boiron M-C, Cathelineau M, Tarantola A, Leisen M, Boulvais P, Maacha L (2016) Basinal Brines at the Origin of the Imiter Ag-Hg Deposit (Anti-Atlas, Morocco): Evidence from LA-ICP-MS Data on Fluid Inclusions, Halogen Signatures, and Stable Isotopes (H, C, O) Economic Geology 111:1753-1781

Essarraj S, Boiron M-C, Cathelineau M, Tarantola A, Leisen M, Hibti M (2017) Mineralogy and ore fluid chemistry of the Roc Blanc Ag deposit, Jebilet Hercynian massif, Morocco Journal of African Earth Sciences 127:175-193

Etiope G, Sherwood Lollar B (2013) Abiotic methane on Earth Reviews of Geophysics 51:276-299

Fanlo I, Subías I, Gervilla F, Manuel J (2006) Textures and compositional variability in gersdorffite from the Crescencia Ni–(Co–U) showing, Central Pyrenees, Spain: primary deposition or re-equilibration? The Canadian Mineralogist 44:1513-1528

Fanlo I, Subías I, Gervilla F, Paniagua A, García B (2004) The composition of Co–Ni–Fe sulfarsenides, diarsenides and triarsenides from the San Juan de Plan deposit, Central Pyrenees, Spain The Canadian Mineralogist 42:1221-1240

Feitzinger G, Günther W, Brunner A (1998) Bergbau-und Hüttenaltstandorte im Bundesland Salzburg. Land Salzburg,

Feuerbacher B (1989) Phase formation in metastable solidification of metals Materials science reports 4:1-40

Franklin J, Kissin S, Smyk M, Scott S (1986) Silver deposits associated with the Proterozoic rocks of the Thunder Bay District, Ontario Canadian Journal of Earth Sciences 23:1576-1591

Frezzotti ML, Tecce F, Casagli A (2012) Raman spectroscopy for fluid inclusion analysis Journal of Geochemical Exploration 112:1-20

Friedrich OM (1933) Die Erze und der Vererzungsvorgang der Kobalt-Nickel-Lagerstätte Zinkwand-Vöttern in den Schladminger Tauern Berg- und Hüttenmännisches Jahrbuch 81:1–44

Frisch W (1979) Tectonic progradation and plate tectonic evolution of the Alps Tectonophysics 60:121-139

Fuchs HW (1988) Erzmikroskopische und mineralchemische Untersuchungen der Erzvorkommen Zinkwand - Vöttern in den Niederen Tauern bei Schladming Archiv für Lagerstättenforschung der Geologischen Bundesanstalt 9:33-45

Garson M, Mitchell A (1981) Precambrian ore deposits and plate tectonics Developments in Precambrian Geology 4:689-731

Genier F, Epard J-L, Bussy F, Magna T (2008) Lithostratigraphy and U-Pb zircon dating in the overturned limb of the Siviez-Mischabel nappe: a new key for Middle Penninic nappe geometry Swiss Journal of Geosciences 101:431-452

Gerdes A, Zeh A (2006) Combined U–Pb and Hf isotope LA-(MC-) ICP-MS analyses of detrital zircons: comparison with SHRIMP and new constraints for the provenance and age of an Armorican metasediment in Central Germany Earth and Planetary Science Letters 249:47-61

Gerdes A, Zeh A (2009) Zircon formation versus zircon alteration—new insights from combined U–Pb and Lu–Hf in-situ LA-ICP-MS analyses, and consequences for the interpretation of Archean zircon from the Central Zone of the Limpopo Belt Chemical Geology 261:230-243

Gerlach H (1873) Die Bergwerke des Kantons Wallis. Verlag A. Galerini, Sitten, Switzerland

Gervilla F, Fanlo I, Colás V, Subías I (2012) Mineral compositions and phase relations of Ni–Co–Fe arsenide ores from the Aghbar mine, Bou Azzer, Morocco The Canadian Mineralogist 50:447-470

Giggenbach WF (1997) Relative importance of thermodynamic and kinetic processes in governing the chemical and isotopic composition of carbon gases in high-heatflow sedimentary basins Geochimica et Cosmochimica Acta 61:3763-3785

Gilliéron F (1946) Geologisch-petrographische Untersuchungen an der Ni-Co-Lagerstätte Kaltenberg (Turtmanntal, Wallis): mit einem Anhang, Die Bergbauarbeiten in den Gruben Kaltenberg, Grand Praz, Gollyre und Plantorin im Sommer 1942. Kuemmerly und Frey,

Gleeson S, Yardley B (2002) Extensional veins and Pb-Zn mineralisation in basement rocks: the role of penetration of formation brines. In: Water-Rock Interaction. Springer, pp 189-205

Gleeson S, Yardley BD, Munz I, Boyce A (2003) Infiltration of basinal fluids into high-grade basement, South Norway: sources and behaviour of waters and brines Geofluids 3:33-48

Glodny J, Ring U, Kühn A (2008) Coeval high-pressure metamorphism, thrusting, strike-slip, and extensional shearing in the Tauern Window, Eastern Alps Tectonics 27

Goldstein RH, Reynolds TJ (1994) Fluid inclusion petrography. In: Goldstein RH, Reynolds TJ (eds) Systematics of Fluid Inclusions in Diagenetic Minerals, vol Short Course Notes Volume 31. The Society for Sedimentary Geology, Tulsa, Oklahoma, pp 69-86

Golyshev S, Padalko N, Pechenkin S (1981) Fractionation of stable oxygen and carbon isotopes in carbonate systems Geochemistry International 18:85-99

Goodz M, Watkinson D, Smejkal V, Pertold Z (1986) Sulphur-isotope geochemistry of silver–selpnarsenide vein mineralization, Cobalt, Ontario Canadian Journal of Earth Sciences 23:1551-1567

Halls C, Stumpfl E The five-element (Ag-Bi-Co-Ni-As) vein deposit–A critical appraisal of the geological environments in which it occurs and of the theories affecting its origin: Proceedings. In: 24 th International Geological Congress, Montreal, Sec, 1972. p 540

Haßler K, Taubald H, Markl G (2014) Carbon and oxygen isotope composition of Pb-, Cu-and Bi-carbonates of the Schwarzwald mining district: Carbon sources, first data on bismutite and the discovery of an oxidation zone formed by ascending thermal water Geochimica et Cosmochimica Acta 133:1-16

Helgeson H (1974) Chemical interaction of feldspars and aqueous solutions The Feldspars:184-217

Henwood WJ (1871) Observations on Metalliferous Deposits: On the Mines of Chalanches d'Allemont, in France Transactions of the Royal Geological Society of Cornwall 8:517-529

Heusler C (1876) Ueber das Vorkommen von Nickel-und Cobalterzen mit gediegenem Wismuth an der Crête d'Omberenza im Kanton Wallis Zeitschrift der Deutschen Geologischen Gesellschaft 28:238-247

Hießleitner G (1929) Die Nicketkobalterzvorkommen Zinkwand-Vöttern in den Niederen Tauern bei Schladming Berg- und Hüttenmännisches Jahrbuch 77:104-123

Hinsbergen DJ, Vissers RL, Spakman W (2014) Origin and consequences of western Mediterranean subduction, rollback, and slab segmentation Tectonics 33:393-419

Hirschi H (1939) Radiohalos im Chlorit der Erzlagerstätte von Kaltenberg im Turtmanntal (Wallis) Bulletin suisse de minéralogie et pétrographie 19:221-223

Hofmann B, Knill M (1996) Geochemistry and genesis of the Lengenbach Pb-Zn-As-Tl-Ba-mineralisation, Binn Valley, Switzerland Mineralium Deposita 31:319-339

Holloway JR (1984) Graphite-CH4-H2O-CO2 equilibria at low-grade metamorphic conditions Geology 12:455-458

Huang E-P, Huang E, Yu S-C, Chen Y-H, Lee J-S, Fang J-N (2010) In situ Raman spectroscopy on kerogen at high temperatures and high pressures Physics and Chemistry of Minerals 37:593-600

Huttenlocher H (1925) Zur Kenntnis verschiedener Erzgange aus dem Pennmikum und ihre Metamorphose Swiss Bulletin of Mineralogy and Petrology 5:181-229

Jambor J (1971) Origin of the silver veins of the Cobalt-Gowganda region. In: Berry L (ed) The silverarsenide deposits of the Cobalt-Gowganda region, Ontario, vol The Canadian Mineralogist 11. vol 1. pp 402-413

Johnson J, Anderson G, Parkhurst D (2000) Database 'thermo. com. V8. R6. 230,'Rev. 1.11 Lawrence Livermore Natl Lab, Livermore, California

Kampschulte A, Strauss H (2004) The sulfur isotopic evolution of Phanerozoic seawater based on the analysis of structurally substituted sulfate in carbonates Chemical Geology 204:255-286

Keil K (1933) Über die Ursachen der charakteristischen Paragenesenbildung von gediegen Silber und gediegen Wismut mit den Kobalt-Nickel-Eisen-Arseniden auf den Gängen der Kobalt-Nickel-Wismut-Silber-Erzformation im sächsisch-böhmischen Erzgebirge und dem Cobalt-District Neues Jahrbuch für Mineralogie Geologie und Paläontologie 66:407-424

Kerrich R, Strong D, Andrews A, Owsiacki L (1986) The silver deposits at Cobalt and Gowganda, Ontario. III: Hydrothermal regimes and source reservoirs-evidence from H, O, C, and Sr isotopes and fluid inclusions Canadian Journal of Earth Sciences 23:1519-1550

Kiefer S, Majzlan J, Chovan M, Števko M (2017) Mineral compositions and phase relations of the complex sulfarsenides and arsenides from Dobšiná (Western Carpathians, Slovakia) Ore Geology Reviews 89:894-908

Kissin S (1988) Nickel-cobalt-native silver (five-element) veins: A riftrelated ore type North American ConL on Tectonic Control of Ore Deposits and the Vertical and Horizontal Extent of Ore Systems Univ Missouri Press, Rolla:268-279

Kissin SA (1992) Five-element (Ni-Co-As-Ag-Bi) veins Geoscience Canada 19

Knill MD (1995) Geochemistry and genesis of the metadolomite-hosted Pb-Zn-As-Tl-Ba-deposit and Lengenbach, Binn Valley, Switzerland.

Kotková J, Kullerud K, Šrein V, Drábek M, Škoda R (2017) The Kongsberg silver deposits, Norway: Ag-Hg-Sb mineralization and constraints for the formation of the deposits Mineralium Deposita:1-15

Kretschmar U, Scott S (1976) Phase relations involving arsenopyrite in the system Fe-As-S and their application Canadian mineralogist 14:364-386

Kutina J Regularities in the distribution of hypogene mineralization along rift structures. In: Intern. Geol. Congress, 24th Sess., Sec, 1972. pp 65-73

Leblanc M (1986) Co–Ni arsenide deposits, with accessory gold, in ultramafic rocks from Morocco Canadian Journal of Earth Sciences 23:1592-1602

Levresse G et al. (2016) Degassing as the Main Ore-Forming Process at the Giant Imiter Ag–Hg Vein Deposit in the Anti-Atlas Mountains, Morocco. In: Mineral Deposits of North Africa. Springer, pp 85-106

Li Y (2017) Immiscible CHO fluids formed at subduction zone conditions Geochem Pespect Lett 3:12-21

Lipp U, Flach S (2003a) Wismut-, Kobalt-, Nickel-und Silbererze im Nordteil des Schneeberger Lagerstättenbezirkes

Lipp U, Flach S (2003b) Wismut-, Kobalt-, Nickel-und Silbererze im Nordteil des Schneeberger Lagerstättenbezirkes vol 10. Bergbau in Sachsen. Sächsisches Landesamt für Umwelt und Geologie, Dresden

Ludwig KR (2012) Isoplot v. 3.75: A Geochronological Toolkit for Microsoft Excel vol 5. Berkeley Geochronological Center, University of California at Berkeley,

Mancktelow N (1985) The Simplon Line: a major displacement zone in the western Lepontine Alps Eclogae Geologicae Helvetiae 78:73-96

Mandel N, Donohue J (1971) The refinement of the crystal structure of skutterudite, CoAs3 Acta Crystallographica Section B: Structural Crystallography and Crystal Chemistry 27:2288-2289

Manuel J, Subías I, Fanlo I, Arranz E, Gervilla F (2018) Multi-isotope survey on the metallogenesis of the hydrothermal Co-Ni deposits in the Alpine Central Pyrenees of Spain Ore Geology Reviews

Markl G, Burisch M, Neumann U (2016) Natural fracking and the genesis of five-element veins Mineralium Deposita 51:703-712

Markley MJ, Teyssier C, Cosca MA, Caby R, Hunziker JC, Sartori M (1998) Alpine deformation and 40Ar/39Ar geochronology of synkinematic white mica in the Siviez-Mischabel Nappe, western Pennine Alps, Switzerland Tectonics 17:407-425

Marshall DD, Diamond LW, Skippen GB (1993) Silver transport and deposition at Cobalt, Ontario, Canada; fluid inclusion evidence Economic Geology 88:837-854

Maurer H, Burkhard M, Deichmann N, Green A (1997) Active tectonism in the central Alps: contrasting stress regimes north and south of the Rhone Valley Terra Nova 9:91-94

McCollom TM (2003) Formation of meteorite hydrocarbons from thermal decomposition of siderite (FeCO 3) Geochimica et Cosmochimica Acta 67:311-317

Meisser N (1990) Etude minéralogique des gîtes métallifères au sud-est d'Ayer. Lausanne

Meisser N (2003) Le district cobalto-nickélifère d’Anniviers - Tourtemagne (Valais, Suisse) Minaria Helvetica 23b:57-64

Merino E (1975) Diagenesis in Tertiary sandstones from Kettleman North Dome, California. I. Diagenetic mineralogy Journal of Sedimentary Research 45

Milesi V et al. (2015) Formation of CO 2, H 2 and condensed carbon from siderite dissolution in the 200–300° C range and at 50MPa Geochimica et Cosmochimica Acta 154:201-211

Milesi V, Prinzhofer A, Guyot F, Benedetti M, Rodrigues R (2016) Contribution of siderite–water interaction for the unconventional generation of hydrocarbon gases in the Solimões basin, north-west Brazil Marine and Petroleum Geology 71:168-182

Millonig LJ, Gerdes A, Groat LA (2012) U–Th–Pb geochronology of meta-carbonatites and meta-alkaline rocks in the southern Canadian Cordillera: a geodynamic perspective Lithos 152:202-217

Mindat.org (2017) the mineral and locality database. Hudson Institute of Mineralogy.

Mücke A, Chaudhuri JB (1991) The continuous alteration of ilmenite through pseudorutile to leucoxene Ore geology reviews 6:25-44

Munson RA (1968) The synthesis of iridium disulfide and nickel diarsenide having the pyrite structure Inorganic Chemistry 7:389-390

Munz I, Yardley B, Gleeson S (2002) Petroleum infiltration of high-grade basement, South Norway: Pressure-Temperature-time-composition (P–T–t–X) constraints Geofluids 2:41-53

Naitza S, Conte A, Cuccuru S, Funedda A, Oggiano G, Secchi F (2017) A tentative chronological scheme for the Variscan metallogenic peaks in Sardinia ITALIAN JOURNAL OF GEOSCIENCES:386-386

Naitza S, Garbarino C, Secchi F, Tocco S The Ni-Co hydrothermal ore deposits of the Arburese Variscan district (SW Sardinia, Italy). In: Geoitalia 2013, Pisa, Italy, 2013.

Naitza S, Secchi F, Oggiano G, Cuccuru S New observations on the Ni-Co ores of the southern Arburese Variscan district (SW Sardinia, Italy). In: EGU General Assembly Conference Abstracts, 2015.

Neumann H (1944) Silver deposits at Kongsberg Nor Geol Unders 162:1-133

Nickel E (1970) The application of ligand-field concepts to an understanding of the structural stabilities and solid-solution limits of sulphides and related minerals Chemical Geology 5:233-241

Nievergelt P, Liniger M, Froitzheim N, Mählmann RF (1996) Early to mid Tertiary crustal extension in the Central Alps: The Turba mylonite zone (eastern Switzerland) Tectonics 15:329-340

Norman DI (1978) Ore deposits related to the Keweenawan rift. In: Petrology and geochemistry of continental rifts. Springer, pp 245-253

O'Neil JR, Clayton RN, Mayeda TK (1969) Oxygen isotope fractionation in divalent metal carbonates The Journal of Chemical Physics 51:5547-5558

Oberti R, Cannillo E, Toscani G (2012) How to name amphiboles after the IMA2012 report: rules of thumb and a new PC program for monoclinic amphiboles Periodico di Mineralogia 81:257-267

Ondrus P et al. (2003a) Ore-forming processes and mineral parageneses of the Jáchymov ore district Journal of GEOsciences 48:157-192

Ondrus P, Veselovsky F, Gabasova A, Hlousek J, Srein V (2003b) Geology and hydrothermal vein system of the Jáchymov (Joachimsthal) ore district Journal of GEOsciences 48:3-18

Ondrus P et al. (2003c) Primary minerals of the Jáchymov ore district Journal of GEOsciences 48:19-147

Oxtoby DW (1992) Homogeneous nucleation: theory and experiment Journal of Physics: Condensed Matter 4:7627

Paar DIDW, Chen T (1979) Gersdorffit (in zwei Strukturvarietäten) und Sb-hältiger Parkerit, Ni3 (Bi, Sb) 2 S2, von der Zinkwand, Schladminger Tauern, Österreich Tschermaks mineralogische und petrographische Mitteilungen 26:59-67

Passchier CW, Trouw RA (2005) Microtectonics vol 1. Springer Science & Business Media,

Petruk W (1968) Mineralogy and origin of the Silverfields silver deposit in the Cobalt area, Ontario Economic Geology 63:512-531

Pfiffner OA (2015) Geologie der Alpen. 3 edn. Haupt UTB, Berne

Rasbury ET, Cole JM (2006) Directly Dating Sedimentary Rocks The Paleontological Society Papers 12:77-105

Rasbury ET, Cole JM (2009) Directly dating geologic events: U-Pb dating of carbonates Reviews of Geophysics 47

Ring U, Gerdes A (2016) Kinematics of the Alpenrhein-Bodensee graben system in the Central Alps: Oligocene/Miocene transtension due to formation of the Western Alps arc Tectonics 35:1367-1391

Robinson B, Badham J (1974) Stable isotope geochemistry and the origin of the Great Bear lake silver deposits, Northwest Territories, Canada Canadian Journal of Earth Sciences 11:698-711

Robinson B, Ohmoto H (1973) Mineralogy, fluid inclusions, and stable isotopes of the Echo Bay U-Ni-Ag-Cu deposits, Northwest Territories, Canada Economic Geology 68:635-656

Romer R, Schneider J (2010) Hydrothermal vein mineralization–markers for post-Variscan brittle deformation of Western Europe: a geochronologic review. in ‘‘From the Cadomian Active Margin to the Variscan Orogen: the pre-Mesozoic geology of Saxo-Thuringia (NE Bohemian Massif)’’, U. Linnemann & RL Romer, eds Pre-Mesozoic Geology of Saxo-Thuringia From the Cadomian Active Margin to the Variscan Orogen: the Pre-Mesozoic Geology of Saxo-Thuringia (NE Bohemian Massif) Schweizerbart Science Publishers, Stuttgart:347-360

Roseboom EH (1962) Skutterudites (Co, Ni, Fe)As_{3-x}; composition and cell dimensions American Mineralogist 47:310-327

Rosenbaum G, Lister GS, Duboz C (2002) Reconstruction of the tectonic evolution of the western Mediterranean since the Oligocene Journal of the Virtual Explorer 8:107-130

Rossi M, Gattiglia A (2013) Terre rosse, pietre verdi e blu cobalto. Miniere a Usseglio. Seconda raccolta di studi. Museo civico alpino "Arnaldo Tazzetti,

Rossi M, Gattiglia A (2015) Le Complexe Minier Médiéval de Punta Corna (Usseglio, Turin, Italie) Minaria Helvetica 35

Rossi M et al. (2013) The Ancient Mines of Usseglio (Torino, Italy) Multi-Year Programme of Recording, Study, Preservation and Cultural Development of the Archaeological Mining Heritage in an Alpine Valley. In: Filippi M, Bosák P (eds) 16th Iinternational Congress of Speleology, Proceedings. pp 242-246

Sampson E, Hriskevich ME (1957) Cobalt-arsenic minerals associated with aplites, at Cobalt, Ontario Economic Geology 52:60-75

Sartori M (1990) L'unité du Barrhorn (Zone pennique, Valais, Suisse) vol 6. Lausanne

Sartori M, Della Valle G (1986) La minéralisation en nickel et cobalt du Pipjitälli (Turtmanntal, Valais) Eclogae Geologicae Helvetiae 79:685-703

Sartori M, Gouffon Y, Marthaler M (2006) Harmonisation et définition des unités lithostratigraphiques briançonnaises dans les nappes penniques du Valais Eclogae Geologicae Helvetiae 99:363-407

Schafer M (1996) Ba-Co-Ni-Vererzungen im Turtmanntal und Geochemie am Omen Roso (Wallis, Schweiz). University Basel

Schaltegger U (1990) Post-magmatic resetting of Rb-Sr whole rock ages—a study in the Central Aar Granite (Central Alps, Switzerland) Geologische Rundschau 79:709-724

Schaltegger U, Gebauer D (1999) Pre-Alpine geochronology of the central, western and southern Alps Schweizerische Mineralogische und Petrographische Mitteilungen 79:79-87

Scharrer M, Kreissl S, Markl G (in. prep.) The mineralogical variability of hydrothermal native element-arsenide (five-element) mineralizations Mineralium Deposita

Schmidt C (1920) Texte explicatif de la Carte des Gisements des matières premières minérales de la Suisse 1: 500000. Impr. E. Birkhaeuser & Cie,

Schmutz L (1986) Mine de Plantorin (Valais) Ein Beispiel fiir mineralbildende Prozesse auf Erzlagerstiitten Min Helv 6b:1-44

Schrödinger E (1985) Mein Leben, meine Weltansicht. Zsolnay, Wien, Hamburg

Schumacher ME (2002) Upper Rhine Graben: role of preexisting structures during rift evolution Tectonics 21

Schumer BN, Andrade MB, Evans SH, Downs RT (2017) A new formula and crystal structure for nickelskutterudite,(Ni, Co, Fe) As3, and occupancy of the icosahedral cation site in the skutterudite group American Mineralogist 102:205-209

Schwinn G, Wagner T, Baatartsogt B, Markl G (2006) Quantification of mixing processes in ore-forming hydrothermal systems by combination of stable isotope and fluid inclusion analyses Geochimica et Cosmochimica Acta 70:965-982

Seward D, Mancktelow NS (1994) Neogene kinematics of the central and western Alps: Evidence from fission-track dating Geology 22:803-806

Sibson RH (1996) Structural permeability of fluid-driven fault-fracture meshes Journal of Structural Geology 18:1031-1042

Smyk MC, Watkinson DH (1990) Sulphide remobilization in Archean volcano-sedimentary rocks and its significance in Proterozoic silver vein genesis, Cobalt, Ontario Canadian Journal of Earth Sciences 27:1170-1181

Spiridonov EM, Chvileva TN The Boundary Between Gersdorffite NiAsS and Krutovite $NiAs_2$. In: TRANSACTIONS DOKLADY-RUSSIAN ACADEMY OF SCIENCES EARTH SCIENCE SECTIONS, 1996. SCRIPTA TECHNICA, INC., A WILEY COMPANY, pp 119-123

Stampfli G, Borel GD, Marchant R, Mosar J (2002) Western Alps geological constraints on western Tethyan reconstructions Journal of the Virtual Explorer 8:77

Stampfli G, Mosar J, Marquer D, Marchant R, Baudin T, Borel G (1998) Subduction and obduction processes in the Swiss Alps Tectonophysics 296:159-204

Stampfli GM, Borel G (2002) A plate tectonic model for the Paleozoic and Mesozoic constrained by dynamic plate boundaries and restored synthetic oceanic isochrons Earth and Planetary Science Letters 196:17-33

Staude S, Bons PD, Markl G (2009) Hydrothermal vein formation by extension-driven dewatering of the middle crust: An example from SW Germany Earth and Planetary Science Letters 286:387-395

Staude S, Mordhorst T, Nau S, Pfaff K, Brügmann G, Jacob DE, Markl G (2012a) Hydrothermal carbonates of the Schwarzwald ore district, southwestern Germany: Carbon source and conditions of formation using δ18O, δ13C, 87Sr/86Sr, and fluid inclusions The Canadian Mineralogist 50:1401-1434

Staude S, Wagner T, Markl G (2007) Mineralogy, mineral compositions and fluid evolution at the Wenzel hydrothermal deposit, Southern Germany: Implications for the formation of Kongsberg-type silver deposits The Canadian Mineralogist 45:1147-1176

Staude S, Werner W, Mordhorst T, Wemmer K, Jacob DE, Markl G (2012b) Multi-stage Ag–Bi–Co–Ni–U and Cu–Bi vein mineralization at Wittichen, Schwarzwald, SW Germany: geological setting, ore mineralogy, and fluid evolution Mineralium Deposita 47:251-276

Steck A (2008) Tectonics of the Simplon massif and Lepontine gneiss dome: deformation structures due to collision between the underthrusting European plate and the Adriatic indenter Swiss Journal of Geosciences 101:515-546

Steele-MacInnis M, Bodnar R, Naden J (2011) Numerical model to determine the composition of H 2 O–NaCl–CaCl 2 fluid inclusions based on microthermometric and microanalytical data Geochimica et Cosmochimica Acta 75:21-40

Stober I, Bucher K (2004) Fluid sinks within the earth's crust Geofluids 4:143-151

Sue C, Tricart P (2002) Widespread post-nappe normal faulting in the Internal Western Alps: a new constraint on arc dynamics Journal of the Geological Society 159:61-70

Takahashi M, Nagahama H, Masuda T, Fujimura A (1998) Fractal analysis of experimentally, dynamically recrystallized quartz grains and its possible application as a strain rate meter Journal of Structural Geology 20:269-275

Thélin P, Sartori M, Burri M, Gouffon Y, Chessex R (1993) The pre-Alpine basement of the briançonnais (Wallis, Switzerland). In: Pre-Mesozoic Geology in the Alps. Springer, pp 297-315

Truesdell A (1974) Oxygen isotope activities and concentrations in aqueous salt solutions at elevated temperatures: consequences for isotope geochemistry Earth and Planetary Science Letters 23:387-396

Wagner T, Lorenz J (2002) Mineralogy of complex Co-Ni-Bi vein mineralization, Bieber deposit, Spessart, Germany Mineralogical Magazine 66:385-407

Walter BF, Burisch M, Markl G (2016) Long-term chemical evolution and modification of continental basement brines–a field study from the Schwarzwald, SW Germany Geofluids 16:604-623

Walter BF, Immenhauser A, Geske A, Markl G (2015) Exploration of hydrothermal carbonate magnesium isotope signatures as tracers for continental fluid aquifers, Schwarzwald mining district, SW Germany Chemical Geology 400:87-105

Wilkerson G, Deng Q, Llavona R, Goodell PC (1988) Batopilas mining district, Chihuahua Economic Geology 83:1721-1736

Wissing S, Pfiffner O-A (2002) Structure of the eastern Klippen nappe (BE, FR): Implications for its Alpine tectonic evolution Eclogae Geologicae Helvetiae 95:381-398

Wissing S, Pfiffner O-A (2003) Numerical models for the control of inherited basin geometries on structures and emplacement of the Klippen nappe (Swiss Prealps) Journal of structural geology 25:1213-1227

Woodtli R (1985) Projet UROMINE, recherches minières exécutées au Valais par les universités de Lausanne, Fribourg et Genève Swiss Nat Sc Foundation, National Project

Woodtli R, Jaffé FC, von Raumer J (1987) Prospection minière en Valais: le projet Uromine. Schweizerische Geotechnische Kommission [Komm. Kümmerly & Frey],

Wopenka B, Pasteris JD (1993) Structural characterization of kerogens to granulite-facies graphite: applicability of Raman microprobe spectroscopy The American Mineralogist 78:533-557

Yoon W, Paik J, LaCourt D, Perepezko J (1986) The effect of pressure on phase selection during nucleation in undercooled bismuth Journal of Applied Physics 60:3489-3494

Yoshida N, Hattori T, Komai E, Wada T (1999) Methane formation by metal-catalyzed hydrogenation of solid calcium carbonate Catalysis letters 58:119-122

Ypma PJM (1963) Rejuvenation of ore deposits as exemplified by the Belledonne metalliferous province. PhD thesis, University Leiden, Netherlands

Ypma PJM (1972) The Multistage Emplacement of the Chalances (France) Ni-Co-Bi-As-Sb-Ag Deposits and the Nature of the Mineralization Solutions. In: Campbell FA, Wilson HDB (eds) International Geological Congress, vol 24. Campbell, Montreal, p 525

Zheng Y-F, Hoefs J (1993) Carbon and oxygen isotopic covariations in hydrothermal calcites Mineralium Deposita 28:79-89

Ziegler PA, Stampfli GM (2001) Late Palaeozoic-Early Mesozoic plate boundary reorganization: collapse of the Variscan orogen and opening of Neotethys vol 25. Annali Museo Civico Science Naturali, Brescia

Zingg MA (1989) Die Siviez-Mischabel Decke. Entstehung und Entwicklung eines Altkristallins und seiner Vererzungen (Wallis, Schweiz). PhD thesis, ETH Zürich

12. Appendix

Table A1: Compared sample numbers of the Musée cantonal de géologie in Lausanne and Naturhistorisches Museum in Bern used at this study to our sample numbers (SK).

Sample number			Used for					
this study	Musée cantonal de géologie	Naturhistorisches Museum	preparation	EMPA arsenides/sulfides	EMPA carbonates	Isotopes	fluid inclusions	Further information on sample label
SK103	8843.03*			✓	✓	S		
SK105	MS52.2		thin section	✓	✓			
SK107	MS67		thin section	✓	✓		✓	
SK108	MS62.4		thin section	✓	✓			
SK109	8842.01*		thin section		✓			
SK112.1	GP5 (8834.01)*		thin section	✓	✓			
SK112.2	GP5 (8834.01)*		FI thin section					
SK113	8834.03*		thin section	✓	✓		✓	
SK114	8834.02*		thin section	✓	✓			
SK115	MS403		handpicked chalcopyrite			S		
SK116	MS288.2		FI thin section					
SK117	MS52.4		thin section	✓	✓			
SK118	MS52.1		FI thin section					
SK119	8843.02*		thin section	✓	✓	S		
SK120	MS62.5		FI thin section					
SK121	MS48		FI thin section					
SK122	MS62.5		FI thin section					
SK123		7635	polished drill core	✓		U-Pb (low U)		Ni- & Co-Erze/Kaltenbg., Turtmann-Tal/Gesch. Dr. Fehlmann/Studiengesellsch.f.N…/Bern.I.1946
SK126		7637	FI thin section				✓	Ni- & Co-Erze/Kaltenberg Turtmann-Tal/Gesch. Dr. Fehlmann/Studiengesellsch.f.N…/Bern.I.1946
SK130		32883	polished drill core	✓				Minerai de Nickel et Cobalt et purites de fer. Dans Barytime. Vallée de Tourtmagne
SK134	8834.02*		polished drill core			U-Pb (dating SK114)		
SK135	GP5 (8834.01)*		polished drill core			U-Pb (low U)		
SK136	GP5 (8834.01)*		polished drill core			U-Pb (dating SK112.1)		
SK137	8834.03*		polished drill core			U-Pb (low U)		
SK138	8843.04*		handpicked arsenopyrite			S		
SK140	MS124		handpicked pyrite			S		

*no sample number existed, used sample number chosen continuing according the rack numbers the samples took from (Musée cantonal de géologie Musée cantonal de géologie, Lausanne)

Table A2: Classification of different mineral generations ordered after their temporal occurrence. Also shown their used abbreviations, mineral formulas and occurrence within the different deposits KB, Pi, GPg and GPr.

Stage	**Mineral generation** In Figure 8	**abbreviation**	**Formula**	**KB**	**PI**	**GPg**	**GPr**
Prior to stage 1	siderite I	sd I	$FeCO_3$	✓	✓	✓	✓
Stage 1 (Fe-Co early)	native Bi I	Bi I	Bi	✓✓			
	magnetite I	mt I	Fe_3O_4	✓			
	löllingite I	löll I	$FeAs_2$	✓✓			
	arsenopyrite I	asp I	FeAsS	✓✓	✓✓		
	skutterudite I	sk I	$CoAs_3$	✓✓	✓✓	✓✓	
	skutterudite II	sk II		✓✓	✓✓	✓✓	
Stage 1 (Fe-Co intermediate)	siderite II	sd II		✓	✓		
	dolomite	Fe-dol	$(Mg,Fe)Ca(CO_3)_2$	✓	✓	✓	✓
Stage 1 (Fe-Co late)	native Bi II	Bi II		✓✓	✓		
	magnetite II	mt II		✓✓			
	löllingite II	löll II		✓✓	✓	✓	
	arsenopyrite II	asp II		✓✓	✓	✓	
	ankerite I	ank I	$(Fe,Mg)Ca(CO_3)_2$	✓	✓	✓	✓
Stage 2 (sulfide)	Early sulfides: pyrite, bismuthinite; py, bmt		FeS_2, Bi_2S_3	✓			
	Late sulfides: bornite, chalcopyrite; brn, ccp		Cu_5FeS_4, $CuFeS_2$	✓			
	quartz I	qtz I	SiO_2	✓	✓	✓	✓
	calcite I	cal I	$CaCO_3$	✓			
	calcite II	cal II		✓			
	tetrahedrite	ttr	$Cu_{10}(Fe,Zn)_2Sb_4S_{13}$		✓		
	pentlandite	pn	$(Fe,Ni)_9S_8$				✓
	maucherite	mau	$Ni_{11}As_8$				✓
	millerite	mlr	NiS				✓
	End of stage: hematite	hm	Fe_2O_3	✓			
Stage 3 (Ni-Co)	rammelsbergite	rmb	$NiAs_2$	✓			
	symplectic krutovite I	krut I	$NiAs_{2-x}S_x$; $x<0.5$		✓✓	✓✓	
	veinlet krutovite II	krut II			✓✓	✓✓	
	niccolite I	nc I	NiAs	✓✓			✓✓
	tučekite	tuč	$Ni_9Sb_2S_8$				✓✓
	native Bi III	Bi III		✓✓			
	gersdorffite I	gdf I	NiAsS	✓✓			✓✓
	magnetite III	mt III		✓✓			
	skutterudite III	sk III		✓✓			
	siderite III	sd III		✓			
	ankerite II	ank II		✓	✓	✓	✓
Stage 4 (remobilization)	niccolite II	nc II					✓✓
	gersdorffite II	gdf II		✓✓	✓		✓✓
	Alpine cobaltite	Alpine cbt	CoAsS	✓✓			
	Alpine arsenopyrite	Alpine asp		✓✓			
	krutovite III	krut III			✓✓		
	ankerite III	ank III		✓			
	quartz II	qtz II		✓	✓		✓
	chlorite	chl	$(Fe,Mg)_5Al_2Si_3O_{10}(OH)_8$	✓			
	uraninite	urn	UO_2	✓			
	magnetite IV	mt IV		✓✓			
Stage 4 (five-element Co stage)	native Bi IV	bi IV		✓✓			
	Fe-Ni safflorite	Fe-Ni sfl	$CoAs_2$	✓			
	Fe-Ni cobaltite	Fe-Ni cbt		✓✓			
	arsenopyrite III	asp III		✓			
	skutterudite IV	sk IV		✓✓	✓✓		
	sericite	ser	$(K,Na)Al_3Si_3O_{10}(OH)_2$	✓			✓
	albite	ab	$NaAlSi_3O_8$	✓			
	epidote	epi	$Ca_2FeAl_2Si_3O_{12}(OH)$	✓			
	calcite III	cal III		✓		✓	✓
	magnetite IV	mt IV		✓			
	löllingite III	löll III			✓		
Stage 5 (alteration/weathering)	cobaltite-gersdorffite ss	cbt-gdf	$(Co,Ni)AsS$	✓✓			
	niccolite III	nc III		✓✓			✓
	annabergite	anb	$Ni_3(AsO_4)_2{\cdot}8H_2O$	✓	✓	✓	✓
	erythrite	ery	$Co_3(AsO_4)_2{\cdot}8H_2O$	✓	✓	✓	✓

✓✓: major occurrence; ✓: minor/rare occurrences

Table A3: WDS conditions used for EMPA analysis of the arsenides. sulfarsenides and sulfides at the JEOL JXA-8900RL and Cameca SX100 microprobes.

element	fluorescence line analyzed	crystal	standard	counting time (peak|background) [s]	detection limit [ppm]
JEOL JXA-8900RL					
As	Lα	TAP	GaAs	16|8	640[1]
S	Kα	PETJ	FeS$_2$	16|8	100[1]
Fe	Kα	LIFH	FeS$_2$	16|8	75[1]
Co	Kα	LIFH	Co-metal	16|8	70[1]
Ni	Kα	LIF	Ni-metal	30|15	85[1]
Cu	Kβ	LIF	Cu-metal	30|15	590[1]
Zn	Kα	LIFH	Zn-metal	16|8	100[1]
Bi	Lα	LIF	Bi-metal	16|8	490[1]
Ag	Lα	PETJ	Ag-metal	30|15	220[1]
Sb	Lα	PETJ	stibnite	30|15	140[1]
Se	Lα	TAP	PbSe	30|15	160[1]
Pb	Mα	PETJ	galena	16|8	640[1]
Hg	Lα	LIF	HgS	30|15	360[1]
Cameca SX100					
As	Lα	TAP	GaAs	20|10	1510[2]
S	Kα	PET	chalcopyrite	20|10	320[2]
Bi	Lα	LLIF	Bi$_2$Se$_3$	20|10	5800[2]
Zn	Kα	LIF	sphalerite	20|10	1280[2]
Se	Lα	TAP	Bi$_2$Se$_3$	20|10	930[2]
Pb	Mα	LPET	PbTe	20|10	1670[2]
Cu	Kβ	LIF	chalcopyrite	20|10	6120[2]
Co	Kα	LLIF	CoO	20|10	700[2]
Ag	Lα	PET	Ag$_2$Te	20|10	1362[2]
Ni	Kα	LLIF	NiO	20|10	450[2]
Fe	Kα	LIF	chalcopyrite	20|10	510[2]
Sb	Lα	LPET	Sb$_2$S$_3$	20|10	450[2]
Hg	Lα	LLIF	HgS	20|10	4260[2]

[1] as 1σ; [2] as 3σ;

Table A4: WDS conditions used for EMPA analysis of the carbonates.

element	fluorescence line analyzed	crystal	standard	counting time (peak|background) [s]	detection limit [ppm]*
Fe	Kα	LIF	hematite	16|8	140
Mg	Kα	TAP	periclase	16|8	60
Ca	Kα	PETH	dolomite	16|8	100
Mn	Kα	PETJ	rhodonite	16|8	150
Zn	Kα	LIF	Zn-metal	30|15	480
Sr	Lα	PETH	SrTiO$_3$	30|15	350
Ba	Lα	PETH	barite	30|15	230
Si[a]	Kα	TAP	diopside	16|8	-
As[a]	Lα	TAP	GaAs	16|8	-
C[b]	Kα	LDE1H	calcite	30|15	-

[a] detected to identify erroneous measurements due to compounds of arsenides or silicates; [b] detected to improve matrix correction; *detection limit upon oxide components

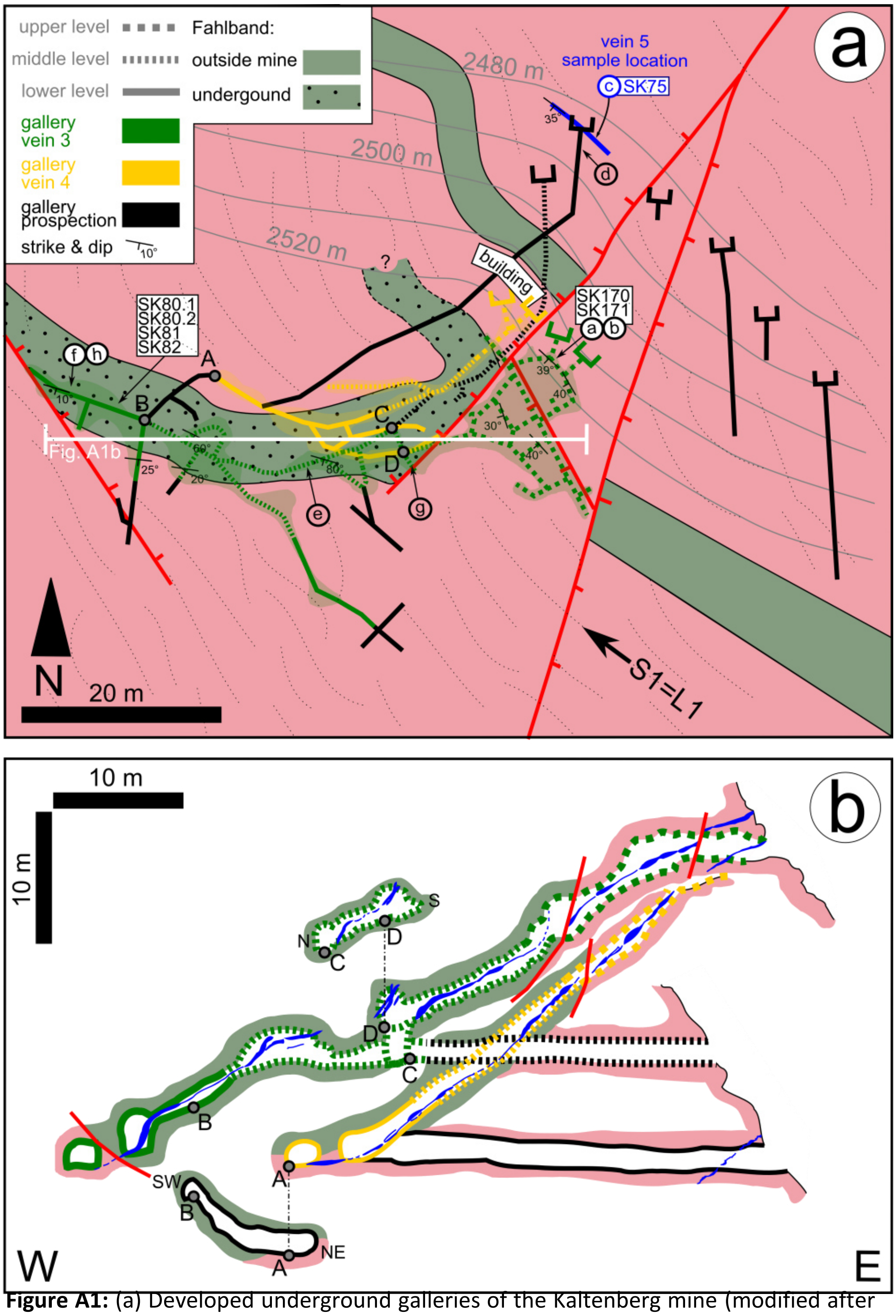

Figure A1: (a) Developed underground galleries of the Kaltenberg mine (modified after Widmer 2013). Green lines show the galleries on vein 3, yellow lines those of vein 4, the blue line the development of vein 5, black lines prospection galleries and red lines corresponds to normal faults. Underground outcrop of the Fahlband relates to its observation within the vein 3 galleries. Different line styles indicate different levels of the veins mentioned in the text and Figure 4a. Capital letters correlate to locations in Figure A1b, small letters and boxes to the locality of photographs in Figures 5a-e and sample localities used for U-Pb age determination. Dotted lines indicate the direction of S1 foliation. (b) Projected W-E profile of the mine galleries at Kaltenberg (modified after Gilliéron 1946). For colors and line-styles, see Figure A1a. Blue color indicates the distribution of main ore shoots; capital letters are for orientation.

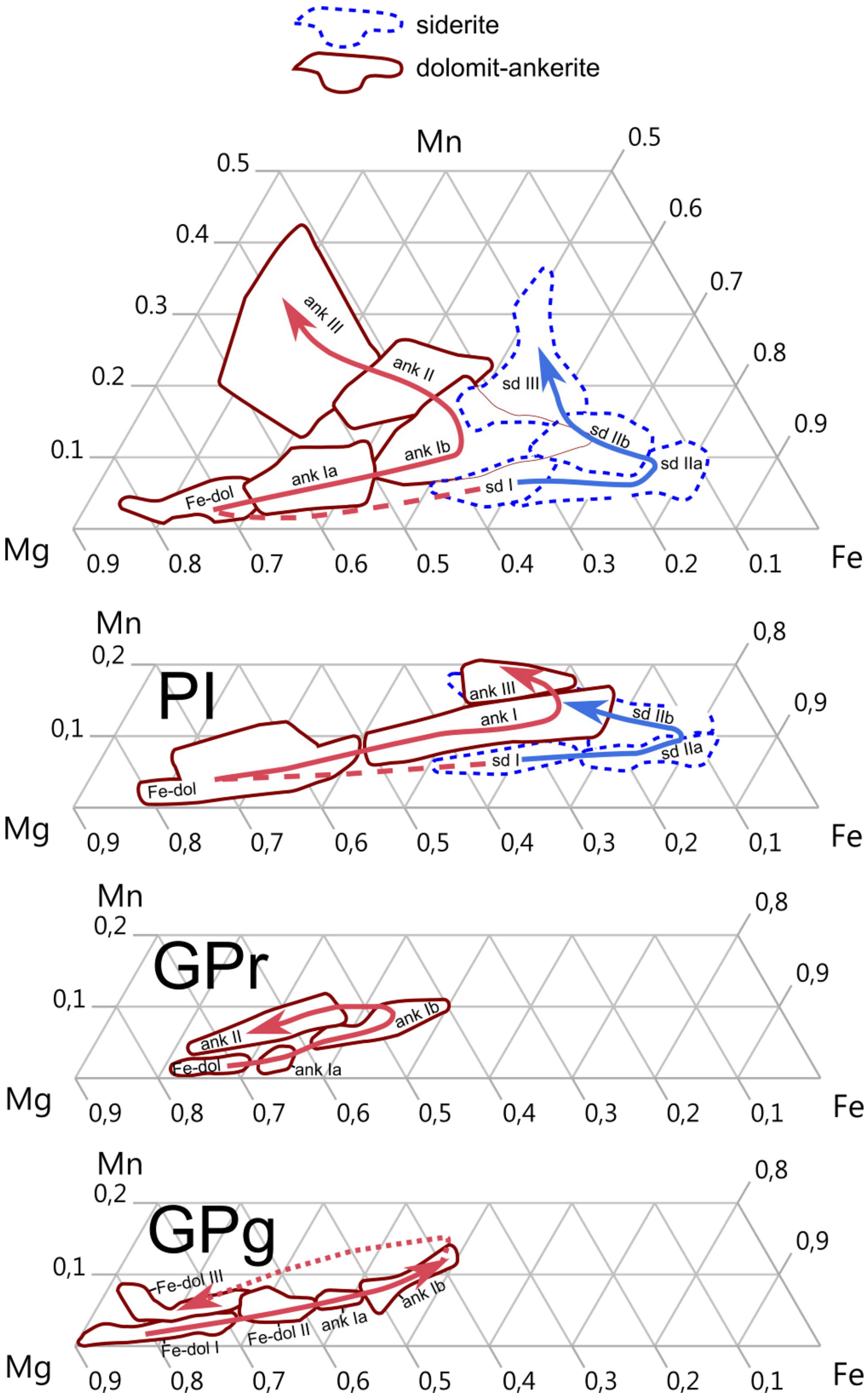

Figure A2: Comparison of carbonate chemistry between PI, GPr and GPg.

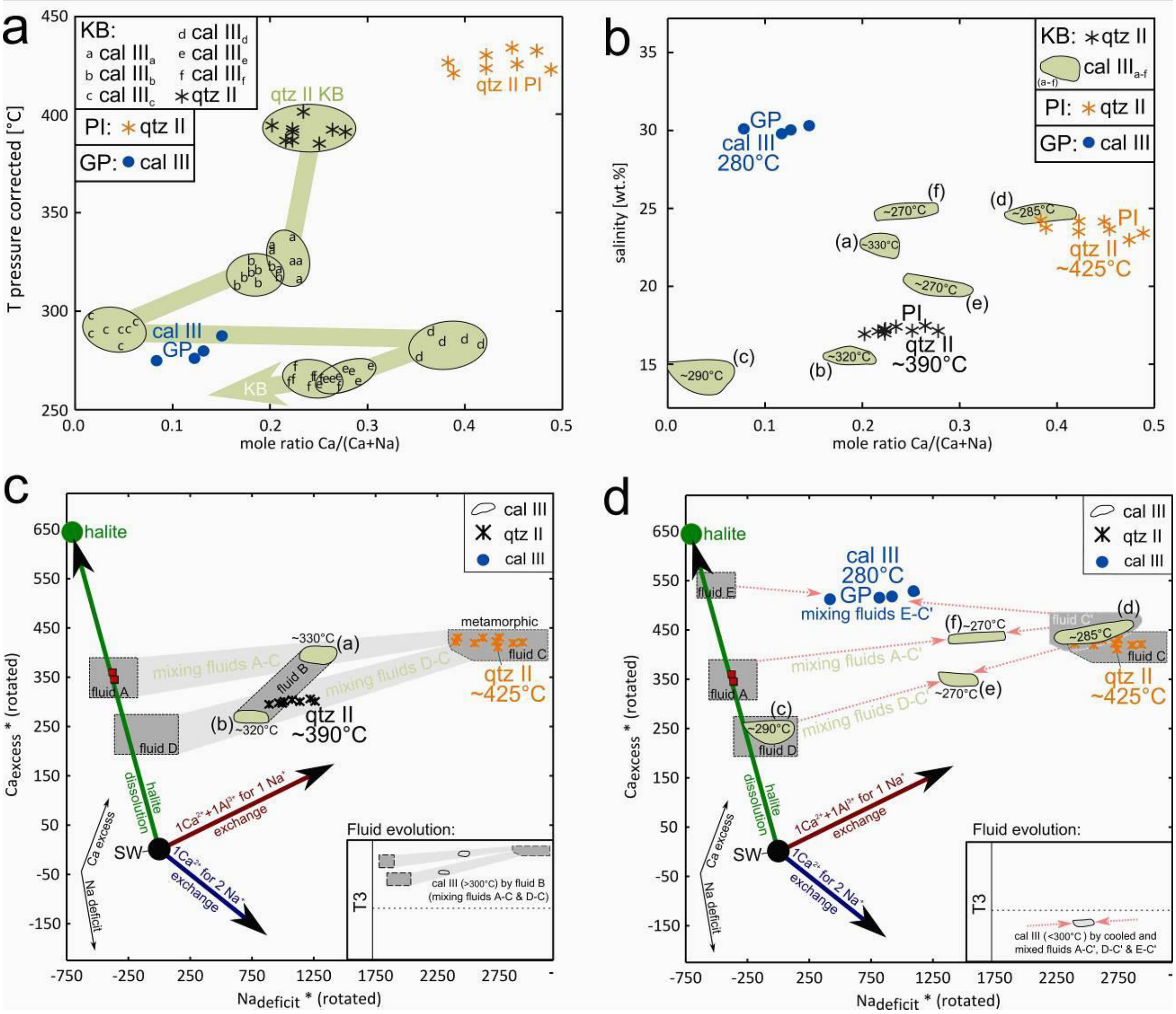

Figure A3: Evolution of the Fluid inclusion temperatures and chemistries during the Alpine Orogeny. For further information about successive cooling and mixing processes, see text.

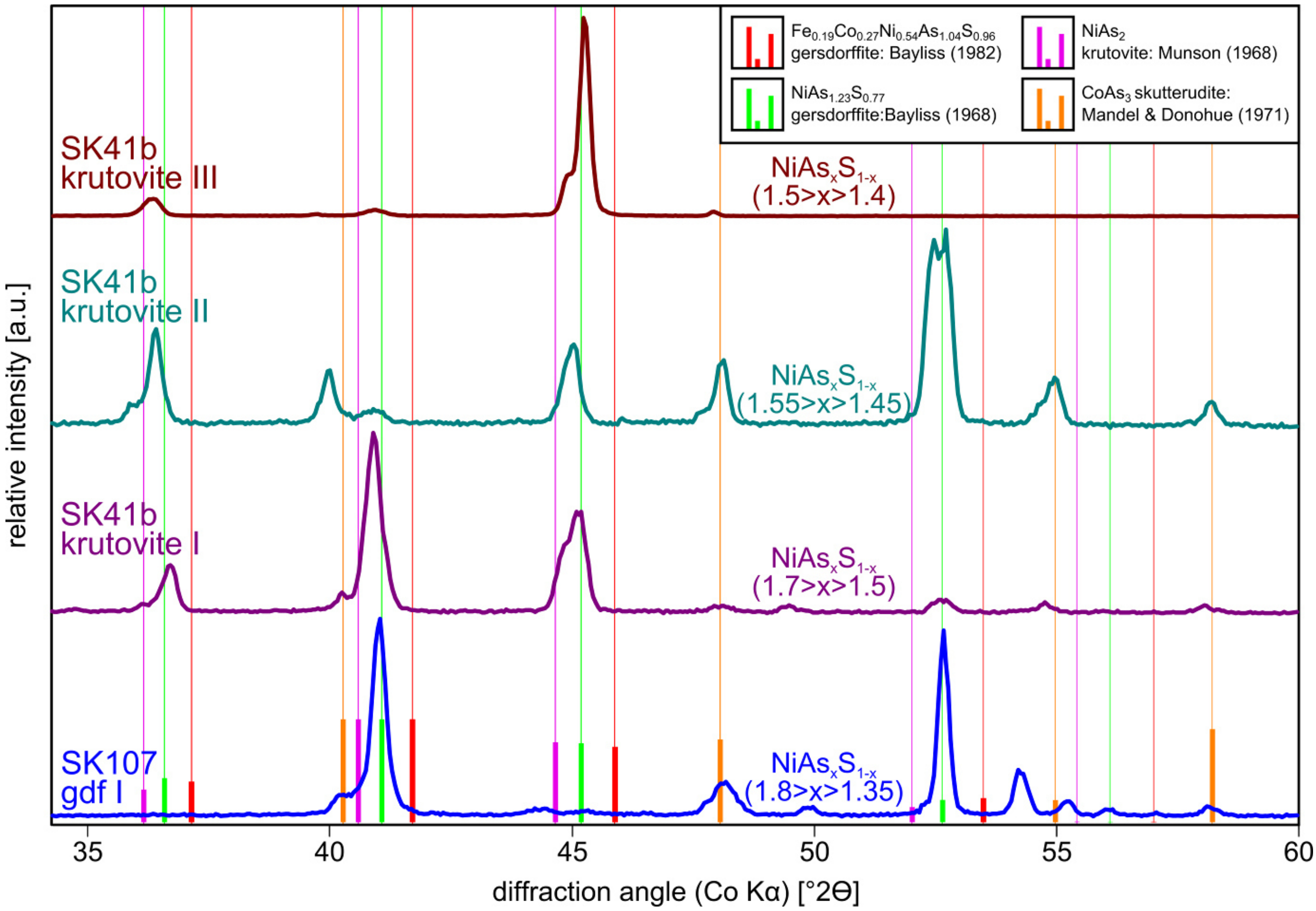

Figure A4: µ-XRD results for differentiation between common gersdorffite structures and other, which show a intermixture of sulfarsenides with more complex structures. See text for further information.

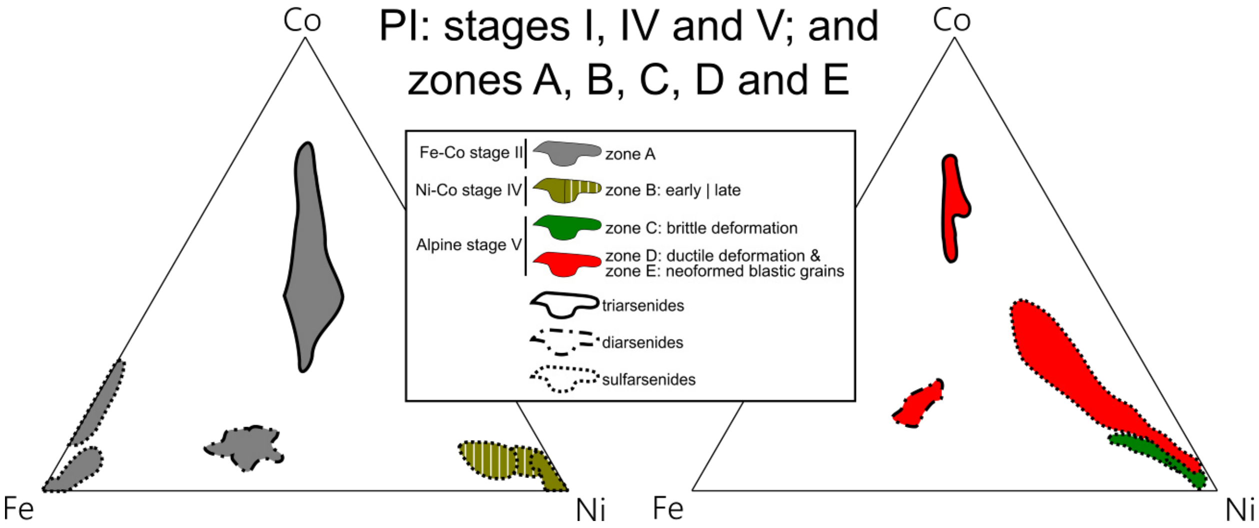

Figure A5: Compared evolution of the Fe-Co-Ni compositions during stage II, IV and V at the different zones A-E in Pipji.

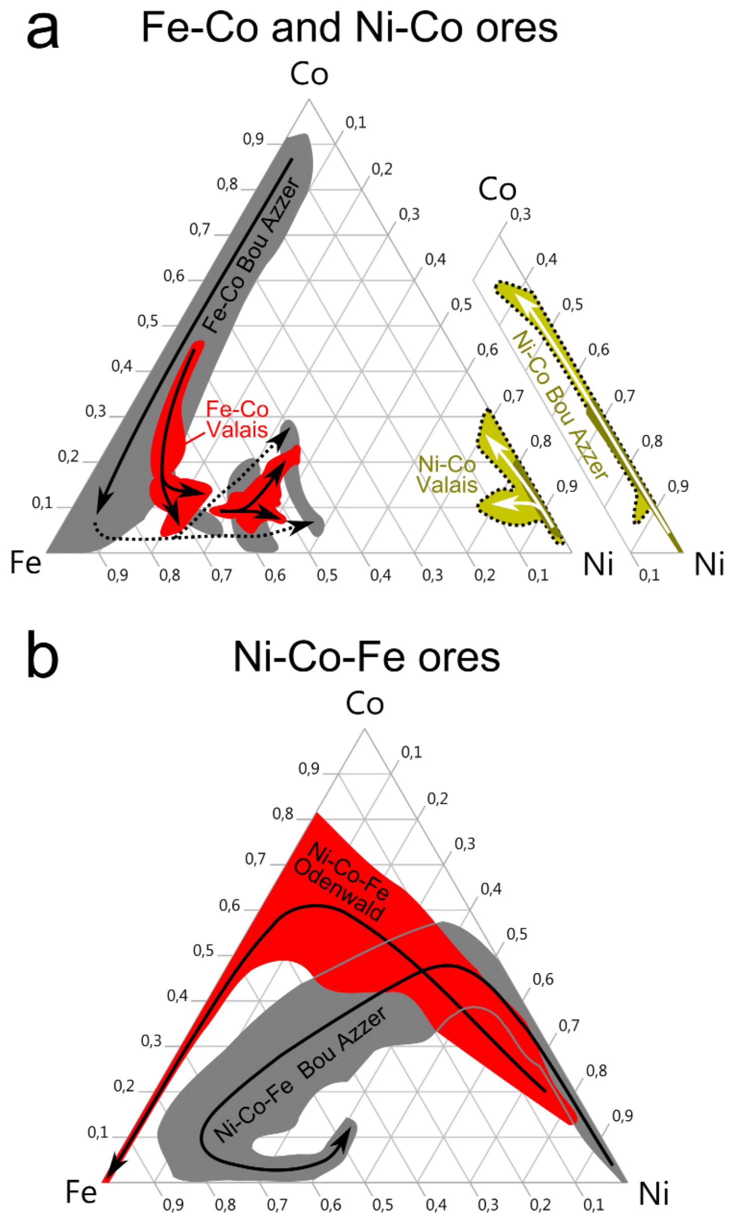

Figure A6: Illustration of the di- and sulfarsenides Fe-Co-Ni evolution according to the sub classification of arsenide-dominated five-element veins in Table 8. For further information see text.